Annual Report for FY 1982

Prepared Under Grant No. 7645

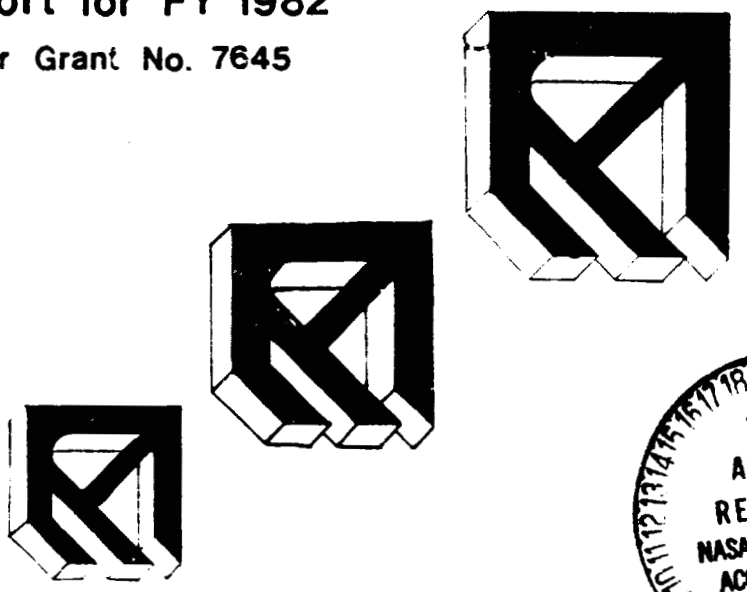

The Materials Processing Research Base of the Materials Processing Center

Submitted by

Merton C. Flemings

Materials Processing Center

Massachusetts Institute of Technology

Cambridge, Massachusetts 02139

Submitted to

National Aeronautics and Space Administration

400 Maryland Avenue S.W.

Washington, D.C. 20548

(NASA-CR-170174) THE MATERIALS PROCESSING RESEARCH BASE OF THE MATERIALS PROCESSING CENTER. REPORT FOR FY 1982 Annual Report, 1 Oct. 1981 - 30 Sep. 1982 (Massachusetts Inst. of Tech.) 305 p HC A14/MF A01 N83-22319

Unclas

G3/23 03303

The Materials Processing Research Base of the Materials Processing Center

Annual Report for FY 1982

Prepared Under Grant No. 7645

Materials Processing Center
Massachusetts Institute of Technology
Cambridge, Massachusetts 02139

Contents

Introduction 1

Nucleation and Rapid Solidification 5

M.C. Flemings and J. Szekely, "Basic Study of the Role of Convection in Grain Refining" 5

N.J. Grant, "The Structure and Properties of Rapidly Solidified, Highly Alloyed Aluminum Materials" 54

G. Yurek, "Development of Rapidly Solidified, Oxidation Resistant Alloys" 66

S.A. Allen, "Processing of Sendust-Type Soft Ferromagnetic Alloys" 83

Fluid Flow and Crystallization Processes 89

A.F. Witt, "Heat Flow and Segregation in Directional Solidification" 89

R.A. Brown, "Fluid Flow in Crystal Growth: Analysis of the Floating Zone Process" 200

R.A. Brown and A.F. Witt, "Solutal Convection and Its Effects on Crystal Growth in Binary and Pseudo-Binary Systems with Large Liquidus-Solidus Separation" 238

D.K. Roylance, "Analysis of Polymer Melt Processing Operations" 264

D.R. Sadoway, "Studies of Metals Electroprocessing in Molten Salts" 286

Adaptive Materials Processing 295

T.W. Eagar, "Adaptive Control of Welding Processes" 295

Introduction

This is the third annual report of the research activities conducted at the Materials Processing Center under the Materials Processing Research Base of NASA Grant #7645 during the period October 1, 1981 through September 30, 1982. Research projects conducted under the auspices of this grant include work in the areas of nucleation and rapid solidification, fluid flow and crystallization processes, and adaptive materials processing.

NASA's initial and continuing funding of the Materials Processing Research Base has contributed significately to the research and industrial activities of the Center to develop and mature in an expeditious manner. The actual dollar support provided by NASA has been effectively leveraged to promote research and industrial interactions in areas of national interest and of particular relevance to the Space Program.

Since its inception in 1979, the Materials Processing Center has sustained very rapid growth. The Center's staff has grown to some 15 faculty members, 30 research staff, and 56 graduate students, all drawn from a number of MIT Departments, including Materials Science and Engineering, Chemical Engineering, Mechanical Engineering, and Electrical Engineering and Computer Science. The total funding level has grown to $3.425M, of which $1.267M is derived from industrial sources.

A very important activity which came to fruition in 1982 was the creation of the Materials Processing Center/Industry Collegium, which has provided an excellent focal point for close interaction with industrial organizations. Founded on November 1, 1981, the Collegium currently has more than forty industrial members and has a goal of

one hundred members for 1983. The Collegium promotes information and technology exchange through its Collegium Reports and Workshops. The Collegium also facilitates personnel exchange between industry and government agencies and MIT. In addition, the Collegium provides fellowships and scholarships to focus attention upon and attract top students to materials processing research. There are currently three fellowships for the 1982-1983 academic year, with commitments for four 1983 summer scholarships and ten full-year fellowships for the 1983-1984 academic year. The Collegium also provides seed research funds, assists in acquiring necessary equipment, and supports the development of new curriculum and text books.

Research efforts within the Materials Processing Center strive to control the structure, shape, and properties of materials at acceptable economic and social costs, through the effective utilization of the scientific and engineering base. The research activities of the Center may be divided into the following two broad categories:

1) the Materials Processing Research Base, that is, work which is directly supported by NASA; and
2) the overall materials processing research effort, which is supported by other governmental or industrial sources.

The present report describes individual projects completed under the Materials Processing Research Base. Information pertaining to the general research effort will be contained in the 1982 Materials Processing Center Annual Report. While very substantial in its own right, the Materials Processing Research Base has further served as an extremely important nucleus for facilitating the growth of research efforts in related areas.

The work described in this report, while involving research in the broad field of materials processing, has two common features: the problems are closely related to space processing of materials and have both practical and fundamental significance. An interesting and important feature of many of the projects is that the interdisciplinary

nature of the problem mandates complementary analytical modeling/experimental approaches which are best undertaken by several investigators. The joint projects of Professors Brown and Witt, involving crystal growth, and Flemings and Szekely, dealing with rapid solidification and grain refining, are excellent examples of such cooperative efforts. Very close collaboration between investigators occurs in many other instances, although this may not appear formally in the project description. Indeed, the facilitation of such close cooperation is a major function of the Center.

Another important aspect of many of the projects funded under the NASA grant is the increasing use of mathematical modeling techniques as one of the research tools. The predictive capability of these models, when tested against measurements, plays a very important role in both the planning of experimental programs and in the rational interpretation of the results.

Finally, and perhaps most important, many of the projects described in this report will have a space experiment as their ultimate objective. Allowing for the realities of the 1980's, these space experiments cannot be undertaken lightly, but require extensive ground-based preparations. Mathematical models are proving to be extremely valuable in projecting the findings of ground-based experiments to microgravity conditions.

Of the projects funded by NASA, the Grain Refining/Rapid Solidification program directed jointly by Professors Flemings and Szekely is the closest to realization as a space experiment. The space apparatus has been designed (on the basis of very extensive ground-base measurements and sophisticated calculations) and a formal proposal for the space experiments is being submitted. A formal proposal for space experiments on electromagnetically-driven flows in transparent media (Professor Szekely) will be submitted to NASA during the early part of 1983. Other space experiments on crystal growth under conditions of microgravity (Professors Witt and Brown) and electrolytic processing (Professor Sadoway) are also being contemplated.

Nucleation and Rapid Solidification

Basic Study of the Role of Convection in Grain Refining

Principal Investigators: **Merton C. Flemings**
and
Julian Szekely

RESEARCH SUMMARY

The scientific aim of this program is to obtain a better understanding of fluid flow, nucleation, grain refinement and structure in undercooled melts. Work under Professor J. Szekely has the following principal components:

(i) Calculation of the electromagnetic force field, the fluid flow field and the temperature field in levitation melted (positioned) specimens both under earthbound and zero gravity conditions, and the verification of these through a comparison with experimental results.

(ii) The use of the above techniques for the rational design of in-flight experiments, fully utilizing the unique features available in a zero gravity environment.

(iii) Fundamental studies of electromagnetic force field-turbulence interactions.

(iv) The interfacing of these results with the undercooling studies conducted under Professor Flemings' direction.

(v) The broad dissemination of the fundamental findings through potential applications in metals processing.

Work under the direction of Professor M.C. Flemings and Dr. Y. Shiohara is in the following four areas:

PRECEDING PAGE BLANK NOT FILMED

ORIGINAL PAGE IS
OF POOR QUALITY

(1) Emulsification studies on undercooling and levitation melting Sn-Pb alloys.

(2) Fine droplet studies on iron and nickel base alloys.

(3) Thermal and structural measurements on levitation melted droplets of iron and nickel base alloys.

(4) Emulsification studies on iron and nickel base alloys.

To date, a total of 3 publications have resulted from this work; these are listed at the end of this section of the report[7-9].

The Mathematical and Physical Modelling of Electromagnetically Driven Fluid Flow and Associated Transport in Contained and in Containerless Melts

(i) Electromagnetic Force Field and Fluid Flow Field Calculations Concerning Levitated Specimens

A formulation has been developed to represent turbulent, recirculating flow as driven by the combination of buoyancy and electromagnetic forces in levitated specimens. The general vectorial form of the governing equation is given as:

$$\nabla \cdot u = 0 \tag{1}$$

equation of continuity

$$-\nabla \cdot \rho \underset{\sim}{u} \; \underset{\sim}{u} - \underset{\sim\sim}{\nabla o} - \underset{\sim\sim}{\nabla \tau}^{(t)} + \rho F_{\underset{\sim}{b}} \tag{2}$$

where $\nabla \cdot \tau$ is the turbulent stress tensor and F_b is the body force field, which in general will include both the buoyancy and the electromagnetic forces. The electromagnetic component of the body force was calculated using the technique of mutual inductances[1]. The buoyancy component, which is of relevance only for ground based applications was obtained through the simulataneous solution of the thermal energy balance equation.

The thermal energy balance equation takes the following form:

$$\underset{\sim}{U} \nabla T = \nabla k \nabla T \tag{3}$$

ORIGINAL PAGE IS
OF POOR QUALITY

where k_e is the effective thermal conductivity.

The system of equations (1-3) was solved numerically, utilizing the k-ε model to represent the components of the turbulent stress tensor. An extensive set of the computed results pertaining to ground based conditions has been published[1,2,3]. Here we shall present a selection of the computed results concerning zero gravity conditions. In the presentation of the computed results emphasis will be placed on the application of these to the interpretation of previous experimental measurements, notably the SPAR 1 series and on their use in the design of the Space Shuttle experiments, which involve scale-up.

SPAR 1 Experiments

In the SPAR 1 experiments zero gravity (actually 10^{-5}g) conditions were produced, for brief time periods, say 5-7 mins. by using a rocket. In the studies beryllium spheres, 9 mm in diameter were levitated, using a spherical coil, sketched in Fig. (1). The coil was made of copper tubing, 2.5 mm in diameter. The coil consisted of two turns, each hemisphere wound on a 16 mm diameter sphere. The aximuthal angles formed by the two turns of the coil are 46^{o} and 74^{o} respectively. The power supply was a 107 kHz radio frequency generator, which drew 1.2 kW, DC from a battery. The coil current was 300A and it was estimated that a power absorption rate of about 46 watts produced a mean sample temperature of 1400^{o}C.

Fig. 2 shows the computed electromagnetic force field and the heat generation pattern, while Fig. 3 shows the computed velocity and temperature fields. It is of interest to compare these results with the corresponding values computed for earthbound conditions using a coil assembly sketched in Fig. 4, for a steel sphere, 6 mm in diameter, given in Fig. 5 and 6.

It is seen that vigorous circulation exists in both cases, but for the zero gravity case we have four, rather than two recirculating loops in each half sphere. This significant difference between the two flow patterns is not due to the absence of gravity, but rather attributable to the difference in coil configuration and the actual position of the sphere within the field

and hence the actual force field induced within the sphere which was depicted in Fig. 3 and 5. This point will be discussed subsequently.

Fig. 7 and 8 show the computed values of the turbulent kinetic energy and the ratio: effective viscosity/molecular viscosity for the zero gravity beryllium run and the earthbound steel run respectively.

It is seen that in both cases the turbulent kinetic energy and the turbulent viscosity are higher in the center than at the outer surface, however there are marked differences in the details of the behavior. In the zero gravity case the isopleths are symmetrical, furthermore, the ratio of the turbulent viscosity to the molecular value is much higher and varies much less than in the earthbound case. The behavior of the turbulent kinetic energy parallels that seen for the turbulent viscosity.

Space Shuttle Experiments

In the proposed space shuttle experiments a variety of materials will be examined, but for the purpose of comparison beryllium will be used in the present example. The same spherical coil design will be used as for SPAR 1, but the linear scale will be increased by a factor of two.

In scaling these systems the following principal factors have to be considered.

(i) A twofold increase in the linear dimension will provide a fourfold increase in the surface area of the specimen over which heat is dissipated.

(ii) Approximate circuit analysis indicates that this scale-up will also increase the energy absorption due to the induced current by a factor of four.

(iii) The above would indicate that the system could be operated at the same current, however due to impendance losses associated with the larger coil a higher coil current would be required.

Calculation have shown that a coil current of $500A \sim \sqrt{2} \times 300A$ would give an energy input of 255W, which in turn would give the desired $1400^{o}C$ specimen temperature.

Fig. 9 shows the computed electromagnetic force field and heat generation pattern for this larger coil, which is quite similar to that computed for the smaller spherical coil.

Fig. 10 shows plots of the computed velocity and temperature field[illegible]e four recirculating loops, characteristic of the spherical coil desig[illegible]re readily apparent, but the numerical value of the absolute velocity smaller, by about a factor of four than that found for the larger coil.

Fig. 11 shows the computed turbulent kinetic energy and the ratio: effective viscosity/molecular viscosity. It is seen that the flow field is highly turbulent but there is very little spatial variation of these properties. The important findings assocated with these results are that there are significant differences in the fluid flow fields in levitation melted droplets under earthbound and zero gravity conditions.

More particularly for a zero gravity condition and the coil configuration employed we found a symmetrical circulation pattern and four recirculating loops in contrast to a asymmetrical circulation pattern and two circulation loops predicted for the earthbound conditions.

The actual dimension of the drop was found to play a major role in determining the structure of the turbulence. For the small, earthbound system there was a marked damping of the turbulence on approaching the free surface, due to the changes in the angular momentum (the centrifugal and the Coriolis forces). In contrast for the larger, zero gravity systems the spatial variation in the turbulent kinetic energy was greatly reduced.

Examination of the larger system (i.e. the planned Space Shuttle experiment) has shown that notwithstanding the increase in the absolute value of the coil current the actual linear velocity would be significantly reduced (by a factor of four compared to an identical geometrical arrangement but having half the linear dimension).

Our ability to quantify these effects is thought to represent significant contribution to the fundamentals of fluid mechanics and at the same time is an important asset in the rational planning of the in-flight experiments.

(ii) The Design of Space Shuttle Experiments

The principal scientific trust of the proposed space experiments is the extension of the ground based experiments to a zero gravity environment. The actual concept of these experiments has been defined as a result of the prior ground based studies; the feasibility of accomplishing the measurements during in-flight conditions has been as certained as a result of discussions with Dr. T. Frost of the GE Space Science Center, in Valley Forge, Pennsylvania.

While essentially the same equipment will be used for both the fluid flow and the undercooling studies, the details of the experimental objectives will necessarily differ.

The purpose of the experiments is to determine the melt velocities on the free surface of levitated specimens at various current levels and thus enable a direct comparison of these experimental measurements with the theoretical predictions that have been developed as part of this program.

In essence the experimental procedure will involve the levitation melting of tin spheres, 1.84 cm in diameter, at various current input levels. The point values of the velocity at the surface of the tin specimens will be determined using tracer particles, the location of which would be followed using a cine camera, with a frame speed of 48 s^{-1}.

The specific experiments to be performed on tin would include:

(a) the determination of the steady velocity, corresponding to a particular current input level at several current inputs.

(b) the rate of velocity decay, once the driving force has been drastically reduced.

Significance of the Experiments

Fluid flow in levitation melted and positioned specimens is an interesting class of problems in electromagnetically driven flows, because it involves a curvi linear coordinate system.

The proposed measurements would enable us to critically test the theoretical representations that have been developed, through verifying -

(a) the predictions made regardi the flow patterns and the velocity fields.

(b) the dependence of the velocity field on coil current.

(c) the turbulent - laminar transition.

(d) the decay times, once the driving force has been discontinued.

These experiments could not be carried out in an earthbound environment, because under the conditions of the earth's gravitational field there is a very narrow limit of coil currents, which allows one to attain levitation; almost invariably this corresponds to turbulent flow. Furthermore, one is limited in the size of the specimens that may be levitated. Under earthbound conditions it would be impossible to:

(i) measure the current dependence of the velocity.

(ii) measure the decay times.

(iii) determine the laminar -turbulent transition.

(iv) ascertain the fundamental difference in the circulation patterns that have been predicted for earthbound and zero gravity conditions.

In addition to testing the theoretical predictions pertaining to zero gravity levitation and positioning, the proposed experimenttal program would make an important contribution to the fundamentals of electromagnetically driven flows - a domain where accurate measurements are difficult to make. Thus the verification of the modelling equations should find rather widespread application in a number of related fields.

Last but not least, the experimentally and theoretically predicted velocity fields will represent an important contribution to the characterization of the temperature and velocity fields needed in the modelling and quantitative description of the undercooling experiments.

(iii) Fundamental Studies of Electromagnetic Force Field - Turbulence Interactions

The containerless processing program inherently involves the interaction of electromagnetic fields and fluid flow fields. One level of these interactions, namely electromagnetically driven flows has been discussed in preceeding sections, in connection with levitation melting. However, there exists another, more subtle level of interactions namely the possible damping of turbulence by an electromagnetic field.

In order to examine this problem an apparatus has been constructed to study heat and fluid flow phenomena in a Woods Metal melt, generated by the passage of an electric current between two electrodes. The apparatus is sketched in Fig. 12. An important component in this project is the use of a hot film anemoneter for the measurement of the velocity and of the turbulent fluctuations. A hot film anemometer assembly usable in molten Woods Metal has been developed for this particular application[5].

The calibration system for the hot film anemometer is given in Fig. 13; this is seen to consist of a shallow boat, containing the molten Woods Metal, through which the probe is being dragged at a predetermined, steady velocity. Quite sophisticated signal processing is required, the arrangements for which are shown in Fig. 14. A typical calibration curve is given in Fig. 15, indicating the drift, which is often associated with hot film anemometry in molten metal systems.

Finally Fig. 16 shows the calibration curve with drift correction. which is quite satisfactory.

Having established the feasibility of hot film anemometry in molten Woods Metal, the work is now continuing with systematic data gathering regarding velocity and turbulence paramenter measurements. The results of this work should be quite important in the containerless processing program, but should also find rather more widespread application in the general field of metals processing.

(iv) The Interfacing of the Heat and Fluid Flow Work with the Undercooling Studies

An important component of the modelling program is its association with the undercooling studies, conducted in Professor M.C. Flemings' laboratory. The detailed description of this work is available in Sections of this report. This effort is primarily experimental with the major thrust of examining undercooling, the subsequent recalescence of various alloy systems under a variety of conditions. Particularly noteworthy features of this work are that very significant undercoolings have been achieved, furthermore the thermal history of the recalescence process has been recorded, and very interesting metastable phases have been produced.

Work is in progress regarding the modelling of the heat flow and the recalescence and metastable phase formation in these systems. The fluid flow and heat flow calculations, reported in the preceeding sections are of course closely related to this effort; more specifically work is in progress to define the fluid flow conditions both earthbound and for zero gravity in these undercooling experiments. Furthermore joint work has been initiated regarding the mathematical modelling of the recalescence process.

(v) Industrial Applications of the Heat and Fluid Flow Calculations

The tackling of the heat and fluid flow problems in containerless processing operations has lead to the development of very powerful computational tools capable of predicting the electromagnetic force fields, fluid flow fields, heat and mass transfer in a variety of metals processing operations. An important, but of course not dominant component of our research program is to disseminate these results broadly to the metals industry, thus providing direct industrial applications of the NASA sponsored basic research program.

Examples of this work include the study of fluid flow in induction durnaces, and other steel processing operations, described in the preceeding report of the Center for Materials Processing.

A more recent industrial application, which is illustrated in the following has been the prediction of the velocity fields and mass transfer rates in a 4 ton induction furnace holding molten steel.

Fig. 17 shows a schematic sketch of the furnace, while the computed electromagnetic force field and the velocity fields are given in Fig. 18, 19 respectively. Fig. 20 depicts the experimental arrangement used for measuring the velocities in the melt, which essentially relied on the deflection of an immersed rod. Finally, Fig. 21 shows a comparison of the experimentally measured and the theoretically predicted dependence of the linear melt velocity on the coil current. The good agreement, for pilot scale type operations, is readily apparent.

Studies were also made to predict the rate at which graphite rods, immersed in the melt would dissolve, and Table 1 shows a comparison between the predictions and the experimental measurement - here again the agreement is excellent.

UNDERCOOLING EXPERIMENTS ON TIN-LEAD, AND IRON AND NICKEL BASE ALLOYS

Emulsification Studies on Sn-Pb Alloys

Emulsifications are prepared using a high-speed stirring device patterned after Perepezko et al., Fig.22. Some of the emulsifications were reheated and the metal droplets then resolidified at controlled cooling rate in a DTA. With the droplet sizes and experimental technique explained, undercoolings of about 95 to 105^{o}C were typically obtained. Other samples were rapidly solidified in the device shown in Fig.23. Thus in these cases, undercoolings of not less than about 110^{o}C were combined with rapid cooling rates (calculated to be in the range of 10^{6} ^{o}C/sec.).

The nucleation temperatures of the different alloys studied, when cooled at 10^{o}C/min. are shown in Fig.24. T_n represents nucleation of a tin-rich phase, and T_n' of a lead-rich phase.

ORIGINAL PAGE IS
OF POOR QUALITY

Sn-5 wt% Pb dropelts, undercooled and rapidly solidified in the agitated bath, show "featureless" structures, Fig. 25, which are supersaturated solid solution. A lead-rich pahse precipitates in the solid state after extensive holding at room temperature or heating above room temperature, Fig. 26. Having a cold bath temoperature for quenching is essential to obtain the supersaturated structure, Fig. 27.

In Sn-Pb alloys of compositions where two phases nucleate, structures are obtained that are strongly sensitive to cooling rate, such as that of the Sn-45 wt% Pb alloy in Figure 28. When rapidly quenched, the solidification structure is composed of a dendritic, lead-rich phase (white, with dark solid-state precipitates) and a dark tin-rich pahse. When slowly cooled (10^{o}C/min.), the lead-rich phase coarsens as shown in Figure 28 on the far right.

Analytical studies are now underway as part of this research to understand and model the nucleation, solidification and heat flow behavior of these undercooled droplets, and there will be reported at a later date.

FINE DROPLET STUDIES ON IRON AND NICKEL BASE ALLOYS

We have developed a method for obtaining high undercooling in metal alloys by mixing fine metal powder with glass powder, and then heating and cooling the composite. To date, we have achieved 475^{o}C undercooling in 316 stainless steel in this way - a substantially higher undercooling than has been obtained by any other worker for an iron base alloy. The former maximum reported for Fe base alloys was 295^{o}C, Table 2.

As undercooling increases and particles size decreases, structures obtained in 316 tend to go from dendritic FCC; to "featureless FCC"; to mixed FCC/BCC; to full BCC. Figure 29 (top) shows the dendritic FCC microstructure characteristic of very low undercoolings. Figure 29 (bottom) shows the "featureless" microstructures characteristic of higher undercoolings. Dark particles are BCC; lighter ones are FCC. Mixed FCC/BCC structures are also obtained, Figure 30. (BCC structure surrounds the smaller FCC area). These results are in general agreement with expectations, and calculations confirm that in this alloy, the BCC structure can be formed (metastably) at undercoolings greater than about 120^{o}C.

THERMAL AND STRUCTURAL MEASUREMENTS ON LEVITATION MELTED DROPLETS OF IRON AND NICKEL BASE ALLOYS

Extended experiments have also been carried out on levitation melting, on solidification of levitation melted droplets, and on structures of droplets produced in this way.

In current work, iron and nickel base alloy droplets are floated in molten glasses to achieve higher undercoolings. Surface temperatures of recalescing, and of subsequently cooling droplets are being measured to provide high-speed data for modelling studies. Figure 31 is a schematic illustration of the equipment, showing the sample, the high speed sensing device, and the digital oscilloscope.

Figure 32 is an example of short time thermal profiels obtained in a Ni-32.5 wt% Sn (eutectic) alloy. It is an interesting and startling observation that the total recalescence time (at least of the surface of the sample) decreases sharply with increasing undercoolings. Figure 33 shows longer time thermal profiles (up to 10 sec.) for these droplets; this figure provides an indication of the time required to complete recalescence. Note that the rapid surface cooling rates are obtained immediately after solidification (> 10^2 ^{o}C/sec.) even in these very large droplets (5 mm = 5,000 μm). This rapid cooling is due to extraction of heat from the recalesced droplet into the much cooler glass. Much more of these data are being obtained and being used as foundation for developing a mathematical model both of solidification of these large droplets, and of the smaller droplets (5-50 μm) studied in other portions of this work.

ORIGINAL PAGE IS
OF POOR QUALITY

IMPLICATIONS FOR SPACE EXPERIMENTS

(1) Fine Metal Droplets Suspended in Glass

The fine droplet approach of mixing metal powder with glass and heating is an effective way of obtaining higher undercooling, in spite of one experimental probelm. That problem is coarsening or agglomeration of the particles. For example, starting with an initial average particle size of 15 μm, the

ORIGINAL PAGE IS
OF POOR QUALITY

typical average particle size after melting and resolidification is approximately 90 μm, an increase in droplet volume of over a factor of 200. This size increase, we believe, is much too large to be accounted for by diffusional coarsening. It most probably results largely from agglomeration due to gravitational settling in the glass, both before and after the glass is molten.

Further experiments are perhaps necessary to confirm this probable gravitational cause of agglomeration. Assuming this is the correct mechanism, an important space experiment becomes self-evident; that is, the carrying out of similar experiments in space. The absence of a gravitational field should permit retaining very fine particle sizes inside the glass, thereby obtaining much higner undercoolings than we have yet been able to achieve.

(2) Levitation Melted Droplet in Glass Blanket

Our current large diameter dorplet work (5 mm dia.) is on nickel base alloys levitated with a glass slag. Thus far, undercoolings obtained have been appreciably less than undercoolings obtained in the fine droplets, but the technique has great interest for us because we can measure the surface temperature of the droplet during recalescence using high speed optical methods.

Performing this experiment in space would permit eliminating both gravitational convection and induction stirring (since the power would not be needed to maintain levitation). Thus, we would have to be able to achieve increased undercoolings in this space experiment and could also measure the rates of recalescence in samples at these undercoolings, recording on telemetering the digitized information.

REFERENCES

1. N. El-Kaddah and J. Szekely, Mat. Res. Soc. Symp. Proc. on Materials Processing in Reduced Gravity Environment of Space. Rindone, Ed., p.191 (1982).

2. N. El-Kaddah, J. Szekely, Met. Trans. B., (1982), in press.

3. Annual Report of the Materials Processing Center, MIT, for 1981, pp.26-46.

4. N. El-Kaddah and J. Szekely, "Heat Transfer and Fluid Flow in Levitation Melted Droplets in a Zero Gravity Environment," submitted to Metallurgical Transactions.

5. A. Murthy and J. Szekely, "Hot Film Anemometry in Molten Woods Metal," submitted to Metallurgical Transactions.

6. N. El-Kaddah, G. Carlsson and J. Szekely, "Fluid Flow and Mass Transfer in an Inductively Stirred 4 Ton Melt," submitted to Metallurgical Transactions.

7. M.G. Chu, Y. Shiohara, M.C. Flemings, "Rapid Solidification of Highly Undercooled Alloy Droplets," submitted to Proceedings of AIME Fall meeting, 1982, St. Louis.

8. D.G. MacIsaac, Y. Shiohara, M.G. Chu, M.C. Flemings, "Structure of Undercooled Iron and Nickel-Based Alloys," submitted to Proceedings of AIME Fall meeting, 1982, St. Louis.

9. J.H. Perepezko, Y. Shiohara, J.S. Paik and M.C. Flemings, "Solidification of Undercooled Liquids," submitted to Proceedings of NBS Conference on Rapid Solidification, Gaithersburg, 1982.

PERSONNEL

Dr. Y. Shiohara
Mr. M.G. Chu
Mr. D. MacIsaac
Mr. Y. Wu

ORIGINAL PAGE IS
OF POOR QUALITY

ORIGINAL PAGE IS
OF POOR QUALITY

Table I

A comparison of the experimentally measured and the theoretically predicted mass transfer coefficients. Rod 10 cm from wall, coil current 2800 A

Immersion depth m	N_{Re}	Tu	Mass transfer coefficient $(m/s) \times 10^9$		
			measured	predicted turbulent	predicted laminar
.05	10800	0.25	1.2	1.87	0.7
.10	5385	0.7	2.5	2.46	0.49
.20	4005	1.1	2.4	2.79	0.43
.40	4315	1.]	2.4	3.18	0.45
.60	4285	1.0	2.4	2.7	0.44
.80	7932	2.8	2.4	1.62	0.595

ORIGINAL PAGE IS
OF POOR QUALITY

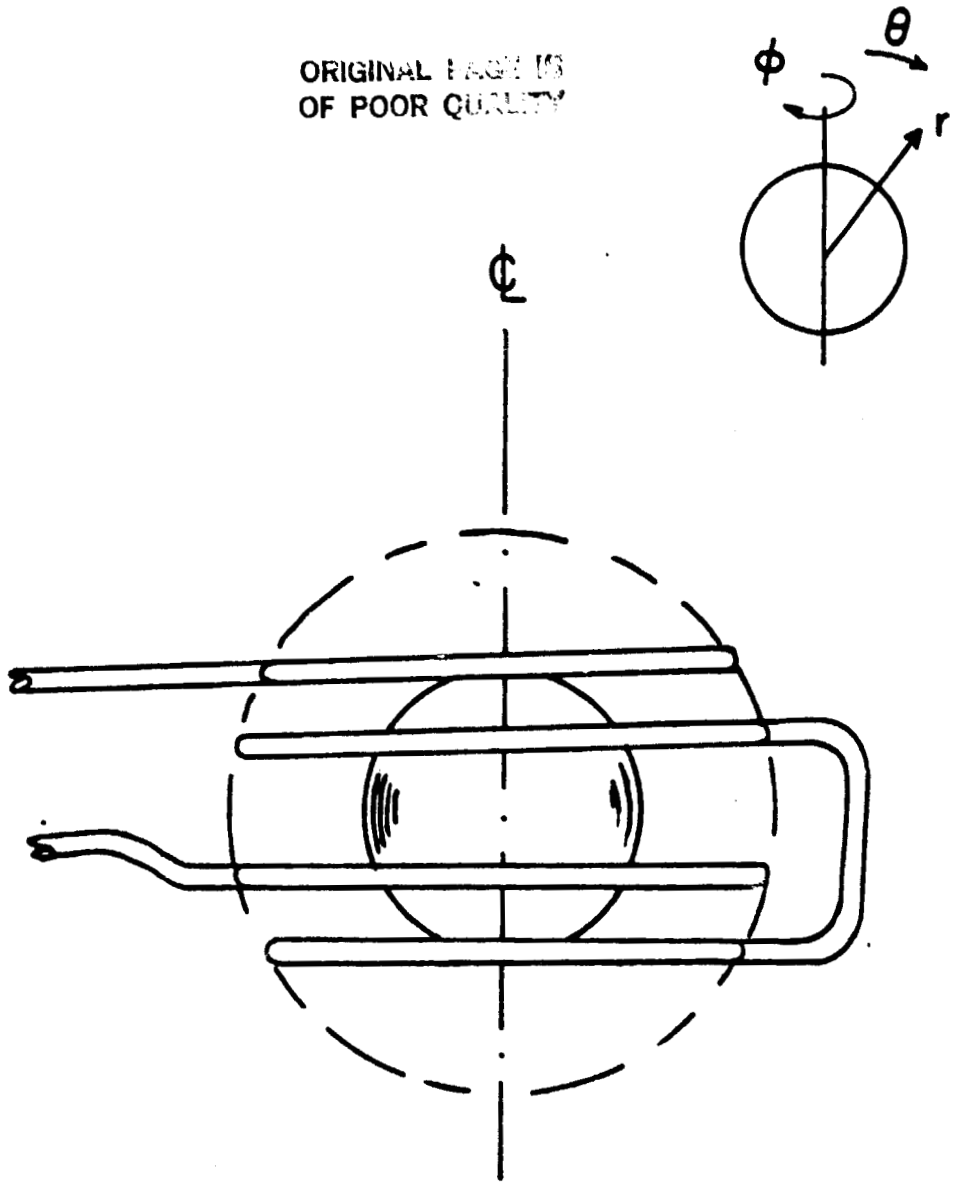

Fig. 1. Schematic sketch of the levitation coil used in SPAR 1 experiments.

ORIGINAL PAGE IS
OF POOR QUALITY

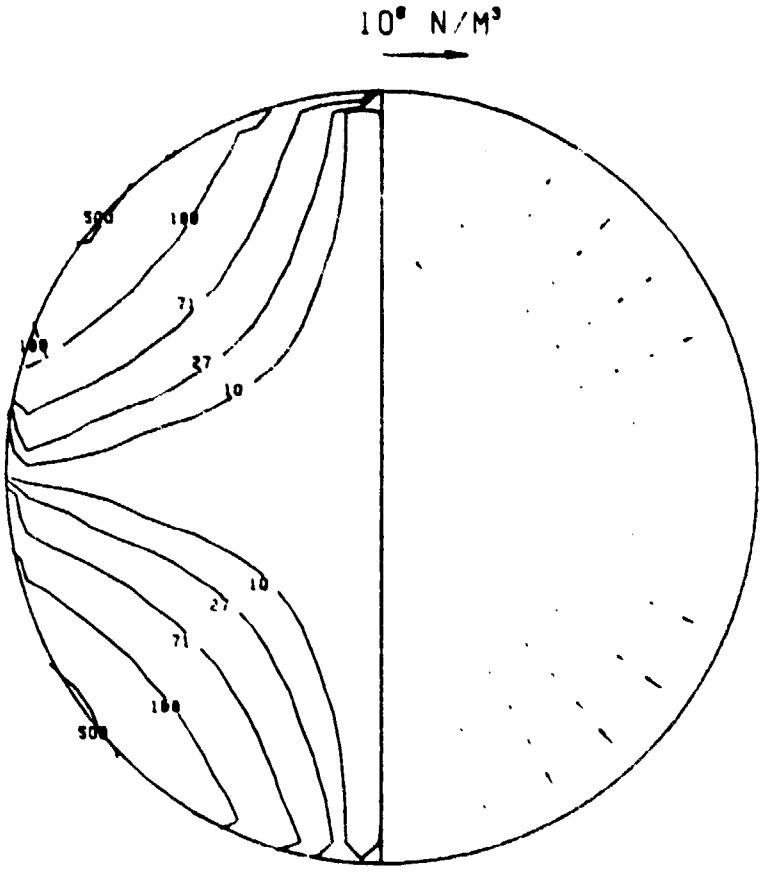

Fig. 2. Computed electromagnetic force field and heat generation distribution for a 9 mm beryllium sphere at zero-g.

ORIGINAL PAGE IS
OF POOR QUALITY

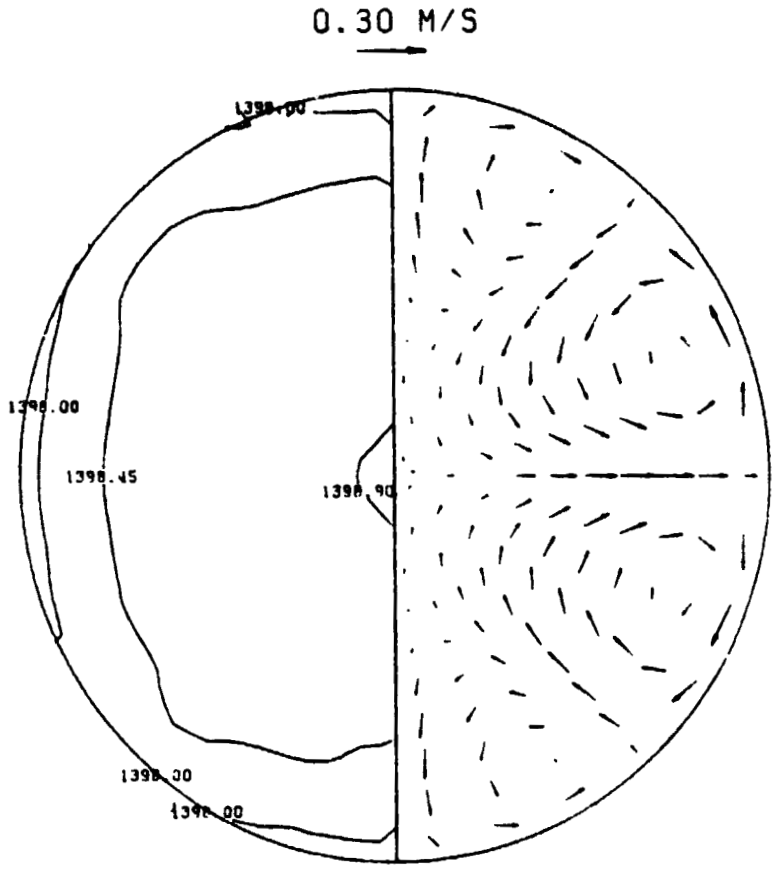

Fig. 3. Computed velocity field and temperature distribution for a 9 mm beryllium drop at zero-g.

ORIGINAL PAGE IS
OF POOR QUALITY

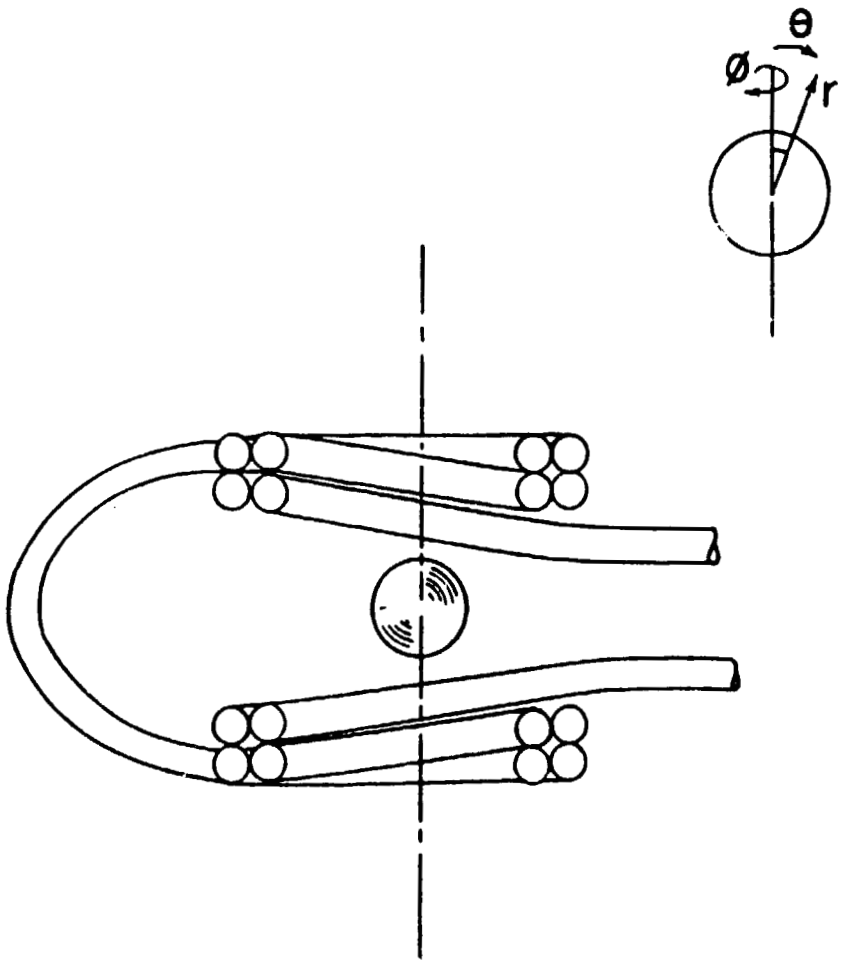

Fig. 4. Sketch of the levitation coil used in the earthbound calculations.

ORIGINAL PAGE IS
OF POOR QUALITY

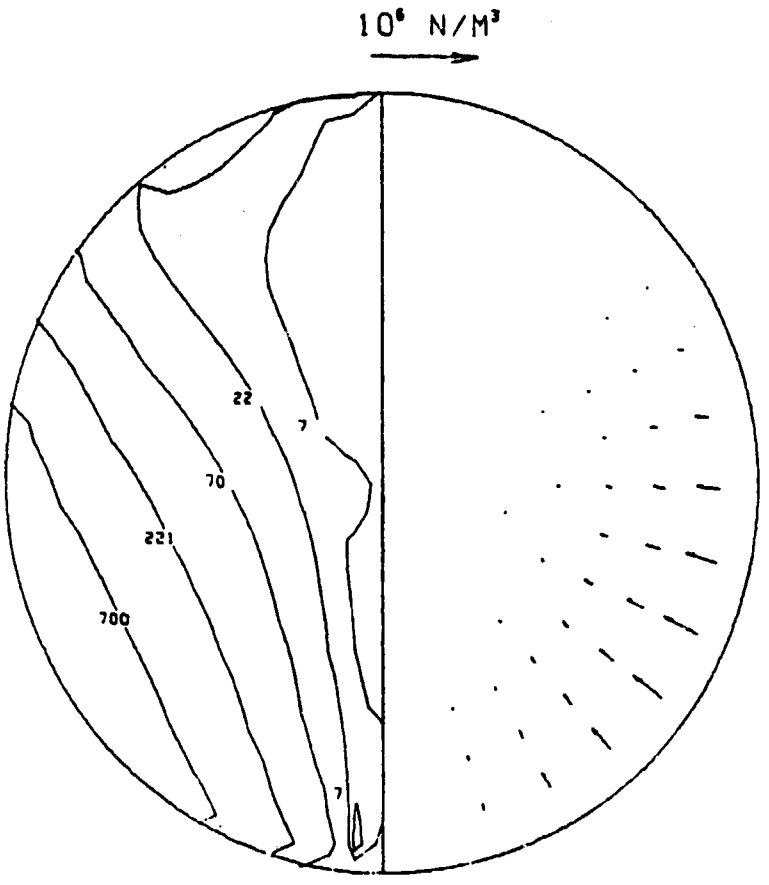

Fig. 5. Computed electromagnetic force field and heat generation distribution in a 6 mm iron drop at earthbound gravity for a coil current 250A.

ORIGINAL PAGE IS
OF POOR QUALITY

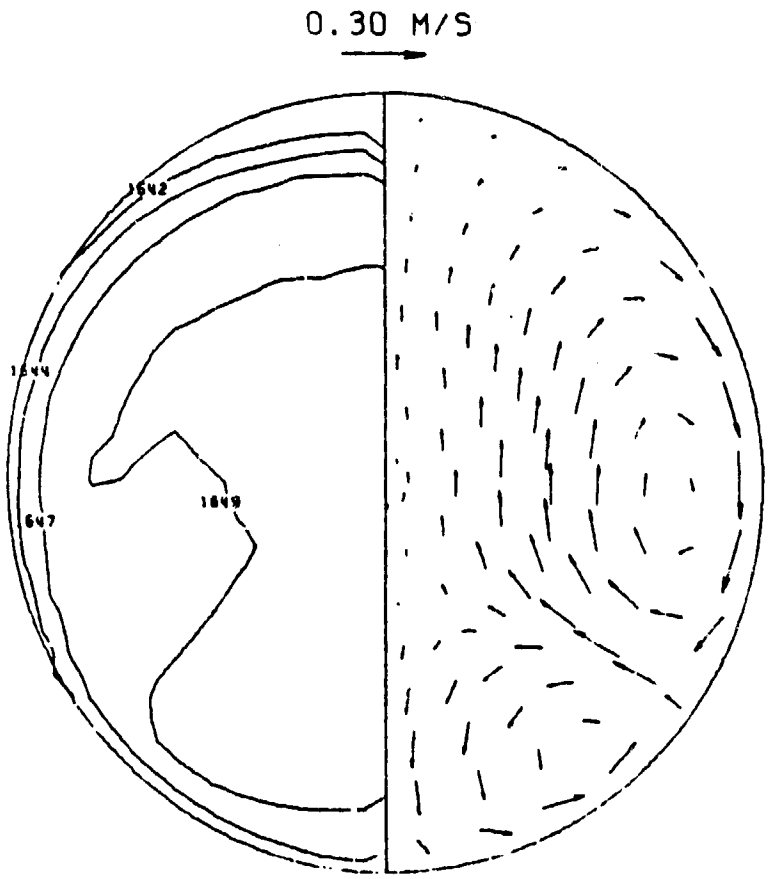

Fig. 6. Computed velocity field and temperature for a 6 mm iron droplet at earthbound gravity for a coil current 250A.

ORIGINAL PAGE IS
OF POOR QUALITY

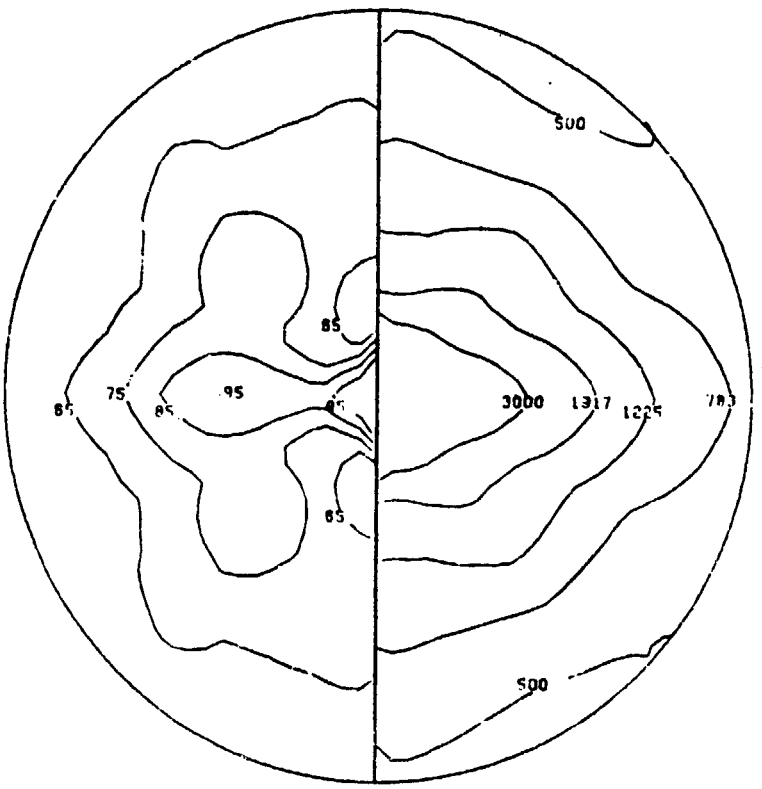

Fig. 7. Plot of computed contours of the turbulent kinetic energy ($\times 10^4$ m^2/s^2) RHS and μ_e/μ_ℓ LHS for 9 mm beryllium drop at zero-g.

ORIGINAL PAGE IS
OF POOR QUALITY

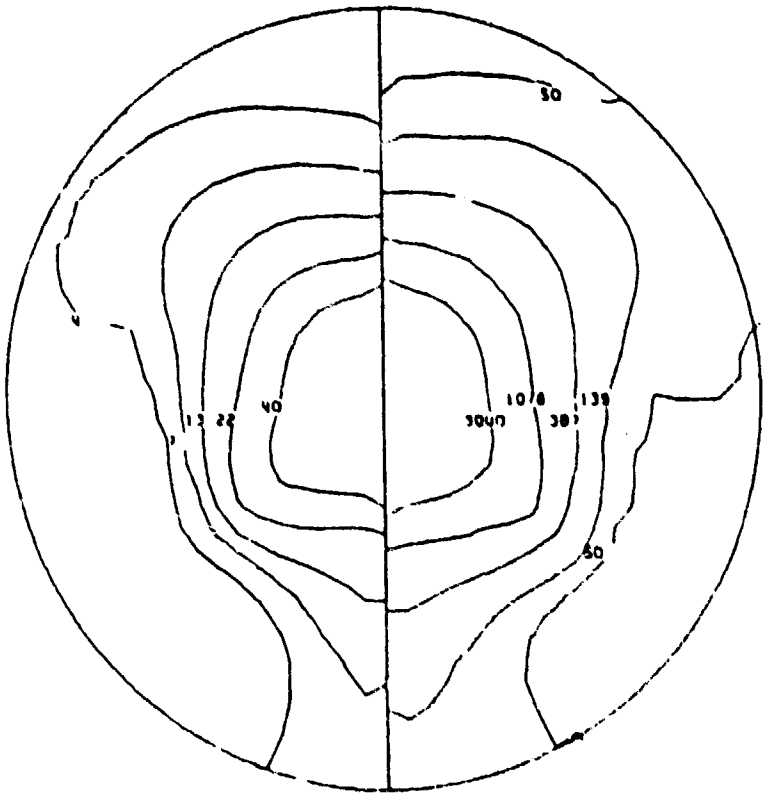

Fig. 8. Plot of computed contours of the turbulent kinetic energy ($x10^4$ m^2/s^2) RMS, and μ_e/μ_ℓ LHS for 6 mm iron drop at earthbound gravity.

ORIGINAL PAGE IS
OF POOR QUALITY

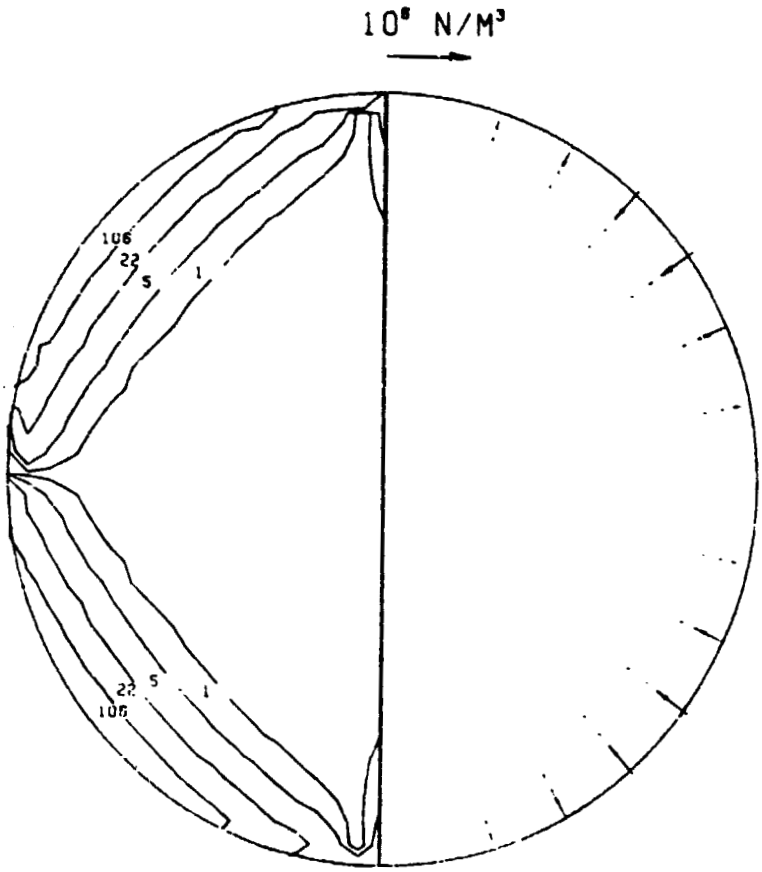

Fig. 9. Computed electromagnetic force field and heat generation distribution for an 18 mm beryllium drop at zero-g.

ORIGINAL PAGE IS
OF POOR QUALITY

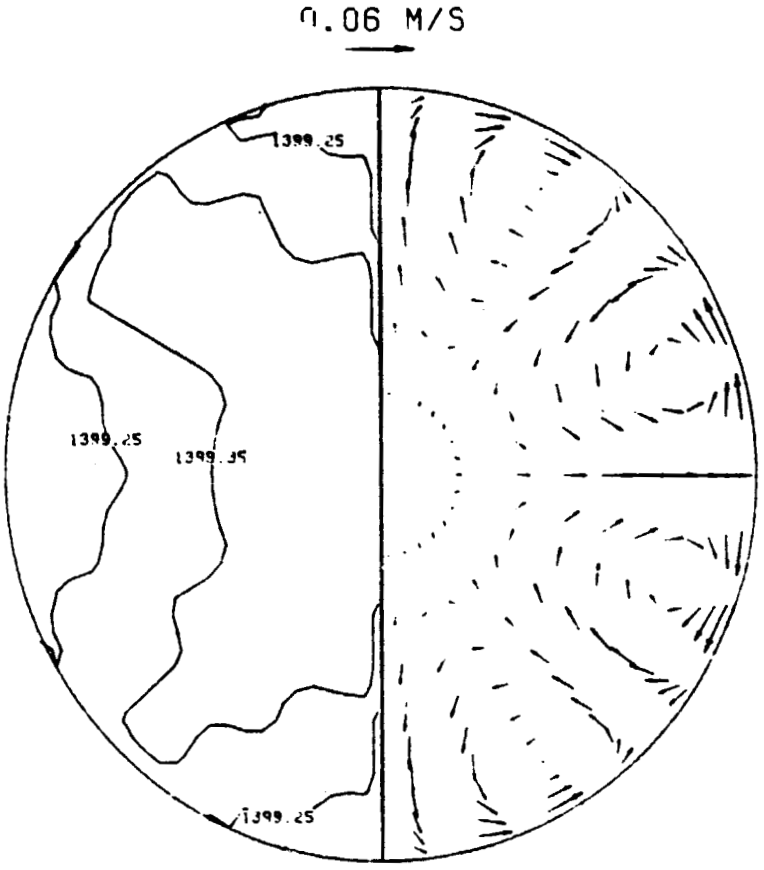

Fig. 10. Computed velocity field and temperature distribution for an 18 mm drop at zero-g.

ORIGINAL PAGE IS
OF POOR QUALITY

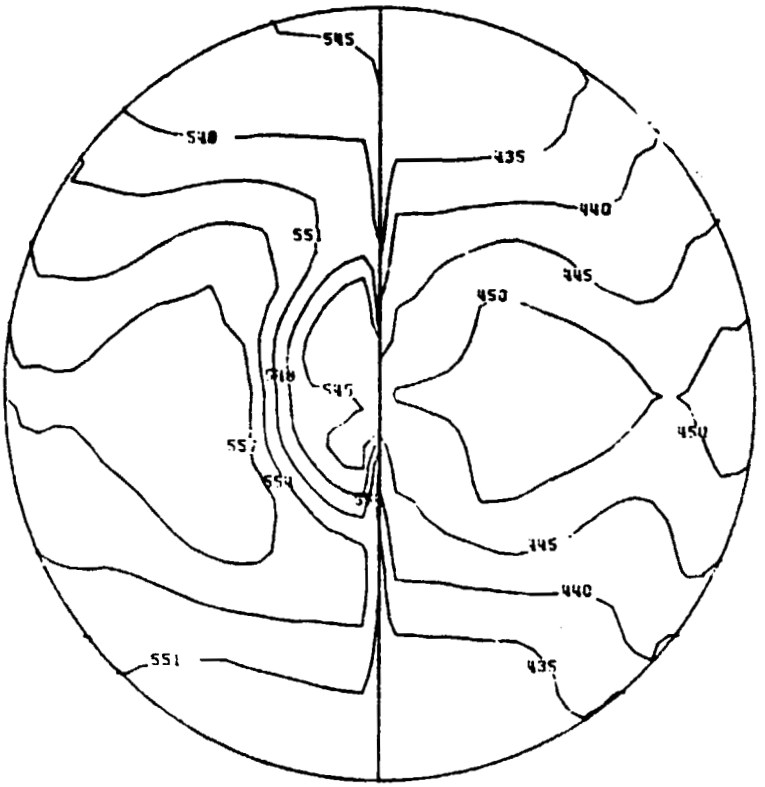

Fig. 11. Plot of the computed contours of the turbulent kinetic energy ($x10^4 m^2/s^2$) RHS and μ_e/μ_ℓ LHS for an 8 mm beryllium drop at zero-g.

ORIGINAL PAGE IS
OF POOR QUALITY

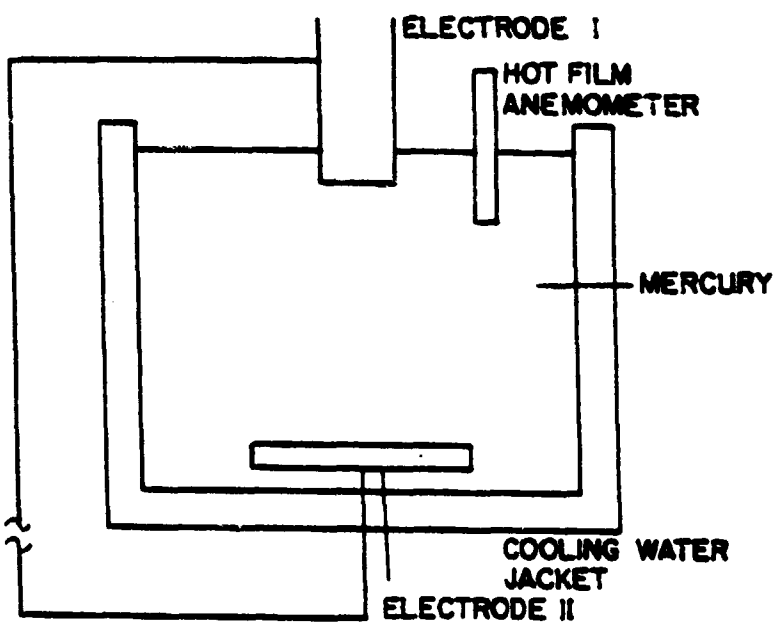

Fig. 12. Schematic sketch of the apparatus designed for measuring the electromagnetically driven velocity field in the Woods Metal system.

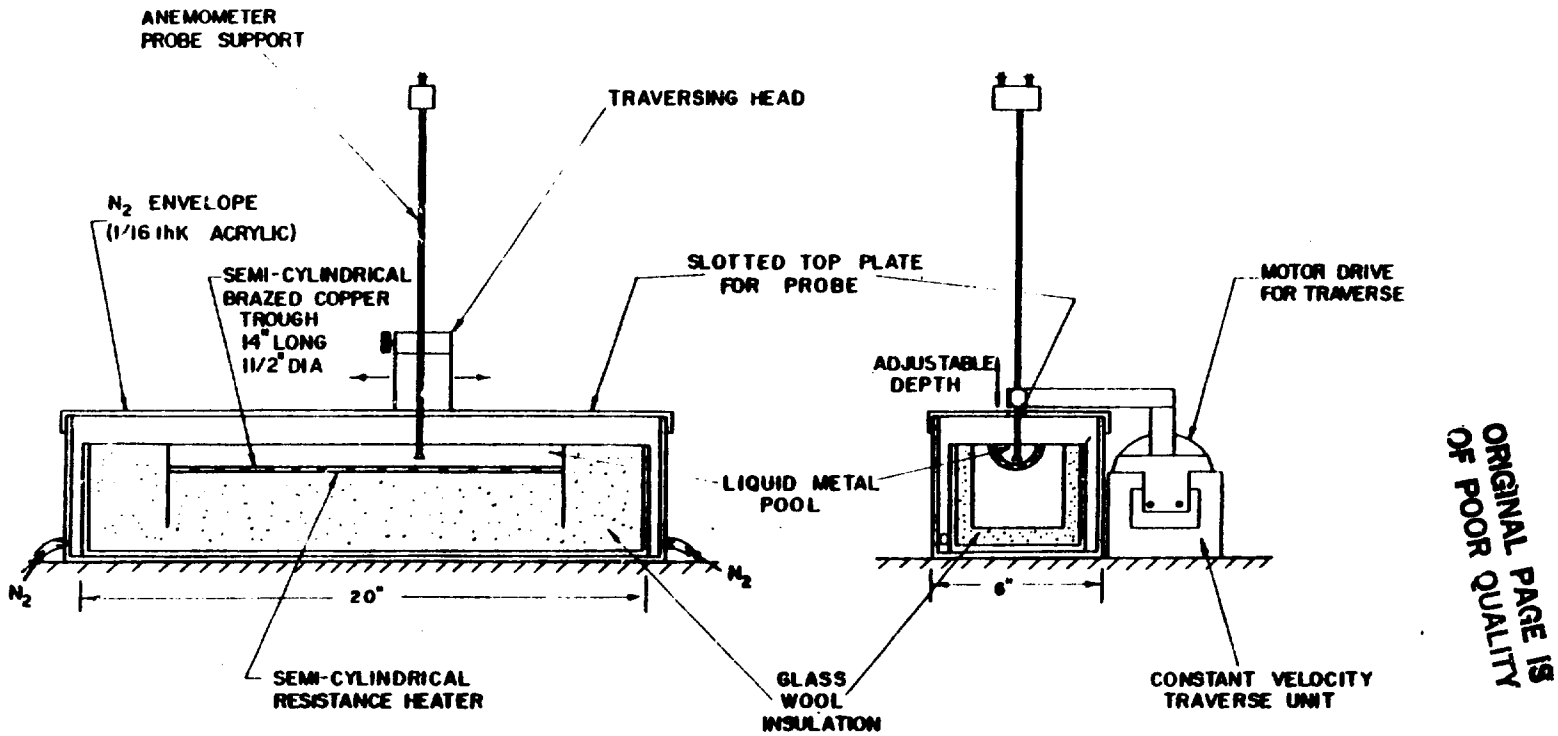

Fig. 13. Sketch of Calibration System.

ORIGINAL PAGE IS
OF POOR QUALITY

ORIGINAL PAGE IS
OF POOR QUALITY

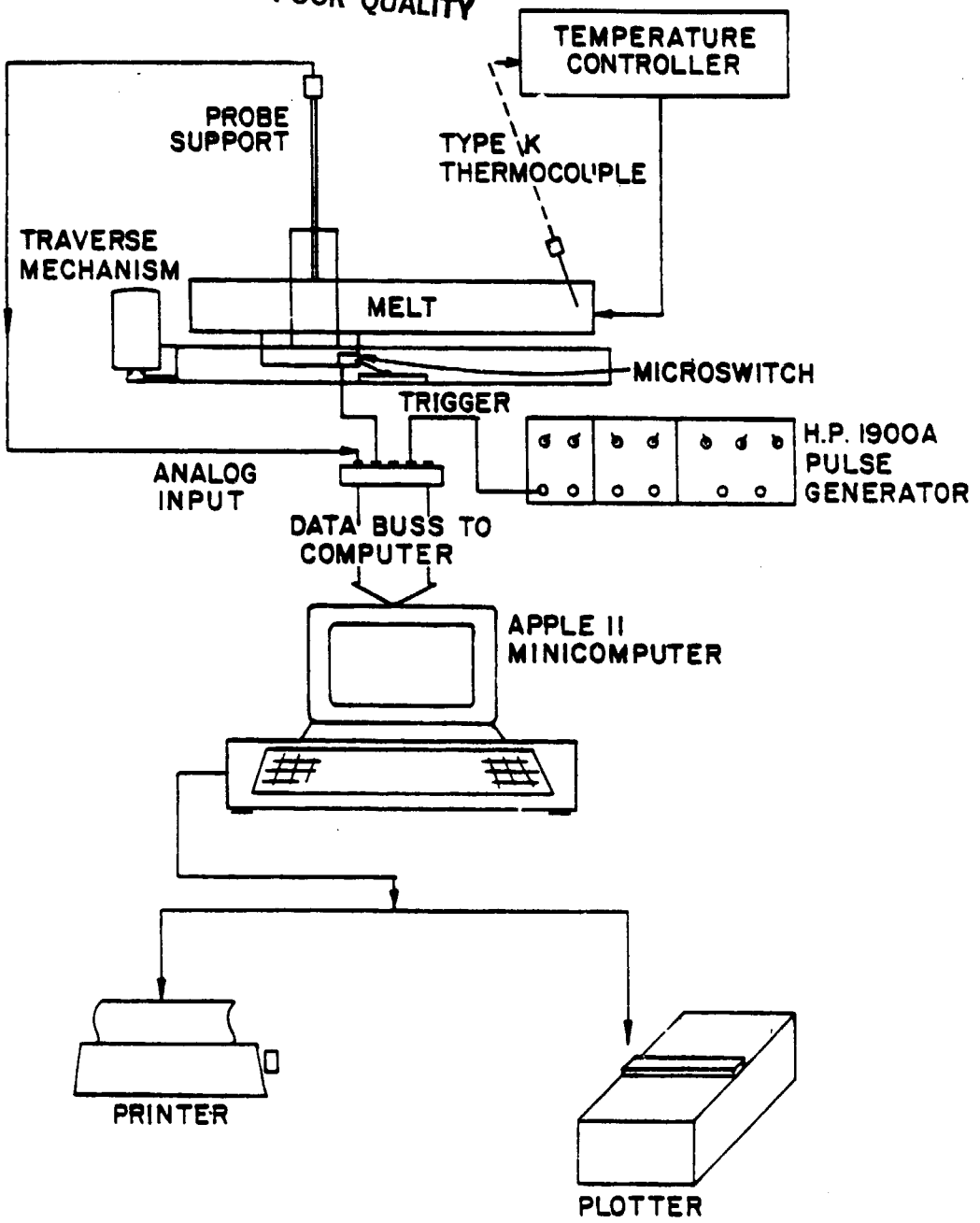

Fig. 14. Sketch of Data Processing Scheme.

ORIGINAL PAGE IS
OF POOR QUALITY

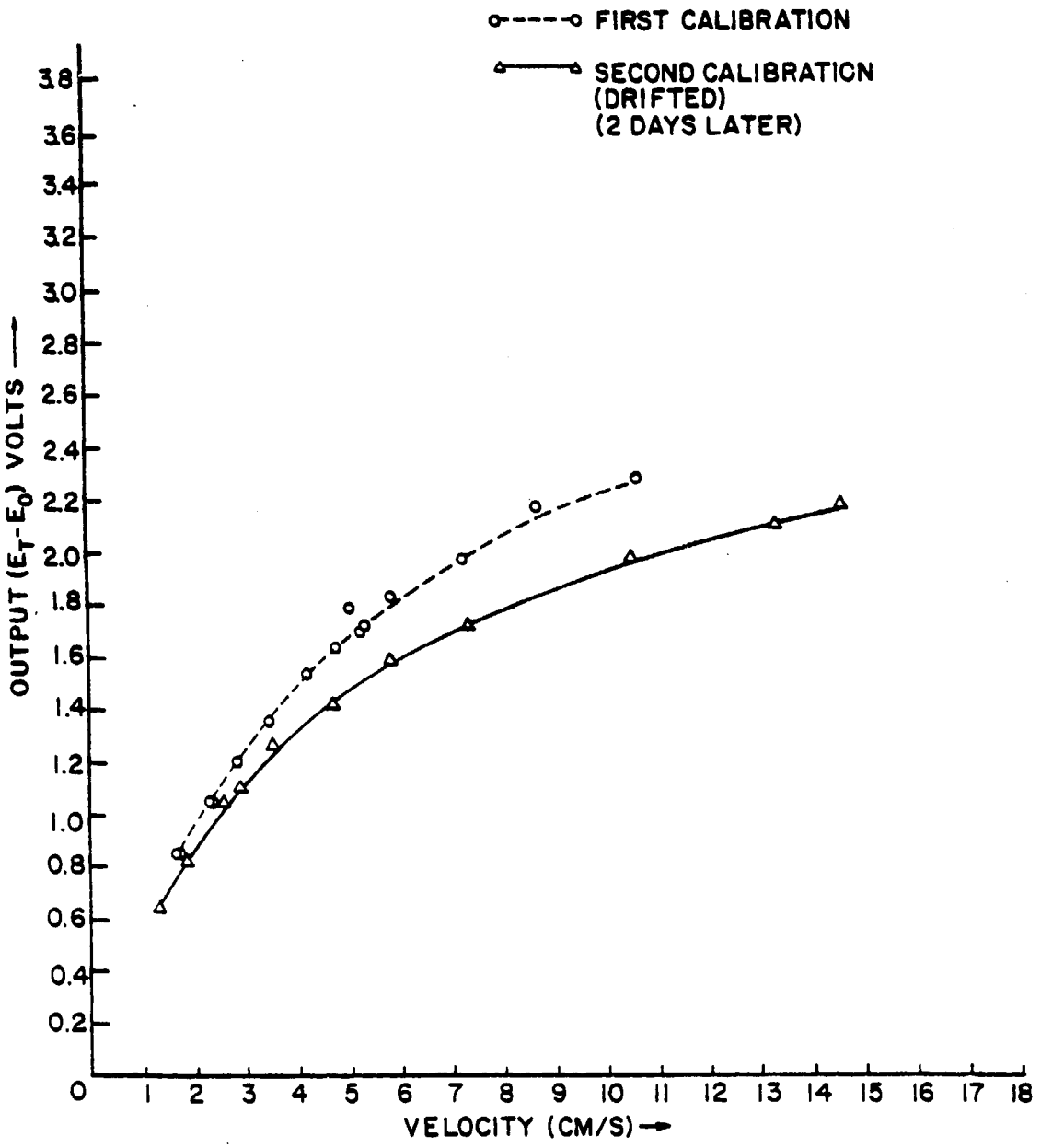

Fig. 15. Calibration curves showing drift.

ORIGINAL PAGE IS
OF POOR QUALITY

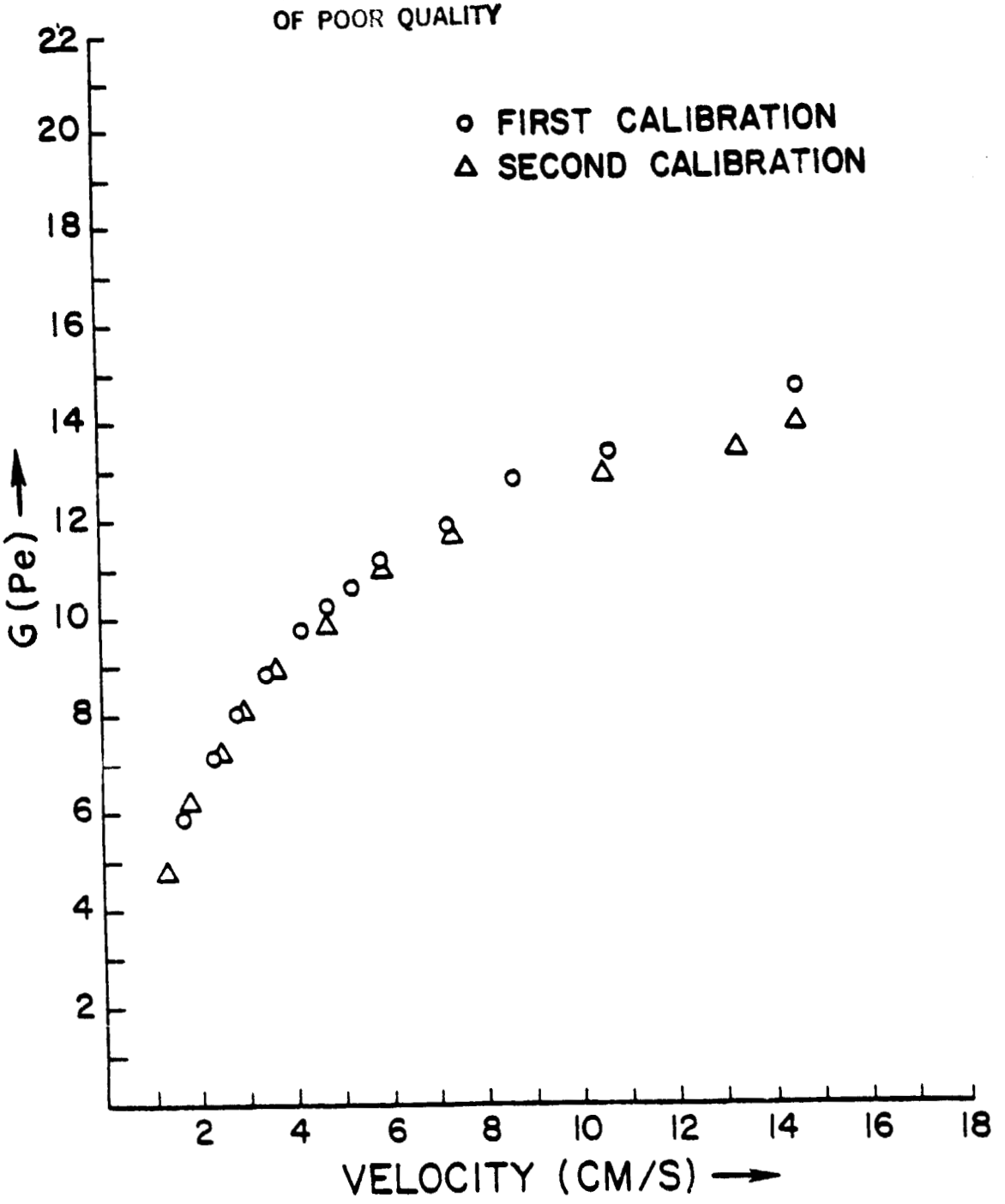

Fig. 16. Calibration curves with drift correction.

ORIGINAL PAGE IS
OF POOR QUALITY

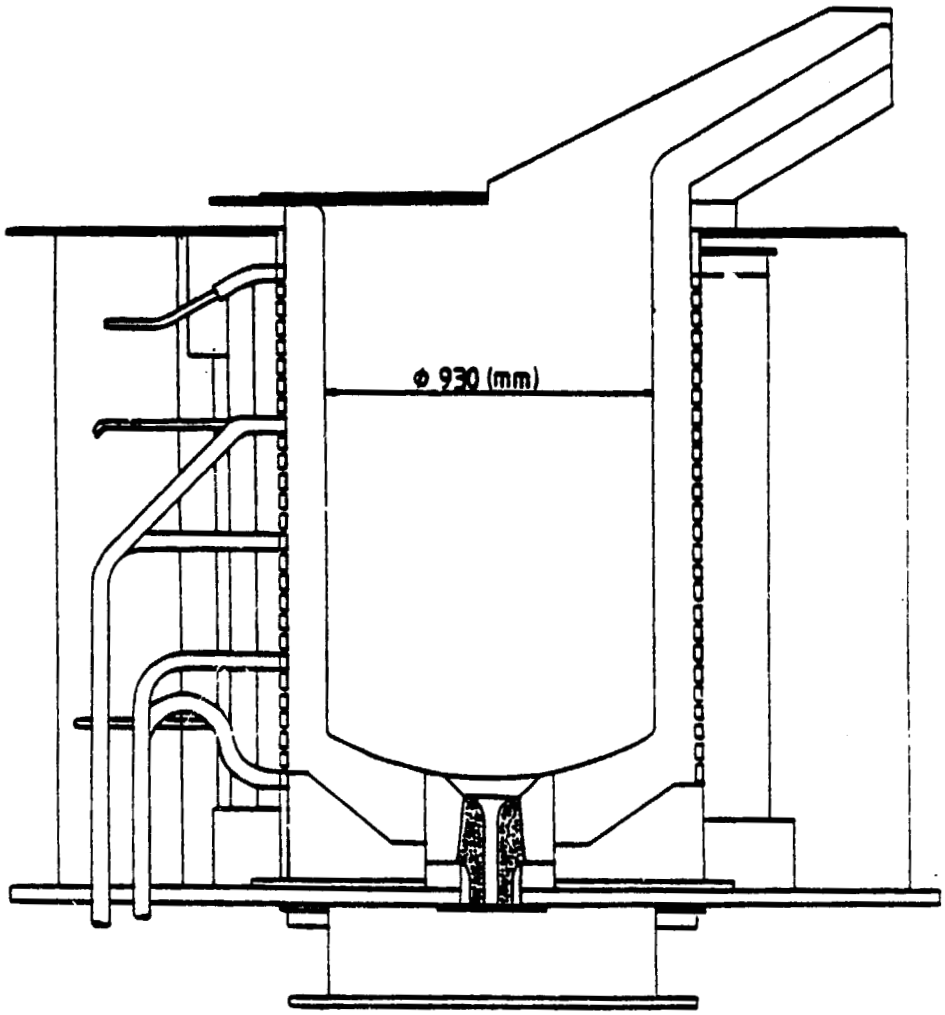

Fig. 17. Schematic sketch of a three phase induction furnace.

ORIGINAL PAGE IS
OF POOR QUALITY

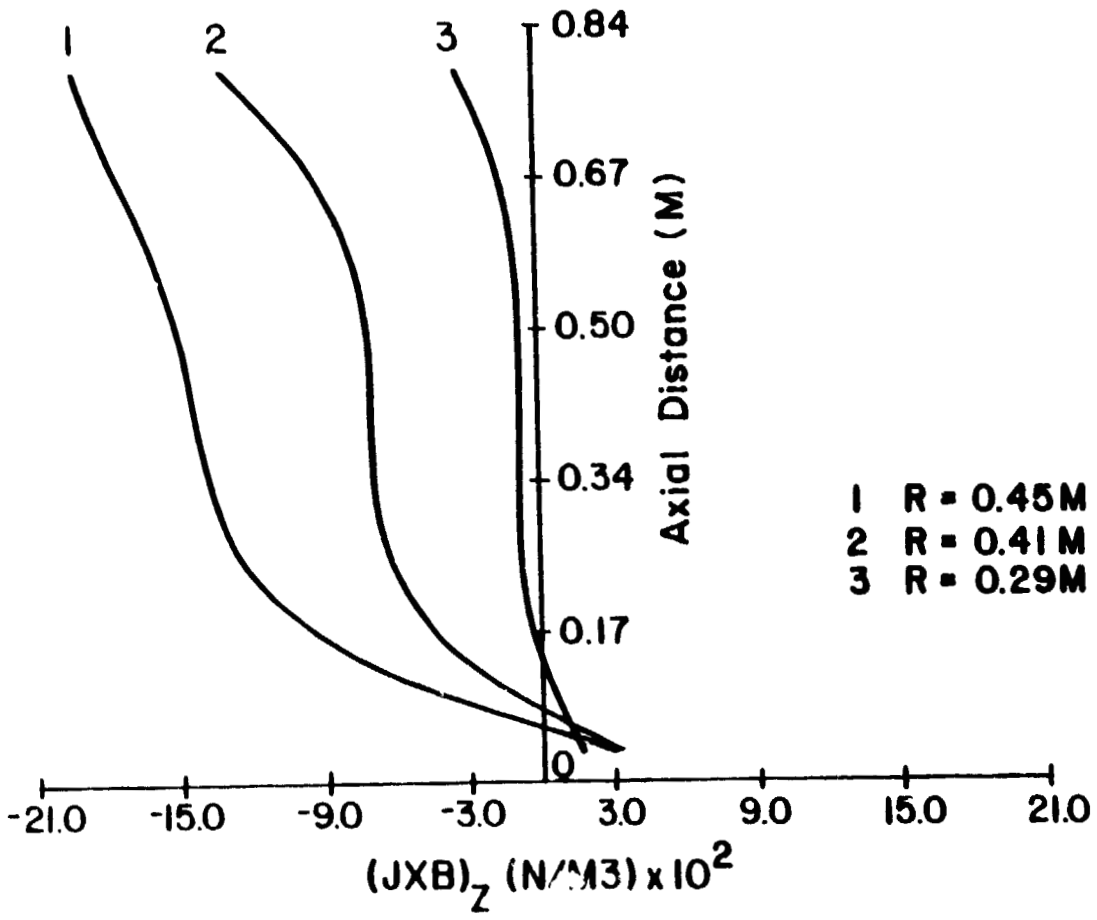

Fig. 18. The computed electromagnetic force F_z for a 4 ton induction furnace. Coil current 2800 Amp.

ORIGINAL PAGE IS
OF POOR QUALITY

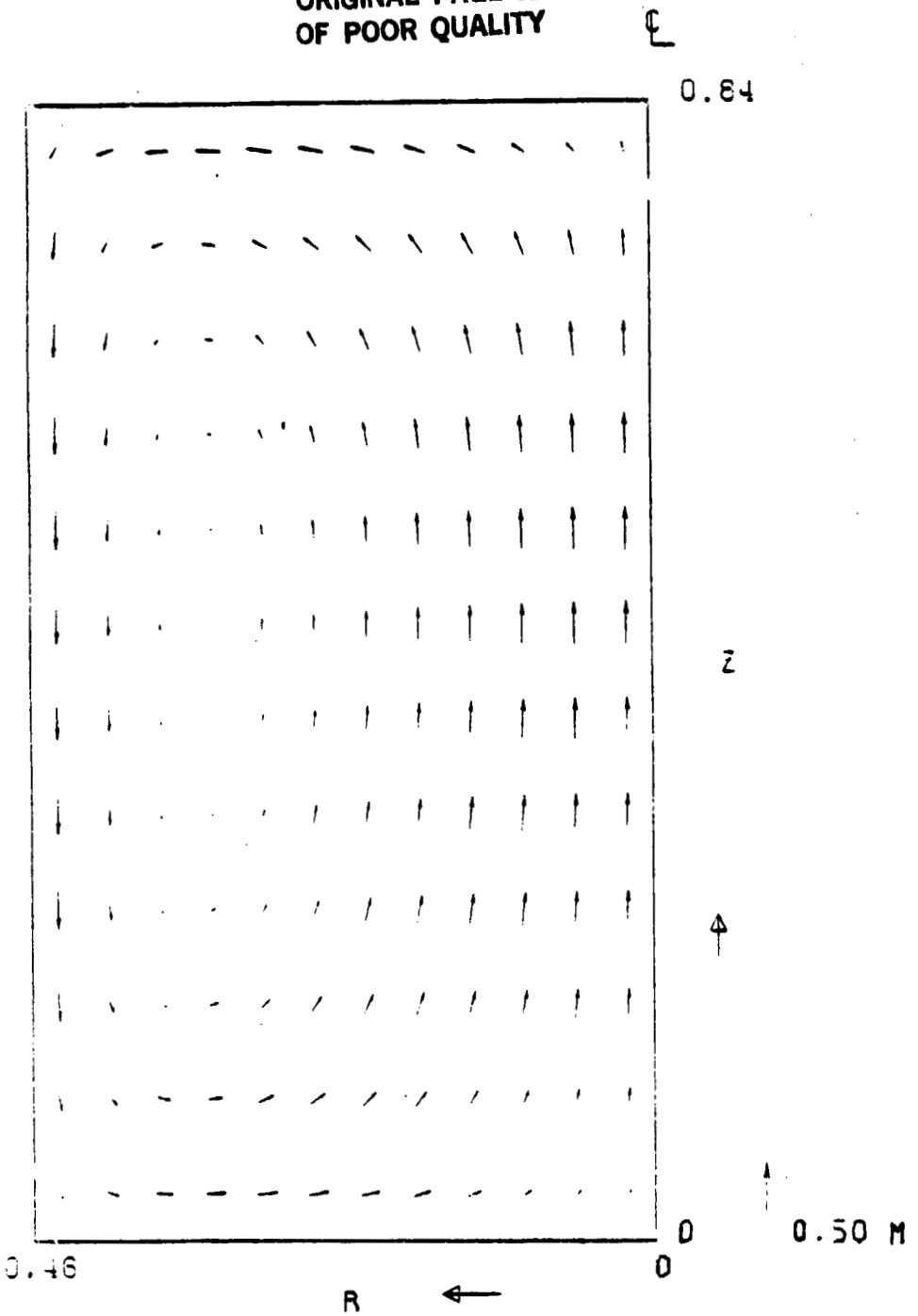

Fig. 19. The computed velocity field for a 4 ton induction furnace and for a 2800 A coil current.

ORIGINAL PAGE IS
OF POOR QUALITY

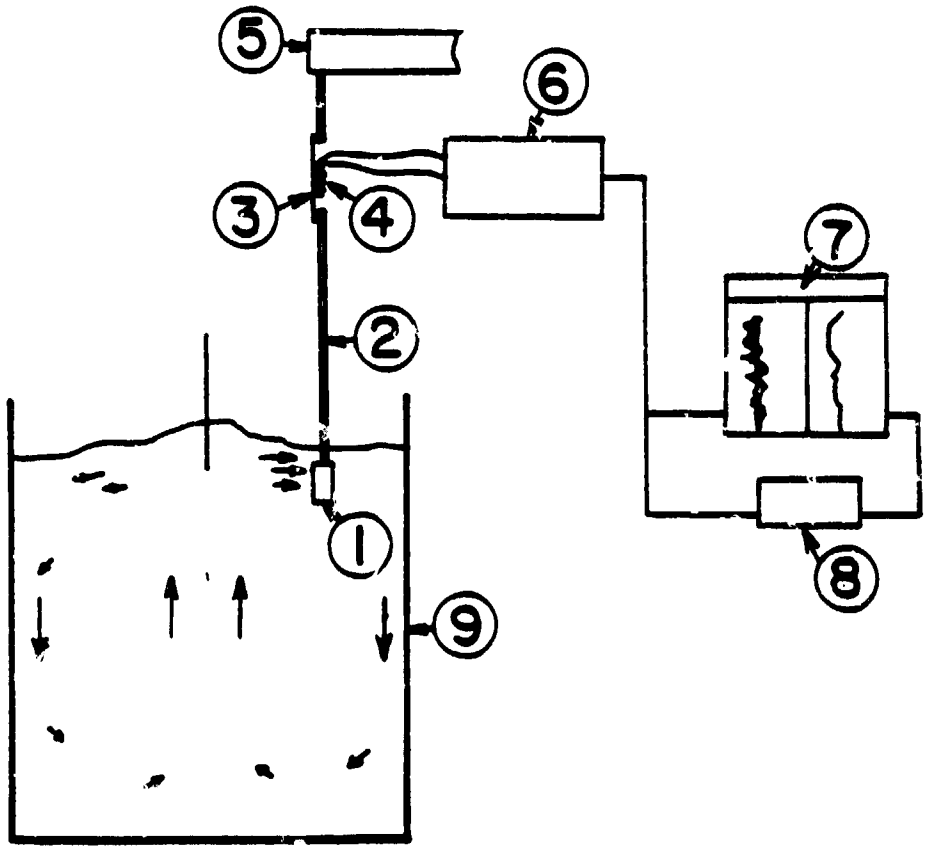

Fig. 20. A sketch of the velocity measurement system

1 - probe	5 - support
2 - arm	6 - instruments
3 - spring plate	7 - x-x-T recorder
4 - strain gauge	8 - RMS converter

ORIGINAL PAGE IS
OF POOR QUALITY

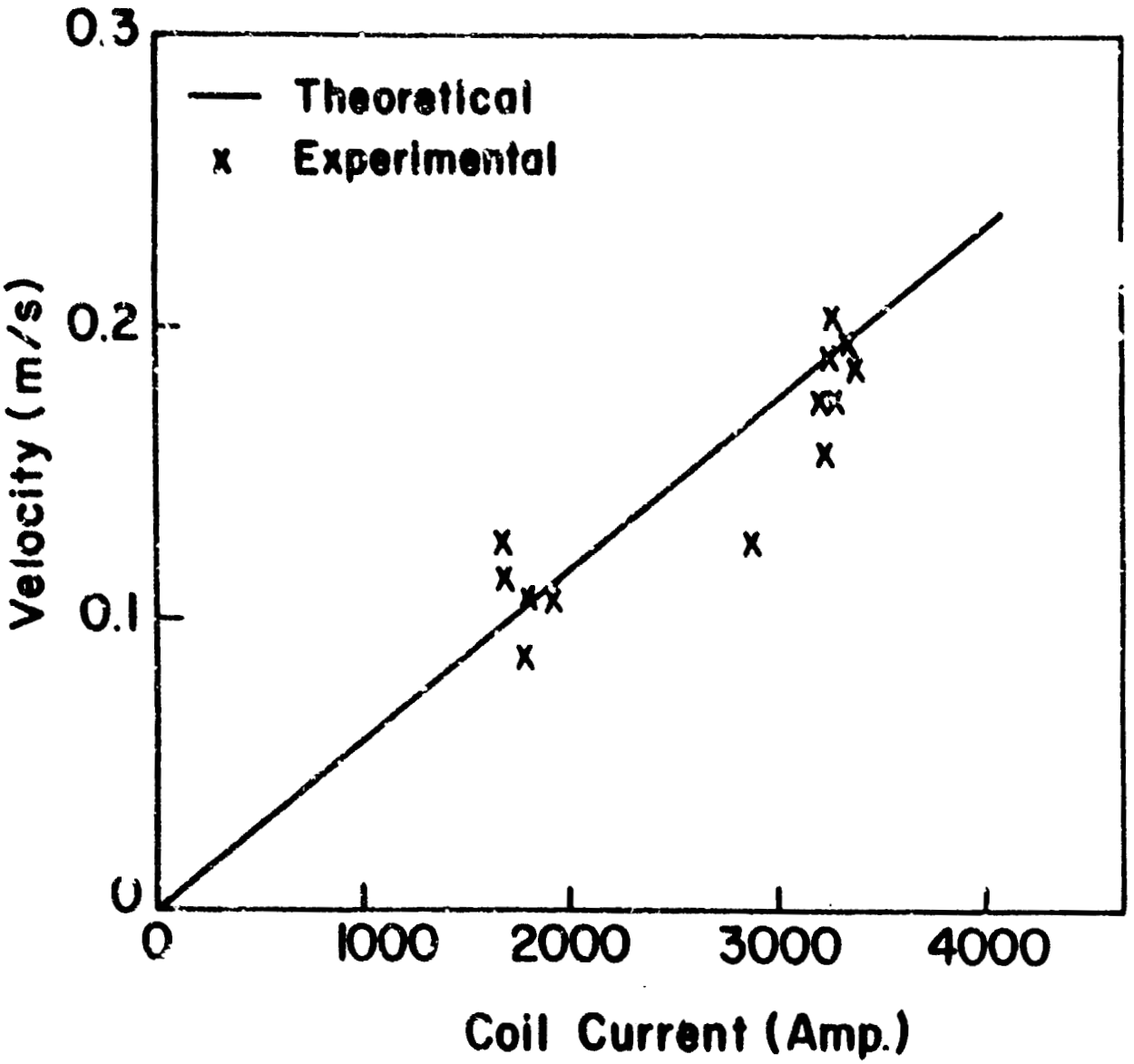

Fig. 21. Comparison between the measured and the computed near surface velocity as a function of coil current.

ORIGINAL PAGE IS
OF POOR QUALITY

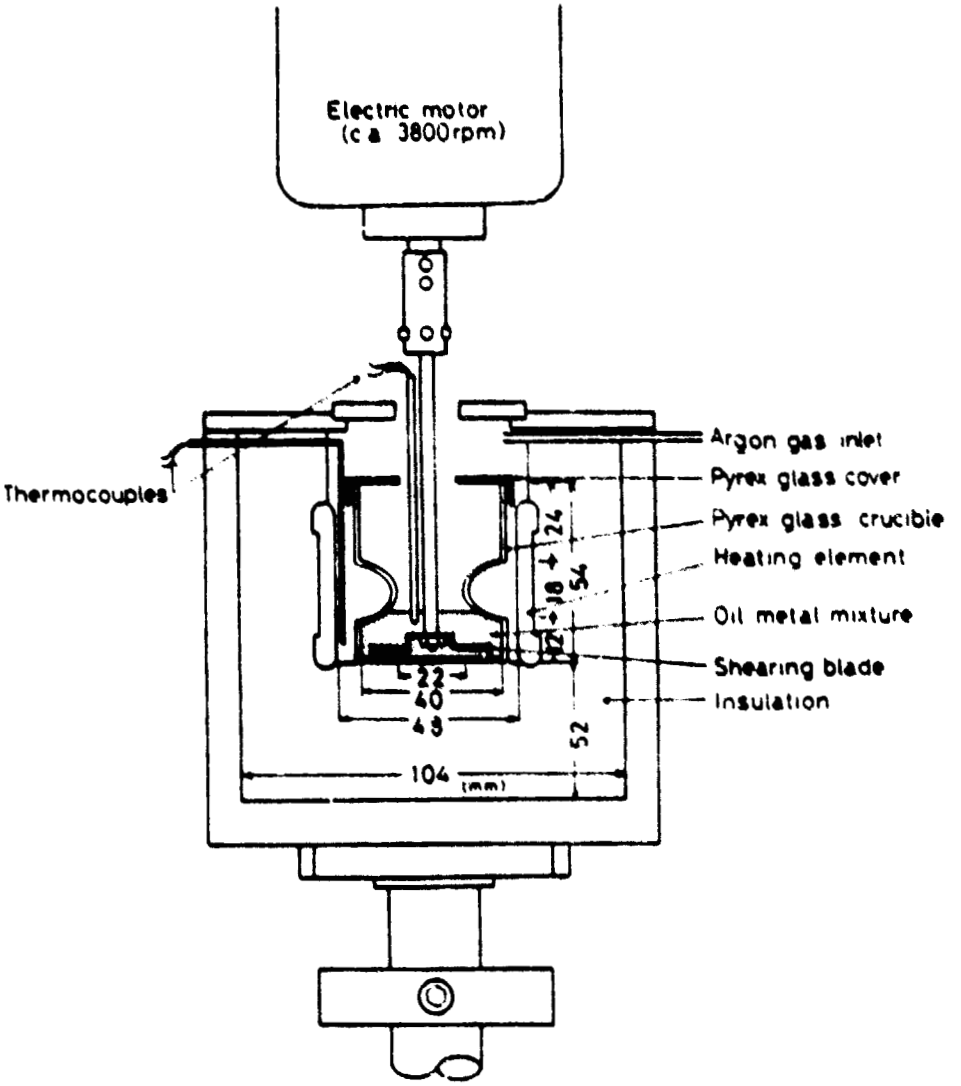

Fig. 22. Schematic diagram of the experimental apparatus for emulsifying droplets of molten low-melting-point alloys.

ORIGINAL PAGE IS
OF POOR QUALITY

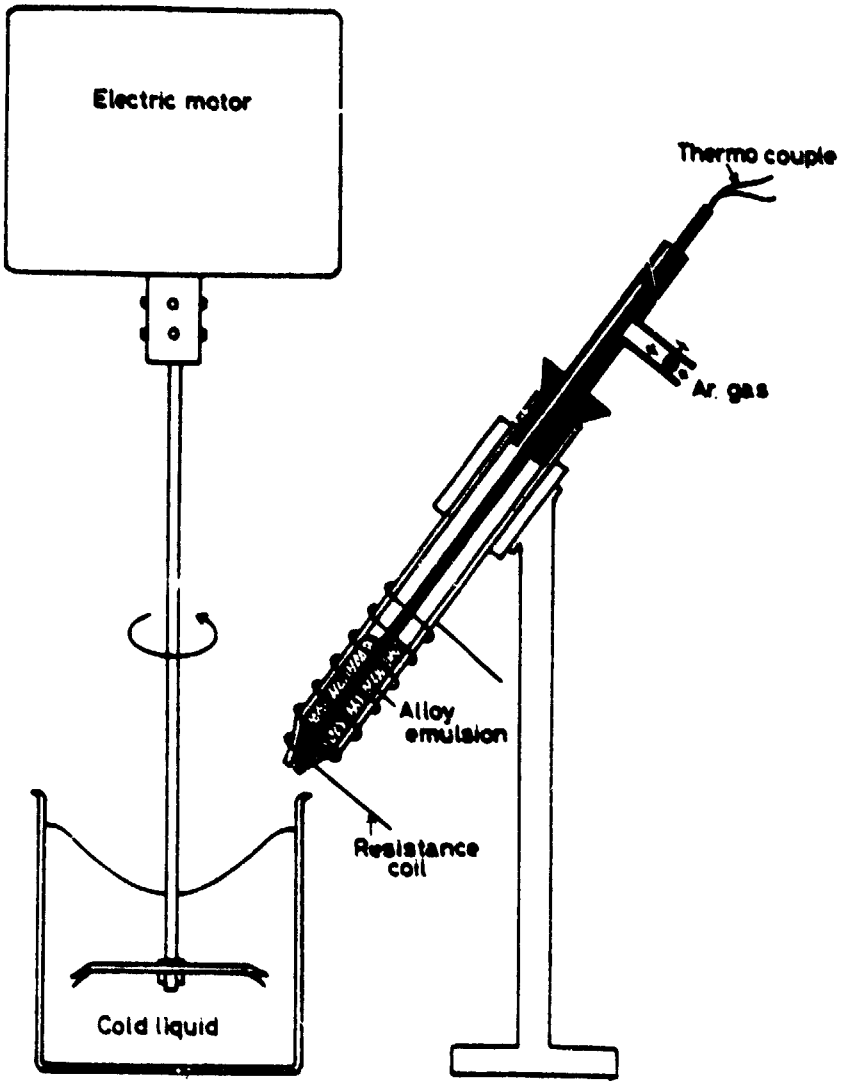

Fig. 23. Schematic diagram of the experimental apparatus for rapid quenching emulsified droplets.

ORIGINAL PAGE IS
OF POOR QUALITY

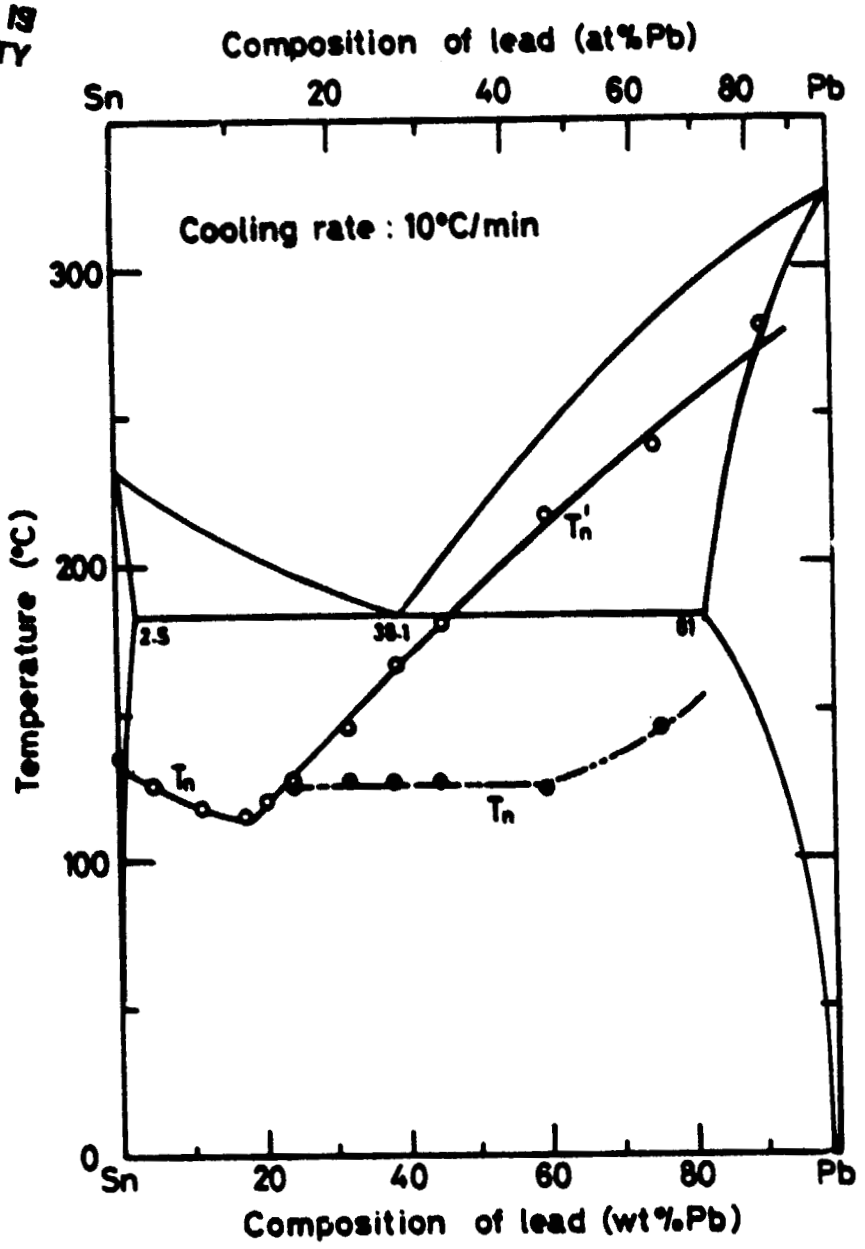

Fig. 24. Composition dependence of nucleation temperatures for Sn-Pb alloy droplets observed in DSC measurement with 10°C/min cooling rate.

ORIGINAL PAGE IS
OF POOR QUALITY

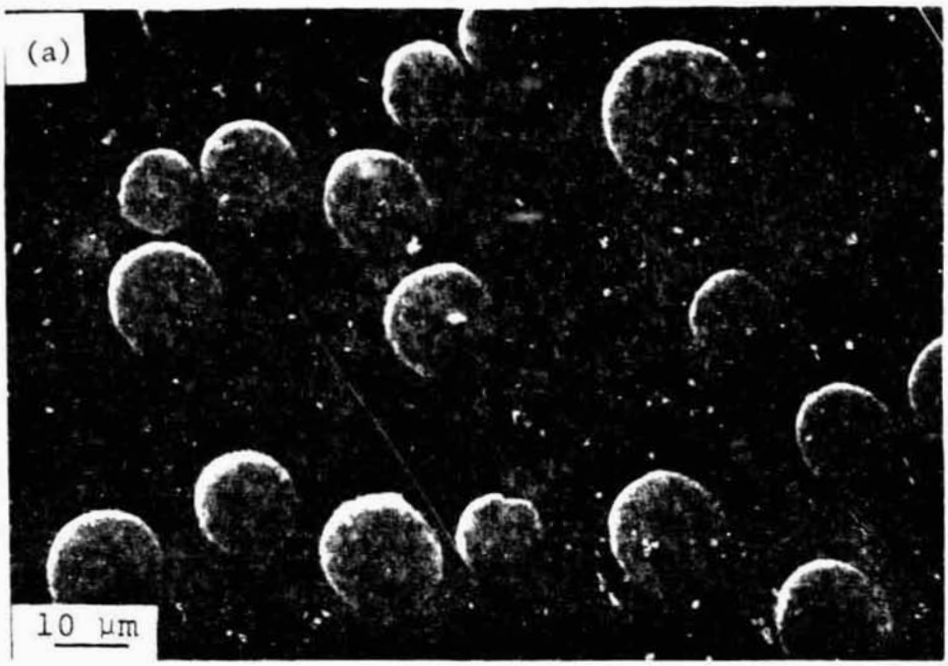

Figure 25 Microstructures of droplets of Sn-5wt%Pb alloy rapidly quenched in a bath at -25°C, 1000X.

ORIGINAL PAGE IS
OF POOR QUALITY

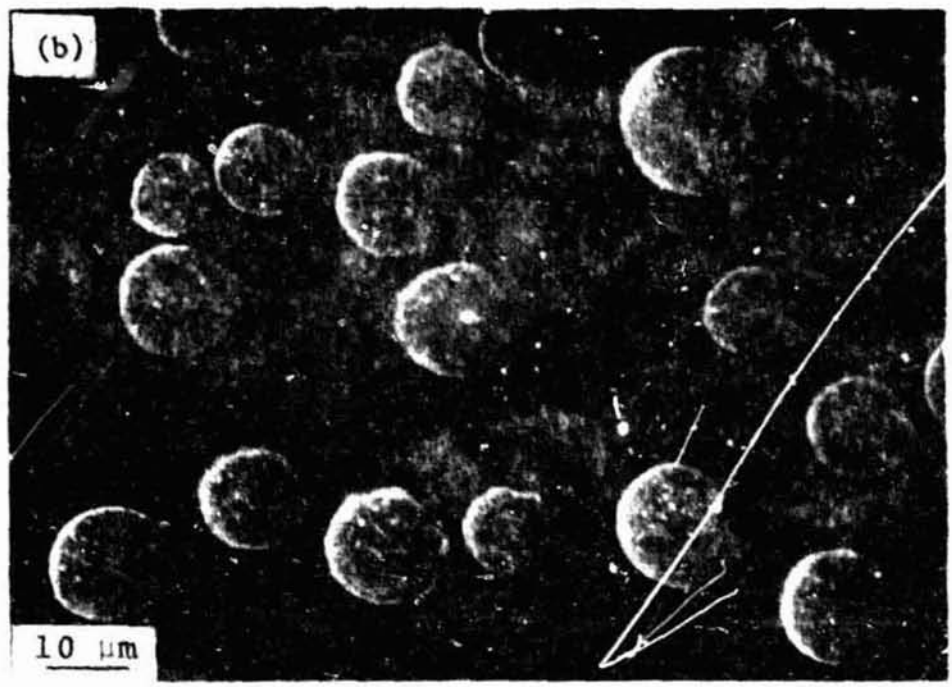

Figure 26 The same droplets shown in Figure 25, after one month at room temperature, note the substantial precipitation of lead-rich phase, 1000X.

ORIGINAL PAGE IS
OF POOR QUALITY

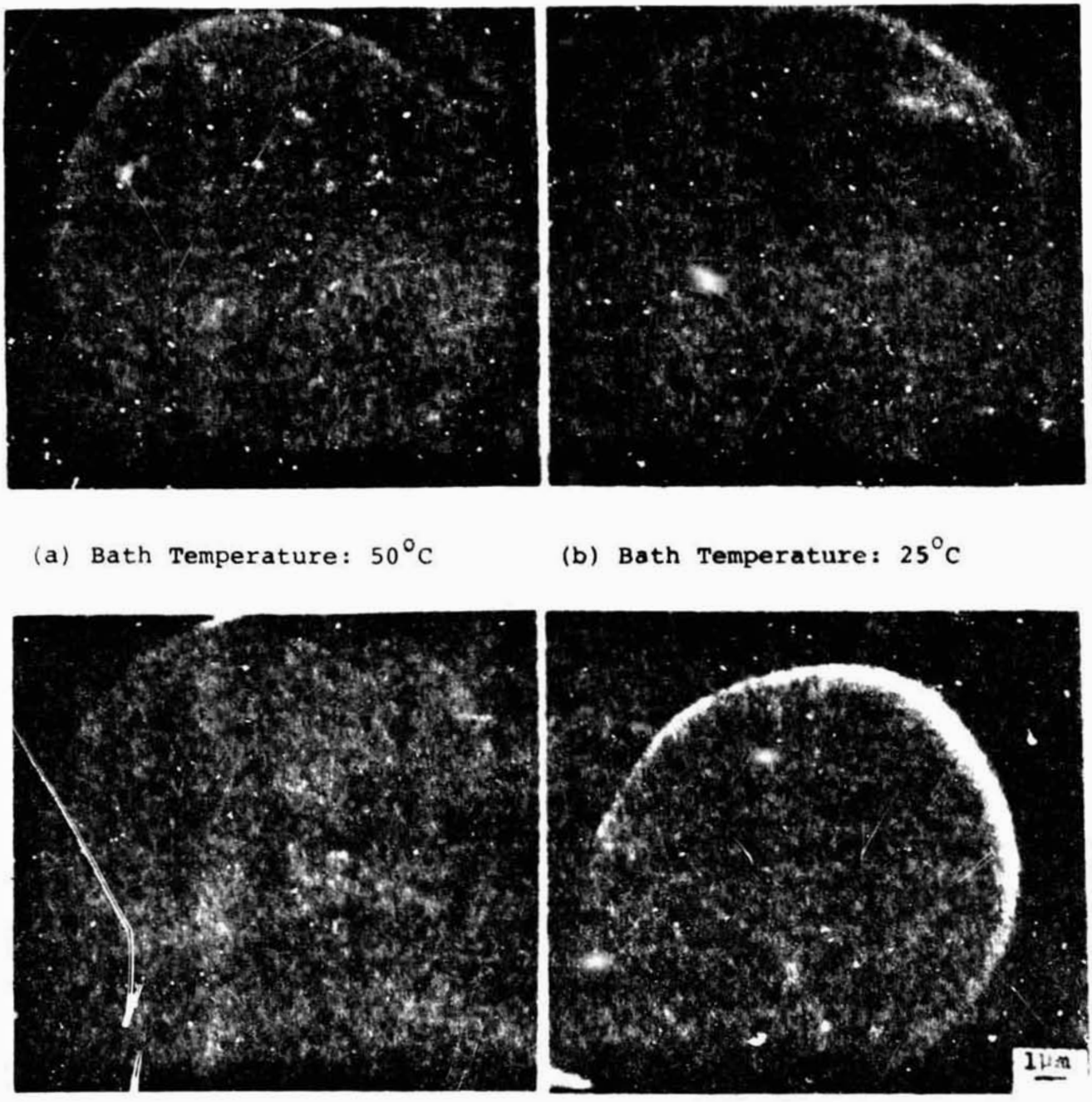

(a) Bath Temperature: 50°C

(b) Bath Temperature: 25°C

(c) Bath Temperature: -4°C

(d) Bath Temperature: -25°C

Figure 27 Microstructures of droplets of Sn-5wt%Pb alloy superheated 50°C and rapidly quenched in bath at temperatures shown, 5000X.

ORIGINAL PAGE IS
OF POOR QUALITY

Figure 28 Microstructures of Sn-45wt%Pb alloy droplets, 7000X. (a) Rapidly quenched (b) Slowly cooled to just below Tn and quenched (c) Slowly cooled to room temperature.

ORIGINAL PAGE IS
OF POOR QUALITY

Table 2

Previous Undercooling Results for Iron and Nickel Base Alloy

Alloy	Undercooling (°C)	Investigators	Sample Size
Ni	319	Cech, Turnbull	50 - 100 μm
Ni	365	Ward	1.5 gm
Fe	295	Cech, Turnbull	30 - 100 μm
Fe	295	Scheil	Bulk melt
Fe-25%Ni	300	Kattamis, Flemings	50 - 500 gm
Fe-25%Ni-0.3%S	225	"	"
AISI 4330 Steel	200	"	"
440 C. Steel	150	"	"
Ni	200-290	Lux, Haour, Mollard	12mmØ x 10cm
Ni-15%Co	200-240	"	"
Ni-12%Co-15%W	130-145	"	"
Ni-13%Al (Ni_3Al)	10-15	"	"
Ni-42∿50%Sn	<138	Kobayashi, Nakao	3 gm
Ni-52%Sb	229	"	"

ORIGINAL PAGE IS
OF POOR QUALITY

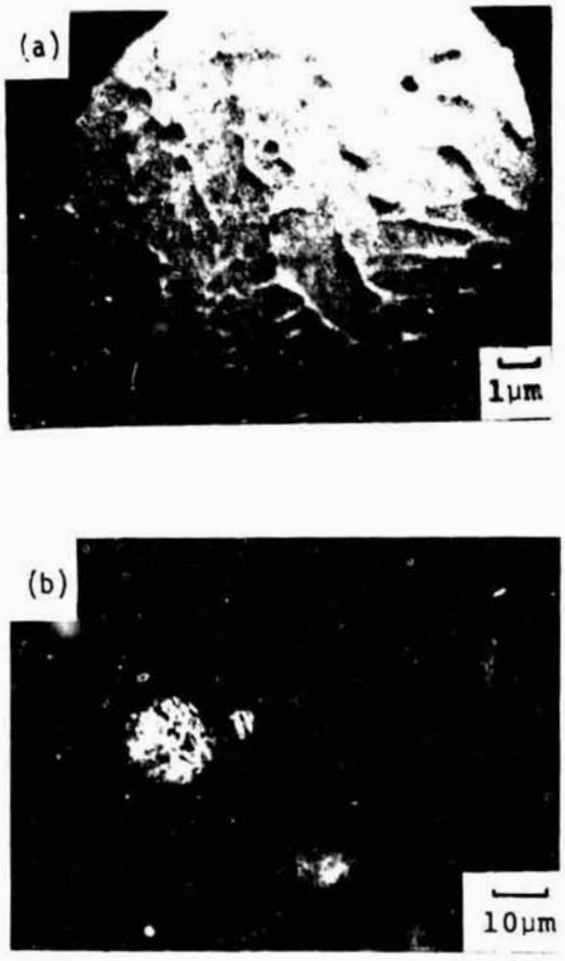

Fig. 29. (a) SEM micrograph of cross-sectioned and etched particles of the as-received 316 stainless steel powder.

(b) Optical micrograph of cross-sectioned and etched 316 BCC and FCC particles after undercooling experiment. (FCC particles are lighter in color).

ORIGINAL PAGE IS
OF POOR QUALITY

Fig. 30. SEM micrograph of a cross-sectioned and etched particle of 316 after high undercooling. Both the BCC and FCC phases co-exist in the same particle.

ORIGINAL PAGE IS
OF POOR QUALITY

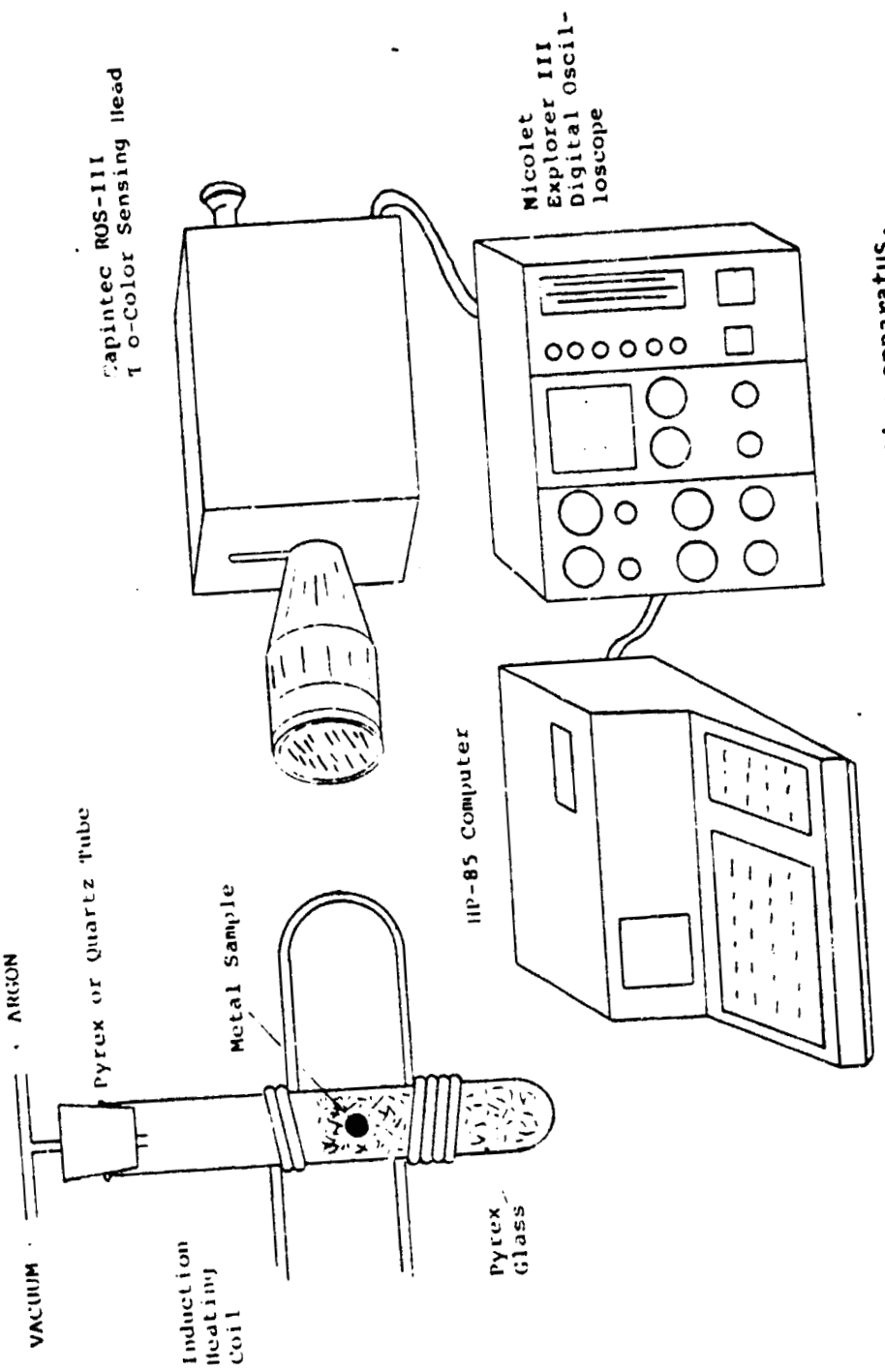

Figure 31 Schematic diagram of large droplet solidification apparatus, showing metal sample induction melted in glass, an optical sensor, a digital oscilloscope and a computer.

ORIGINAL PAGE IS
OF POOR QUALITY

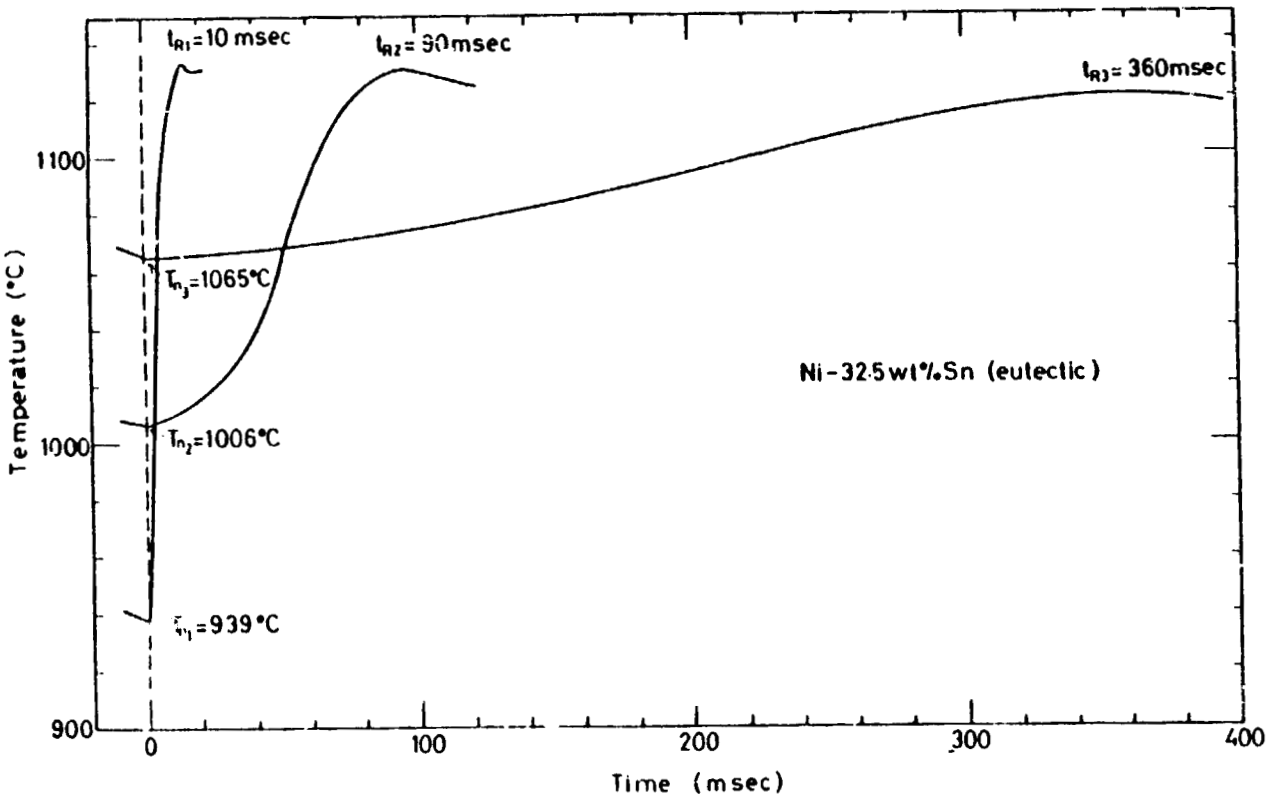

Fig. 32. Eutectic recalescence time profiles for three different undercoolings.

ORIGINAL PAGE IS
OF POOR QUALITY

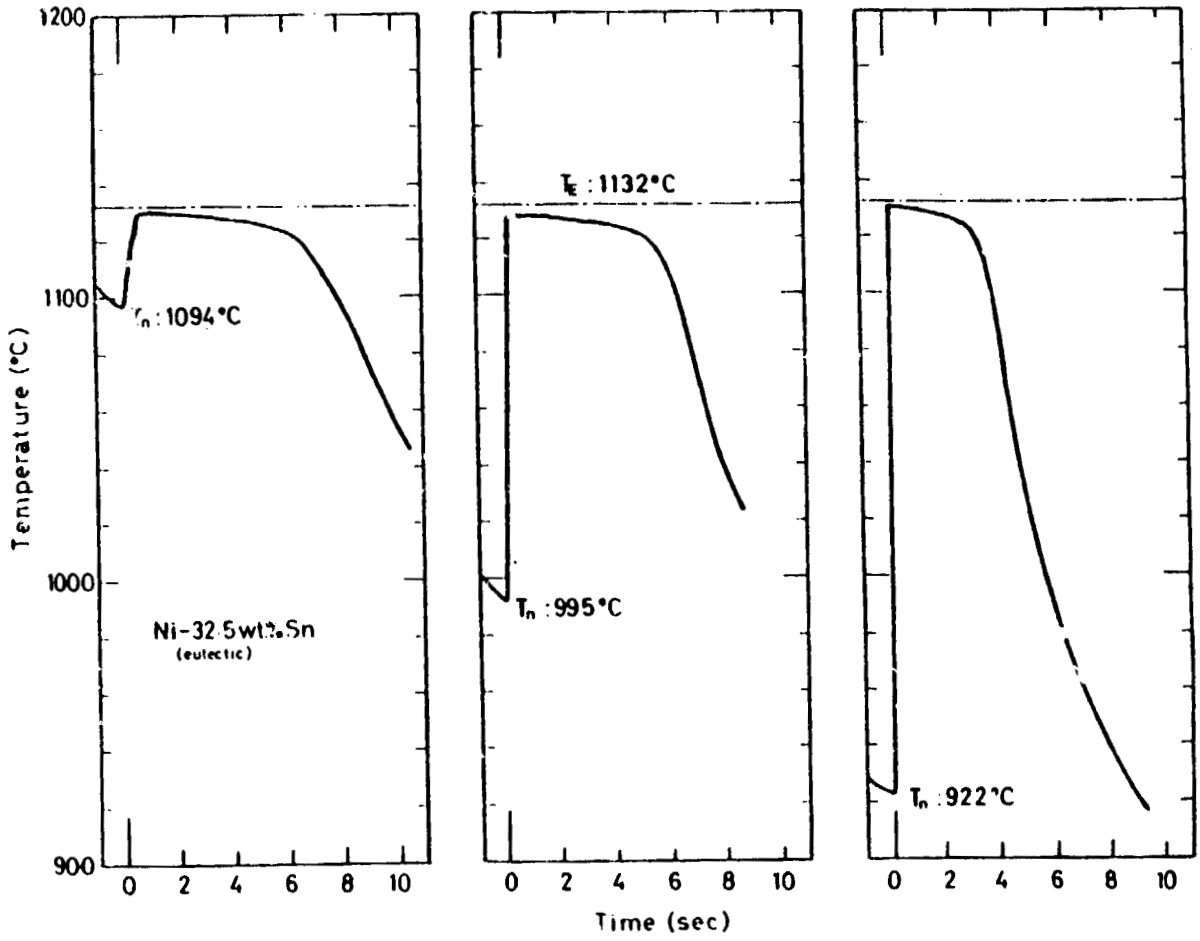

Fig. 33. Eutectic solidification profiles for three different undercoolings.

ORIGINAL PAGE IS
OF POOR QUALITY

The Structure and Properties of Rapidly Solidified, Highly Alloyed Aluminum Materials

Principal Investigator: Nicholas J. Grant

I. THE STRUCTURE AND PROPERTIES OF RS-PM 2024 Al + LITHIUM ALLOYS

RESEARCH ABSTRACT

This study has been completed and a series of publications are in preparation. One phase of the study was concerned with Alloy 2024 modified with additions of 1 to 2% lithium. Further alloying modifications permitted study of the effect of the Cu:Li ratio on the resultant mechanical properties. Alloy 1, incorrectly treated at 500°C for hydrate decomposition, was the high Cu, high Cu:Li ratio alloy, and was negatively influenced by formation of coarse $CuAl_2$ precipitates (in excess of solid solubility at all temperatures). Alloys 2 and 3 showed excellent combinations of both nominal and specific strength and modulus of elasticity. Fatigue properties, notch toughness and crack propagation rates were all significantly improved over I-M 2024 and RS 2024 without lithium additions.

A publication covering this study has been accepted for the Second International Conference on Al-Li Alloys, scheduled for April 1983.

RESEARCH SUMMARY

Table 1 lists the Cu and Li compositional variations, Young's Modulus and the shear modulus values, which in turn are transposed into percent

ORIGINAL PAGE IS
OF POOR QUALITY

increases in both modulus values corrected for specific gravity. These increases are of significant value and interest.

The major strengthening phases in these three alloys are summarized below for aging conditions of 20°C (T-4) and 190°C (T-6):

	Aged at 20°C	Aged at 190°C
Alloy 1	GPB and GP zones	GPB zone, s', γ', θ' and θ"
Alloy 2	GPB zone	GPB zone, s' and γ'
Alloy 3	GPB zone	GPB zone, s' and γ'

Alloys 2 and 3 are similar in structure but otherwise differ significantly in properties. One would expect higher levels of E and G, and of specific modulus values in favor of Alloy 2 with the higher lithium content, which is confirmed in Table 1. Yield strength values for all three alloys are closely matched at about 68 to 69 ksi; however, the UTS is significantly better for Alloy 3 in spite of having the lowest lithium content. Perhaps even more importantly, the ductility at fracture is sharply better for Alloy No. 3. The combination of excellent YS, UTS and ductility shown by Alloy 3 is related to its lower content of oxide derived from the RS powders. The fracture surfaces showed a cleaner, finer, dimpled structure. Alloy 1, which had very coarse $CuAl_2$ precipitates due to initial overheating of the RS powders gave poor strength and ductility values and is not further discussed.

The density corrected values for Alloys 2 and 3 are excellent; the best combination is that for Alloy 3 for the T-6 condition. See Table 2.

The notch tensile properties and fracture toughness values are shown in Table 3. Again Alloy 3 shows the best values.

Figure 1 is a plot of stress amplitude (reversed bending) versus cycles to failure at room temperature in an air atmosphere, and compares data for I-M 2024, RS-splat 2024 (no Li), and for Alloys 2 and 3. There is a significant improvement for Alloys 2 and 3 (uncorrected for density) compared to both I-M 2024 and RS-splat 2024. In the case of Alloy 3, the

ORIGINAL PAGE IS
OF POOR QUALITY

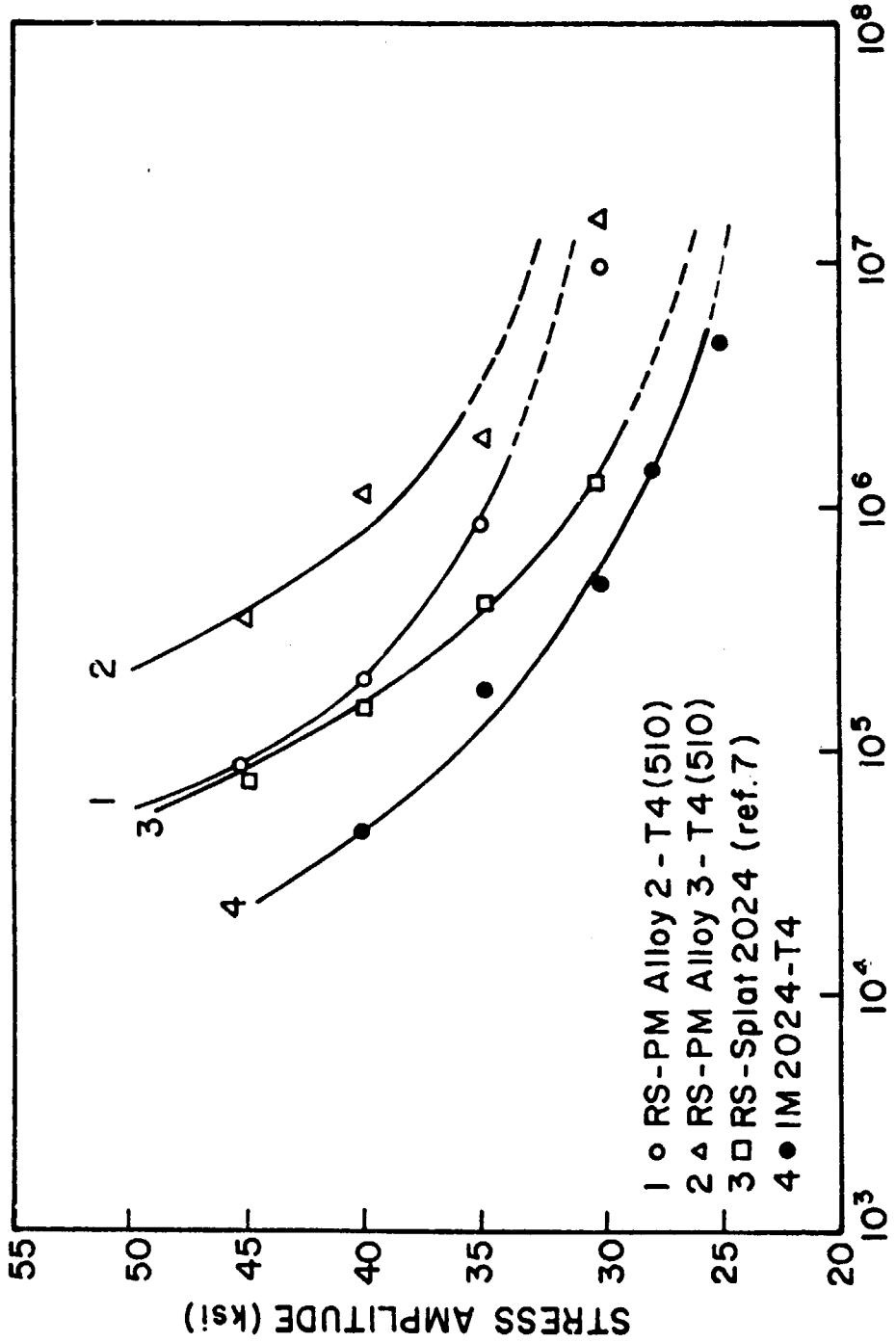

Fig. 1. Reversed Bend Fatigue Data, Smooth Bar, for RS-PM Alloys 2 and 3, for Splat Quenched 2024 and for IM 2024-T4.

improvement at 10^7 cycles, over I-M 2024, is more than 35%.

Figure 2 plots fatigue crack growth rate versus stress intensity range for Alloys 2 and 3 versus that for I-M 2024. Again Alloy 3 shows excellent values.

Alloy No. 3, with only about 1% Li, and apparently with lower oxide content than is frequently the case with RS-PM and RS-splat based alloys, shows excellent properties in all tests performed, including the sharp, precracked notch tests. Corrected for density, this alloy is clearly better than I-M 2024 in terms of its mechanical behavior.

Table 1. Modulus of Elasticity of RS-PM Aluminum Alloy 2024 + Li

Alloy No.	Cu	Li	E	G	Percent Increase in Values vs. I-M 2024			
	%	%	psi x 10^6	psi x 10^7	ΔE	ΔE_ρ x 10^7 in.	ΔG	ΔG_ρ x 10^7 in.
I-M 2024	4.5	--	10.4	3.9	--	--	--	--
1	5.92	1.29	11.3	4.3	8.7	10.8	10.3	12.9
2	3.78	1.63	11.7	4.5	12.5	18.3	15.4	20.5
3	4.16	0.96	11.3	4.3	8.7	12.5	10.3	12.8

ORIGINAL PAGE IS
OF POOR QUALITY

ORIGINAL PAGE IS
OF POOR QUALITY

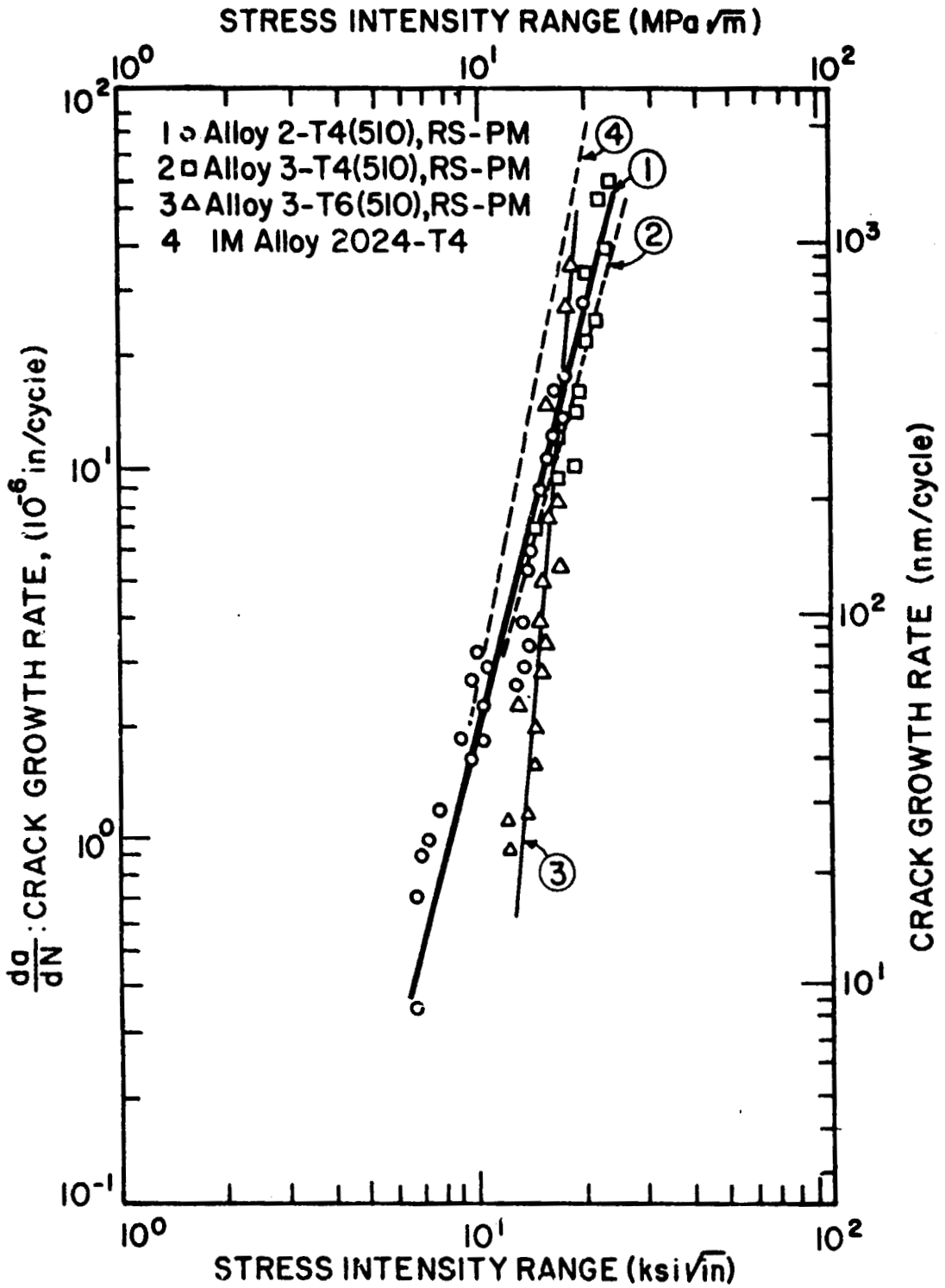

Fig. 2. Crack Growth Rates Versus Stress Intensity Range for Alloys 2 and 3 Compared to that for IM 2024-T4.

Table 2. Room-Temperature Tensile Properties of RS-PM 2024 + Li

Alloy	TMT °C	0.2% YS Ksi	UTS Ksi	Elong %	RA %	σ_{YS} $\rho \times 10^4$ in.	σ_{UTS} $\rho \times 10^4$ in.
1 - T-847	47% C.R.+ 510°, 1h, WQ + 190°, 9h, WQ	64.3	72.2	7.8	10.0	65.6	73.7
1 - T-834	495°, 1h, WQ + 3.4% C.R. + 190°, 9h, WQ	69.6	73.2	5.5	5.0	71.0	74.7
2 - T-4	510°, 1/2 h, WQ + 20° > 15d	63.8	77.2	7.1	10.0	67.2	81.3
2 - T-84	495°, 1h, WQ + 3.8% C.R. + 190°, 24h, WQ	69.2	74.1	6.2	10.0	72.8	78.0
3 - T-4	510°, 1/2 h, WQ + 20°C, 21h, WQ	58.4	81.4	11.9	17.5	60.2	83.9
3 - T-6	510°, 1/2 h, + WQ + 190°C, 21h, WQ	68.2	81.1	9.0	13.3	70.3	83.6

ORIGINAL PAGE IS
OF POOR QUALITY

Table 3. Notch Tensile and Fracture Toughness Properties

Alloy	Treatment	Notched UTS Ksi	Notched Yield Ratio σ_{NTS}/σ_{YS}	Notched Tensile Ratio $\sigma_{NTS}/\sigma_{UTS}$	K_{1C} Ksi $\sqrt{in.}$
1 - T-83	Sol. Treat. 495°C	44.7	0.7	0.6	--
2 - T-6	Sol. Treat. 495°C	58.0	1.0	0.8	--
2 - T-4	Sol. Treat. 510°C	77.6	1.2	1.0	30.8
3 - T-6	Sol. Treat. 510°C	71.9	1.1	0.9	22.7
3 - T-4	Sol. Treat. 510°C	81.4	1.4	1.0	33.9

ORIGINAL PAGE IS
OF POOR QUALITY

II. THE STRUCTURE AND PROPERTIES OF RS-PM Al-Mg-Li ALLOYS

RESEARCH ABSTRACT

In terms of anticipated gains in specific strength and elastic modulus, the Al-Mg-Li system is particularly attractive. Even though the literature shows that Al-Cu-Li alloys have better strength values (nominal and specific), the substitution of 2 to 4% Mg for 4 to 6% Cu in the Al - 1 to 3% Li alloy is expected to be particularly beneficial to specific modulus. Rapid solidification, which has not been researched to an important extent for Al-Mg-Li alloys, was applied in this study in order to produce extruded bar stock for test purposes. The first alloy and test results for an RS-PM alloy look quite promising.

RESEARCH SUMMARY

The composition of the hot extruded (30:1 ratio) Al-Mg-Li alloy was (in weight percent): 6.74Mg - 1.64Li - 0.19Cu - .27Cr - .21Ti - .13Fe and .15Si. Solution heat treating temperatures of 300° to 540°C were studied, along with aging from 20° (T-4) to 190°C (T-6).

Dendrite arm spacing values for USGA powders (helium quench) varied from about 0.5 to about 2 μm over a powder size range which varied from about 1 or 2 μm to 250 μm, indicating a quench rate of about 10^5 K/s.

Aging in Al-Mg-Li alloys is essentially based on formation of the δ (Al_3Li) phase; the magnesium serves primarily to enhance solid solution strengthening. As a secondary effect, the magnesium decreases the solubility of Li in Al, thereby increasing the amount of δ' phase on aging, for a given lithium content.

The results of exploratory aging studies for the Al-Mg-Li alloy are plotted in Fig. 1. Briefly, solution temperatures below about 300°C do not induce important aging benefits. Natural aging results in no change

ORIGINAL PAGE IS
OF POOR QUALITY

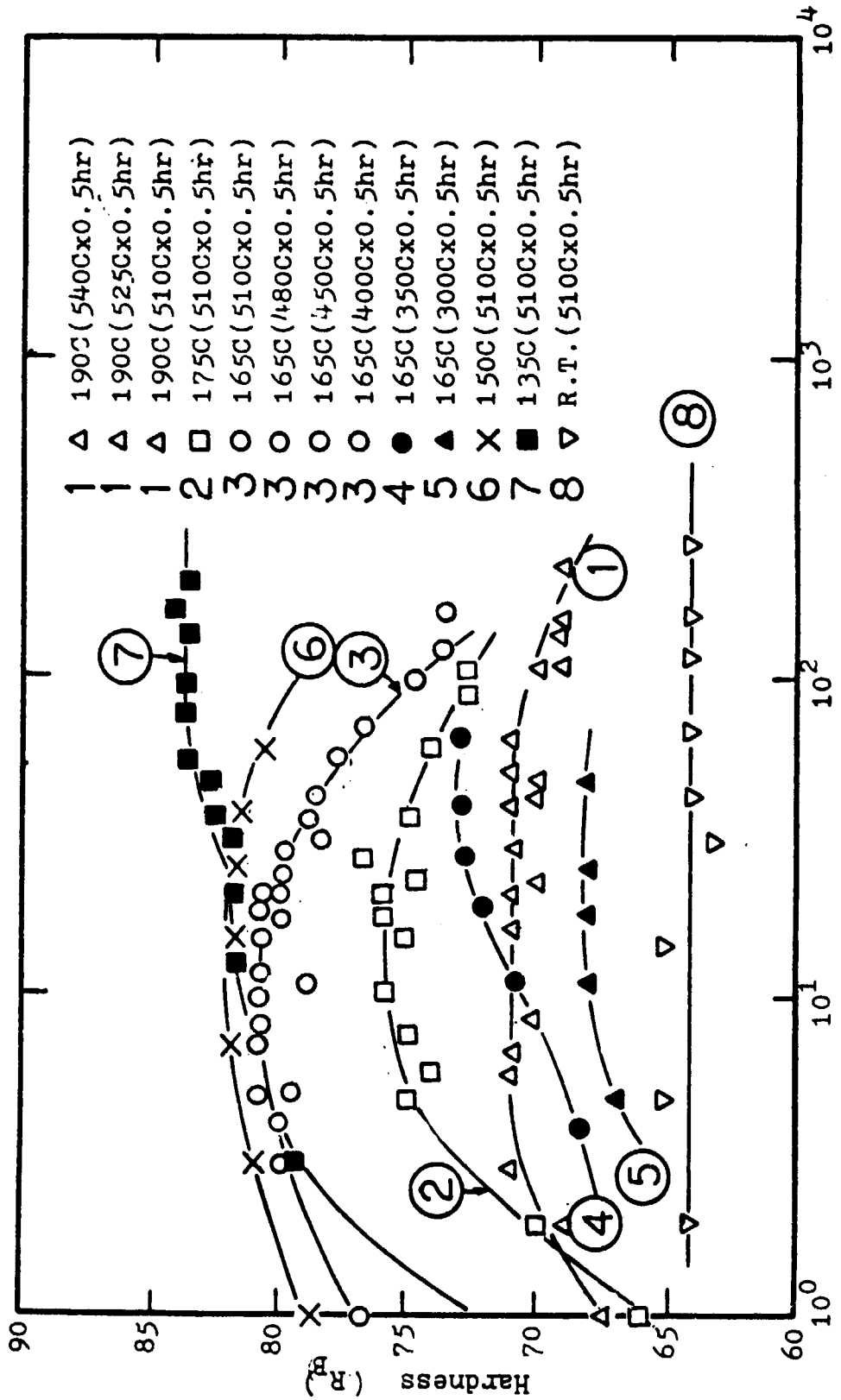

Fig. 1. Aging Curves for Al-Mg-Li Alloy

in hardness. Best results are for a solution temperature of 510°C plus aging at 135°C (curve 7, Fig. 1). Of some interest but not pursued, solution temperatures from 400 to 510°C, with aging at 165°C, result in a narrow spread of hardness values. In this respect, solution temperatures from 400 to 510°C are apparently sufficient to achieve suitable supersaturation; however, aging at 165°C leads to overaging after about 10 hours. Aging at 135° to 150°C seems preferable.

In all cases the δ' (Al_3Li) phase was identified after aging, although some Al_2Mg phase is expected for this 6.7% Mg alloy.

With an addition of only 1.64% Li, the density of this alloy is 2.523 g/cm^3, compared to 2.768 for I-M 2024; this represents a density decrease of 8.85% for the Al-Mg-Li alloy compared to I-M 2024. In turn, Young's modulus for this alloy is 11.2×10^6 psi, yielding a value for the specific Young's modulus of 12.2×10^7 in. These are quite attractive values.

Table 1 lists room-temperature tensile data including specific strength values based on the noted decrease in density. Measured strength and ductility values, in general, are better than those for I-M 2024 - T-4; corrected for density the values are excellent and are as good as those reported for Alloy 3 in Section I above.

Figure 1 indicated optimum hardness on aging at 135°C; this is borne out in Table 1 in terms of yield strength; however the ultimate strength is not the highest among the tests which were made, largely due to considerably lower ductility values for this aging condition. Aging at 150° or 165° results in lower yield values, equally high ultimate strength values and progressively improved ductiliy. In fact [illegible]tion at 450° plus aging at 165°C yields the best combination of strength and ductility while preserving a Notch Yield ratio of 1.0. Crack growth rates were the poorest among the group of alloys discussed in Sections I and II, for reasons which are not now apparent.

ORIGINAL PAGE IS
OF POOR QUALITY

Nevertheless, it is clear that further studies of RS-PM Al-Mg-Li alloys are warranted, in particular in compositions which will provide an additional hardening effect to that provided by δ' precipitation in this alloy.

Table 1. Tensile Properties of Al - 6.74Mg - 1.64Li Alloy at 20°C

Solution and Aging Conditions	0.2% YS	UTS	Elong	RA	Spec. YS	Spec. UTS
°C	Ksi	Ksi	%	%	$\rho \times 10^4$ in.	$\rho \times 10^4$ in.
510°, 1/2 h, WQ + 135%, 170h	64.0	75.7	5.5	5.0	70.4	82.3
510°, 1/2 h, WQ + 150°, 15h, WQ	63.4	74.6	7.0	10.0	68.9	81.2
510°, 1/2 h, WQ + 165°, 10h, WQ	60.2	75.1	8.9	10.0	65.4	81.6
450°, 1/2 h, WQ + 165°, 10h, WQ	61.2	76.7	11.0	15.0	66.5	83.4
400°, 1/2 h, WQ + 165°, 10h, WQ	61.6	77.0	8.0	10.0	67.0	83.7

III. MODIFICATION OF STRUCTURE AND PROPERTIES OF RS-PM 7075 ALLOY CONTAINING 1% ADDITIONS OF Zr AND Ni

RESEARCH ABSTRACT

In general, a great deal of the alloy studies using RS particulates leads to small compacts weighing between 1.5 and 5 kg, measuring 4 to 15 cm diameter to produce hot extrusions typically 12 mm diameter to 12 x 35 mm cross section, and representing extrusion ratios (area) of 16-30:1. This is often an inadequate amount of hot working to disperse oxide films on the particulates, or to break down occasional trapped impurities. Industrial R & D powder billets, in contrast, will weigh 50 to 100 kg and will receive considerably greater hot reduction. Using USGA powders, a 35 kg batch of powders will be hot extruded to achieve from 60 to 100:1 extrusion ratios (area). Various subsequent cold and hot work cycles will

be tried in order to achieve finer and more uniform dispersions of oxide films and dirt which may accidentally be included in the powder batch.

RESEARCH SUMMARY

Excellent structures and mechanical test data were obtained from small extrusions (5 kg) of an RS 7075 alloy containing 0.7% Zr and 1% Ni. Yield strength values in excess of 90 Ksi, UTS values in excess of 100 Ksi and ductility values in excess of 10%, combined with excellent fatigue, fracture toughness, and notched tensile data qualified this alloy for further studies to evaluate the role of total reduction on structure and subsequent properties. The USGA alloy powders have been produced and are currently being canned in preparation for extrusion from an 18 cm round to a 5 cm round (13:1 area reduction). The 5 cm extrusion will be cut to selected lengths and variously processed to smaller cross-sections, for example:

a) Hot re-extrude to 1.2 cm: total final reduction equals 225:1
b) Hot upset the 5 cm round to obtain an alternate grain, oxide, and inclusion pattern at very high reduction
c) Other TMT's including intermediate cold work, hot rolling and cross rolling, etc.

Based on expected beneficial effects, an alloy much more prone to develop heavier oxides, such as a 2 or 3% Li alloy, will be similarly processed.

LIST OF PUBLICATIONS

1. N. J. Grant, "Powder and Particulate Production of Metallic Alloys." Advances in Powder Metallurgy: 1981 ASM Materials Seminar, Ed. G. Chin, ASM, Metals Park, O, 1982.
2. N. J. Grant, "Rapid Solidification of Metallic Particulates," J. Metals, January 1982.
3. W. Wang, P. Domalavage and N. J. Grant, "Advanced Lithium-Containing 2024 Aluminum Alloys Made from Rapidly Solidified Powders," accepted for publication, Second International Al-Li Conference, April 1983.

ORIGINAL PAGE IS
OF POOR QUALITY

Development of Rapidly Solidified, Oxidation Resistant Alloys

Principal Investigator: Gregory Yurek

ABSTRACT

A fine-grained rapidly solidified 18-8 stainless steel (AISI 303) exhibited enhanced resistance to oxidation under isothermal conditions compared with a conventional wrought alloy of the same composition. The enhanced resistance to oxidation is attributed to three factors: (1) The formation and growth of protective scales is promoted by the fine alloy grain size (<10μm) and probably by the presence of a dispersion of fine MnS precipitates in the steel matrix, (2) scale adherence is increased by the formation of intrusions of oxide from the external scale into the alloy, which form along closely-spaced alloy grain boundaries and probably around the dispersed phase, and which act to key the scale mechanically to the alloy, and (3) growth stresses in the scales are reduced by the formation of scales of uniform composition, which are promoted by the uniform composition of the alloy. Modification of the microstructure of 18-8 stainless steels through rapid solidification processing appears to allow an increase in operating temperature of about 75°C under isothermal conditions.

INTRODUCTION

Very fine grained alloys are typically obtained by compaction of alloy powders produced by rapid solidification processing. In a number of cases, the fine grain sizes (<10μm) remain stable at elevated temperatures. The grains in these alloys are apparently pinned by very fine nonmetallic inclusions that are formed in the alloys during rapid solidification and/or

ORIGINAL PAGE IS
OF POOR QUALITY

during subsequent compaction of rapidly solidified products. The combination of a stable, fine alloy grain size, a fine, uniform dispersion of nonmetallic inclusions and a homogeneous alloy composition should provide an excellent alloy microstructure for oxidation resistance, provided the alloy composition is adjusted properly.

The objective of this program of research was to determine the effects of rapid solidification processing on the high-temperature oxidation behavior of alloys. It was demonstrated in a previous investigation [1] that a fine-grained, rapidly solidified 18Cr-8Ni stainless steel exhibited superior resistance to oxidation at 900°C under cyclic conditions compared with a conventional, wrought alloy of the same composition. The present study focussed on the oxidation behavior of the same rapidly solidified alloy under isothermal conditions over the temperature range of 800-1100°C.

EXPERIMENTAL METHODS AND MATERIALS

The material selected for this investigation was a fine-grained rapidly solidified 303 stainless steel (designated herein as 303RS), which contained a fine dispersion of MnS precipitates. Rapid solidification of this alloy was carried out by forced convective cooling (in helium) of centrifugally atomized metal droplets to achieve cooling rates on the order of 10^5 °C/sec. The resultant powder, which was 5 to 200 microns in diameter, was sieved to -140 mesh, enclosed in a stainless steel can, and consolidated to a fully dense one-inch diameter rod by hot extrusion at 900°C and a 10:1 extrusion ratio. According to Kelley and Vander Sande [2], the 303RS alloy comprised a duplex grain structure of 5-10 micron grains surrounded by heavily dislocated grains that were less than one micron in diameter. The alloy contained about 1vol% of MnS in the form of a uniform dispersion of fine precipitates (0.01-0.2 microns in diameter).

The oxidation behavior of the 303RS was compared to that of a conventional wrought 304 stainless steel (designated herein as 304W). The nominal composition of both steels, which are given in Table 1, are vir-

ORIGINAL PAGE IS
OF POOR QUALITY

tually the same, except that the 303RS has a higher content of sulphur and silicon. A wrought 303 stainless steel was not used as the standard for comparison because that material contains very large MnS precipitates which would disrupt the oxide scale and cause rapid oxidation.

TABLE 1: Compositions of Steels

Steel	Composition, Wt. Pct.						
	C	Mn	P	S	Si	Ni	Cr
304W	0.04	1.62	0.033	0.016	0.13	8.78	18.28
303RS	0.059	1.60	0.028	0.34	0.62	8.68	17.21

The oxidation specimens were disks approximately 1mm thick and 16 and 11.5mm in diameter for the 303RS and 304W alloys, respectively. These disks were sealed in an evacuated quartz capsule and annealled for 2h at 1100°C. The specimens were then ground through 600 grit SiC paper, polished with 6 micron diamond paste, ultrasonically cleaned and then finally rinsed with distilled water and methanol. After the stabilization anneal, the average grain sizes of the 303RS and the 304W were 6.5 and 85 microns, respectively. The MnS precipitates were 0.2 to 0.4 microns in diameter, indicating that particle coarsening occurred during annealing.

Oxidation experiments were conducted using a thermogravimetric apparatus that employed an Ainsworth Semi-Microbalance as the weighing unit. Experiments were conducted at 800, 900, 1000 and 1100°C in an atmosphere of dry oxygen at 1 atm pressure. Temperature control was $\pm$5°C as measured by a Pt/Pt-10%RH thermocouple placed approximately 5mm from the specimens. The microbalance was interfaced with a strip-chart recorder that produced a continuous record of the weight gained by the specimens as they oxidized. The accuracy of the balance was $\pm$.02 gm. The weight gains (Δm) measured by the balance were then normalized by dividing by the specimen area (A).

Scanning electron microscopy (SEM) was used to examine the surfaces and polished cross-sections of the oxidized specimens in order to deter-

mine the oxide morphology. The relative proportions of the elements in the oxides were determined from the ratios of the K_{α} peaks in EDX spectra. An electron microprobe was used to measure concentration profiles on the polished cross-sections of oxidized alloys.

RESULTS

Values of ($\Delta m/A$) are plotted as a function of time in Fig. 1 for the isothermal oxidation of 304W and 303RS steels at 800-1100°C. The total times of exposure varied, but the tendency was to terminate the tests after breakaway oxidation occurred. Two tests were conducted on the 303RS material at each temperature. The data discussed throughout this report are from whichever of the two tests resulted in the largest weight gains. Figures 2 and 3 show the complete sets of data for both tests at each temperature. Reproducibility of results was poor at 1100°C, but at all lower temperatures the results of the two tests were within $\pm$ 20% of each other. Data for the 304W steel were produced by a single test at each temperature.

The kinetic data show that the 303RS alloy was more resistant to oxidation than the 304W alloy over the entire range of temperatures tested. The general trends may be summarized as follows. The 304W formed protective scales at 800 and 900°C; at 1000°C a protective scale formed on 304W but soon broke down as thick iron oxides began to grow on the surface and pitting occurred. At 1100°C, breakaway oxidation began almost immediately.

By comparison, the 303RS alloy formed protective scales at 800, 900, and at 1000°C. Even at 1000°C there was no evidence of pitting or scale breakdown. At 1100°C, the oxidizing conditions were too severe and breakaway oxidation set in quickly. The most significant difference between the two alloys is that the 303RS was resistant to oxidation at temperatures up to 1000°C, while the 304W was only resistant to oxidation up to 900°C.

ORIGINAL PAGE IS
OF POOR QUALITY

DISCUSSION OF RESULTS

Oxidation of 304W Alloys

The maximum recommended temperature for the use of a wrought 304W stainless steel under isothermal oxidation conditions is 925°C [3]. Therefore, it was expected that the 304W would show adequate oxidation resistance at 900°C and below, but not at 1000°C and above.

The scales observed on specimens oxidized at 800 and 900°C consisted of thick, relatively iron-rich oxides over the grain interiors and thin, relatively chromium-rich oxides over the alloy grain boundaries. A protective chromium-rich oxide also formed beneath the iron-rich oxides over the grain interiors and was subsequently exposed when many of the oxide mounds spalled during cooling. When the stainless steel was initially exposed to the high-temperature, oxidizing atmosphere, oxides of every metal in the alloy probably formed, including the rapidly growing wustite, "FeO". Wustite can grow so quickly that a thick, Fe-rich scale formed first, followed by the formation of the underlying protective chromium-rich scale at the alloy surface. The formation of wustite in the early or transient stage of oxidation was apparently responsible for the rapid initial weight gains of the 304W specimens (Fig. 1). The chromium-rich oxides at the grain boundaries were able to form rapidly enough to prevent the formation of thick iron-rich oxides at these sites. This phenomenon is attributed to the preferential nucleation of Cr_2O_3 at the boundaries and to the rapid transport of Cr to the alloy surface by grain boundary diffusion.

Oxide-filled pits that occasionally developed on the 304W/900°C specimen were able to reform a protective Cr-rich layer at the base of the pits. The formation of such pits is generally attributed to local cracking or spallation of the protective scale [4,5]. Once formed, the pits can continue to grow until they reach a depth in the alloy where the chromium concentration is above the critical level for the formation of a protective film [5]. Because there were relatively few pits and a protective scale reformed at the base of the pits, this steel is sufficiently oxidation resistant to be useful up to 900°C.

At 1000°C the 304W began to passivate, but then breakaway oxidation kinetics set in as iron-rich oxide mounds and pits began forming over a significant portion of the surface. These pits usually did not reform a protective scale at their base, indicating that the underlying alloy no longer had a high enough chromium concentration to reform a continuous layer of Cr_2O_3. In addition, the very steep chromium concentration profile in the alloy near the interface (Fig. 4) and the high proportion of iron in the scale (30-70 wt%) indicate that the supply of chromium to the surface was probably insufficient to maintain a protective scale. That is, the oxidation conditions were so severe that the scale degraded to a less protective structure or composition even in the absence of cracking or spallation. Therefore, catastrophic degradation of the alloy is expected and observed at this temperature and at higher temperatures.

ORIGINAL PAGE IS
OF POOR QUALITY

Development of Protective Scales on 303RS Alloys

The 303RS alloy exhibited much better oxidation resistance than the 304W, although both had the same nominal composition. The 303RS specimens had a relatively smooth Cr-rich protective scale at temperatures up to 1000°C, although at temperatures of 900°C and above the scale was dotted with oxide mounds that were rich in iron and chromium. However, even the scales with the oxide mounds were distinctly more uniform than the scales found on the 304W alloys. The oxide mounds appeared to be the remnants of rapidly growing iron-rich oxides that formed during the initial stages of oxidation. Polished cross-sections of the specimens revealed that all mounds that formed on 303RS at or below 1000°C were undercut by a protective chromium-rich scale. The formation of pits was commonplace on 304W at 1000°C, but they were not observed at all on the 303RS specimens.

The preferential formation of a uniform chromium-rich scale on the 303RS alloy is attributed to its fine grain size and the presence of a fine dispersion of MnS in the alloy matrix. Grain boundaries and second-phase particles that intersect the surfaces of alloys may be sites for the preferential nucleation of Cr_2O_3. Since the 303RS exhibits both a fine grain size and a uniform dispersion of MnS precipitates, it is expected that there would

be a high density of closely spaced Cr_2O_3 nuclei on the alloy surfaces during the initial stages of oxidation. Therefore, relatively little sideways growth of these nuclei would be required to form a continuous, protective chromium oxide scale. The grain boundaries are also paths for rapid diffusion of chromium to the surface of the alloy. This increases the availability of chromium in the vicinity of the grain boundaries and promotes the formation of protective chromium oxide films in these areas.

The protective chromium-rich oxides formed over grain boundaries in the 304W stainless steel at 800 and 900°C were approximately 10 microns wide. Since the grain size of the 303RS alloy is only 6-8 microns, the presence of a 10 micron wide protective film along the grain boundaries would cover the entire surface of the alloy.

Maintenance of Protective Scales on 303RS Alloys

The 303RS alloys were more effective both at forming and maintaining protective Cr-rich oxide scales on their surfaces. The breakdown of Cr-rich scales may occur by spalling or cracking or by chemical destabilization caused by chromium depletion of the base metal and the simultaneous incorporation of iron or manganese into the scale, which causes a transformation to a less protective scale.

The uniform composition of the 303RS alloy appears to promote the formation of external scales of uniform composition and thickness, which would tend to decrease stresses and stress gradients in the scales, thereby enhancing the ability of the scales to resist spallation. The 304W alloys tended to oxidize nonuniformly, which probably contributed to breakdown of protective scales and promotion of the growth of iron-rich oxides.

Although the tendency for cracking of a chromium-rich scale may be reduced on 303RS, it would be expected that occasional breaks in the scale would occur. However, no pitting of the alloy surface or rapid growth of Fe-rich oxide mounds was observed at 1000°C and below. Therefore, it is assumed that any breaks in the scale that may have occurred were rapidly

healed by the formation of a new protective scale. Apparently, the interface of Cr content of the 303RS alloy (13.7 wt%, see Fig. 5) was not below the critical level for reformation of a protective scale at 1000°C. Rapid transport of Cr by grain boundary diffusion in the 303RS alloy, which had retained its fine grain size, apparently accelerated reformation of the protective scale relative to the rate of reformation of protective scales on 304W.

Development SiO_2 Subscales and Spinel Layers on 303RS

The protective scales on the 303RS alloy were enriched in Si at the alloy/scale interface and in Mn at the scale/gas interface. Both of these effects are commonly observed on commercial stainless steels.

The kinetic data and EDAX analyses of polished cross-sections indicate that the formation of SiO_2 subscales was more prevalent on 303RS than on 304W and occurred more readily at higher temperatures. These effects were expected since 303RS has both a significantly higher concentration of silicon (0.62 vs. 0.13 wt%) and a finer grain size (6.5 vs. 85 microns) to enhance Si transport to the outer surface.

The silica subscales were highly convoluted and formed intrusions into the alloy along the alloy grain boundaries where the transport of oxygen and silicon is believedto be more rapid [1]. The silica intrusions have been observed to increase the adherence of oxide scales to the substrate [1,6]. Both the subscale and the intrusions decreased the oxidation rate since further oxidation was dependent upon the transport of reactants through the silica scale as well as through the chromium-rich outer scale.

Analysis of the kinetic data for the 303RS specimens oxidized at 900 and 1000°C demonstrated that the rate of oxidation during approximately the first 40h was controlled by diffusion in Cr_2O_3, followed by a transition to an even slower rate of oxidation. This transition is believed to be caused by the development of the SiO_2 subscale on these alloys.

ORIGINAL PAGE IS
OF POOR QUALITY

The manganese-enriched outer scales frequently had the approximate composition of the manganese-chromium spinel, $MnCr_2O_4$. The formation of this spinel probably consumed some of the protective Cr_2O_3 and produced the faceted crystals that were observed on the 303RS alloy surfaces. The spinel also appears to have spalled frequently upon cooling, particularly at 1000°C.

The formation of a manganese enriched outer scale layer on the 303RS is due to the high affinity of manganese for oxygen and the rapid diffusion of Mn through Cr_2O_3 [7]. The preferential transport of Mn through the chromium-rich outer scale may be assisted by the presence of an SiO_2 subscale which serves as a differential diffusion barrier to inhibit the transport of chromium [1] while allowing the flux of manganese and iron [5] to continue unabated.

Long-Term Oxidation Resistance of the 303RS Alloy

The protective oxide scales which form on the 303RS alloy are expected to exhibit very little cracking or spallation during long-term oxidation. The uniformity of thickness and composition apparently minimizes internal stresses in the oxide, thereby limiting the incidence of cracking of the scale. At the same time, the oxide intrusions which key the scale to the alloy help prevent spallation.

In the event of scale breakdown after the alloy has been in service for a long period of time, continued resistance to oxidation requires that the alloy be able to reform a protective surface scale. Therefore, it is essential that the alloy retain the microstructural characteristics which were responsible for its original oxidation resistance. In the case of 303RS, these characteristics include a fine dispersion of MnS precipitates to pin the alloy grain boundaries and to serve as heterogeneous nucleation sites for Cr_2O_3, and a fine grain size to promote both heterogeneous nucleation of Cr_2O_3 and Cr transport from the bulk alloy to the surface.

Optical microscopy was performed on the 303RS specimens to determine

the grain size after oxidation at 900, 1000 and 1100°C (Table 2). The measured grain sizes indicate that the alloy strongly resists grain coarsening at 1000°C and below, and less strongly at 1100°C. Transmission electron microscopy studies of the alloys after oxidation were not performed, so the size and distribution of MnS particles is not know. However, Yurek et al. [1] observed that the MnS particles in a 303RS alloy did not noticeably coarsen during 300h at 900°C, but remained 0.2 to 0.5 microns in diameter.

Olson et al. [8] presented a model for the growth of grains in alloys in which the grain boundaries are pinned by second phase particles. This model predicts that the grain coarsening process will obey a cubic rate law of the form:

$$(r - r_o) = k\, t^{1/3}$$

where r is the size of the grains, r_o is the original grain size, k is a constant, and t is time. The grain growth which was measured during the oxidation tests (Table 2) was used to calculate k for 900, 1000, and 1100°C. The model was then used to predict the alloy grain size expected after 1000 and 10,000 hours at each of these temperatures. The results are also presented in Table 2. The model predicts that a relatively fine grain size (13.9 microns) will be maintained in the 303RS alloy even after 10,000 hours at 900°C, so the enhanced oxidation resistance of this alloy should be maintained for relatively long periods of time. At 1000°C grain growth proceeds more rapidly, and after 10,000 hours a grain size of approximately 28 microns is predicted. This large degree of grain growth will almost certainly have an adverse effect on the long-term oxidation resistance of the alloy, but the magnitude of the effect cannot be predicted. It should also be noted that the silica intrusions at the surface of the alloy will still serve as mechanical pegging points even after grain growth, and will actually limit the severity of grain growth that is possible in the near-surface region.

ORIGINAL PAGE IS
OF POOR QUALITY

TABLE 2: Predicted Grain Growth of 303RS

Thermal History	Measured Grain Size	k	Predicted Grain Size 1000 hrs.	Predicted Grain Size 10,000 hrs.
900°C/200 hr	8.5 micron	0.34	9.9	13.9
1000°C/135 hr	11.7	1.01	14.9	28.3
1100°C/50 hr	22	4.48	46	92

(The initial grain size was 6.5 microns)

Improvements in the long-term oxidation resistance of rapidly solidified alloys may be achieved if the fine grain sizes inherent in these alloys can be stabilized. Recent work at M.I.T. [9] demonstrates that the control of small quantities of impurities in these alloys, which eventually yield very stable, complex oxide precipitates that are very effective in pinning grain boundaries, may be of paramount importance in the processing sequence. More studies in this area would be beneficial because additional knowledge of how to control alloy microstructure, and hence alloy properties, through rapid solidification processing would help significantly in the development of new alloys with improved properties.

ORIGINAL PAGE IS
OF POOR QUALITY

ORIGINAL PAGE IS
OF POOR QUALITY

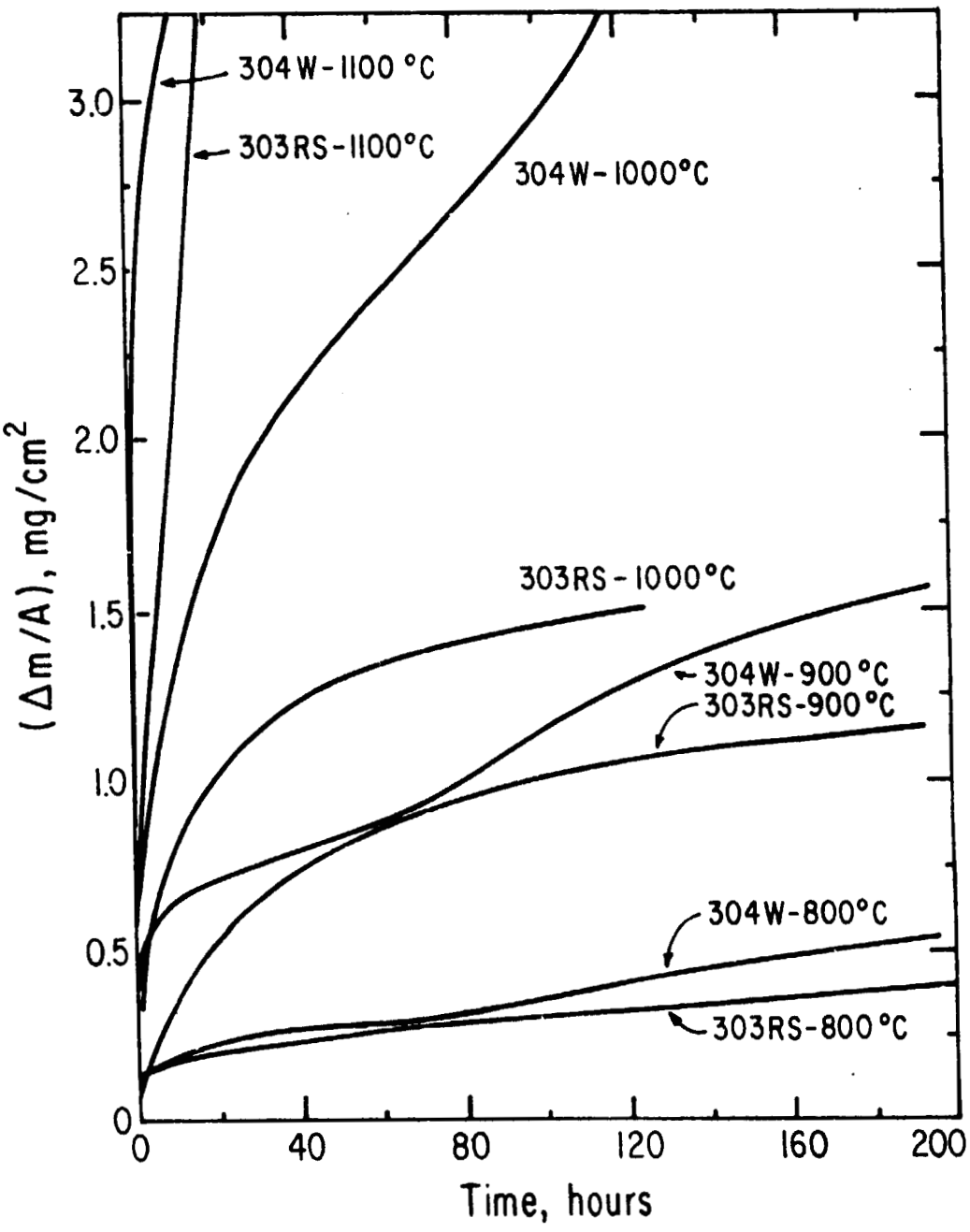

Figure 1. Kinetics of the isothermal oxidation of 303RS and 304W steels.

ORIGINAL PAGE IS
OF POOR QUALITY

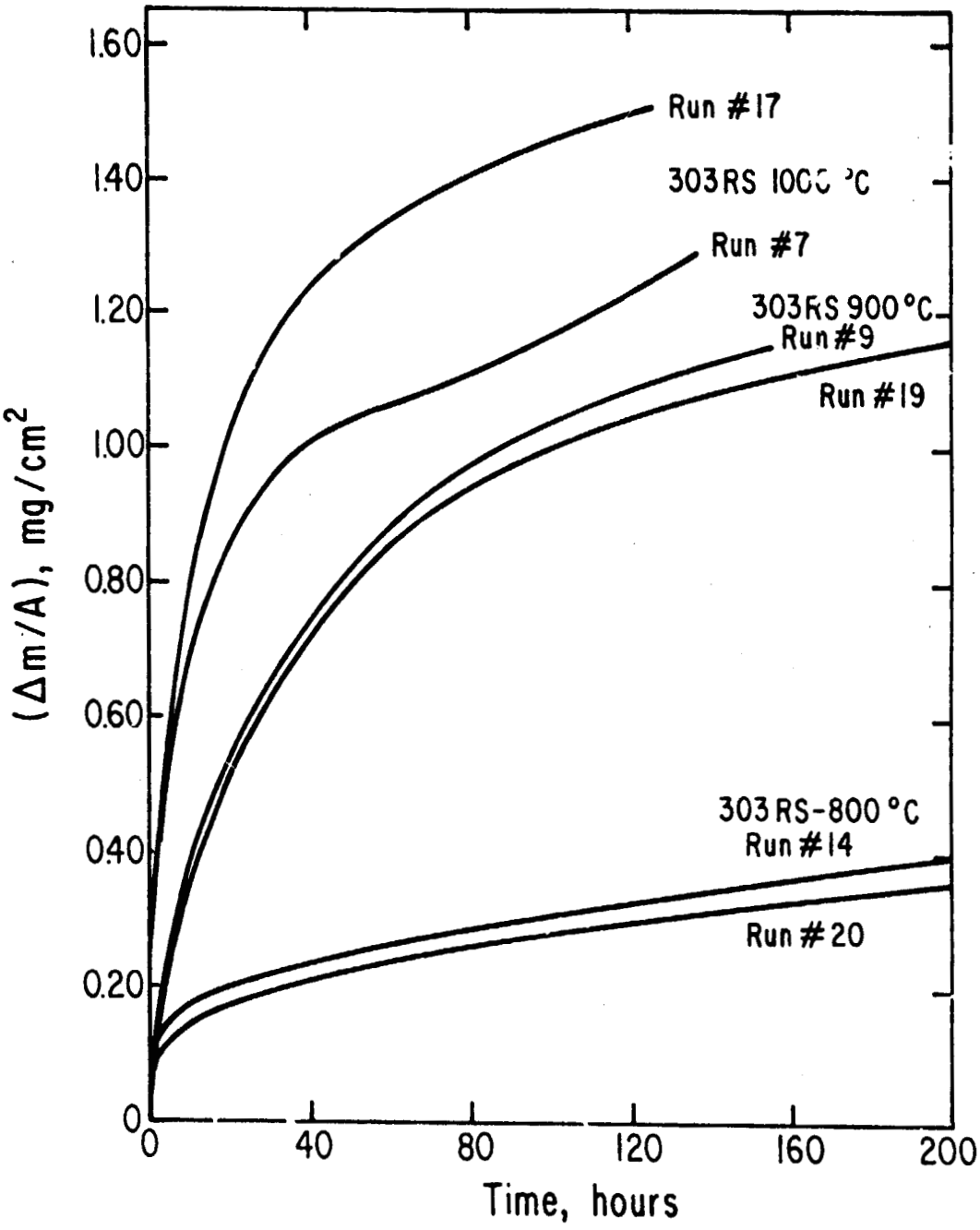

Figure 2. Kinetics of the oxidation of 303RS at 800 to 1000°C.

ORIGINAL PAGE IS
OF POOR QUALITY

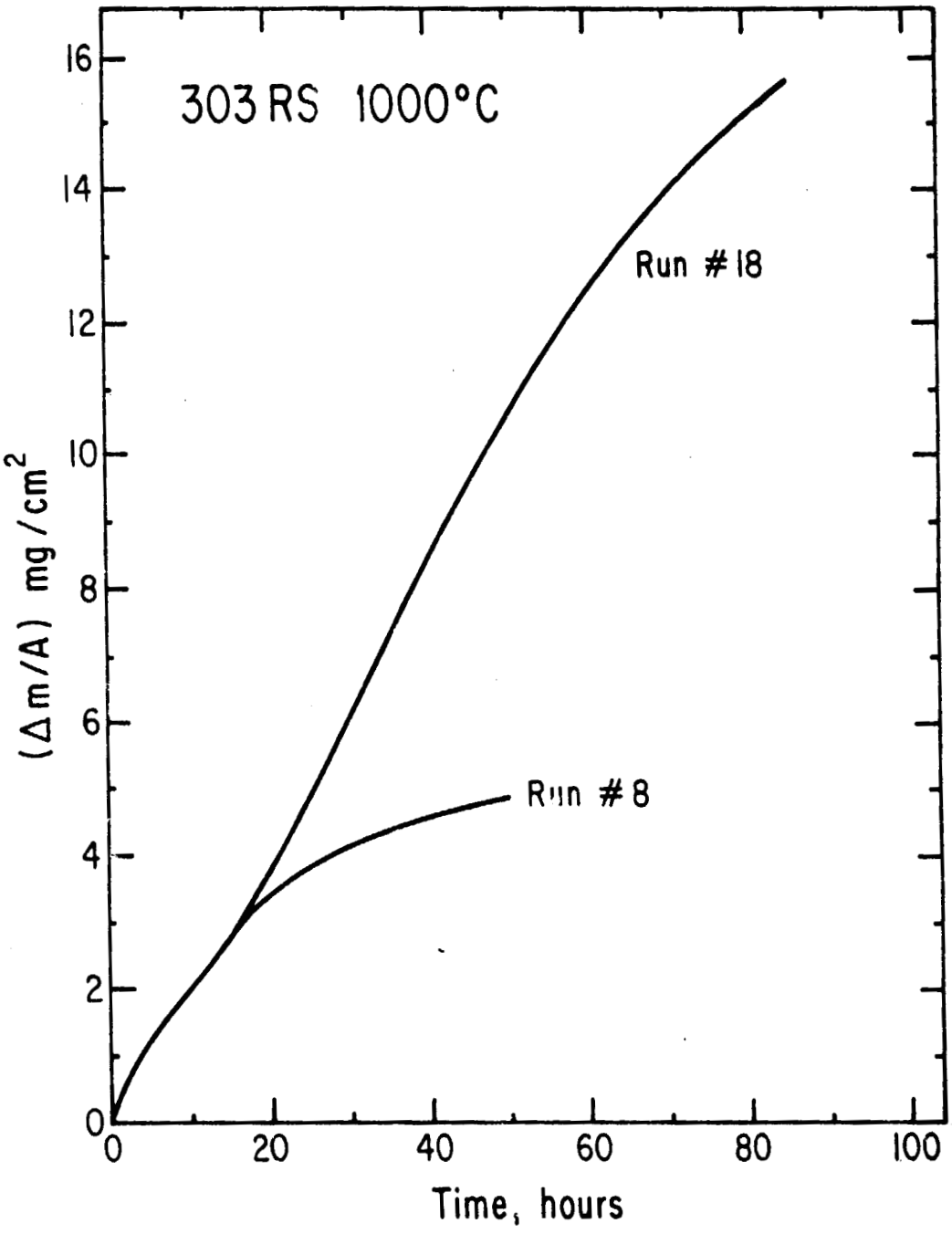

Figure 3. Kinetics of the oxidation of 303RS at 1100°C.

ORIGINAL PAGE IS
OF POOR QUALITY

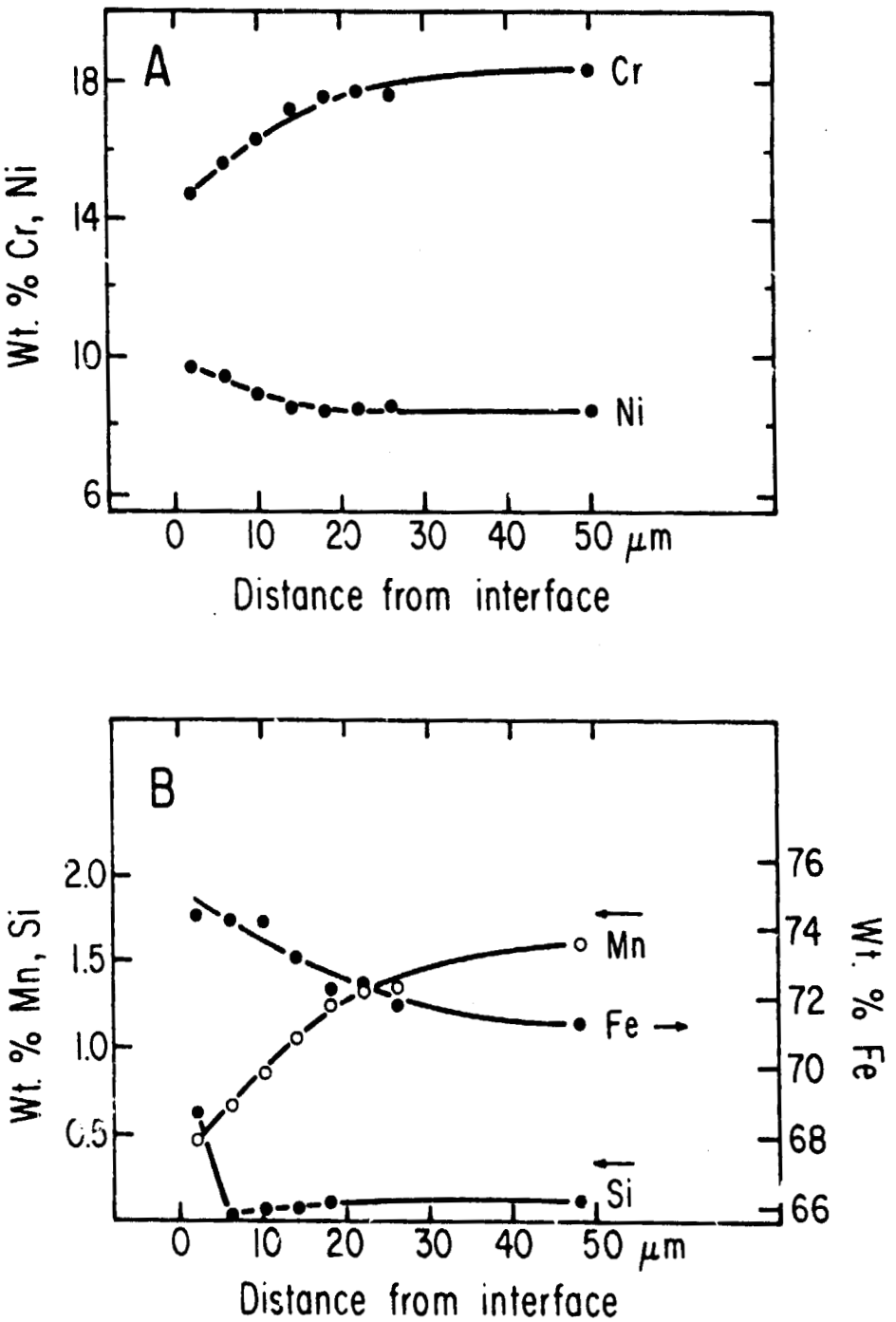

Figure 4. Concentration profiles in a 304W alloy that had been oxidized for 126h at 1000°C. The abscissa is the distance from the alloy/scale interface.

ORIGINAL PAGE IS
OF POOR QUALITY

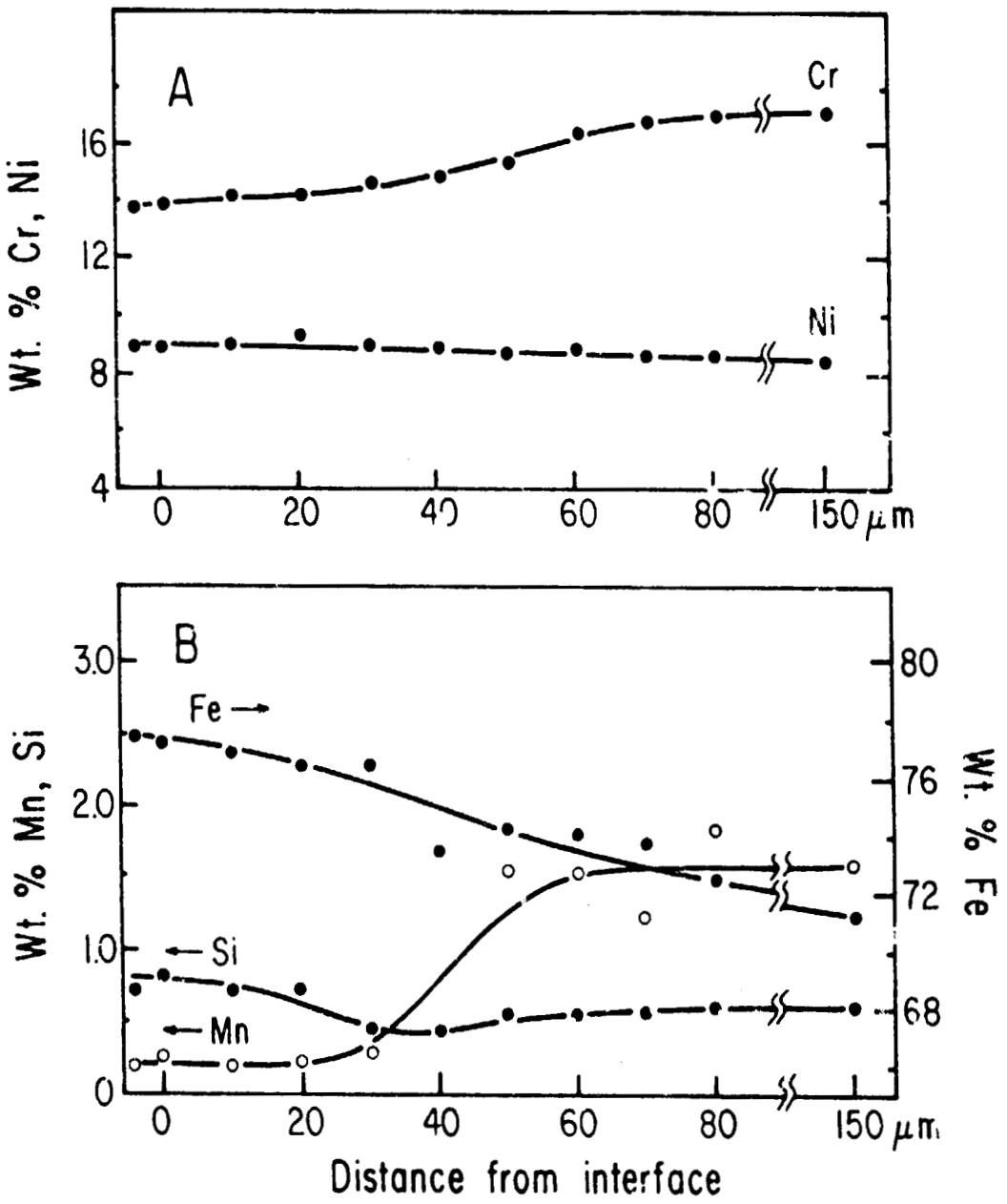

Figure 5. Concentration profiles in a 309RE alloy that had been oxidized for 10 h at 1000°C. The abscissa is the distance from the alloy/scale interface.

REFERENCES

1. G. J. Yurek, D. Eisen and A. Garratt-Reed, Met Trans A, 1982, vol. 13A, p. 473.

2. T. Kelly and J. Vander Sande, 2nd Int. Conf. on Rapid Solidification Processing: Principles and Technology, March 23-26, 1980, Reston, Va.

3. L. A. Morris, Handbook of Stainless Steels, D. Peckner and I. M. Bernstein, eds., McGraw-Hill, N. Y., 1977, p. 17-1.

4. D. Caplan and M. Cohen, Corrosion, 1959, vol. 15, p. 141t.

5. H. Evans, D. Hilton, R. Holm, and S. Webster, Oxid. Met., 1980, vol. 14, p. 235.

6. G. Wood, M. Hobby and B. Vaszko, JISI, 1974, vol. 202, p. 685.

7. R. Wild, Corr. Sci., 1977, vol. 17, p. 87.

8. G. Olson, H. Ling, J. Montgomery, J. Vander Sande and M. Cohen, "Grain Coarsening Resistance and the Stability of Second-Phase Dispersions in Rapidly Solidified Steels," M.I.T., 1982.

9. G. Olson, M. Cohen and G. J. Yurek, Proceedings of the Third Conference on Rapid Solidification Processing: Principles and Technologies, Dec. 6-8, 1982, National Bureau of Standards.

ORIGINAL PAGE IS
OF POOR QUALITY

Processing of Sendust-Type Soft Ferromagnetic Alloys

Principal Investigator: Samuel A. Allen

RESEARCH ABSTRACT

Super Sendust is a quaternary iron-base with 5.3 w/o Si, 4.2 w/o Al and 3.1 w/o Ni. It was developed from a ternary iron-silicon-aluminum alloy, Sendust, with the aim of improvements both in soft ferromagnetic properties and in mechanical ductility. The present study focussed on processing of Super Sendust by a combination of melt-spinning rapid-solidification, deformation, and thermal annealing techniques. The objective was to obtain material in the form of thin ribbons, with modest ductility, and excellent soft ferromagnetic properties.

The melt spinning of Super Sendust was shown to give ribbon geometries that was strongly dependent on nozzle geometry of the melt crucible. The most rapidly cool ribbons were ductile in the as-cast condition. As cast, the ribbons had a coercive force H_c of about 1.9 Oe. Two-stage heat treatments were devised that enabled H_c to be reduced to 0.5 Oe, but in addition embrittled the material. The optimum annealing schedule consisted of one hour at 1200°C, cooling at -10°C/minute to 690°C, holding at 690°C for three hours, and air quenching. Transmission electron microscopy was used to study microstructures of the as-cast and annealed ribbons. A phase transition from the B2 to DO_3 superlattice structures was found to occur on cooling at about 680°C. Magnetic properties of samples with the B2 structure were superior to those with the DO_3 structure.

INTRODUCTION

The Sendust composition, Fe-9.6 w/o Si-5.4 w/o Al, has long been recognized as an alloy with exceptional characteristics as a soft ferromagnetic material. These are: High permeability, low coercivity, high electrical resistance, and reasonably good saturation magnetization. These excellent properties result primarily from the fact that the composition has near-zero magnetostriction as well as near-zero magnetic anisotropy. Unfortunately, the material is also very brittle and applications in the past have been limited mainly to cast shapes and to forms made from compressed powder.

Two recent studies give promising results with respect to processing-related improvements for these alloys. The first is a report by Tsuya et al. [1] of the use of a melt-spinning rapid-solidification technique to produce Sendust alloy ribbons of fine grain size. As cast, these ribbons were ductile enough to be rolled to 25% of their original thickness. After annealing treatments to optimize magnetic properties, however, the material was embrittled. The second study, by Yamamoto and Utsushikawa [2] focussed on alloy modification through 3 w/o additions of nickel to an Fe-6 w/o Si-4 w/o Al alloy. Although the mechanical properties to the Super Sendust alloy were not studied, there is reason to expect that it will have better ductility than Sendust: Nickel additions to soft ferromagnets are generally believed to contribute to both magnetic and mechanical softness. Also, Super Sendust has approximately one-third less aluminum and silicon, each of which embrittles iron.

The aim of the present study was to employ rapid solidification techniques to produce Super Sendust alloy ribbons, and to study processing-structure-property relations of the resulting material in order to optimize soft ferromagnetic properties. The results of the study are reported in detail in the Master's thesis of Eric P. Kvam [3].

ORIGINAL PAGE IS
OF POOR QUALITY

RESEARCH REPORT

Alloy Preparation and Melt Spinning

Super Sendust alloy buttons were prepared by vacuum arc melting. The ingots were then remelted and cast in a melt spinning apparatus onto either the inside or the outside of a rapidly rotating drum. Ribbons rangeed in thickness from 30 to 100 μm, and in width from 2-5 mm. Ribbon quality proved difficult to control. Frequently, ragged edges were obtained and ribbon surfaces were rough. A ribbon of typical quality is shown in Figure 1. It was generally difficult to produce continuous long straight segments of ribbon, and although process parameters like wheel speed, distance of the nozzle from the wheel, and degree of superheat of the melt were varied, no particular combination of parameters were found that consistently produced smooth uniform ribbons.

Figure 1. Macrograph of ribbon showing typical appearance of surfaces and edges. Roughness of as-spun Super Sendust ribbons could not be eliminated.

Effect of Processing on Magnetic Properties

The magnetic properties of the ribbon material were studied. Our efforts centered on developing processing schedules to minimize the coercive force of the material. As a target value, the lowest value of coercive force reported for the ternary Sendust composition is about 10 mOe [4].

As melt-spun, the coercive force of the Super Sendust ribbons was approximately 1.9 Oe, which is comparable to the value reported for as-

spun Sendust ribbons prior to thermal annealing treatments. [1] Two types of processing treatments have been used in an attempt to dramatically reduct coercive force in the Super Sendust ribbons: thermal annealing treatments, and combined deformation and annealing treatments.

A variety of thermal annealing treatments were used. Annealing temperatures, times and quench rates were varied. The lowest values of H_c were obtained from ribbons annealed for 1 hour at 1200°C, (T_1 temperature), cooling to 690°C at -10°C/min, holding at 690°C (T_2 temperature) for 3 hours, and finally air cooling to ambient temperature. This treatment resulted in a reduction of H_c to 0.5 Oe. The influence of temperature T_1 and T_2 on measured values of H_c is shown in Figure 2.

ORIGINAL PAGE IS
OF POOR QUALITY

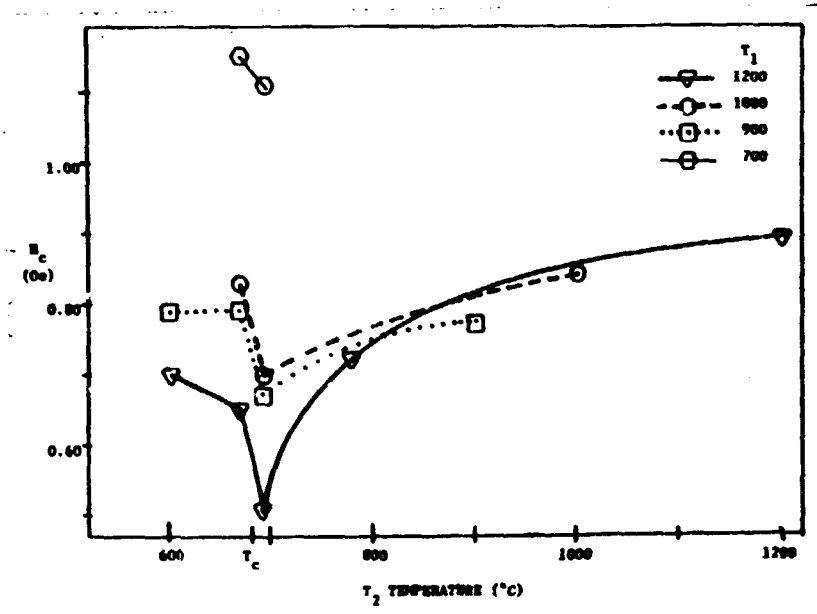

Figure 2. Coercive force of Super Sendust ribbons after two-stage annealling treatments at temperatures T_1 and T_2. H_c is a minimum for T_2 slightly above the critical temperature T_c for the B2→DO_3 phase transition.

Rolling of as-melt-spun ribbons was done to reduce suface roughness of the ribbons in an attempt to provide further reductions in H_c. After thermal annealing of the rolled ribbons, H_c was still at the 0.5 Oe level. This compares unfavorably with the 0.01 Oe value obtained for Sendust ribbons [4].

Effect of Processing on Microstructure

An order-disorder phase transformation from the B2 (CsCl) high temperature phase to the DO_3 (BiF_3) low temperature phase was found to occur

at 680°C by electron microscopy examination of Super Sendust samples annealed over a range of temperatures from 570°C to 800°C. The primary defects in these phases are antiphase boundaries (APBs). Because antiphase domain sizes which are of similar scale to magentic domain wall widths (~0.1μm) can interfere with magnetic domain wall motion, we studied the kinetics of antiphase domain coarsening. The measured kinetics for thee Super Sendust alloy fit a coarsening model developed by Allen and Cahn [5]. A 4-hour annealing treatment at 670°C produced an antiphase domain size in the DO_3 phase of about 1.4μm, which should be coarse enough to minimize this particular source of resistance to magnetic domain wall motion in specimens with the DO_3 structures.

The minimum coercivity measured in our alloys after heat treatment at 690°C thus corresponds to equilibration at a temperature just slightly above the B2→DO_3 phase transformation, in the single-phase B2 phase field. Our results show that sample with the DO_3 structure have higher coercivity by comparison.

Grain size of the as-spun ribbons was found to increase with increasing ribbon thickness. A 30 μm thick ribbon had a 1.5 μm grain size, while a 100 μm thick ribbon had a 10 μm grain size. Annealing at temperatures over 900°C produced nearly complete grain growth (so that the grain size was limited by ribbon thickness) in one hour. Only those ribbons with the smallest grain sizes were found to have significant ductility.

References

1. N. Tsuya, K. Arai, and K. Ohmori, IEEE Tran. Magn. MAG-15, 1149 (1979).

2. T. Yamamoto and Y. Utsushikawa, Trans. JIM 19, 326 (1978).

3. E.P. Kvam, "Soft Ferromagnetic Properties of Rapidly Solidified Super Sendust Alloy Ribbons", S.M. Thesis, Department of Materials Science and Engineering, Massachusetts Institute of Technology, June 1982.

4. N. Tsuya, K. Arai, K. Ohmori and T. Homma, "Annealing of Rapidly Quenched Sendust Ribbon", presented at the 27th Annual Conference on Magnetism and Magnetic Materials, Atlantic Georgia, Nov. 10-13, 1981.

5. S.M. Allen and J.W. Cahn, Acta Met. 27. 1085 (1979).

ORIGINAL PAGE IS
OF POOR QUALITY

Fluid Flow and Crystallization Processes

Heat Flow and Segregation in Directional Solidification

Principal Investigator: August F. Witt

RESEARCH ABSTRACT

The thrust of this research program continues to be the optimization of heat transfer control in melt and solution growth of elemental and compound semiconductor systems. Focus is placed on the development of an optimized crystal growth facility which will permit a meaningful exploration of the potential of reduced gravity for growth of electronic materials. Significant developments during the past year include the following.

(1) A computer controlled, heat pipe based Bridgman growth facility has been completed and is currently undergoing extensive thermal characterization.

(2) A two-dimensional heat transfer analysis for Bridgman growth, based on boundary conditions which are realizable in the constructed facility, has been completed and is used for the optimization of critical gradient zone configuration in this facility; it is also used as a basic criterion for crucible and ampoule design.

(3) The heat transfer control concepts developed in this research program had a major impact on Army and NRL sponsored research and have led to the submission of a

PAGE 88 INTENTIONALLY BLANK

PRECEDING PAGE BLANK NOT FILMED

patent disclosure (with joint NASA-Army sponsorship) on a "heat exchange system for optimized control of interdependent thermal parameters in crystals grown by LEC and the conventional Czochralski technique". The extension of the heat transfer control concepts developed for Bridgman growth to industrial Czochralski growth is considered by many as a major breakthrough.

(4) NRL sponsorship for the preparation of a flight experiment involving CdTe has been ascertained.

(5) It has been determined that, contrary to assertions in the STAMPS report, transverse magnetic fields of up to 5 kG applied to vertical Bridgman growth will not establish diffusion controlled segregation during growth; the effective distribution coefficient for growth in the presence of a magnetic field is not significantly larger than that in the absence of a magnetic field. For growth systems with a diameter of more than 1 cm, magnetic fields are no substitute for reduced gravity environment.

(6) During the past year this research program enjoyed two supporting graduate fellowships from IBM and BTL.

(7) The research conducted during the past year is documented in seven publications (one published, two in print and four being prepared for publication), one Ph.D. thesis and one Masters thesis.

This research program has now reached a phase where preparation of flight experiments for implementation in the Shuttle program can and should be initiated. In this context it is also suggested to conduct a detailed analysis of the developed growth facility with regard to its suitability for flight operation.

ORIGINAL PAGE IS
OF POOR QUALITY

(Basic elements of submitted patent disclosure
on heat transfer control in Czochralski growth.)

Heat Exchange System for Optimized Control of the Following Interdependent Parameters:

- Crystal temperature (range 500 °C - 1100 °C)
- Growth interface morphology
- Temperature gradients about the growth interface
- Thickness of encapsulating B_2O_3 layer
- Radial thermal symmetry in the vicinity of the growth interface
- Radial thermal gradient in growing crystal

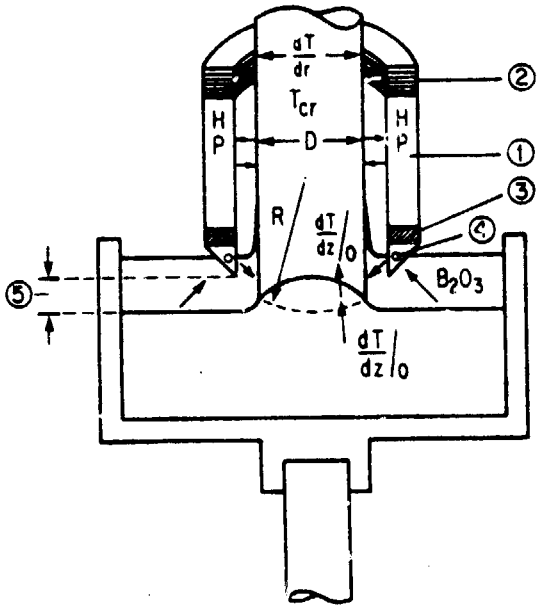

① Inconel Heat Pipe with Operating Range from 500 °C - 1100 °C

② Peltier Heating / Cooling System

③ Thermal Insulation

④ Auxiliary Heating Element

⑤ Axial Position of Heat Exchange System (adjustable)

ORIGINAL PAGE IS
OF POOR QUALITY

VERTICAL BRIDGMAN TYPE CRYSTAL GROWTH: A HEAT TRANSFER ANALYSIS

INTRODUCTION

Semiconductor crystal growth experiments carried out in a reduced gravity environment using a conventional Bridgman configuration revealed deficiencies in crystalline and chemical perfection which have been attributed primarily to inadequate heat transfer control during growth. Since this growth technique is of importance for the growth of electronic materials on earth and, moreover, is a viable technique for the exploration of the potential of growth in a reduced gravity environment, a comprehensive, NASA sponsored effort has been made for its optimization. This work addresses the thermal characteristics of crystal growth by the vertical Bridgman method to (1) evaluate its inherent limitations and (2) to develop an understanding of the primary parametric behavior necessary for a cognizant appraisal of thermal design alternatives. The first part of the thermal analyses, concerned with the axial temperature distribution of the charge, has been discussed in the 1981 Materials Processing Center Annual Report; a brief summary of these results is included here. Presently, focus is placed on the radial temperature variations within the charge. A complete account of both thermal analyses is contained in the Ph.D. thesis of T. Jasinski, Department of Mechanical Engineering, 1983.

The basis for the thermal models is an experimental growth system in which well defined thermal boundary conditions are achieved through the use of coaxial heat pipes. A schematic of this configuration is shown in Fig. 1.1. The gradient control region located between the hot and cold heat pipes is envisioned as providing a degree of flexibility for the thermal boundary conditions of the furnace near the growth interface.

ORIGINAL PAGE IS
OF POOR QUALITY

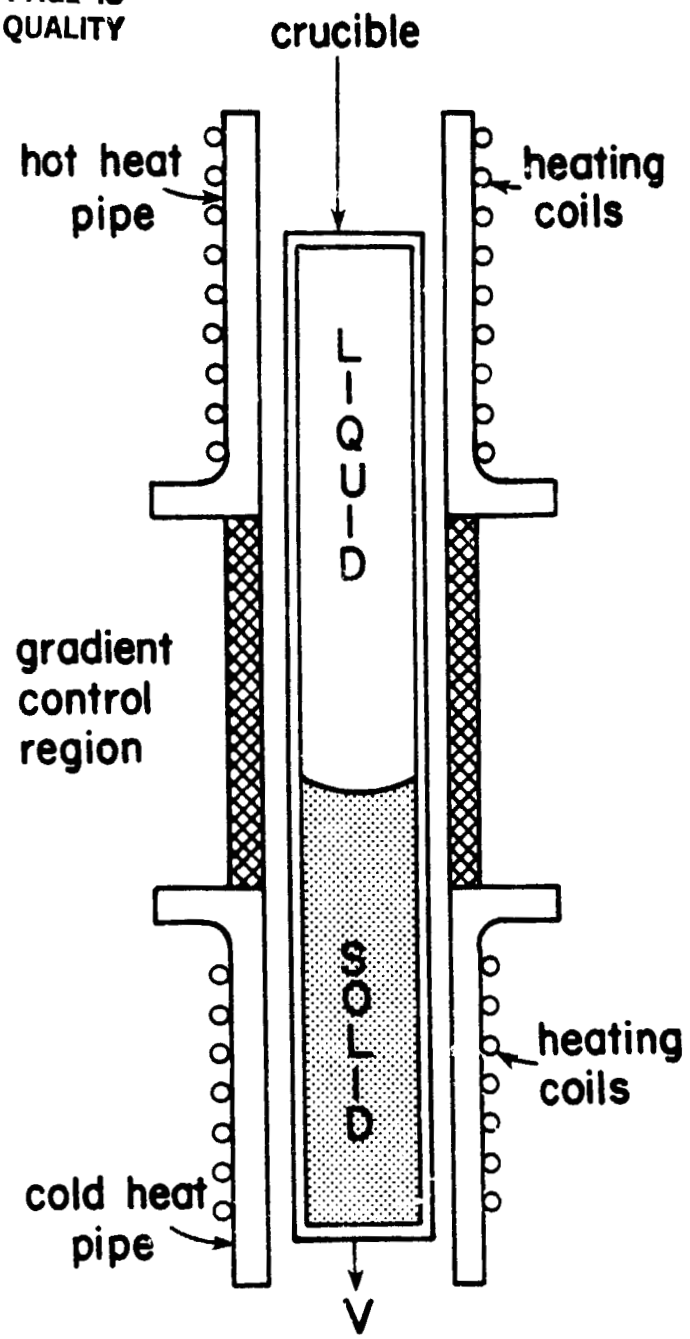

Fig. 1.1. The experimental vertical Bridgman crystal growth system.

ORIGINAL PAGE IS
OF POOR QUALITY

SUMMARY OF ONE-DIMENSIONAL RESULTS

The one-dimensional thermal model considers the charge and crucible to be a fin moving through the boundary conditions imposed by the furnace. This model is hereafter referred to as the moving fin model. The axial temperature distribution is described by a second order, ordinary differential equation within each axial region of uniform furnace boundary conditions and charge thermal properties. Given the assumptions employed by the one-dimensional model, there are four such regions. The solution for the axial temperature distribution is readily obtained by computer. Carrying out the analytical solution, however, yields relatively simple expressions for (1) the axial temperature gradient in the liquid at the growth interface, G_L, and (2) the axial position of the growth interface, ζ_i. These expressions include the effects of the thermal coupling between the hot and cold zones and the charge, gradient zone length, thermal conductivity change and generation of latent heat at the growth interface, charge lowering rate, and charge diameter. Criteria are also developed which indicate under which conditions the effects of the lowering rate of the charge, generation of latent heat and finite length of the charge may be neglected. Finally, the effects of the crucible and radial thermal resistance within the charge are shown analytically to result in a decrease of the effective thermal coupling between the furnace and the charge.

THE TWO-DIMENSIONAL THERMAL MODEL

Thermal criteria for satisfactory Bridgman crystal growth include requirements for the shape of the solidification temperature isotherm. The moving fin model does not permit evaluation of the isotherm shape since it neglects radial temperature variations within the charge. For this purpose, a two-dimensional model of the Bridgman growth system is developed in the present section. Results from the two-dimensional model are used in Section 4 in order to establish the causes of radial temperature variations within the charge and to study their dependence on the thermal parameters of the Bridgman growth system.

ORIGINAL PAGE IS
OF POOR QUALITY

The Concentric Fin Approach

The present two-dimensional thermal model of vertical Bridgman growth treats the entire system as a set of coaxial fins. Radial temperature variations are thus accounted for by differences in the fin temperatures at the same axial location. The model can therefore be considered a hybrid between a continuous description in the axial direction and a finite difference description in the radial direction. This approach, rather than a complete finite difference or finite element formulation, is taken for several reasons:

(1) The primary objective of the two-dimensional model is to develop insight into the origin and behavior of radial temperature gradients near the growth interface for the purpose of controlling the shape of this interface through system design. The increased accuracy achievable using a fine grid network in a finite difference or finite element model is not considered essential for this objective and, furthermore, does not appear warranted for systems for which reliable thermal property data are not yet available. The present model incorporates all the critical thermal effects; it is expected, therefore, to be able to predict the radial gradient behavior at least to first order approximations. (By utilizing enough coaxial fins, the present model should, in principle, be as accurate as a finite difference model.)

(2) The present model is easily implemented on the computer and is a simple extension of the one-dimensional moving fin model.

(3) Even with the simplifications inherent to the concentric fin approach, the added complexity of a two-dimensional formulation necessitates the use of a computer to calculate the two-dimensional temperature distribution of the charge. The concentric fin model can be simplified,

ORIGINAL PAGE IS
OF POOR QUALITY

however, without loss of pertinent information, to a point which permits presentation of some important results in analytical form.

The Describing Equations For The Concentric Fin Model

The factors of concern for the development of the concentric fin model of the Bridgman growth system depicted in Fig. 1.1 are indicated in Figs. 3.1 and 3.2. The two-dimensional thermal model incorporates the following assumptions.

(1) Radial temperature variations within the charge are accounted for by modeling the charge as two radially distinct fins. The inner fin is a cylinder of diameter D_{in} and has an axial temperature distribution $T_{in}(Z)$. The outer fin is an annulus of inner and outer diameters, D_{in} and D, and has an axial temperature distribution $T_{out}(Z)$. The diameter D_{in} is chosen so that the inner and outer fins have equal cross sectional area. The temperature of each charge fin is not considered a function of radius. The difference in temperature between T_{in} and T_{out} is indicative of radial temperature variations within the charge.

(2) The crucible is modeled as a coaxial annular fin in contact with the outer charge fin. The crucible fin temperature, $T_{cr}(Z)$, is not a function of radius.

(3) As opposed to the corresponding assumption in the moving fin model, the gradient zone is not adiabatic. This assumption is relaxed in the two-dimensional model so that the effect of radial heat transfer between a non-perfectly insulating gradient zone and the charge can be studied.

ORIGINAL PAGE IS
OF POOR QUALITY

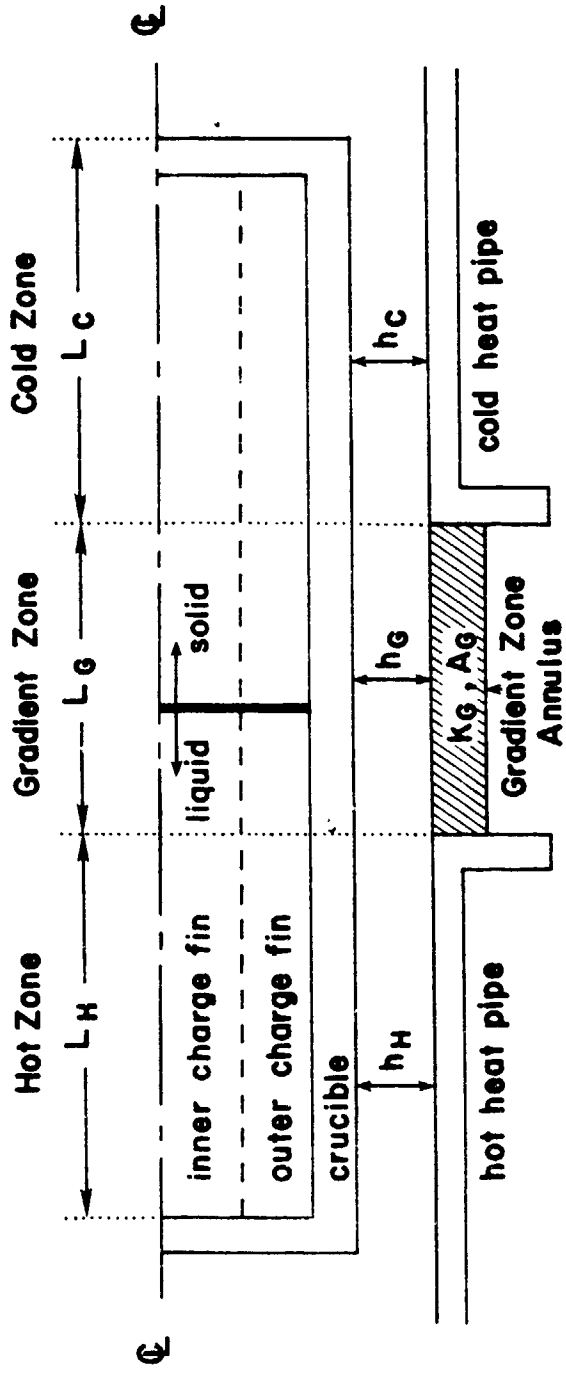

Fig. 3.1. Schematic of the charge, crucible, gradient zone annulus and furnace heat pipes in the concentric fin model.

C-2

ORIGINAL PAGE IS
OF POOR QUALITY

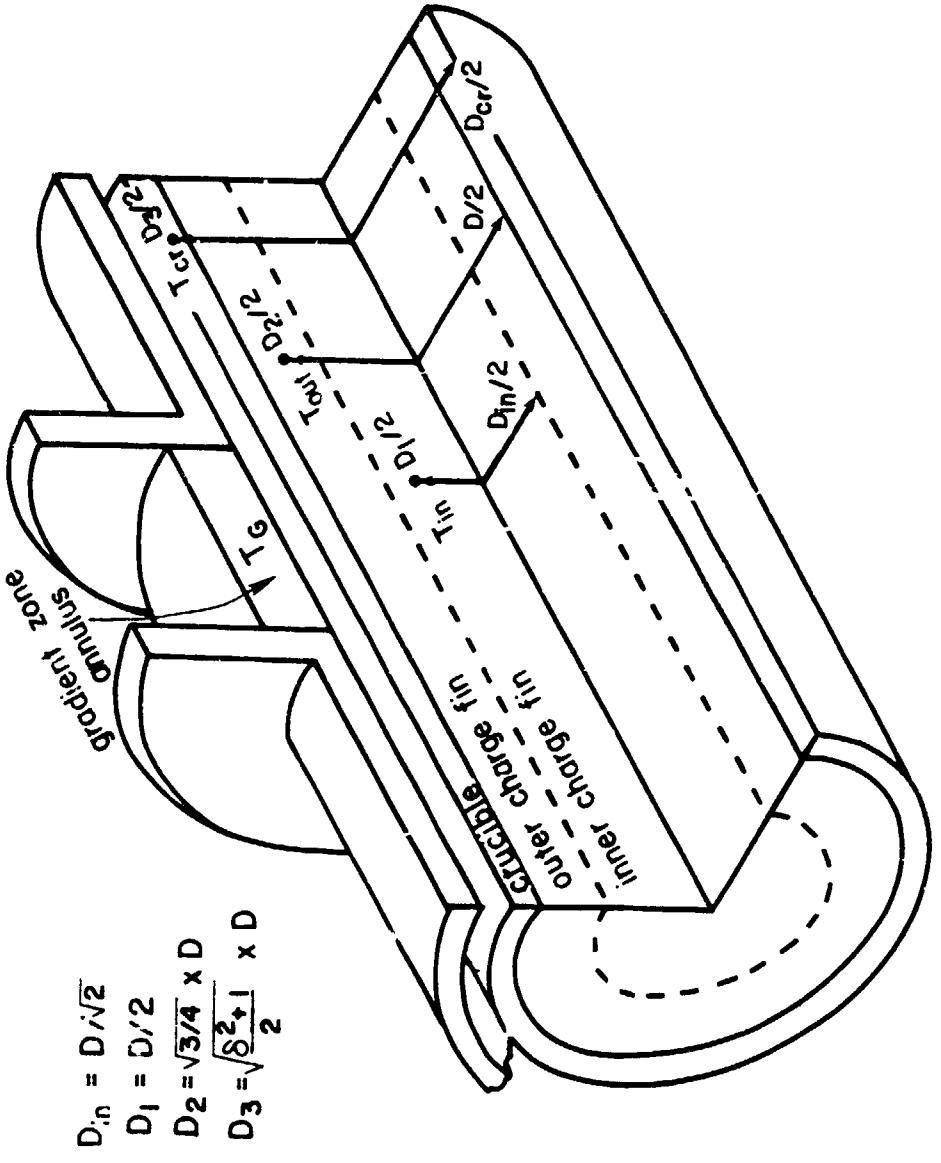

Fig. 3.2. Cut-away sketch of charge, crucible and gradient zone annulus showing the geometry of the concentric fins.

ORIGINAL PAGE IS
OF POOR QUALITY

(4) The portion of the furnace in the gradient zone is considered to be an annulus of conductivity k_G and cross-sectional area A_G located coaxially with the charge and crucible. The temperature of the gradient zone annulus is assumed constant in the radial direction; its axial temperature distribution, $T_G(Z)$, depends on its thermal interaction with the charge and crucible. Temperature boundary conditions are used at the ends of the gradient zone annulus and no heat loss is assumed at its outer diameter.

(5) Hot and cold zone furnace temperatures, $T_{f,H}$ and $T_{f,C}$ respectively, are uniform, reflecting the heat pipe behavior. The lengths of the heat pipes are assumed infinite.

(6) The system is at all times in a quasi-steady state; i.e., transients are neglected.

(7) No heat transfer by natural convection in the melt.

(8) Heat exchange between the furnace and the outer crucible surface is described by a heat transfer coefficient, h, which is constant within each zone.

(9) Thermal properties do not depend on temperature except for a difference in conductivity between the melt and crystal portions of the charge.

Assumptions (5) through (9) are also used in the moving fin model.

On the basis of the above assumptions, each of the concentric fins is analogous to the moving thin rod treated by Carslaw and Jaeger [1]:

$$k A_x \frac{d^2T}{dZ^2} - A_x V \rho c_p \frac{dT}{dZ} + q = 0 \qquad [3.1]$$

ORIGINAL PAGE IS
OF POOR QUALITY

where: k = thermal conductivity of a fin
A_x = cross sectional area of a fin
T = fin temperature
Z = axial coordinate measured from the center of the gradient zone toward the cold zone
V = lowering rate
ρ = mass density of a fin
c_p = specific heat of a fin
q = heat transfer per unit length to the fin from its surroundings

In Appendix A, the q term of eq. [3.1] is approximated resulting in the following set of coupled ordinary differential equations for the axial temperature distribution of the fins:

$$\frac{d^2\phi_m}{d\zeta^2} - Pe_{loc}\frac{d\phi_m}{d\zeta} + A_1(\phi_{cr} - \phi_m - \phi_\Delta) = 0 \qquad [3.2a]$$

$$\frac{d^2\phi_\Delta}{d\zeta^2} - Pe_{loc}\frac{d\phi_\Delta}{d\zeta} + A_1(\phi_{cr} - \phi_m - \phi_\Delta) = 0 \qquad [3.2b]$$

$$\frac{d^2\phi_{cr}}{d\zeta^2} - Pe_{cr}\frac{d\phi_{cr}}{d\zeta} + A_3(\phi_\Delta + \phi_m - \phi_{cr}) + A_4(\phi_f - \phi_{cr}) = 0 \qquad [3.2c]$$

$$\frac{d^2\phi_c}{d\zeta^2} + A_5(\phi_{cr} - \phi_c) = 0 \qquad [3.2d]$$

where: ζ = dimensionless axial coordinate, Z/D

$$\phi \equiv (T - T_{f,c})/(T_{f,H} - T_{f,c})$$

$$\phi_m \equiv \tfrac{1}{2}(\phi_{out} + \phi_{in})$$

$$\phi_\Delta \equiv \tfrac{1}{2}(\phi_{out} - \phi_{in})$$

$$Pe_{loc} = VD\rho c_p/k_{loc}$$

$$Pe_{cr} = VD(\rho c_p/k)_{cr}$$

ORIGINAL PAGE IS
OF POOR QUALITY

subscript "loc" refers to local charge properties or zone heat transfer coefficient

subscript "cr" refers to the crucible

The coefficients A_1, A_2, A_3, A_4, and A_5 depend on the radial thermal resistance between the concentric fins. They are given by:

$$A_1 = \frac{8}{\ln\sqrt{\frac{4}{3}} + \frac{1}{K_{loc}} \ln\left(\frac{\delta^2+1}{2}\right)^{1/2}} \qquad [3.3a]$$

$$A_2 = \frac{32}{\ln\sqrt{3}} \qquad [3.3b]$$

$$A_3 = \frac{A_1}{K_{loc}(\delta^2-1)} \qquad [3.3c]$$

$$A_4 = \frac{8}{K_{loc}(\delta^2-1)} \cdot \frac{1}{\frac{2}{\delta\, Bi_{loc}} + \frac{1}{K_{loc}} \ln\left(\frac{1}{1+\delta^{-2}}\right)^{1/2}} \qquad [3.3d]$$

$$A_5 = \frac{A_4 K_{loc}(\delta^2-1)}{R_{G,loc}} \qquad [3.3e]$$

where: $\delta = D_{cr}/D$

D_{cr} = crucible diameter

D = charge diameter

$K_{loc} = k_{cr}/k_{loc}$

$Bi_{loc} = h_{loc} D/k_{loc}$

$R_{G,loc} = k_G A_G/k_{loc} A$

The fin equations for ϕ_{out} and ϕ_{in} have been added to and subtracted from one another in order to produce eqs. [3.2a] and [3.2b] for ϕ_m and ϕ_Δ respectively. Since the cross sectional areas of the inner and outer

ORIGINAL PAGE IS
OF POOR QUALITY

charge fins are equal, ϕ_m is interpreted as the mean cross sectional temperature of the charge; ϕ_Δ is a measure of the radial temperature difference within the charge. Within the hot and cold zones, the furnace temperature, ϕ_f, is the temperature of the hot and cold heat pipes, respectively, and eq. [3.2d] for the gradient zone annulus in not needed. Within the gradient zone, ϕ_f is identified with $\phi_a(\zeta)$ and eq. [3.2d] has no Peclet term since the gradient zone annulus is stationary.

Solution Of The Concentric Fin Equations

The set of eqs. [3.2] has constant coefficients if a separate set of equations is employed for each axial region of uniform thermal properties and furnace boundary conditions. As in the moving fin model, four such axial regions are present in the concentric fin model: the hot and cold zones and the liquid and solid portions of the gradient zone. (It is assumed that the growth interface is in the gradient zone.) The hot and cold zones are therefore described by eqs. [3.2a], [3.2b] and [3.2c]; the two regions within the gradient zone include, in addition, eq. [3.2d], representing the gradient zone annulus.

The solution of eqs. [3.2] within a particular axial region is described in many texts (e.g., [2,3]). A system of p second order differential equations can be changed to an equivalent system of 2p first order differential equations by the definition:

$$\Phi' \equiv d\Phi/d\zeta \qquad [3.4]$$

Performing this transformation and putting the result in matrix notation, eqs. [3.2] become:

$$\frac{dX}{d\zeta} = PX + F \qquad [3.5]$$

ORIGINAL PAGE IS
OF POOR QUALITY

where:

$$\mathbf{X} = \begin{bmatrix} \phi_m \\ \phi_\Delta \\ \phi_{cr} \\ \phi'_m \\ \phi'_\Delta \\ \phi'_{cr} \end{bmatrix}$$

hot and cold zone

$$\mathbf{X} = \begin{bmatrix} \phi_m \\ \phi_\Delta \\ \phi_{cr} \\ \phi_G \\ \phi'_m \\ \phi'_\Delta \\ \phi'_{cr} \\ \phi'_G \end{bmatrix}$$

gradient zone

(Variables in boldface denote matrices.) The elements of **P** and **F** are found by direct substitution. In the gradient zone, **F** is an empty matrix.

The solution of eq. [3.5] is of the form:

$$\mathbf{X} = c_1\mathbf{E}_1 e^{w_1\zeta} + c_2\mathbf{E}_2 e^{w_2\zeta} + \cdots + c_{2p}\mathbf{E}_{2p} e^{w_{2p}\zeta} \qquad [3.6]$$

The values of w are commonly called the eigenvalues of the matrix **P** and the values of **E** are commonly called the eigenvectors of **P**. The eigenvalues and eigenvectors are easily found by standard computer subroutines. The coefficients denoted by c in eq. [3.6] are the unknown constants of integration. $\mathbf{x}_p$ denotes the particular solution of eq. [3.5].

Equation [3.6] is written for each axial region. The hot and cold zones each contribute six unknown constants of integration; the liquid and solid parts of the gradient zone each contribute eight unknown constants of integration. There are, therefore, 28 unknown constants of integration which must be determined by using boundary conditions of (a) equality of temperature and (b) continuity of flux between corresponding fins of adjacent axial regions as well as (c) heat transfer coefficients at the ends of charges of finite length and (d) imposed temperature boundary conditions at the ends of the gradient zone annulus. Application of the boundary conditions results in a set of 28 simultaneous linear algebraic equations whose unknowns are the required constants of

ORIGINAL PAGE IS
OF POOR QUALITY

integration. The solution of these simultaneous equations is easily accomplished by standard computer subroutines.

Approximation For The Growth Interface Boundary Condition

The solution of the fin equations requires a trial and error procedure when the extent of each axial region is not initially known. For example, the moving fin model shows that the interface location, ζ_i, and the non-dimensional interface temperature, $\theta_i = (T_i - T_{f,C})/(T_{f,H} - T_{f,C})$, are functionally related. When θ_i is chosen as the independent variable, ζ_i must be found by iteration. When ζ_i is taken as the independent variable, the location of the interface boundary conditions is known a priori resulting in a direct solution for θ_i as well as the entire axial temperature distribution.

Figure 3.3 shows that the axial position of the growth interface in the inner and outer charge fins is, in general, not the same; they are the same only when the interface is flat. The correct application of the concentric fin model requires that a separate set of eqs. [3.2] be written for the short region between the axial locations of the interface. In this case, the interface temperature, θ_i, is coupled with the interface locations within both the inner and outer charge fins, $\zeta_{i,in}$ and $\zeta_{i,out}$ respectively:

$$f(\theta_i, \zeta_{i,in}, \zeta_{i,out}) = 0 \qquad [3.7]$$

Since this functional relationship is not known a priori, it is not possible to choose initial values of $\zeta_{i,in}$ and $\zeta_{i,out}$ which satisfy eq. [3.7]; i.e., fin boundaries at the interface are not initially known and therefore the solution requires an iterative procedure in order to locate these boundaries. The remainder of this section describes an approximate model of the interface which precludes the use of a trial and error solution for the concentric fin model.

The length of the region separating the interface in the inner and outer charge fins is normally small since it is desired to have an

ORIGINAL PAGE IS
OF POOR QUALITY

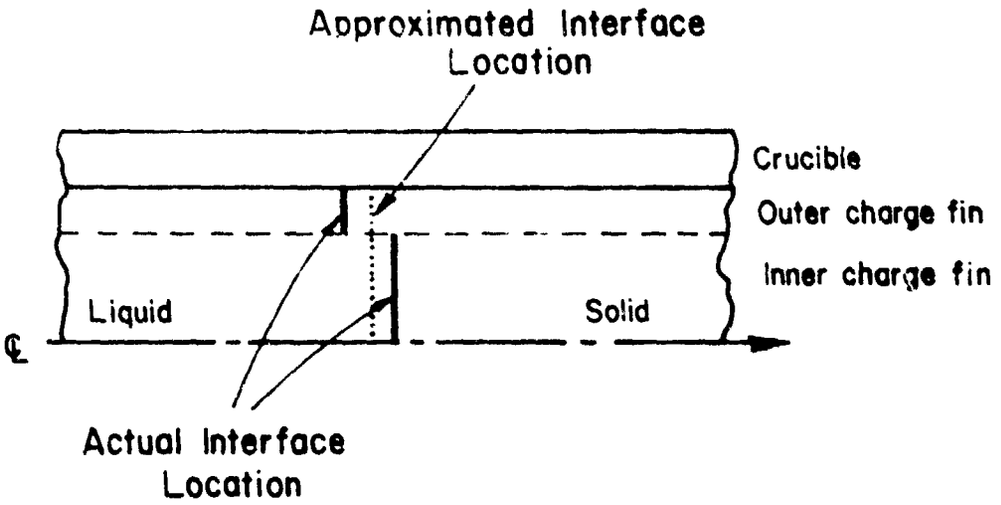

Fig. 3.3. Approximation for the interface boundary conditions used in the concentric fin model.

ORIGINAL PAGE IS
OF POOR QUALITY

interface of small curvature. The present model neglects this axial region and applies the boundary conditions of the interface at the same axial location for each of the inner and outer charge fins. The axial location of the interface is taken to be the location where the mean charge temperature, ϕ_m, is equal to the interface temperature, θ_i (see Fig. 3.3). In this sense, the axial location where $\phi_m = \theta_i$ denotes an "average" interface position (i.e., between the actual interface positions of the inner and outer charge fins). The value of ϕ_Δ at this location, $\phi_\Delta(\zeta_i)$, is indicative of the curvature of the interface.

The use of the above approximation for the interface boundary condition permits the a priori choice of the "average" interface location and, therefore, the solution for the temperature field in the charge is not a trial and error procedure. The approximation introduces no error if the thermal conductivities of the melt and crystal are equal and in the absence of the generation of latent heat, or if the interface is flat. Otherwise, when the interface curvature is small, the error should likewise be small and the predictions of the present model concerning the radial temperature variations in the charge are expected to be correct to a first-order approximation.

The interface flux boundary conditions, assuming that the melt/crystal conductivity change and the generation of latent heat occur at the same axial location in each of the charge fins, are:

$$R_K \left(\frac{d\phi_m}{d\zeta}\right)_L = Pe_S R_H + \left(\frac{d\phi_m}{d\zeta}\right)_S \qquad [3.8a]$$

$$R_K \left(\frac{d\phi_\Delta}{d\zeta}\right)_L = \left(\frac{d\phi_\Delta}{d\zeta}\right)_S \qquad [3.8b]$$

$$\left(\frac{d\phi_{cr}}{d\zeta}\right)_L = \left(\frac{d\phi_{cr}}{d\zeta}\right)_S \qquad [3.8c]$$

ORIGINAL PAGE IS
OF POOR QUALITY

$$\left(\frac{d\phi_a}{d\zeta}\right)_L = \left(\frac{d\phi_a}{d\zeta}\right)_S \qquad [3.8d]$$

where: $R_K = k_L/k_S$

$R_H = \Delta H_{s\ell}/c_p(T_{f,H} - T_{f,c})$

$\Delta H_{s\ell}$ = latent heat of solidification

(The subscripts "L" and "S" refer to the melt and crystal side of the interface, respectively.) Equation [3.8a] assumes that the solidification rate is equal to the lowering rate, V.

RADIAL TEMPERATURE VARIATIONS WITHIN THE CHARGE

Radial temperature variations near the growth interface are shown in this section to result from several effects usually present in Bridgman crystal growth. Systems with an adiabatic gradient zone, first studied by Chang and Wilcox [5], addresses only one of these factors. The other factors have not been adequatley considered in the literature: non-perfectly insulating gradient zone ($h_G \neq 0$), and thermal conductivity charge and/or generation of latent heat at the growth interface in the presence of a crucible. Computer solutions of the concentric fin model are utilized to graphically illustrate the parametric behavior of the radial temperature variations. Special attention is given, however, to the development of approximate analytical expressions which serve to emphasize the relative importance of the various growth parameters on radial temperature variations.

The variable ϕ_Δ defined by the concentric fin model of section 3 is used to indicate the radial temperature variations within the charge. The results for ϕ_Δ to be shown in this section are conveniently approximated to the interface shape by the following relation developed in Appendix B:

$$N \simeq -\frac{1}{16}\,\frac{(d\phi_m/d\zeta)}{\phi_\Delta} \qquad [4.1]$$

ORIGINAL PAGE IS
OF POOR QUALITY

where N is the radius of curvature of an isotherm at a particular axial location in number of charge radii. (N is negative for an interface which is concave toward the melt as shown in Fig. 1.1.) Accordingly, the degree of flatness of isotherms is enhanced by large axial temperature gradients ($d\phi_m/d\zeta$) and small radial temperature gradients (ϕ_a).

A system defined by the following parameter values is used as a reference system against which changes in individual parameters can be compared:

1. Equal heat transfer coefficients in the hot and cold zones.

2. Axial convection of heat due to charge motion is small; i.e., Pe is negligible. This condition is shown by the moving fin model to be satisfied if:

$$Pe/4(Bi^{**})^{1/2} \ll 1$$

where Bi^{**} is called the effective Biot number. Bi^{**} is related to the Biot number, Bi, additionally accounting for the presence of the crucible and radial thermal resistance within the charge on the axial temperature distribution of the charge.

3. No generation of latent heat; i.e., $Pe_S R_H = 0$.

4. Equal thermal conductivities in the melt and crystal; i.e., $R_K = 1$. With condition (1) above, $Bi_H = Bi_C$.

5. Equal charge lengths in the hot and cold zone; i.e., $\lambda_H = \lambda_C$ where λ is the dimensionless axial length of a furnace zone, L/D.

6. Temperature boundary conditions on the ends of the gradient zone annulus which satisfy $\phi_G(-\lambda_G/2) + \phi_G(\lambda_G/2) = 1$.

ORIGINAL PAGE IS
OF POOR QUALITY

A system which has the above parameter values is referred to as a symmetric system. The temperature distributions of a symmetric system are of the following form:

$$\phi_m(\zeta) + \phi_m(-\zeta) = 1$$
$$\phi_{cr}(\zeta) + \phi_{cr}(-\zeta) = 1$$
$$\phi_G(\zeta) + \phi_G(-\zeta) = 1$$
$$\phi_\Delta(\zeta) + \phi_\Delta(-\zeta) = 0$$

Accordingly, it is seen that it is only necessary to consider one-half of a symmetric system, either $\zeta < 0$ or $\zeta > 0$.

Causes Of Radial Temperature Variations Within The Gradient Zone

Subtracting eq. [3.2b] from eq. [3.2a], and assuming that the Peclet term is negligible (one-dimensional results indicate that the Peclet term is small for typical semiconductor crystal growth conditions), yields:

$$\frac{d^2\phi_\Delta}{d\zeta^2} - A_2\phi_\Delta = \frac{d^2\phi_m}{d\zeta^2} \qquad [4.2]$$

The particular solution of eq. [4.2], denoted by ϕ_Δ^P, may be solved by using the appropriate Green's function:

$$G(\zeta, x) = -\frac{1}{2A_2^{1/2}} \exp\left(-A_2^{1/2}|\zeta - x|\right) \qquad [4.3]$$

Using eq. [4.3], the particular solution of eq. [4.2] is:

$$\phi_\Delta^P(\zeta) = -\frac{1}{15.26}\int_{\zeta_H}^{\zeta_c}\left[\frac{d^2\phi_m}{dx^2}\right]\exp\left(-7.63|\zeta - x|\right)dx \qquad [4.4]$$

ORIGINAL PAGE IS
OF POOR QUALITY

where the value of Λ_2 given by eq. [3.3b] has been used, x is a dummy variable of integration, and ζ_c and ζ_H are the axial locations of the cold and hot ends of the charge, respectively. (Note that eq. [4.4] is not the complete solution for ϕ_Δ^p since ϕ_m and ϕ_Δ are not independent by virtue of the coupled nature of the fin equations. Nevertheless, the actual distributions for ϕ_Δ^p and ϕ_m must satisfy eq. [4.4].)

$d^2\phi_m/d\zeta^2$ is non-zero when the combined axial heat conduction within the inner and outer charge fins is not constant with axial position; i.e., when there is heat addition to or removal from the charge. Equation [4.4], therefore, clearly demonstrates that radial temperature gradients within the charge are caused by heat exchange between the charge and its surroundings. Such heat exchange occurs:

(1) if, in the idealized case of no crucible, there is a difference between the temperatures of the outer charge fin and the furnace, and the heat transfer coefficient between them is not zero.

(2) if, when a crucible is present, there is a difference between the temperatures of the crucible and the outer charge fin.

Equation [4.4] expresses ϕ_Δ^p at a particular axial location as the superposed effects of heat transfer to the charge along its entire length. However, the effect of heat transfer to the charge at one location, x, on the radial temperature gradient at another location, ζ, attenuates rapidly with the distance between the two locations, being proportional to the factor $\exp(-7.63|\zeta - x|)$. For example, when $|\zeta - x| = 1$, the value of this exponential function is 0.00049. Therefore, the radial variation in temperature at the location ζ is primarily affected by heat exchange with the charge within the range $\zeta \pm 1$ (i.e., one charge diameter to either side of the given location).

ORIGINAL PAGE IS
OF POOR QUALITY

Analysis of Radial Temperature Variations in the Gradient Zone

The total solution for $\phi_\Delta(\zeta)$ includes, in addition to eq. [4.4], the homogenous part of the solution:

$$\phi_\Delta(\zeta) = C_1 e^{-7.635\zeta} + C_2 e^{7.635\zeta} + \phi_\Delta^P \qquad [4.5]$$

Equation [4.5] is applied separately to each region of the charge of uniform properties; given the assumptions of the concentric fin model, there are two such regions -- the liquid and the solid portions of the charge. The coefficients C_1 and C_2 in eq. [4.5] are found by applying boundary conditions at the ends of the charge and at the growth interface.

Radial temperature variations near the growth interface are of primary concern. Since the interface is assumed to be in the gradient zone, eq. [4.5] is applied, in the remainder of this section only to the gradient zone; i.e., $-\lambda_G/2 < \zeta < \lambda_G/2$. It is also assumed that there is at least one diameter of charge in both the hot and cold zones:

$$\zeta_H < -(\lambda_G/2 + 1) \qquad [4.6a]$$

$$\zeta_C > (\lambda_G/2 + 1) \qquad [4.6b]$$

As noted earlier, heat exchange with the charge at distances greater than about one diameter from the ends of the gradient zone contribute little to the radial temperature variations in the gradient zone. Equations [4.6] thus permit the limits of integration in eq. [4.5] to be contracted if desired, and further, the effects of the boundary conditions at the ends of the charge on ϕ_Δ can be neglected.

When the solid and liquid thermal properties of the charge are equal, i.e., $R_K = 1$, eq. [4.5] need be applied only once to the entire length of the charge. The homogenous part of the solution disappears

ORIGINAL PAGE
OF POOR QUALITY

under the restrictions of eq. [4.6] and the total solution for $\phi_\Delta(\zeta)$ within the gradient zone becomes:

$$\phi_\Delta(\zeta) = -\frac{1}{15.26}\int_{\zeta_N}^{\zeta_c}\left[\frac{d^2\phi_m}{dx^2}\right]\exp\left(-7.63|\zeta - x|\right)dx \qquad [4.7]$$

where: $-\lambda_G/2 \le \zeta \le \lambda_G/2$
$R_K = 1$

When $R_K \neq 1$, eq. [4.5] must be applied separately to the liquid and solid portions of the charge using the following boundary conditions at the growth interface:

$$\left[\phi_\Delta(\zeta_i)\right]_L = \left[\phi_\Delta(\zeta_i)\right]_S \qquad [4.8a]$$

$$R_K\left[\frac{d\phi_\Delta(\zeta_i)}{d\zeta}\right]_L = \left[\frac{d\phi_\Delta(\zeta_i)}{d\zeta}\right]_S \qquad [4.8b]$$
(also eq. [3.8b])

Applying these boundary conditions yields:

$$\left[\phi_\Delta(\zeta)\right]_L = \frac{2I_S(\zeta_i) + (R_K-1)I_L(\zeta_i)}{R_K+1}e^{-7.63(\zeta_i-\zeta)} + I_L(\zeta) \qquad [4.9]$$

where: $-\lambda_G/2 < \zeta \le \zeta_i$

$$\left[\phi_\Delta(\zeta)\right]_S = \frac{-(R_K-1)I_S(\zeta_i) + 2R_K I_L(\zeta_i)}{R_K+1}e^{-7.63(\zeta-\zeta_i)} + I_S(\zeta) \qquad [4.10]$$

ORIGINAL PAGE IS
OF POOR QUALITY

where: $\zeta_i \leq \zeta \leq \lambda_6/2$

The variables $I_L(\zeta)$ and $I_S(\zeta)$ represent the respective contributions of radial heat exchange with the liquid and solid portions of the charge to the value of ϕ_Δ at any axial location ζ within the gradient zone. They are defined as follows:

$$I_L(\zeta) = -\frac{1}{15.26}\int_{\zeta_H}^{\zeta_i}\left[\frac{d^2\phi_m}{dx^2}\right]\exp\left(-7.63|\zeta - x|\right)dx \qquad [4.11a]$$

$$I_S(\zeta) = -\frac{1}{15.26}\int_{\zeta_i}^{\zeta_c}\left[\frac{d^2\phi_m}{dx^2}\right]\exp\left(-7.63|\zeta - x|\right)dx \qquad [4.11b]$$

The first term in each of eqs. [4.9] and [4.10] represents a contribution to $\phi_\Delta(\zeta)$ which is produced at the growth interface and which attenuates with distance from the interface. This contribution is absent when $R_K = 1$.

The value of ϕ_Δ at the interface, $\phi_\Delta(\zeta_i)$, is determined from either eq. [4.9] or eq. [4.10]:

$$\phi_\Delta(\zeta_i) = \frac{2}{R_K+1}\left[I_S(\zeta_i) + R_K I_L(\zeta_i)\right] \qquad [4.12]$$

An attractive possibility for the quantitave utilization of eqs. [4.9] and [4.10] is to provide $d^2\phi_m/d\zeta^2$ from the results of one-dimensional modeling. In this way, a two-dimensional temperature distribution is obtained only through these equations and a one-dimensional model. The error in ϕ_Δ calculated in this manner would be due to approximations in (1) the one-dimensional model which estimates $d^2\phi_m/d\zeta^2$ and (2) the concentric fin model which provides eq. [4.2].

ORIGINAL PAGE IS
OF POOR QUALITY

One-dimensional models do provide good approximations for the charge mean temperature distribution. Taking two derivatives of such a distribution in order to obtain a good approximation for $d^2\phi_m/d\zeta^2$ is more likely to be unreliable. Results presented later in this section, in fact, demonstrate that the presence of a crucible produces a distribution of radial heat exchange with the charge which is not predicted by a one-dimensional model; therefore, the use of $d^2\phi_m/d\zeta^2$ calculated from one-dimensional models is not appropriate for use in eqs. [4.11]. Nevertheless, even in these cases, the Green's function approach developed in this section may be used to obtain a qualitative understanding of the behavior of radial temperature variations within the charge.

Penetration Of Radial Temperature Variations Into The Gradient Zone From The Hot And Cold Zones

Heat transfer to the charge in the hot zone and from the charge in the cold zone must occur so that the required axial temperature gradient at the growth interface is obtained. Such heat exchange, according to the results of section 4.1, produces radial temperature variations within the charge which, even within an adiabatic gradient zone, influence the shape of the growth interface.

Fu and Wilcox [6] studied the penetration of radial temperature variations into an adiabatic gradient zone for systems without a crucible through the use of a two-dimensional finite difference model. Isotherm shape indicate, for various Bi and Pe, that radial temperature variations within the charge in the hot and cold zones attenuate rapidly from the ends of the gradient zone. If the gradient zone is sufficiently long, there exists a region within which the shape of isotherms are quite flat.

Systems Without a Crucible

Figure 4.1 shows the variation of ϕ_Δ in an adiabatic gradient zone, obtained by the concentric fin model of section 3 for systems without a crucible. (Note that the vertical scale of Fig. 4.1 changes from

ORIGINAL PAGE IS
OF POOR QUALITY

logarithmic to linear at $\pm 10^{-4}$ so that both negative and positive values of ϕ_Δ may be plotted in the same figure.) Accordingly, it is seen that ϕ_Δ attenuates at a rate approximately proportional to $\exp(-7.6\,\zeta^*)$ where ζ^* is measured from the ends of the gradient zone. It is also seen that ϕ_Δ in the gradient zone increases with the Biot number of the hot and cold zones reflecting greater amounts of radial heat transfer to the charge in these zones.

The variation of the radius of curvature of isotherms for the same cases considered in Fig. 4.1 is shown in Fig. 4.2. These curves were calculated using eq. [4.1] along with values of ϕ_Δ and $d\phi_\Delta/d\zeta$ determined from the concentric fin model. Accordingly, there is a central region of the gradient zone where the isotherm shapes are quite flat. To obtain an interface which is slightly concave toward the crystal, i.e., small but positive N^{-1}, requires that the interface be located slightly to the hot side of the center of the gradient zone. Also seen in Fig. 4.2 is that isotherms are more curved as Bi increases. Therefore, for the parameter values considered, increasing the Biot number of the hot and cold zones has a greater effect on increasing ϕ_Δ than upon increasing the axial temperature gradient of the charge in the gradient zone (c.f., eq. [4.1]).

The effect of unequal hot and cold zone Biot numbers in an otherwise symmetric system is shown in Fig. 4.3. As the hot zone Biot number increases relative to the constant cold zone Biot number, ϕ_Δ becomes more positive in the hot portion of the gradient zone. In this region, therefore, isotherm shapes become more concave toward the crystal and the location of the flat isotherm shifts slightly toward the cold zone. The effect of changing thermal conditions in the hot zone attenuates rapidly from the end of the hot zone and effects only slightly the radial temperature variations near the cold end of the gradient zone.

Figure 4.4 shows the variation of ϕ_Δ in systems which are symmetric except $R_K \neq 1$. In the systems considered, the cold zone Biot number remains constant; the hot zone Biot number therefore changes with R_K ($Bi_H = Bi_C/R_K$). As R_K increases, it is seen that ϕ_Δ in the hot part of

ORIGINAL PAGE IS
OF POOR QUALITY

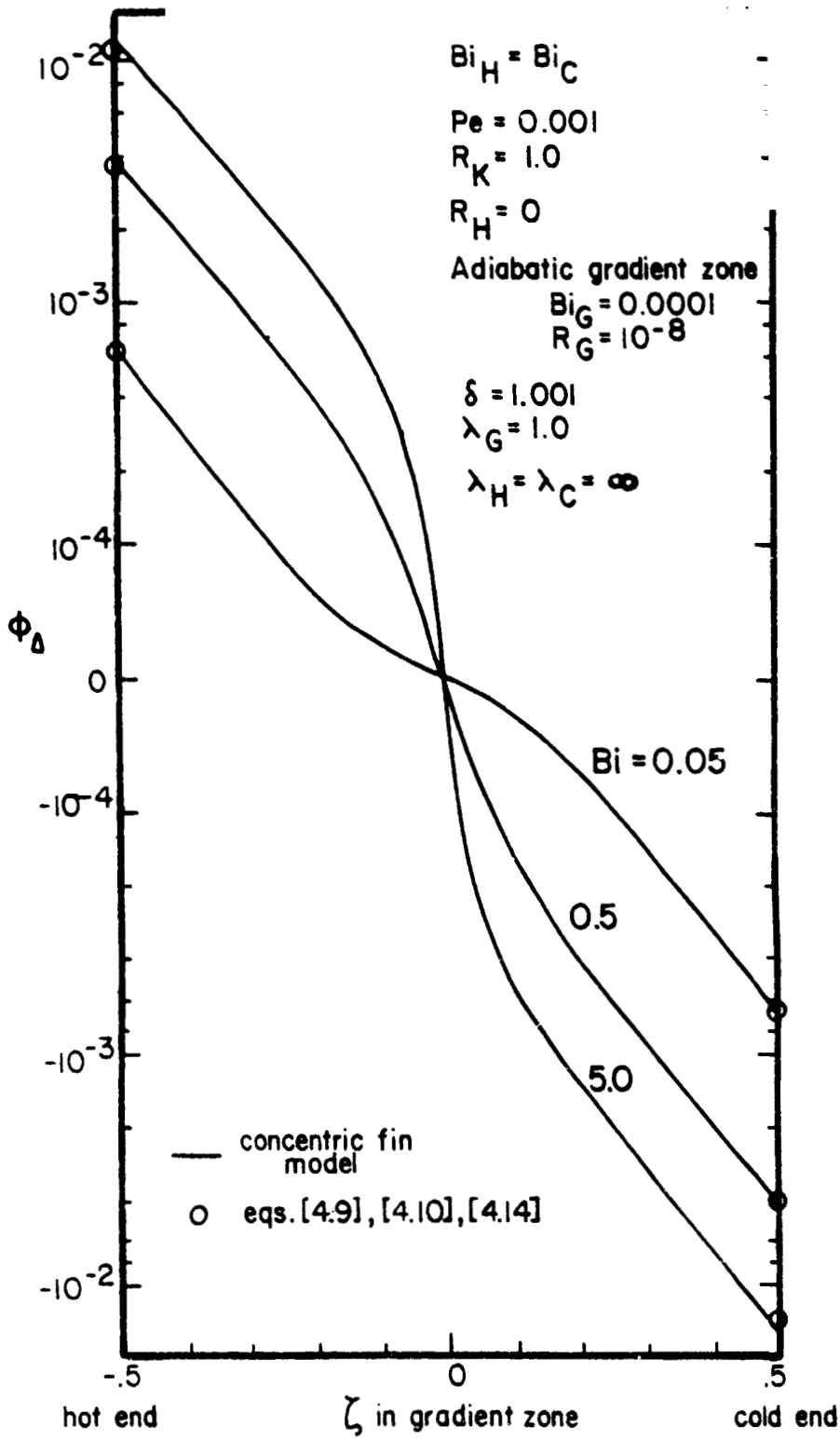

Fig. 4.1. Variation of ϕ_Δ in an adiabatic gradient zone without a crucible. The system is symmetric.

ORIGINAL PAGE IS
OF POOR QUALITY

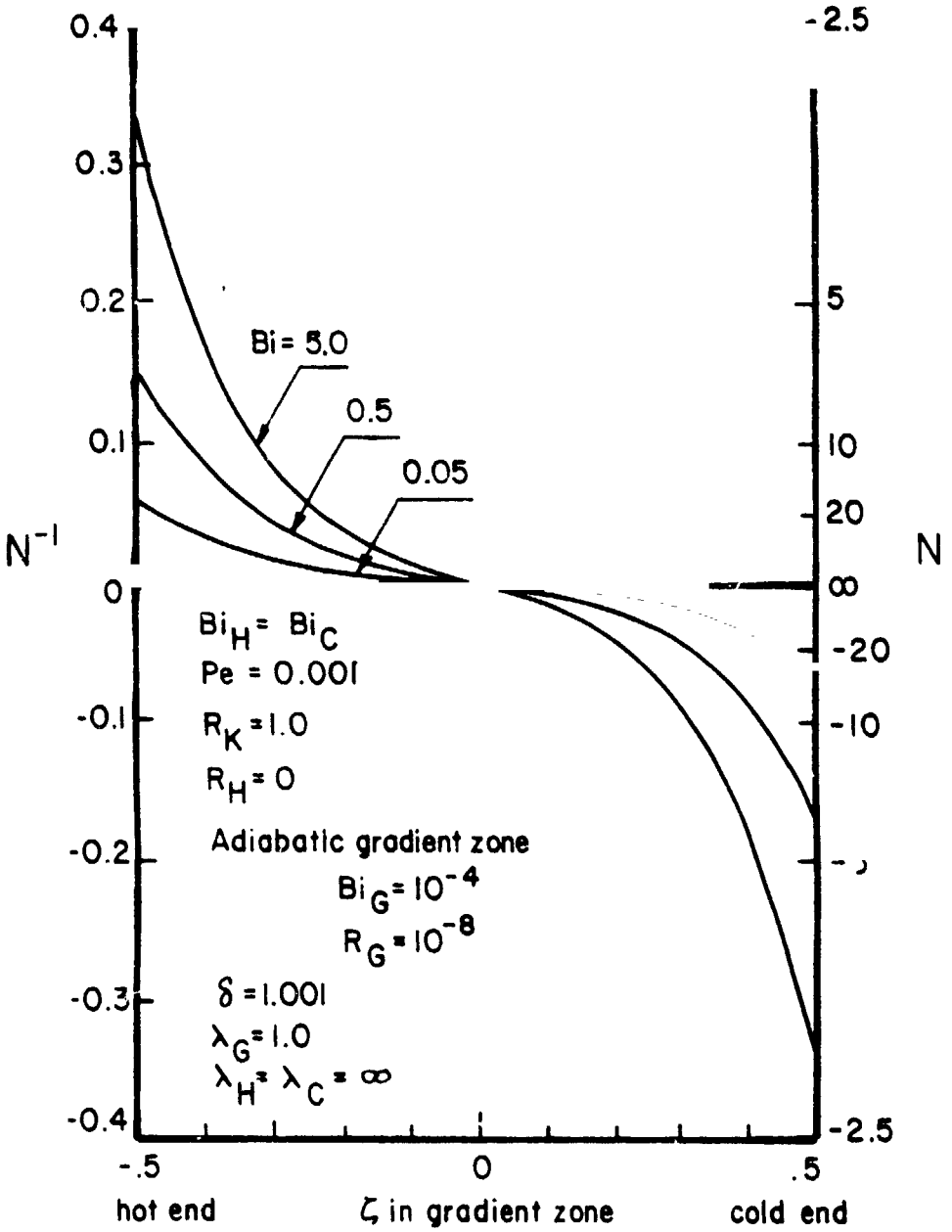

Fig. 4.2. Variation of isotherm shapes for the same cases considered in Fig. 4.1.

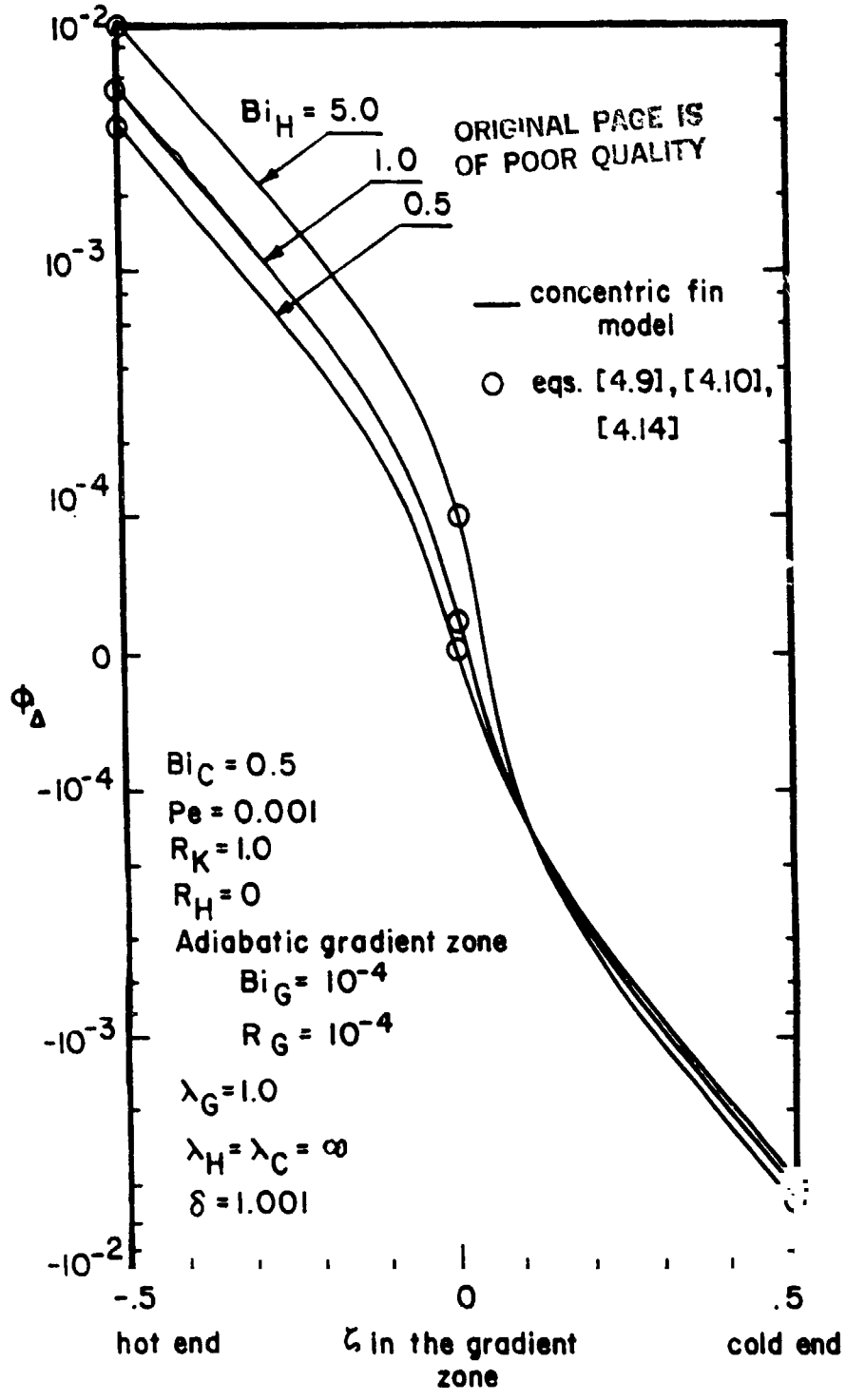

Fig. 4.3. The effect of unequal hot and cold zone Biot numbers on ϕ_Δ in an adiabatic gradient zone. The system is otherwise symmetric.

ORIGINAL PAGE IS
OF POOR QUALITY

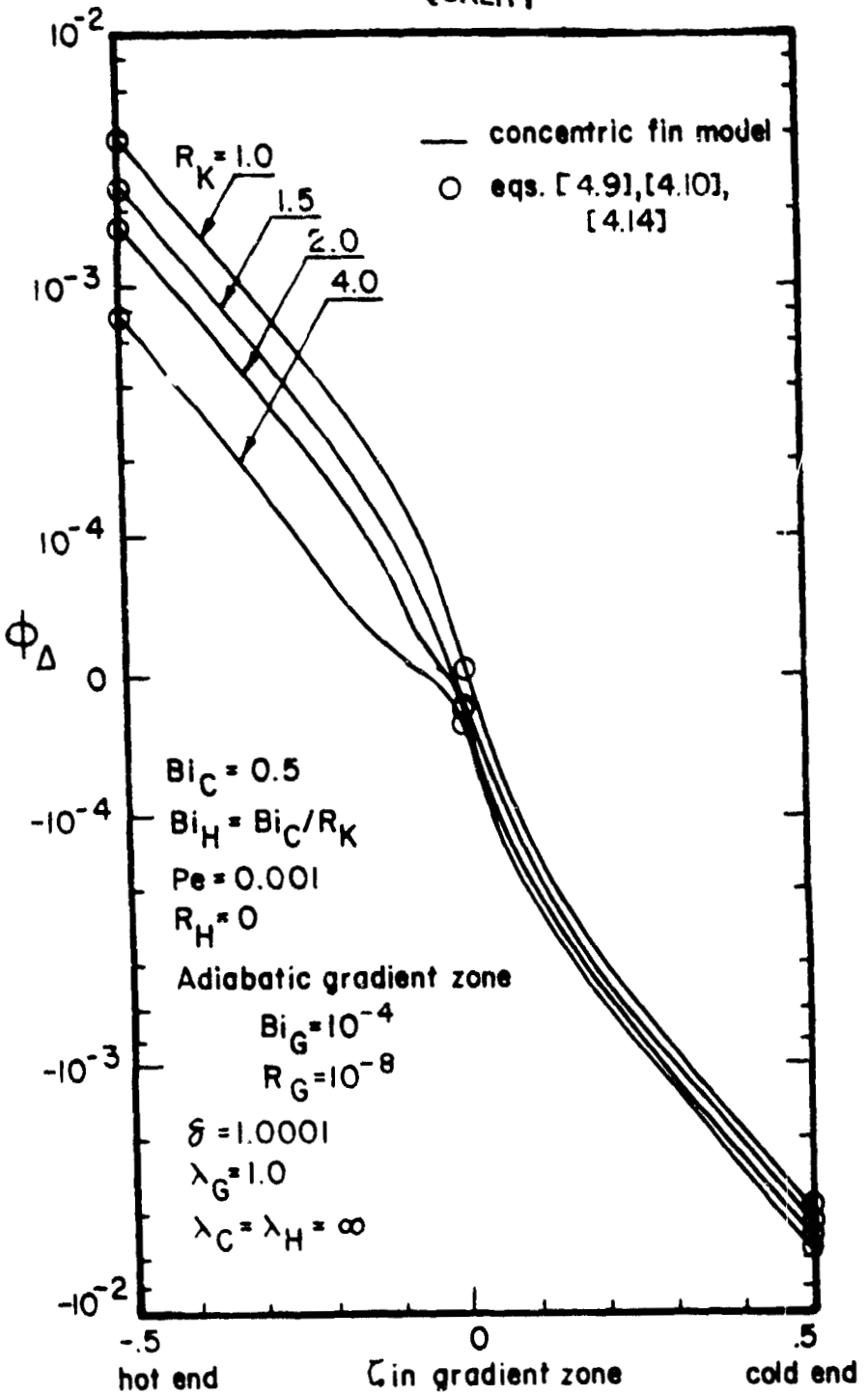

Fig. 4.4. Variation of Φ_Δ in an adiabatic gradient zone without a crucible. The system is symmetric except $R_K \neq 1$.

ORIGINAL PAGE IS
OF POOR QUALITY

the gradient zone decreases whereas ϕ_Δ in the cold part of the gradient zone is little affected. This behavior is similar to that of a changing value of Bi_H exhibited in Fig. 4.3. Further, a disturbance appears at the interface which increases as R_K increases and which dies out with distance from the interface. This disturbance represents the first term in eqs. [4.9] and [4.10] where it is shown that it appears only when $R_K \neq 1$.

An analytical expression for the variation of ϕ_Δ in an adiabatic gradient zone may be obtained by using the mean temperature distribution determined by the moving fin model in order to describe $d^2\phi_m/d\zeta^2$ in eqs. [4.11]. In order to distinguish between the mean temperatures predicted by the moving fin and concentric fin models, θ_m is used to denote the former while ϕ_m continues to denote the latter. The charge is assumed infinite in length; in this case, θ_m is described by a simple exponential function in both the hot and cold zones. Further, the Peclet number is assumed small enough to be negligible; in this case the argument for the exponential function is given by $2(Bi^{**})^{1/2}$.

hot zone: $\zeta \leq -\lambda_G/2$

$$\theta_m(\zeta) = \left[1 - \theta_m(-\lambda_G/2)\right] \exp\left[2(Bi_H^{**})^{1/2}(\zeta + \lambda_G/2)\right] \qquad [4.13a]$$

cold zone: $\zeta \geq \lambda_G/2$

$$\theta_m(\zeta) = \theta_m(\lambda_G/2) \exp\left[2(Bi_c^{**})^{1/2}(\lambda_G/2 - \zeta)\right] \qquad [4.13b]$$

Substituting the second derivatives of eqs. [4.13] into eqs. [4.11] and noting that $d^2\theta_m/d\zeta^2 = 0$ in the adiabatic gradient zone, yields:

$$I_L(\zeta) = \frac{Bi_H^{**}\left[1 - \theta_m(-\lambda_G/2)\right]}{3.82\left[7.63 + 2(Bi_H^{**})^{1/2}\right]} \exp\left[-7.63(\zeta + \lambda_G/2)\right] \qquad [4.14a]$$

ORIGINAL PAGE IS
OF POOR QUALITY

$$I_s(\zeta) = -\frac{Bi_c^* \theta_m(\lambda_G/2)}{3.82\left[7.63 + 2(Bi_c^*)^{1/2}\right]} \exp\left[-7.63(\lambda_G/2 - \zeta)\right] \qquad [4.14b]$$

where: $-\lambda_G/2 \leq \zeta \leq \lambda_G/2$

Equation [4.14a] represents the effect of radial heat transfer between the charge and the furnace in the hot zone on the radial temperature variations in the gradient zone. The effect of the hot zone dies out exponentially with distance from the hot end of the gradient zone at approximately the same rate observed in Fig. 4.1. Equation [4.14b] has an analagous interpretation with regard to heat transfer in the cold zone.

Substituting eqs. [4.14] into eqs. [4.9] and [4.10] produces the desired approximation for ϕ_Δ in the gradient zone due to the generation of radial gradients in the furnace zones. Evaluating eqs. [4.14] at $\zeta = \zeta_i$ and substituting the result into eq. [4.12] yields ϕ_Δ at the growth interface.

The one-dimensional results required by eqs. [4.14] are the effective Biot numbers and the mean charge temperatures at the hot and cold ends of the gradient zone. For a system with $Bi_G = 0$ and which has a negligible Peclet number, the axial temperature gradient in the gradient zone, G, is constant except for a step change at the growth interface. The temperatures at the ends of the gradient zone are therefore given by the following expressions:

$$\theta_m(-\lambda_G/2) = \theta_i - G_L \cdot (\lambda_G/2 + \zeta_i) \qquad [4.15a]$$

$$\theta_m(\lambda_G/2) = \theta_i + G_L (\lambda_G/2 - \zeta_i) \qquad [4.15b]$$

where: Pe is negligible

$Bi_G = 0$

$-\lambda_a/2 \leq \zeta_i \leq \lambda_a/2$

ORIGINAL PAGE IS
OF POOR QUALITY

The non-dimensional interface temperature, θ_i, G_L, and G_S are given by the moving fin model.

The circled points in Figs. 4.1, 4.3, and 4.4 indicate values of ϕ_Δ calculated through the use of eqs. [4.14]. It is seen that the values of ϕ_Δ obtained by the two methods agree very closely indicating that the moving fin model provides a good approximation for $d^4\phi_{...}$ for the systems considered. The largest difference occurs for the largest value of Bi reflecting a decrease in accuracy of the affective Biot number as Bi increases.

Systems With a Crucible

The effect of the presence of a crucible on radial temperature variations in an adiabatic gradient zone are shown in Figs. 4.5 and 4.6. The systems examined are symmetric and infinite in length; Fig. 4.5 considers variable δ (with $K_S = 1$) while Fig. 4.6 considers variable K_S (with $\delta = 1.5$). The primary effects of the crucible are seen to be a reduction in the value of ϕ_Δ at the ends of the gradient zone and a reduction in the rate at which ϕ_Δ attenuates toward the center of the gradient zone.

The reduction in the value of ϕ_Δ at the ends of the gradient zone when a crucible is present is attributable to the effect of the crucible on the effective Biot number, Bi^{**}. In most cases, the presence of a crucible decreases Bi^{**} compared to a charge without a crucible. A reduction in the heat exchange between the charge and furnace is therefore expected, resulting in decreased radial temperature variations within the charge. The individual curves of Figs. 4.5 and 4.6, labeled with their respective values of Bi^{**}, demonstrate the correlation between $\phi_\Delta(\pm\lambda_a/2)$ and Bi^{**}.

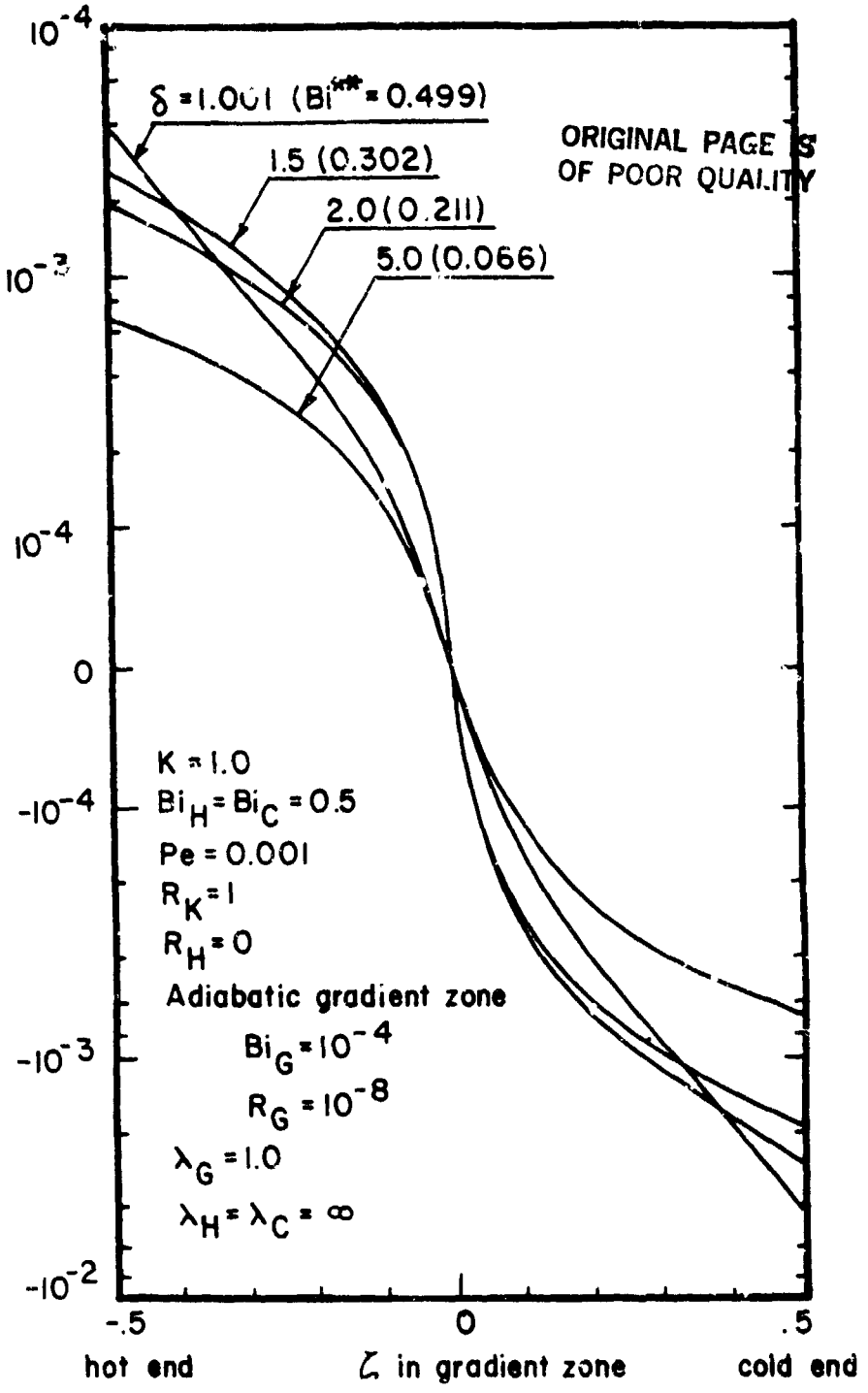

Fig. 4.5. Variation of ϕ_Δ in an adiabatic gradient zone with a crucible. The system is symmetric with variable diameter ratio δ (K = 1.0).

ORIGINAL PAGE IS
OF POOR QUALITY

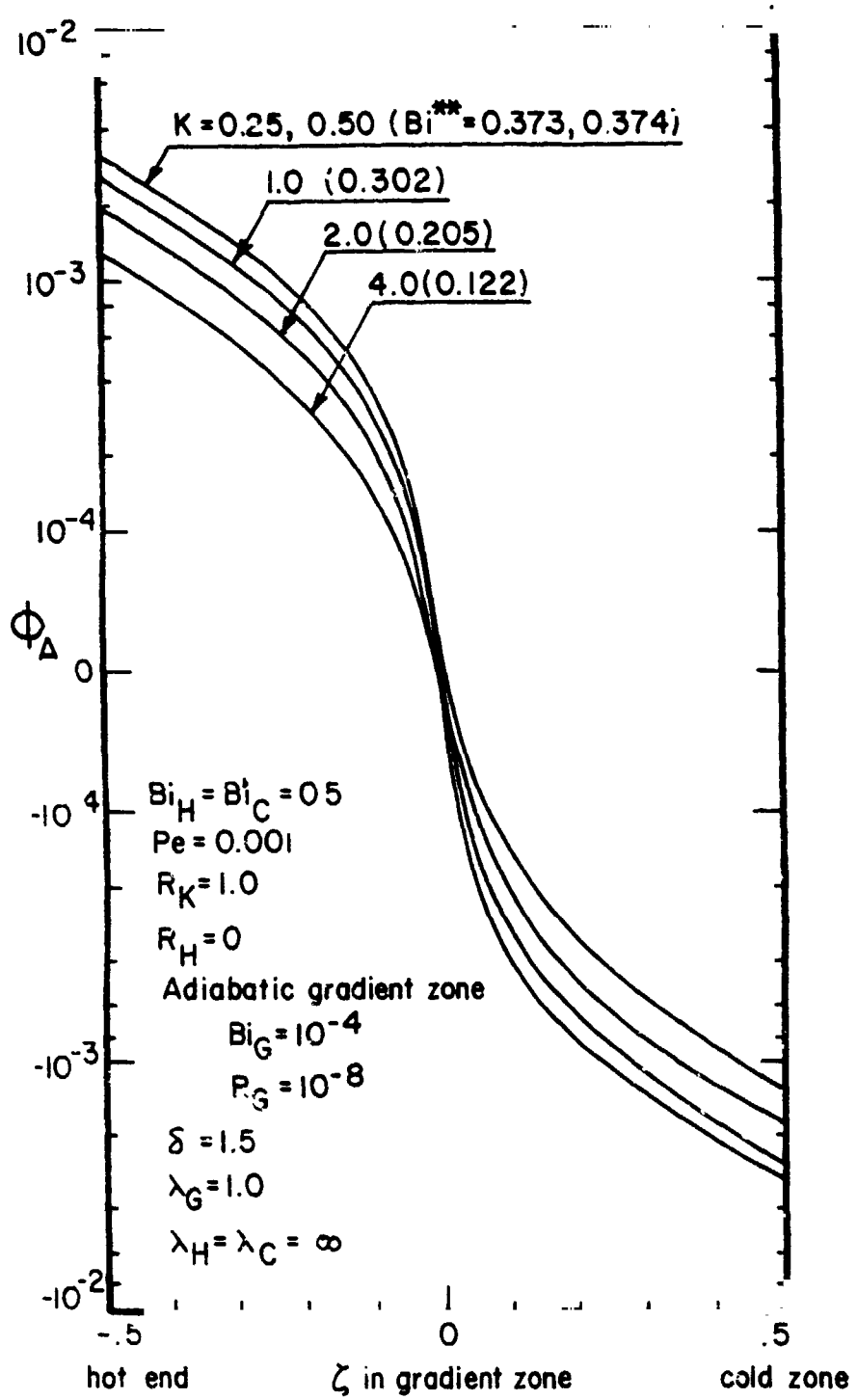

Fig. 4.6. Variation of ϕ_Δ in an adiabatic gradient zone with a crucible. The system is symmetric with variable thermal conductivity K (δ = 1.5).

ORIGINAL PAGE IS
OF POOR QUALITY

The reduction in the rate of attenuation of ϕ_Δ when a crucible is present results from radial heat exchange between the crucible and the charge near the ends of the gradient zone. Such heat transfer occurs when the crucible and the charge temperatures are not equal. A value of zero for the local Biot number is no longer sufficient to eliminate heat transfer to the charge in the gradient zone.

The variation of $\phi_{cr} - \phi_m$ near the hot end of the gradient zone, is shown in Fig. 4.7 for the case of $\delta = 2$ from Fig. 4.5. It is seen that the difference in the crucible and charge temperatures created by heat transfer in the hot zone furnace extends into the adiabatic gradient zone. The resultant effect on radial heat exchange with the charge is indicated by the distribution of $d^2\phi_m/d\zeta^2$ in Fig. 4.8 (lower solid curve). It is seen that $d^2\phi_m/d\zeta^2$ is not zero in the adiabatic gradient zone; the effect of the crucible is to extend radial heat transfer taking place in the hot zone into the gradient zone. Analysis of eqs. [4.11] verifies that this extension of radial heat exchange serves to decrease the apparent rate of attenuation of ϕ_Δ at the ends of the gradient zone.

Assuming that the Pe term is negligible, the one-dimensional moving fin model predicts:

$$\frac{d^2\theta_m}{d\zeta^2} = -4\,Bi^{**}_{lc}\,(\theta_{f,lc} - \theta_m) \qquad [4.16]$$

Since $Bi_G = 0$, the moving fin model therefore predicts that $d^2\theta_m/d\zeta^2 = 0$ in an adiabatic gradient zone, whether a crucible is present or not. The dashed curve of Fig. 4.8 is the distribution of $d^2\theta_m/d\zeta^2$ determined from the moving fin model. The moving fin model is unable to account for the particular nature of radial heat transfer between the charge and crucible caused by the abrupt change in furnace boundary conditions at the ends of the gradient zone. Although the error is of minor consequence in calculating the distribution of θ_m, results from the moving fin model, in particular $d^2\theta_m/d\zeta^2$, are inadaquate to describe the local variation of

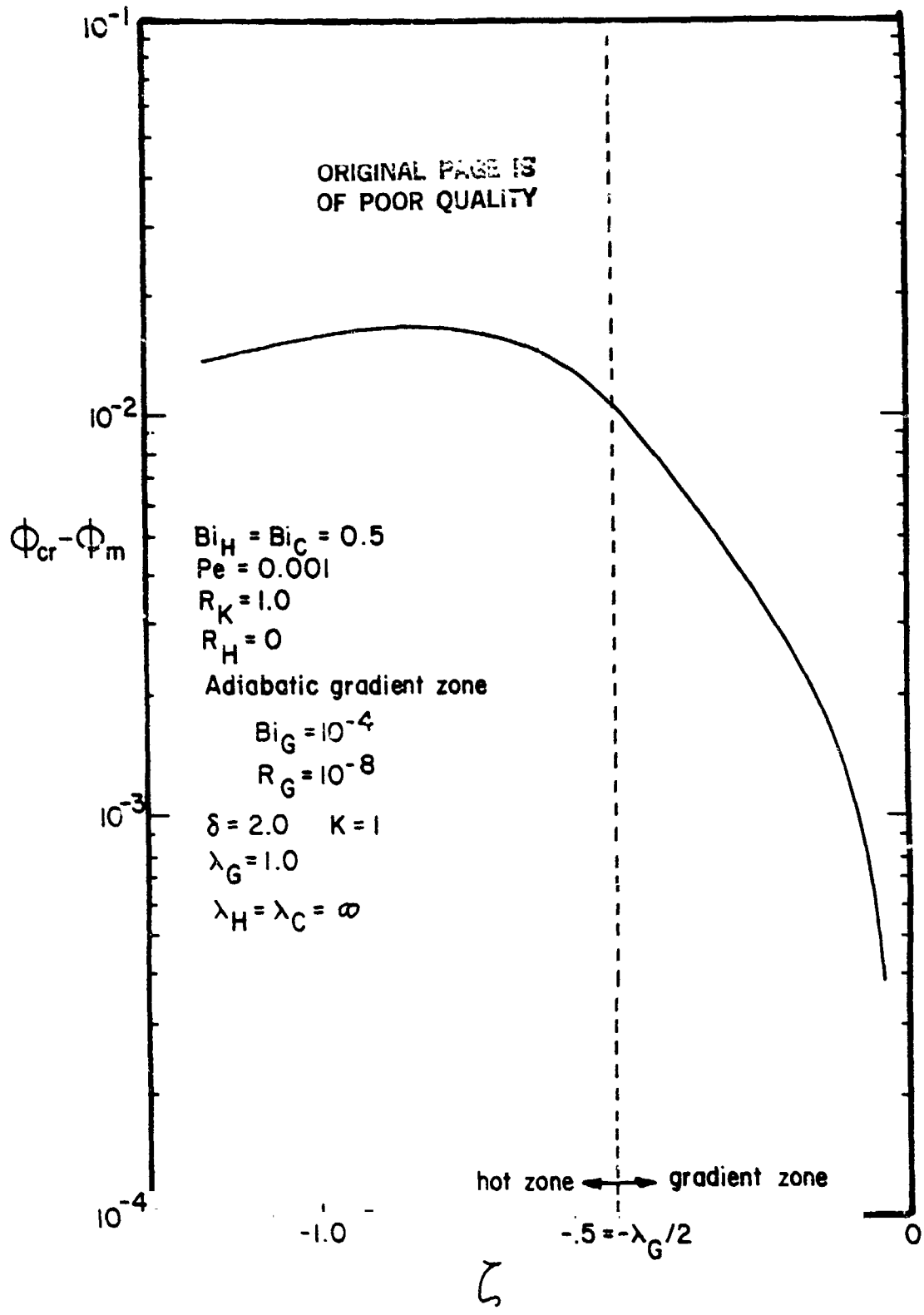

Fig. 4.7. The distribution of $\phi_{cr} - \phi_m$ near the hot and cold end of an adiabatic gradient zone, calculated by the concentric fin model.

ORIGINAL PAGE IS
OF POOR QUALITY

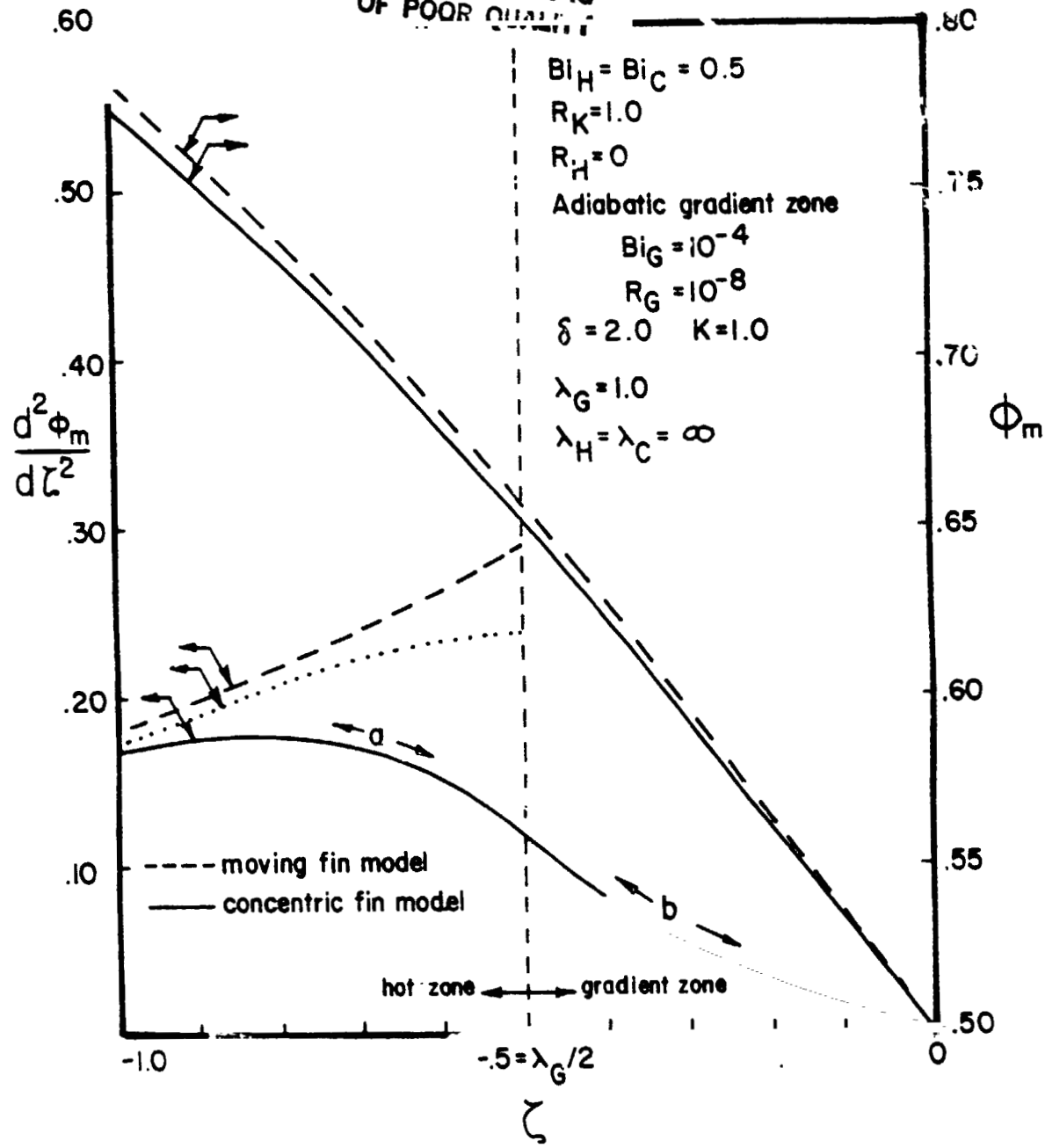

Fig. 4.8. Distributions of ϕ_m and $d^2\phi_m/d\zeta^2$ near the hot end of the gradient zone, calculated by the moving fin and concentric fin models.

ORIGINAL PAGE IS
OF POOR QUALITY

radial heat transfer near the ends of an adiabatic gradient zone when a crucible is present.

Table 4.1 compares values of ϕ_Δ at the end of the hot zone (i.e., $\zeta = -0.5$) calculated by eq [4.14a] (i.e., with the use of the moving fin model) and by the concentric fin model for the cases shown in Figs. 4.5 and 4.6. It appears that eq. [4.14a] predicts well the qualitative trends as K and change as well as being, to a certain degree, quantitatively accurate. This conclusion provides further evidence for the correlation between Bi^{**} and $\phi_\Delta(\pm\lambda_c/2)$ noticed in Figs. 4.5 and 4.6. Such a favorable comparison may seem, however, surprising in view of the limitations in the moving fin model discussed in the preceeding paragraph. This apparent anomoly is explained by a closer examination of the distributions of $d^2\phi_m/d\zeta^2$ and $d^2\theta_m/d\zeta^2$ shown in Fig. 4.8.

The abrupt change in $d^2\theta_m/d\zeta^2$ predicted by the moving fin model at the end of the gradient zone becomes smoothed out in the distribution of $d^2\phi_m/d\zeta^2$ given by the concentric fin model. The moving fin model overpredicts the heat transfer to the charge in the hot zone while underpredicting the heat transfer in the gradient zone. The overpredicted heat transfer in the hot zone contributes to ϕ_Δ while the lack of heat transfer in the gradient zone reduces ϕ_Δ; if the effects of the two errors in $d^2\theta_m/d\zeta^2$ approximately balance, the moving fin model provides a good estimation of $\phi_\Delta(\pm\lambda_c/2)$. The balance of the two errors is illustrated by the dotted curve in Fig. 4.8 which is plotted by reflecting the section of the curve for $d^2\phi_m/d\zeta^2$ labeled "a" about the axial location $\zeta = -0.5 = -\lambda_c/2$ and adding to the section of the same curve labeled "b". If the distribution of $d^2\theta_m/d\zeta^2$ calculated by the moving fin model were to exactly match the dotted curve, the value of $\phi_\Delta(-\lambda_c/2)$ from eq. [4.14a] would equal that given by the concentric fin model. Figure 4.8 shows that these curves, while not exactly coinciding, are nevertheless close. Therefore, the use of the moving fin model approximation for $d^2\phi_m/d\zeta^2$ can be expected to provide a reasonable estimate of ϕ_Δ at the end of an adiabatic gradient zone. Table 4.1 indicates that this conclusions is valid at least over the range of K_{loc} and δ examined.

ORIGINAL PAGE IS
OF POOR QUALITY

TABLE 4.1

Comparison of eq. [4.14a] with the concentric fin model in predicting ϕ_0 at the end of the gradient zone. The systems are symmetric with an adiabatic gradient zone.

		moving fin model			$\phi_0(-\lambda_G/2)$	
K_{loc}	δ	Bi^{**}	$d\theta_m/d\zeta$	$\theta_m(-\frac{\lambda_G}{2})$	eq. [4.14a]	concentric fin model
1.0	1.001	0.471	-0.407	0.703	0.00407	0.00407
1.0	1.5	0.291	-0.350	0.675	0.00284	0.00263
1.0	2.0	0.205	-0.312	0.656	0.00216	0.00193
1.0	5.0	0.0619	-0.199	0.600	0.000797	0.000683
0.25	1.5	0.357	-0.374	0.687	0.00331	0.00318
0.50	1.5	0.356	-0.374	0.687	0.00331	0.00310
2.0	1.5	0.200	-0.309	0.654	0.00212	0.00197
4.0	1.5	0.121	-0.258	0.629	0.00141	0.00132

$Bi = Bi_C = Bi_H = 0.5$

Symmetric system

$\lambda_G = 1.0$

$\lambda_H = \lambda_C = \infty$

ORIGINAL PAGE IS
OF POOR QUALITY

Radial Temperature Gradients Generated At The Growth Interface In The Presence Of A Crucible

The axial temperature gradient in the charge, $d\phi_m/d\zeta$, must undergo an abrupt change at the growth interface when $Pe_S R_H \neq 0$ or when $R_K \neq 1$. (c.f., eq [3.8a]). The axial gradient in the crucible, on the other hand, does not change at the growth interface. Figure 4.9 shows that such conditions produce a difference between the charge and crucible temperatures at the interface which diminishes with distance from the interface. The exchange of heat between the charge and the crucible which results from this temperature difference has a profound effect on the distribution of ϕ_Δ in the vicinity of the interface.

Figure 4.10 shows the variation of ϕ_Δ in an adiabatic gradient zone for systems which are symmetric except $R_K \neq 1$. The presence of a crucible is indicated by a value of 1.5 for the diameter ratio δ. As R_K increases, it is seen that the distribution of ϕ_Δ, and more importantly, the value of ϕ_Δ at the interface, becomes more negative, causing isotherm shapes to be curved in the adverse direction (concave toward the melt). Even a small difference in melt and crystal thermal conductivities (e.g., $R_K = 1.1$ in Fig. 4.10) has a pronounced effect on $\phi_\Delta(\zeta_i)$.

Values of R_K greater than unity, being typical of semiconductors, have been considered in Fig. 4.10. The variation of ϕ_Δ which occurs when R_K is less than unity is similar to that shown in Fig. 4.10 except that the curves would be displaced toward more positive values of ϕ_Δ compared to the symmetric case of $R_K = 1$.

The effect of the generation of latent heat at the growth interface on ϕ_Δ in the gradient zone is shown in Fig. 4.11. The systems considered are symmetric except that $Pe_S R_H \neq 0$. It is seen that as R_H increases, $\phi_\Delta(\zeta_i)$ becomes more negative, similar to the effect of $R_K > 1$ shown in Fig. 4.10.

Although the curves of Fig. 4.11 are plotted with R_H as a parameter, it must be noted that the effect of the generation of latent heat is

ORIGINAL PAGE IS
OF POOR QUALITY

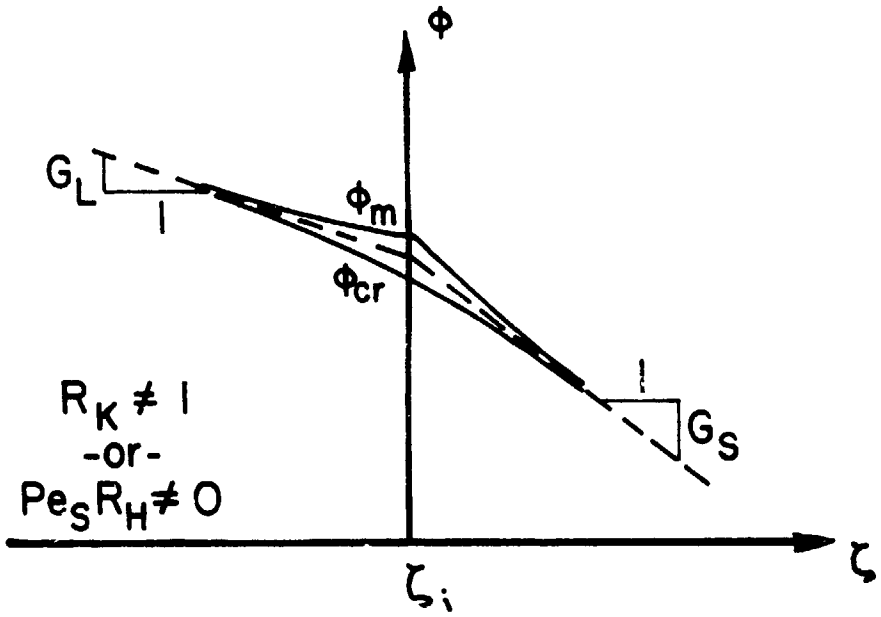

Fig. 4.9. Crucible and mean charge temperature distributions near the interface when $R_K \neq 1$ and/or $Pe_S R_H \neq 0$.

ORIGINAL PAGE IS
OF POOR QUALITY

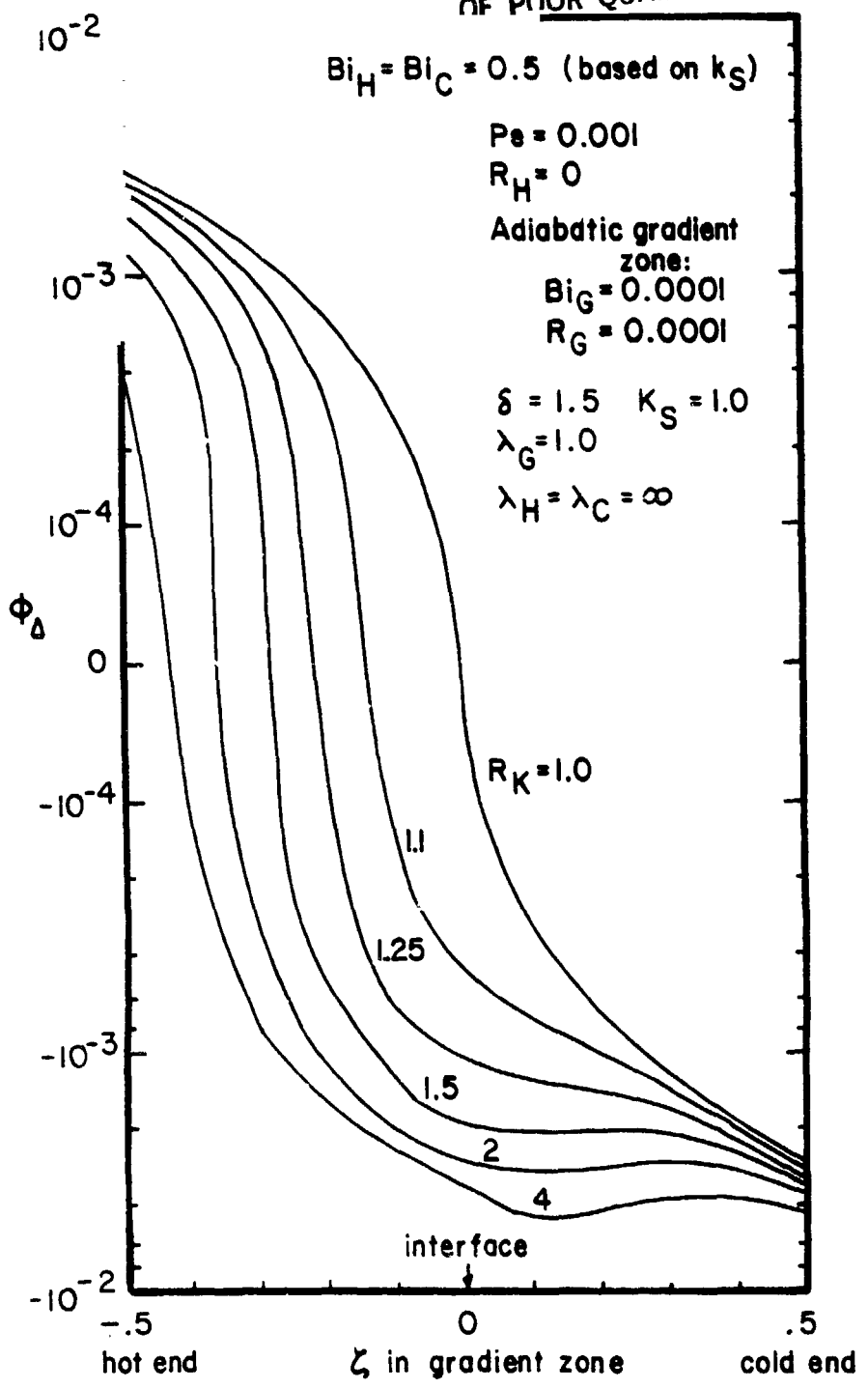

Fig. 4.10. Radial temperature variations generated at the interface when $R_K \neq 1$.

ORIGINAL PAGE IS
OF POOR QUALITY

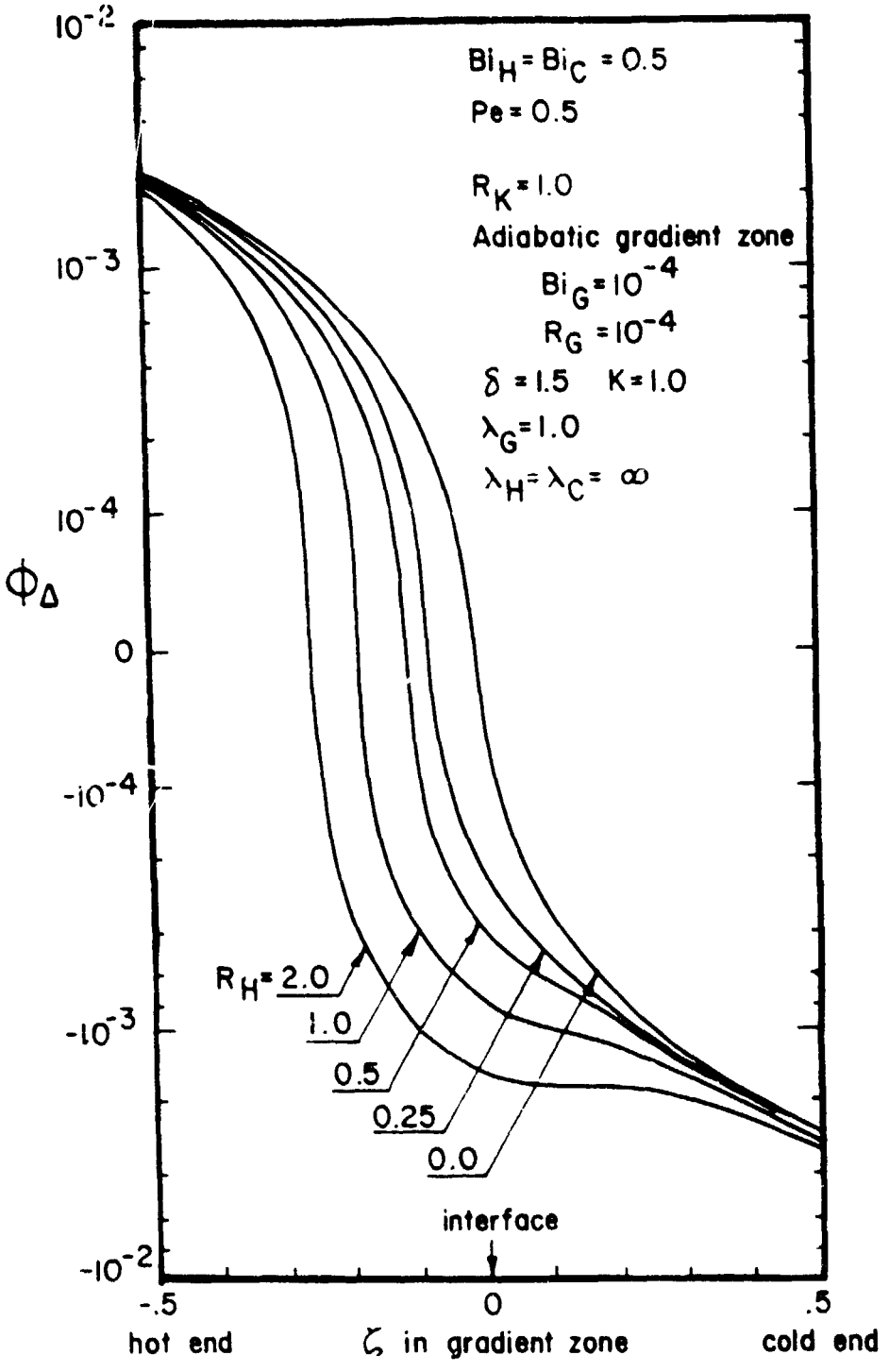

Fig. 4.11. The effect of the generation of latent heat on the radial temperature variations in the gradient zone.

ORIGINAL PAGE IS
OF POOR QUALITY

proportional to the product $Pe_S R_H$. The curves of Fig. 4.11 may also be interpreted as indicating the effects of changing Pe with a constant value of R_H. The value of $Pe_S = 0.05$ used in Fig. 4.11 has been chosen so that $Pe_S R_H$ would be sufficiently large to have an effect on for typical values of R_H.

The generation of radial gradients at the interface is due to the presence of a crucible. Figure 4.12 shows the effect of the crucible diameter ratio, δ, on $\phi_\Delta(\zeta)$ for systems which are symmetric except $R_K = 2$. Accordingly, very thin crucibles are required to eliminate the interface effect.

Figure 4.13 shows the effect of changing the location of the interface on the distribution of ϕ_Δ in the adiabatic gradient zone for systems which are symmetric except that $R_K = 2$. As the interface approaches the hot zone, the value of ϕ_Δ at the interface becomes more positive due to the influence of radial temperature variations created in the hot zone (c.f., section 4.2). For the systems considered in Fig. 4.13, however, the dominant factor is clearly the conductivity change at the interface. In general, the importance of radial temperature variations generated at the interface depends on their relative magnitude compared to radial temperature variations created by other effects.

The Two-Fin Thermal Model

In order to obtain from the results of section 4.1 a useful analytical relation which expresses the primary effects of the thermal parameters on the radial temperature variations near the growth interface, a simple and accurate analytical expression for $d^2\phi_m/d\zeta^2$ is necessary. Radial heat exchange between the charge and crucible in the vicinity of the interface is not accounted for in the one-dimensional moving fin model; approximating $d^2\phi_m/d\zeta^2$ by $d^2\theta_m/d\zeta^2$, therefore, is not accurate near the interface when a crucible is present. The concentric fin model is too complex to yield a simple analytical solution for $d^2\phi_m/d\zeta^2$. This section describes a thermal model of the heat transfer near the interface which provides a simple approximation for $d^2\phi_m/d\zeta^2$.

ORIGINAL PAGE IS
OF POOR QUALITY

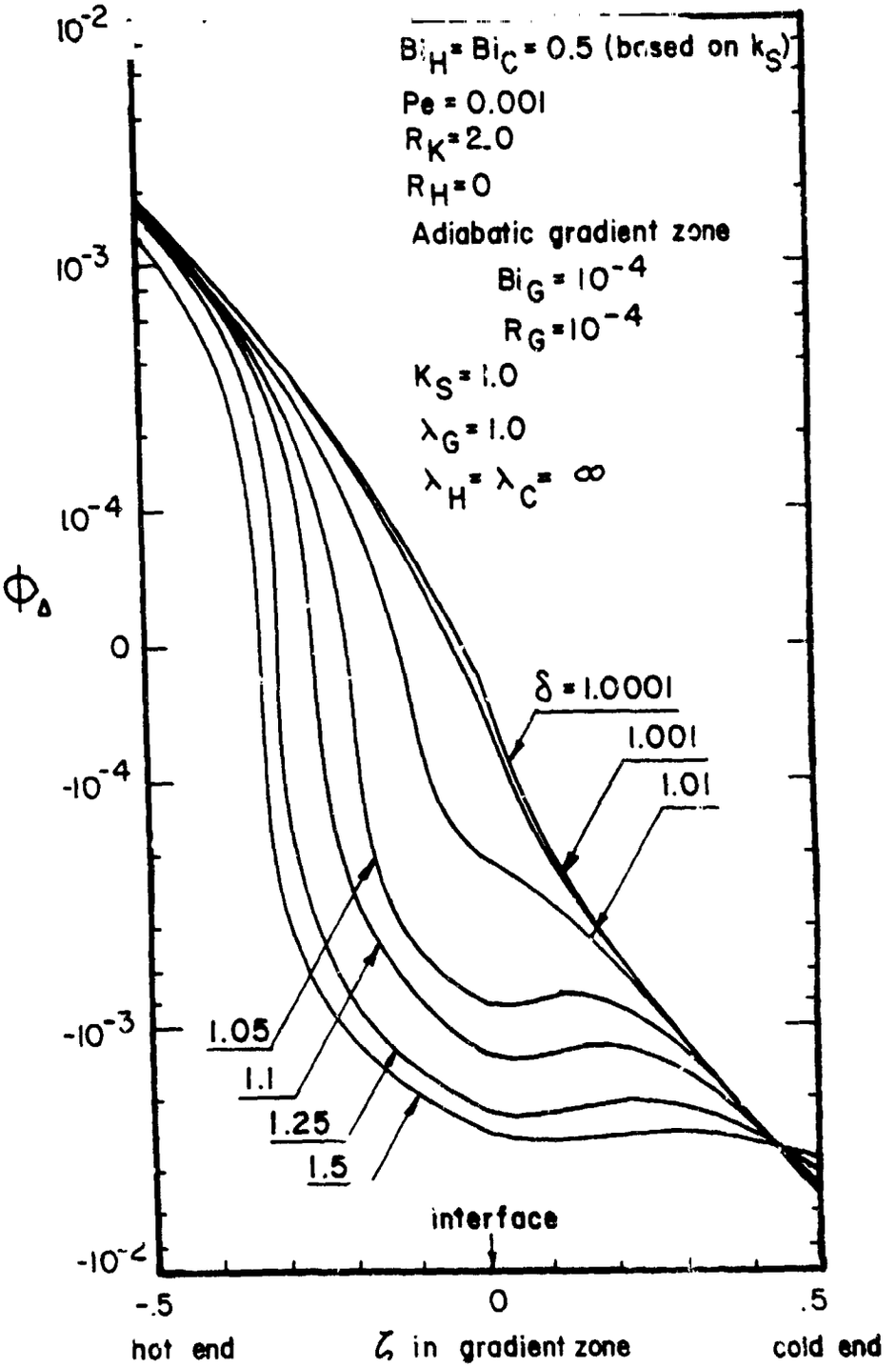

Fig. 4.12. The effect of the thickness of the crucible on the radial temperature variations generated at the interface.

ORIGINAL PAGE
OF POOR QUALITY

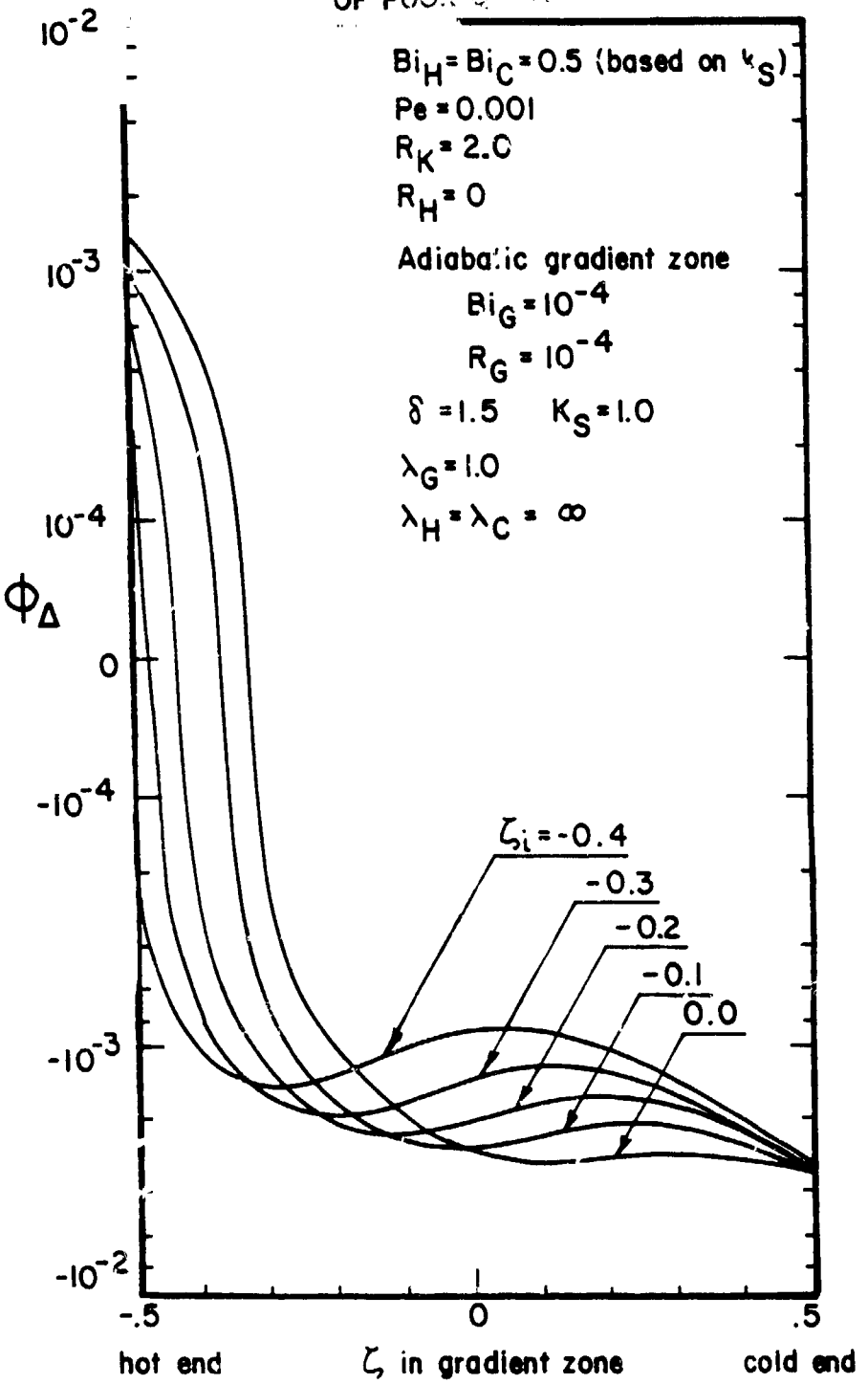

Fig. 4.13. The effect of interface position on radial temperature variations generated at the interface.

ORIGINAL PAGE IS
OF POOR QUALITY

The new thermal model is equivalent to the concentric fin model described in section 3 except for the following:

(1) The charge is modeled as a single fin as shown in Fig. 4.14. Since there are only two concentric fins -- the charge and the crucible -- the present thermal model is called the "two-fin" thermal model. The representative radial location for the charge temperature is taken as $D_{in}/2$, as first defined in Fig. 3.2, since this location divides the charge equally with regard to its cross sectional area. The representative radial location for the crucible temperature is again $D_3/2$ (c.f., Fig 3.2).

(2) The Peclet number is assumed negligible.

(3) The gradient zone is assumed adiabatic; hence the gradient zone annulus fin is neglected.

(4) Only the region in the vicinity of the interface is modeled. This region extends [illegible] the interface, in either direction, at least the distance required for the interface effect to significantly die out. The effect of the remainder of the growth system is included only through imposing the average charge/crucible axial temperature gradients in the gradient zone, G_L and G_S, in the liquid and solid respectively. These parameters are obtained from the one-dimensional moving fin model. Radial temperature gradients generated by other factors are neglected.

In accordance with the assumptions listed above, the fin equations for the charge and crucible are:

$$k_{cr} A_{cr} \frac{d^2 T_{cr}}{dz^2} + \frac{T_m - T_{cr}}{R_{mcr,loc}} = 0 \qquad [4.17]$$

ORIGINAL PAGE IS
OF POOR QUALITY

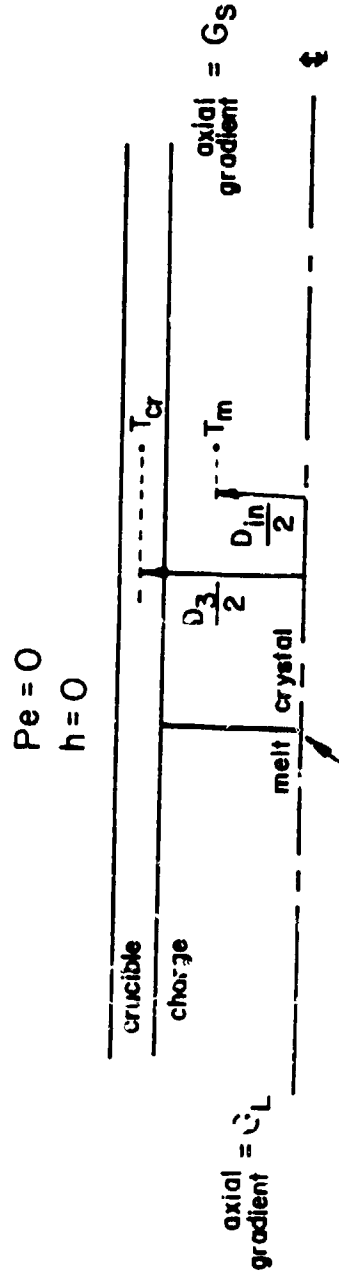

$$D_{in} = D/\sqrt{2}$$

$$D_3 = D\left[\frac{\delta^2+1}{2}\right]^{1/2}$$

Fig. 4.14. The two-fin thermal model.

ORIGINAL
OF POOR

$$k_{loc} A \frac{d^2 T_m}{dz^2} + \frac{T_{cr} - T_m}{R_{mcr,loc}} = 0 \qquad [4.18]$$

The thermal resistance, $R_{mcr,loc}$, defining the thermal coupling between the crucible and the charge, is given by [4]:

$$R_{mcr,loc} = \frac{\ln \sqrt{2}}{2\pi k_{loc}} + \frac{\ln\left(\frac{\delta^2+1}{2}\right)^{1/2}}{2\pi k_{cr}} \qquad [4.19]$$

Define the following non-dimensional temperatures:

$$\bar{\phi} \equiv \frac{k_{loc} A \phi_m + k_{cr} A_{cr} \phi_{cr}}{k_{loc} A + k_{cr} A_{cr}} \qquad [4.20a]$$

$$\phi_{m,cr} \equiv \phi_m - \phi_{cr} \qquad [4.20b]$$

is the average charge/crucible temperature weighted by their respective axial thermal conductances. Using eqs. [4.19] and [4.20] in eqs. [4.17] and [4.18], and non-dimensionalizing, results in the following form for the two-fin model fin equations:

$$\frac{d^2 \bar{\phi}}{d\zeta^2} = 0 \qquad [4.21]$$

$$\frac{d^2 \phi_{m,cr}}{d\zeta^2} - W_{loc}^2 \phi_{m,cr} = 0 \qquad [4.22]$$

$$W_{loc}^2 = \frac{8\left[1 + \frac{1}{K_{loc}(\delta^2+1)}\right]}{\ln\sqrt{2} + \frac{1}{K_{loc}} \ln\left(\frac{\delta^2+1}{2}\right)^{1/2}} \qquad [4.23]$$

Equation [4.21] indicates that $\bar{\phi}$ varies linearly in the gradient zone under the present assumptions. The axial gradient of $\bar{\phi}$, G_L and G_S

ORIGINAL PAGE IS
OF POOR QUALITY

in the liquid and solid respectively, are assumed known from the results of the moving fin model.

The general solution to eq. [4.22] is:

In the liquid: $\zeta < \zeta_i$

$$(\Phi_{m,cr})_L = C_{1L}\exp(-w_L\zeta) + C_{2L}(w_L\zeta) \qquad [4.24a]$$

In the solid: $\zeta > \zeta_i$

$$(\Phi_{m,cr})_S = C_{1S}\exp(-w_S\zeta) + C_{2S}\exp(w_S\zeta) \qquad [4.24b]$$

where the coefficients denoted by C are the unknown constants of integration.

The assumptions of the two-fin model require that $\Phi_{m,cr} \to 0$ as $\zeta \to \infty$; therefore, $C_{1L} = C_{2S} = 0$. Continuity of temperature at the interface requires $(\Phi_{m,cr})_L = (\Phi_{m,cr})_S$; therefore $C_{2L} = C_{1S}$. Finally, continuity of flux in the crucible fin at the interface requires $(d\Phi_{cr}/d\zeta)_L = (d\Phi_{cr}/d\zeta)_S$; this boundary condition yields:

$$C_{1S} = C_{2L} = \frac{G_L - G_S}{\dfrac{W_S}{1+K_S(\delta^2-1)} + \dfrac{R_K W_L}{R_K + K_S(\delta^2-1)}} \qquad [4.25]$$

The difference between G_L and G_S is, in dimensionless form:

$$G_L - G_S = \frac{Pe_S R_H - G_L(R_K - 1)}{1 + K_S(\delta^2 - 1)} \qquad [4.26]$$

Substituting these results into eqs. [4.24] produces the solution for $\Phi_{m,cr}$:

ORIGINAL PAGE IS
OF POOR QUALITY

$$(\phi_{m,cr})_L = C\exp[-w_L(\zeta_i - \zeta)] \qquad [4.27a]$$

$$(\phi_{m,cr})_S = C\exp[-w_s(\zeta - \zeta_i)] \qquad [4.27b]$$

where:
$$C = \frac{Pe_s R_H - G_L(R_K - 1)}{\frac{w_s}{1 + K_s(\delta^2 - 1)} + \frac{R_K w_L}{R_K + K_s(\delta^2 - 1)}} \cdot \frac{1}{1 + K_s(\delta^2 - 1)} \qquad [4.28]$$

The constant C defined by eq. [4.28] includes in the numerator the superposed effects of the generation of latent heat and change in charge thermal conductivity at the interface. The axial gradient in the liquid, G_L, is always negative; if $R_K > 1$, as is typical of semiconductors, these two effects reinforce each other, causing a larger disturbance at the interface than would occur by either effect acting alone. On the other hand, if $R_K < 1$, it may be possible to eliminate the interface disturbance by choosing a value for the product $Pe_S R_H$ that would make the numerator of eq. [4.28] equal to zero. This could be accomplished by changing either the lowering rate (thus changing Pe_S) or the temperature difference between the hot and cold zone furnaces (thus changing R_H). Either possibility, however, has potentially harmful side effects on the constitutional supercooling requirement.

Radial Temperature Variations Near the Growth Interface

Substituting eqs. [4.27] into the non-dimensional form of eq. [4.18] yields an expression for $d^2\phi_m/d\zeta^2$ due to the heat exchange between the charge and the crucible near the interface:

$$\frac{d^2\phi_{m,L}}{d\zeta^2} = \frac{w_L K_s(\delta^2 - 1)}{R_K + K_s(\delta^2 - 1)} C\exp[-w_L(\zeta - \zeta_i)] \qquad [4.29a]$$

$$\frac{d^2\phi_{m,s}}{d\zeta^2} = \frac{w_s K_s(\delta^2 - 1)}{1 + K_s(\delta^2 - 1)} C\exp[-w_s(\zeta - \zeta_i)] \qquad [4.29b]$$

ORIGINAL PAGE IS
OF POOR QUALITY

Using eqs. [4.29] in eqs [4.11] and [4.12] produces the value of ϕ_Δ at the interface:

$$\phi_\Delta(\zeta_i) = -\frac{C}{7.63}\frac{K_s(\delta^2-1)}{R_K+1}\left[\frac{R_K w_L^2}{R_K+K_s(\delta^2-1)} + \frac{w_s^2}{1+K_s(\delta^2-1)}\right] \qquad [4.30]$$

The value of ϕ_Δ at the interface determined by eq. [4.30] is compared to the results shown previously in Figs. 4.10 to 4.13 in Table 4.2. In general, the comparison is favorable, indicating that the two-fin model provides a reasonable approximation for $d^2\phi_m/d\zeta^2$ in the vicinity of the interface. The largest differences occur for those cases which exhibit effects not included in the two-fin model. For example, the cases considered in Fig. 4.11 use a larger Peclet number, 0.05, compared to that used for the other figures, 0.001, in order to accentuate the liberation of latent heat. The effect of the larger Peclet number, not included in the two-fin model, is to create a more negative value of $\Phi_\Delta(\zeta_i)$.

A small error in eq. [4.30] compared to results from the concentric fin model is also apparent for the cases of small δ considered in Fig. 4.12. This error is attributable to the neglect, by the two-fin model, of the radial gradients generated in the furnace zones. In order to approximate the attenuation effect, the value of $\phi_\Delta(\zeta_i)$ determined by eqs. [4.9], [4.10], and [4.14] is simply added to that determined by eq. [4.30]. The results of this approximation, shown in the last column of Table 4.2, are seen to improve the estimation of $\phi_\Delta(\zeta_i)$ for small values of δ. As δ increases, the contribution to $\phi_\Delta(\zeta_i)$ due to the attenuation effect becomes less important.

Table 4.2 also demonstrates that eq. [4.30] is unable to account for the effects of the changing interface location on $\phi_\Delta(\zeta_i)$. This error is

ORIGINAL PAGE IS
OF POOR QUALITY

TABLE 4.2

Comparison of the approximate methods of calculating $\phi_\Delta(\zeta_i)$ to results of the concentric fin model for the cases considered in Figs. 4.10 to 4.13.

		$\phi_\Delta(\zeta_i)$		
Figure	variable parameter	concentric fin model	eq. [4.30]	eq. [4.30] plus attenuation effect from eq. [4.9], [4.10], and [4.14]
4.10	R_K = 1.0	.000000	.000000	.000000
	1.1	-.000493	-.000464	-.000464
	1.25	-.00110	-.00114	-.00114
	1.5	-.00186	-.00176	-.00175
	2.0	-.00274	-.00261	-.00260
	4.0	-.00343	-.00330	-.00329
4.11	R_H = 0.0	-.000023	.000000	.000000
	0.25	-.000219	-.000179	-.000179
	0.5	-.000416	-.000358	-.000360
	1.0	-.000810	-.000716	-.000720
	2.0	-.00160	-.00143	-.00144
4.12	δ = 1.0001	-.000021	-.000002	-.000021
	1.001	-.000040	-.000021	-.000039
	1.01	-.000214	-.000183	-.000201
	1.05	-.000818	-.000730	-.000744
	1.1	-.00136	-.00122	-.00123
	1.25	-.00227	-.00207	-.00207
	1.5	-.00274	-.00261	-.00260
4.13	ζ_i = 0.0	-.00274	-.00261	-.00260
	-0.1	-.00245	-.00258	-.00248
	-0.2	-.00210	-.00254	-.00231
	-0.3	-.00166	-.00252	-.00200
	-0.4	-.00108	-.00249	-.00138

The values of G_L and θ_i required for use in eqs. [4.14] and [4.30] are listed in Tables 4.3 and 4.4.

ORIGINAL PAGE IS
OF POOR QUALITY

again attributable to the relative importance at the interface of radial gradients generated in the hot and cold zones compared to those generated at the interface. As the interface approaches the end of the gradient zone, the influence of radial gradients generated in the adjacent furnace zone becomes increasingly important.

The last column of Table 4.2 provides an approximation for the effect of changing interface location on $\phi_\Delta(\zeta_i)$. The correction provided by these values to the results calculated by eq. [4.30] (i.e., the second column of Table 4.2) assumes that the radial gradients generated in the hot and cold zones attenuate at a rate proportional to $\exp(-7.63\zeta)$. The actual rate of attenuation is, however, smaller when a crucible is present (c.f., section 4.2). It is expected that use of the actual rate of attenuation would produce a better correction to eq. [4.30] for the effect of changing interface location. Unfortunately, a simple analytical expression for the attenuation of ϕ_Δ from the ends of the gradient zone in the presence of a crucible is not available.

Correction to the Axial Temperature Gradient in the Liquid At The Growth Interface:

The moving fin model predicts the value of $G_L = d\bar{\phi}_L/d\zeta$ for the axial temperature gradient in the liquid at the interface. The constitutional supercooling requirement, however, depends on the value of $(d\phi_m/d\zeta)_L$ at the interface. The difference between these temperature gradients is approximated from the results of the two-fin model. Differentiating eqs. [4.20] with respect to ζ_i and solving for $(d\phi_m/d\zeta)_L$ yields:

$$\left[\frac{d\phi_m(\zeta_i)}{d\zeta}\right]_L = G_L + \frac{K_s(\delta^2-1)}{R_K+K_s(\delta^2-1)}\left[\frac{d\phi_{m,cr}(\zeta_i)}{d\zeta}\right]_L \qquad [4.31]$$

Differentiating eq. [4.27a] with respect to ζ and substituting into eq. [4.31] yields:

ORIGINAL PAGE IS
OF POOR QUALITY

$$\left[\frac{d\phi_m(\zeta_i)}{d\zeta}\right] = G_L + \frac{K_s(\delta^2-1)}{R_K + K_s(\delta^2-1)} W_L C \qquad [4.32]$$

The second term on the right side of eq. [4.32] is a correction to be applied to G_L in order to account for the effect of radial heat transfer near the interface on the axial gradient in the charge at the interface.

The axial temperature gradient in the liquid at the interface calculated by the moving fin model, G_L, and by eq. [4.32] are compared to results from the concentric fin model in Table 4.3 for the cases considered in Figs. 4.10 to 4.13. It is seen that eq. [4.32] provides an excellent approximation to $[d\phi_m(\zeta_i)/d\zeta]_L$ even though the correction term may be significant (e.g., large R_K or large R_H). The approximation is most in error as the interface approaches the hot zone (c.f., ζ_i = -0.3, -0.4 in Fig. 4.13) due to the additional influence of radial heat transfer in the hot zone.

Correction To the Interface Temperature:

The moving fin model predicts for the interface temperature the average charge/crucible temperature; i.e., θ_i is interpreted as $\bar{\phi}(\zeta_i)$. The difference between $\phi_m(\zeta_i)$ and θ_i found by the two-fin model may be used as a simple correction to θ_i:

$$\theta_i - \phi_m(\zeta_i) \simeq \left[\bar{\phi}(\zeta_i) - \phi_m(\zeta_i)\right] \qquad [4.33]$$

Rearranging eqs. [4.20] yields:

$$\left[\bar{\phi}(\zeta_i) - \phi_m(\zeta_i)\right]_L = -\frac{K_s(\delta^2-1)}{R_K + K_s(\delta^2-1)} \phi_{m,cr}(\zeta_i) \qquad [4.34a]$$

$$\left[\bar{\phi}(\zeta_i) - \phi_m(\zeta_i)\right]_s = -\frac{K_s(\delta^2-1)}{1 + K_s(\delta^2-1)} \phi_{m,cr}(\zeta_i) \qquad [4.34b]$$

Since $\phi_{m,cr}(\zeta_i)$ and $\phi_m(\zeta_i)$ are equal in the liquid and solid at the

ORIGINAL PAGE IS
OF POOR QUALITY

TABLE 4.3

Comparison of the approximate methods of calculating $d\phi_m/d\zeta$ to results of the concentric fin model for the cases considered in Figs. 4.10 to 4.13.

		axial temperature gradient in the liquid at the growth interface		
Figure	variable parameter	concentric fin model	moving fin model G_L	eq. [4.32]
4.10	R_K = 1.0	-.351	-.350	-.350
	1.1	-.332	-.340	-.332
	1.25	-.308	-.326	-.307
	1.5	-.275	-.306	-.275
	2.0	-.228	-.272	-.228
	4.0	-.140	-.190	-.140
4.11	R_H = 0.0	-.351	-.350	-.350
	0.25	-.344	-.348	-.344
	0.5	-.338	-.345	-.338
	1.0	-.325	-.339	-.325
	2.0	-.300	-.328	-.300
4.12	δ = 1.0001	-.251	-.252	-.252
	1.001	-.251	-.252	-.252
	1.01	-.251	-.252	-.251
	1.05	-.249	-.256	-.249
	1.1	-.247	-.260	-.246
	1.25	-.240	-.267	-.239
	1.5	-.228	-.272	-.228
4.13	ζ_i = 0.0	-.228	-.272	-.228
	-0.1	-.225	-.269	-.225
	-0.2	-.222	-.266	-.223
	-0.3	-.217	-.262	-.220
	-0.4	-.211	-.260	-.217

ORIGINAL PAGE IS
OF POOR QUALITY

interface, eqs. [4.34] imply that $[\bar{\phi}(\zeta_i)]_L \neq [\bar{\phi}(\zeta_i)]_S$; that is, the two-fin model predicts a step change in $\bar{\phi}$ at the interface. This is due to the definition of $\bar{\phi}$ which averages the charge and crucible temperatures according to their respective axial thermal conductances.

In order to approximate the effect of radial heat transfer near the interface on the interface temperature, the correction term within brackets in eq. [4.33] will be taken simply as the arithmetic average of eqs. [4.34a] and [4.34b]. Using eq. [4.27] evaluated at $\zeta = \zeta_i$ yields:

$$\phi_m(\zeta_i) = \theta_i + \tfrac{1}{2} C \left[\frac{K_s(\delta^2-1)}{1 + K_s(\delta^2-1)} + \frac{K_s(\delta^2-1)}{R_K + K_s(\delta^2-1)} \right] \qquad [4.35]$$

The interface temperature determined by eq. [4.35] is compared to that found from the concentric and moving fin models in Table 4.4 for the cases considered in Figs. 4.10 to 4.13. It is seen that the moving fin model, provides a reasonable estimation to the interface temperature, θ_i, without the correction afforded by eq. [4.35]; this indicates that radial heat transfer at the interface between the charge and the crucible has a relatively small effect on the interface temperature or location. Utilizing the corresponding values of G_L listed in Table 4.3, the moving fin model would mislocate the interface by at most 0.1 charge diameter for the cases considered (c.f., $R_K = 4$ from Fig. 4.10). Results calculated from eq. [4.35], however, do compare yet more favorably to those of the concentric fin model.

Diabatic Gradient Zone

Two additional parameters are required by the concentric fin model when heat transfer in the gradient zone is considered: Bi_G and R_G. The Biot number in the gradient zone indicates the thermal coupling between the gradient zone annulus and the charge. R_G is the ratio of the axial heat conducting capacities of the gradient zone annulus and the charge (c.f., eqs. [3.3]). A diabatic gradient zone approaches abiadatic conditions as either Bi_G or R_G approach zero. Otherwise, the temperature

ORIGINAL PAGE IS
OF POOR QUALITY

TABLE 4.4

Comparison of the approximate methods of calculating $\phi_m(\zeta_i)$ to results of the concentric fin model for the cases considered in Figs. 4.10 to 4.13.

		temperature of the growth interface		
Figure	variable parameter	concentric fin model	moving fin model θ_i	eq. [4.35]
4.10	R_K = 1.0	.500	.500	.500
	1.1	.509	.507	.509
	1.25	.522	.518	.522
	1.5	.540	.534	.540
	2.0	.570	.561	.572
	4.0	.648	.634	.651
4.11	R_H = 0.0	.517	.500	.500
	0.25	.522	.504	.505
	0.5	.527	.508	.509
	1.0	.536	.516	.519
	2.0	.554	.532	.537
4.12	δ = 1.0001	.619	.619	.619
	1.001	.619	.618	.618
	1.01	.617	.617	.617
	1.05	.610	.610	.611
	1.1	.603	.602	.604
	1.25	.587	.584	.588
	1.5	.570	.561	.572
4.13	ζ_i = 0.0	.570	.561	.572
	-0.1	.602	.593	.604
	-0.2	.633	.624	.635
	-0.3	.664	.655	.665
	-0.4	.693	.685	.695

The values of G_L required for use in eqs. [4.35] are listed in Tables 4.3.

ORIGINAL PAGE IS
OF POOR QUALITY

difference between the gradient zone annulus and charge ($\phi_A - \phi_m$) produces heat transfer which affects axial temperature gradients and also, as shown in this section, radial temperature gradients within the charge.

Results From the Concentric Fin Model

Figures 4.15a, 4.15b and 4.15c show the variation of ϕ_Δ in a diabatic gradient zone as calculated by the concentric fin model. The systems in these figures are symmetric and do not consider a crucible. Since the systems are symmetric, the curves have been plotted only for the hot side of the gradient zone. Each figure considers a constant Biot number throughout the furnace while the separate curves in each figure consider various values of R_G. The graphs inserted in each figure are axial temperature distributions of ϕ_A and ϕ_m corresponding to the individual curves of ϕ_Δ. As a reference, the distribution of ϕ_Δ in an adiabatic gradient zone (i.e., $Bi_G = 0$) is also included in each figure.

According to Figs. 4.15, the value of R_G significantly affects the distribution of ϕ_Δ in the gradient zone. When R_G is small, heat exchange between the charge and the gradient zone annulus occurs only near the ends of the gradient zone; toward the center of the gradient zone ϕ_A is nearly equal to ϕ_m. In such cases, the distribution of ϕ_Δ is only slightly altered from that in the corresponding system with an adiabatic gradient zone. As R_G increases, the temperature difference $\phi_A - \phi_m$ is more pronounced increasing the radial heat transfer to the charge; as a consequence, ϕ_Δ increases as well. For sufficiently large values of R_G, ϕ_A is approximately linear; further increases in R_G do not affect either $\phi_A - \phi_m$ or ϕ_Δ but serve only to conduct more heat from the hot to the cold zone furnaces through the gradient zone annulus.

Figure 4.16 demonstrates the effect of increasing Bi_G for systems which have a linear variation of ϕ_A as calculated by the concentric fin model. A linear variation of has been obtained by choosing a large value of R_G (i.e., R_G=1000). Increasing Bi_G has a slight effect on the axial temperature distribution in the gradient zone, tending to reduce the driving force for heat transfer in the gradient zone, $\phi_A - \phi_m$. This

$Bi_H = Bi_C = Bi_G = 0.05$

No crucible

Symmetric system

$\lambda_G = 1.0$

$\lambda_H = \lambda_C = \infty$

ORIGINAL PAGE IS
OF POOR QUALITY

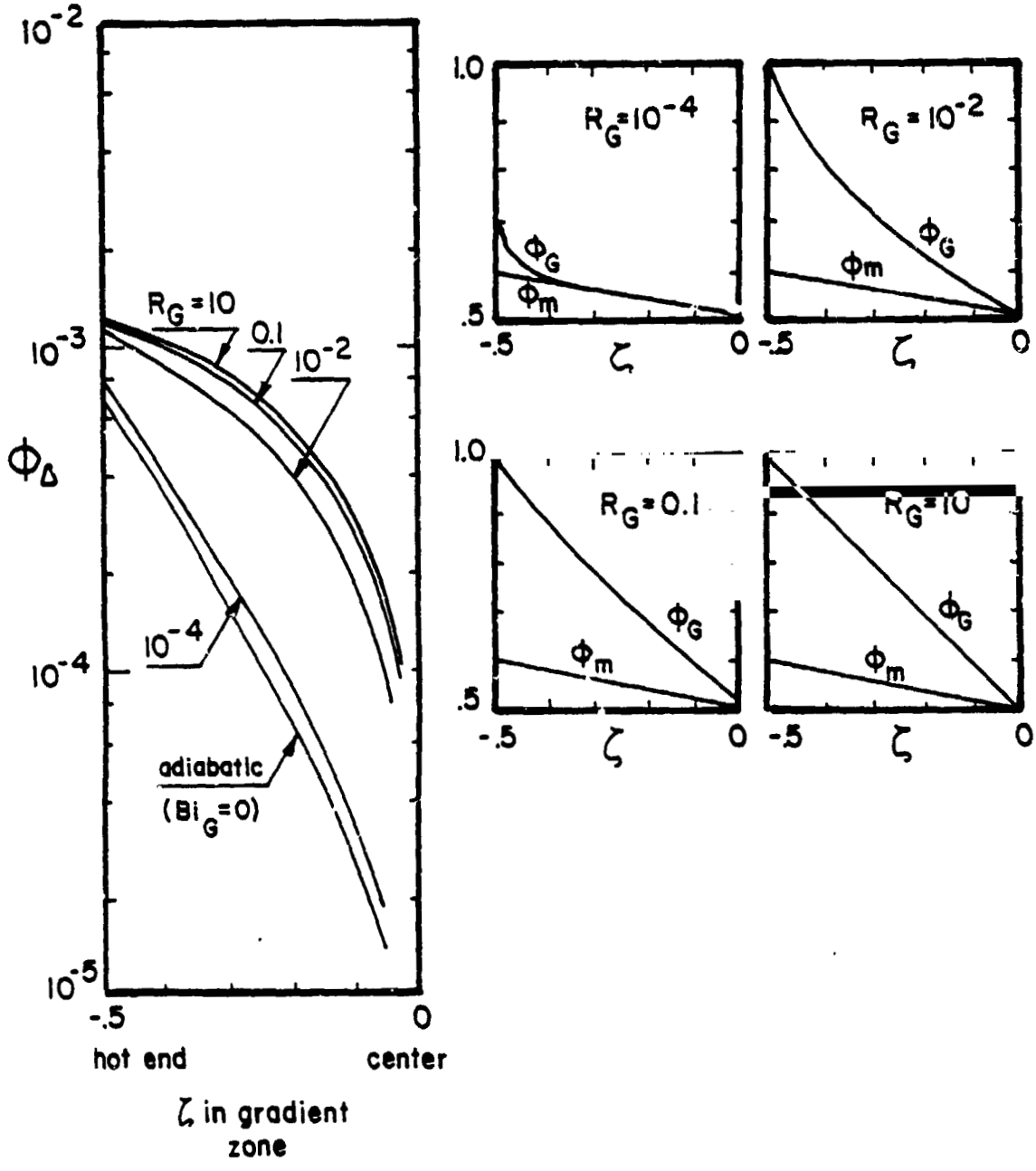

Fig. 4.15a. Φ_Δ, Φ_m, and Φ_G in a diabatic gradient zone. Bi = 0.05, no crucible and symmetric system.

ORIGINAL PAGE IS
OF POOR QUALITY

$Bi_H = Bi_C = Bi_G = 0.5$

No crucible

Symmetric system

$\lambda_G = 1.0$

$\lambda_H = \lambda_C = \infty$

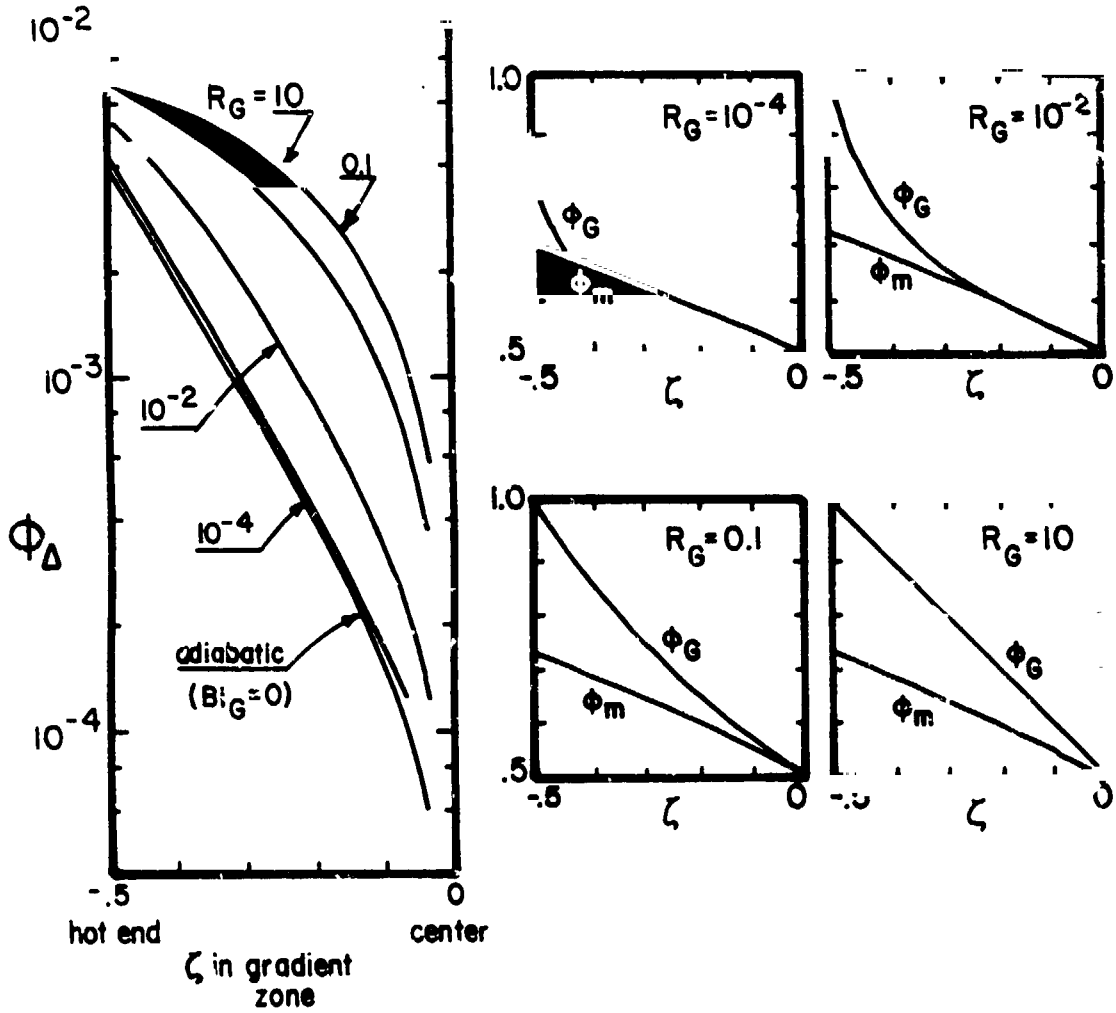

Fig. 4.15b. ϕ_Δ, ϕ_m, and ϕ_G in a diabatic gradient zone. Bi = 0.5, no crucible and symmetric system.

ORIGINAL PAGE IS
OF POOR QUALITY

$Bi_H = Bi_C = Bi_G = 5.0$

No crucible

Symmetric system

$\lambda_G = 1.0$

$\lambda_H = \lambda_C = \infty$

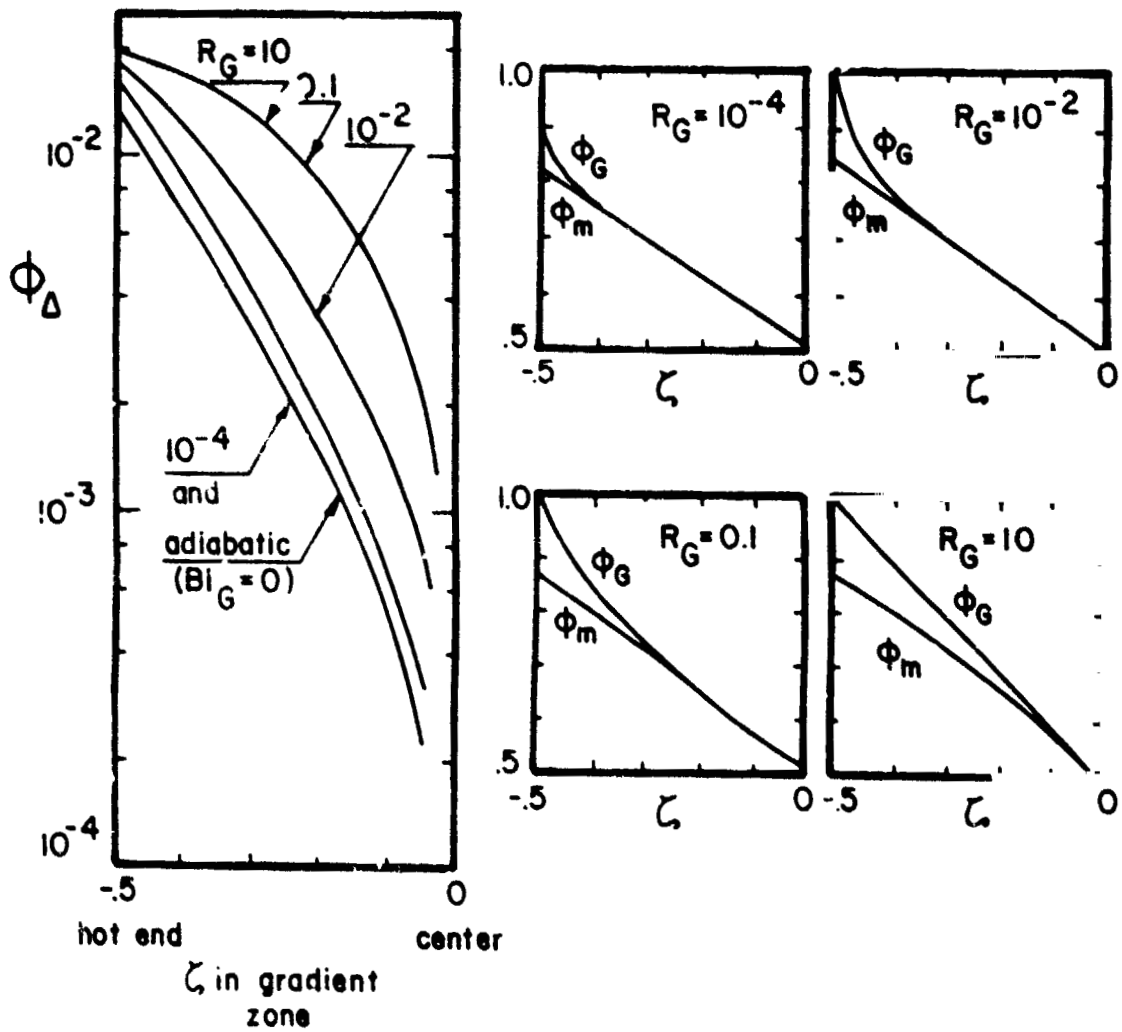

Fig. 4.15c. Φ_Δ, Φ_m, and Φ_G in a diabatic gradient zone. Bi = 5.0, no crucible and symmetric system.

ORIGINAL PAGE IS
OF POOR QUALITY

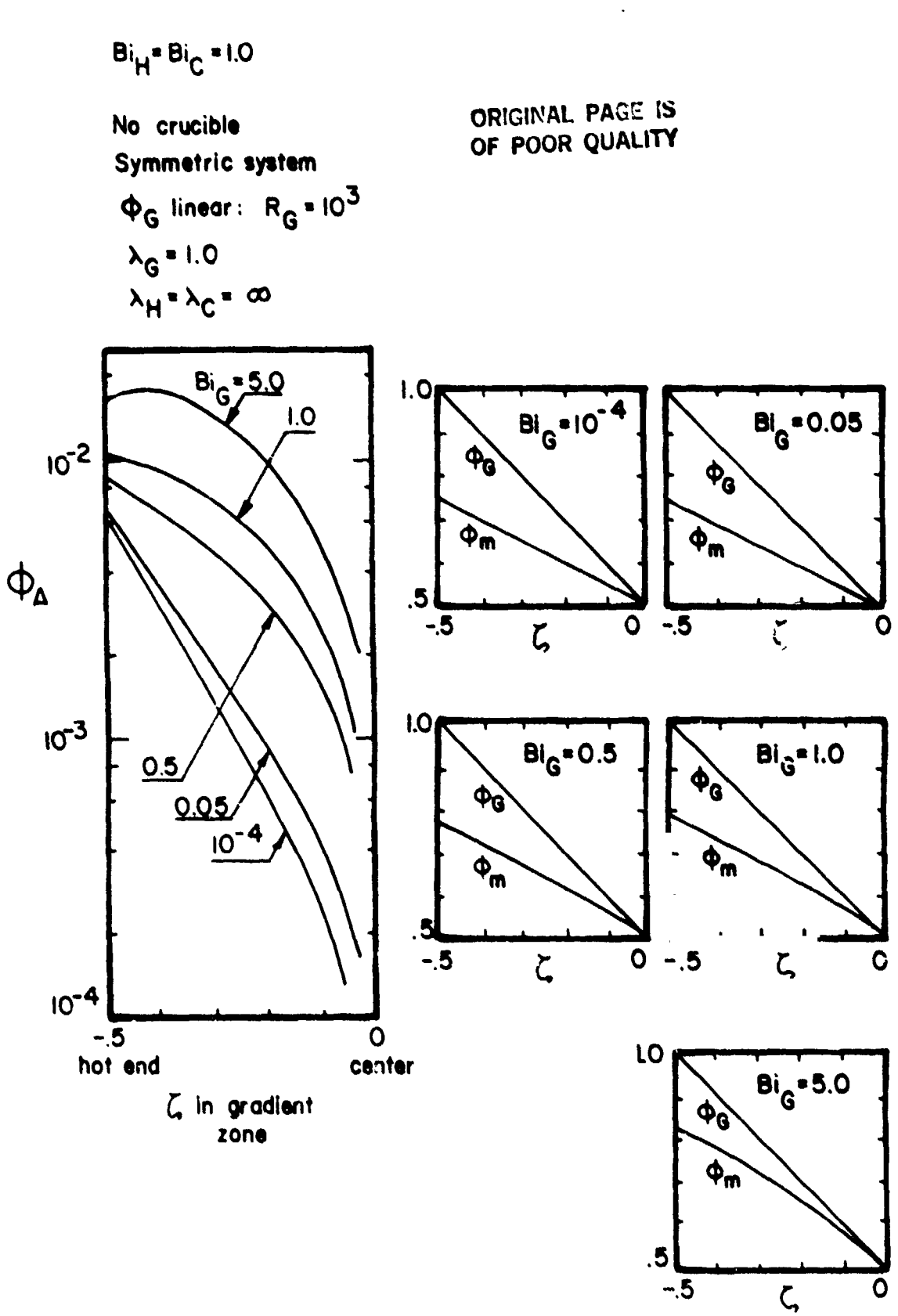

Fig. 4.16. Φ_A, Φ_m and Φ_G in a diabatic gradient zone for increasing Bi_G. No crucible, symmetric system and linear Φ_G.

ORIGINAL PAGE IS
OF POOR QUALITY

effect, however, is more than offset by the augmented thermal coupling between the charge and gradient zone annulus represented by the larger Bi_G. As shown in Fig. 4.16, the result is that ϕ_Δ increases with Bi_G. The curve for $Bi_G = 5$ shows, for example, that ϕ_Δ increases, rather than attenuates, from the end of the gradient zone when the gradient zone Biot number is greater than those in the hot and cold zones.

Figure 4.17 shows that the effect on ϕ_Δ of heat transfer in the gradient zone when a crucible is present is similar to those systems examined above without a crucible. (The system considered in Fig. 4.17 is analogous to that of Fig. 4.15b except for the presence of a crucible.)

Analytical Expression For the Effect of a Diabatic Gradient Zone On Radial Temperature Variations

The development of an analytical expression for $\phi_\Delta(\zeta)$ in a diabatic gradient zone, through the use of the Green's function approach discussed in section 4.1, requires a simple analytical expression for $d^2\phi_m/d\zeta^2$ within the diabatic gradient zone as well as within the furnace zones. The present model assumes that the primary effect of heat transfer between the gradient zone annulus and the charge is attributable to thermal conditions near the axial location of interest. This assumption is qualitatively justified by the high rate of attenuation of the effects of radial heat transfer distant from the location of interest; indicated by eq. [4.4]. Accordingly, a linearized description for $d^2\phi_m/d\zeta^2$ about the location of interest, ζ, is employed:

$$\frac{d^2\phi_m(x)}{dx^2} = \frac{d^2\phi_m(\zeta)}{d\zeta^2}\bigg|_{x=\zeta} + \frac{d}{dx}\left[\frac{d^2\phi_m(x)}{dx^2}\right]_{x=\zeta}(x-\zeta) \qquad [4.36]$$

Substituting eq. [4.36] into eq. [4.7] yields:

$$\phi_\Delta(\zeta) = -\frac{1}{66.2}\,\frac{d^2\phi_m(\zeta)}{d\zeta^2} \qquad [4.37]$$

ORIGINAL PAGE IS
OF POOR QUALITY

$Bi_H = Bi_C = Bi_G = 0.5$

$\delta = 1.5 \quad K_S = 1.0$

Symmetric system

$\lambda_G = 1.0$

$\lambda_H = \lambda_C = \infty$

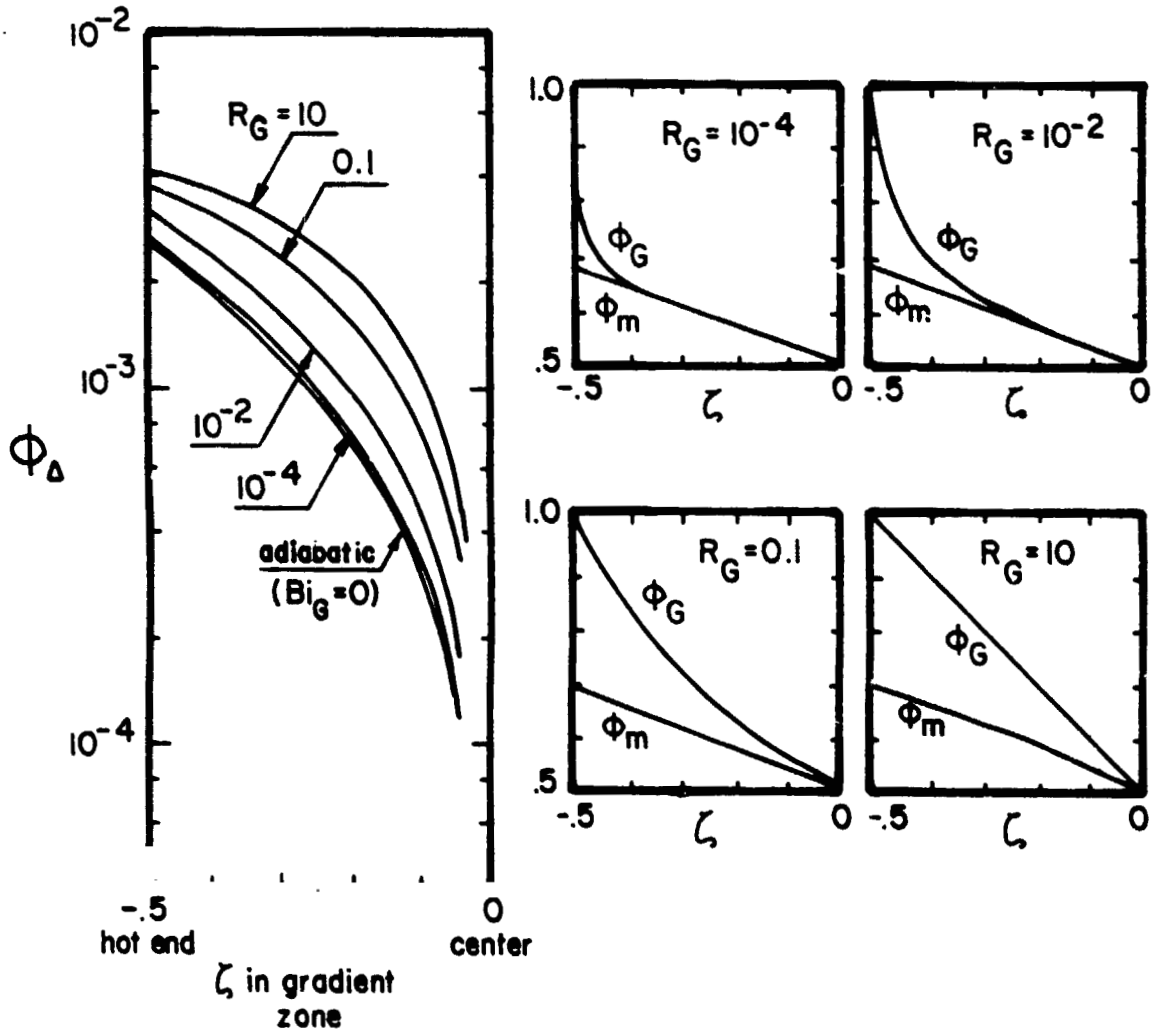

Fig. 4.17. ϕ_Δ, ϕ_m, and ϕ_G in a diabatic gradient zone with a crucible. The other parameters are the same as those used in Fig. 4.15b.

ORIGINAL PAGE IS
OF POOR QUALITY

Next, eq. [4.16] is used to approximate $d^2\phi_m/d\zeta^2$; this approximation assumes that $d^2\theta_m/d\zeta^2$ of the moving fin model accurately represents $d^2\phi_m/d\zeta^2$ of the concentric fin model and that $Bi^{**}_{loc}(\phi_f - \phi_m)$ varies linearly near the location of interest. These assumptions are not always valid since:

(1) Bi^{**}_{loc} may abruptly change at the ends of the gradient zone or at the interface.

(2) $(\phi_f - \phi_m)$ may not vary approximately linearly at the ends of the gradient zone, at the interface, or when R_G is small.

(3) When a crucible is present, $d^2\theta_m/d\zeta^2 \neq d^2\phi_m/d\zeta^2$ at the ends of the gradient zone.

Consequently, the expressions which are obtained through the present model are suggested for use under the following constraints: (1) qualitatively, to indicate the thermal parameters most affecting radial temperature gradients caused by a diabatic gradient zone, and (2) quantitatively, as order of magnitude estimations.

Subsituting eq. [4.16] into [4.37] yields:

$$\phi_\Delta(\zeta) \cong \frac{Bi^{**}_{loc}\left[\phi_f(\zeta) - \phi_m(\zeta)\right]}{14.55} \qquad [4.38]$$

(Within the gradient zone, ϕ_f becomes ϕ_G.) According to eq. [4.38], the value of ϕ_Δ at a certain location, ζ, depends only on the local Biot number and the local temperature difference between the furnace and the charge.

Constant Interface Shape in the Gradient Zone

Equation [4.38] suggests, in accordance with its limitations

ORIGINAL PAGE IS
OF POOR QUALITY

discussed above, that ϕ_Δ may be maintained at a constant value over a portion of the gradient zone if the product $Bi_G^{**}(\phi_{G_1} - \phi_m)$ is constant over a sufficiently long region near the center of the gradient zone, i.e., not near the ends of the gradient zone. The following set of "design rules" illustrates how the heat transfer in the gradient zone can be "tailored" so that these conditions may be approximately achieved for systems in which the interface disturbance is not present:

(1) Calculate $d\theta_m/d\zeta$ in the gradient zone, assuming that $Bi_G = 0$, by using results of the moving fin model.

(2) Allow R_G to be sufficiently large so that ϕ_G is linear.

(3) Alter the end temperatures of the gradient zone annulus so that $d\phi_{G_1}/d\zeta = d\theta_m/d\zeta$. In this way, $\phi_{G_1} - \phi_m$ is constant in the gradient zone, neglecting the effects of the crucible near the ends of the gradient zone. In the present development, it is arbitrarily chosen to maintain $\phi_G(-\lambda_G/2) = 1$ while altering $\phi_G(\lambda_G/2)$. In this case:

$$\phi_G(\lambda_G/2) = 1 + \lambda_G \frac{d\theta_m}{d\zeta} \qquad [4.39]$$

$$(\phi_{G_1} - \phi_m) = \frac{1}{2}\left(1 + \lambda_G \frac{d\theta_m}{d\zeta}\right) \qquad [4.40]$$

(4) The desired value of ϕ_Δ determines the required value of Bi_G^{**} by substituting eq. [4.40] into eq. [4.38]:

$$Bi_G^{**} = \frac{29.1\,\phi_\Delta}{1 + \lambda_G(d\theta_m/d\zeta)} \qquad [4.41]$$

A non-zero value of Bi_G^{**} leads to a non-symmetric system and non-constant $(\phi_{G_1} - \phi_m)$, thus contradicting the assumptions of steps (1) and (3) above. These effects are shown, however, to be of secondary importance in the results which follow.

ORIGINAL PAGE IS
OF POOR QUALITY

(5) The desired radius of curvature of the interface, N, is next used to eliminate ϕ_Δ from eq. [4.41]. Using eq. [B.6]:

$$Bi_G^{**} = -\frac{29.1}{16N}\,\frac{d\theta_m/d\zeta}{1+\lambda_G(d\theta_m/d\zeta)} \qquad [4.42]$$

Three test cases are employed to demonstrate the procedure described above. The parameters defining the systems and the results of the calculations of steps (1) through (5) are shown in Table 4.5. Figures 4.18, 4.19, and 4.20 plot the resultant temperature and isotherm curvature distributions as calculated by the concentric fin model: part (a) of each figure plots the distribution of ϕ_Δ in the gradient zone while part (b) shows the distribution of ϕ_G and ϕ_m and the inverse radius of curvature, N^{-1} of the isotherms in the gradient zone. The desired constant radius of curvature chosen for use in eq. [4.43] is N = 20; therefore, N^{-1} = 0.05.

Figure 4.18 considers a system without a crucible and with a gradient zone length λ_G = 1.0. It is seen that the distribution of ϕ_Δ and N tend to flatten out near the center of the gradient zone, approximating the desired values of ϕ_Δ = 0.00127 and N^{-1} = 0.05. It is expected that the distributions of ϕ_Δ and N will be yet more flat when the influence from the ends of the gradient zone are even more diminished at its center. This is accomplished in Fig. 4.19 by increasing the length of the gradient zone to λ_G = 2.0. The curves for ϕ_Δ and N are quite flat in a large portion of the center of the gradient zone in this case. Note that the required value of ϕ_Δ = 0.000903 for case 2 (c.f., Table 4.5) is larger than actually present as shown in Fig. 4.19. This is due to heat transfer to the charge in the gradient zone, not considered in eq. [4.40], which causes $\phi_G - \phi_m$ to be slightly smaller than the value predicted for a symmetric system. Reduced heat transfer to the charge, and therefore a reduced value of ϕ_Δ results. If desired, the value of ϕ_Δ can be adjusted upward by an appropriate alteration in Bi_G.

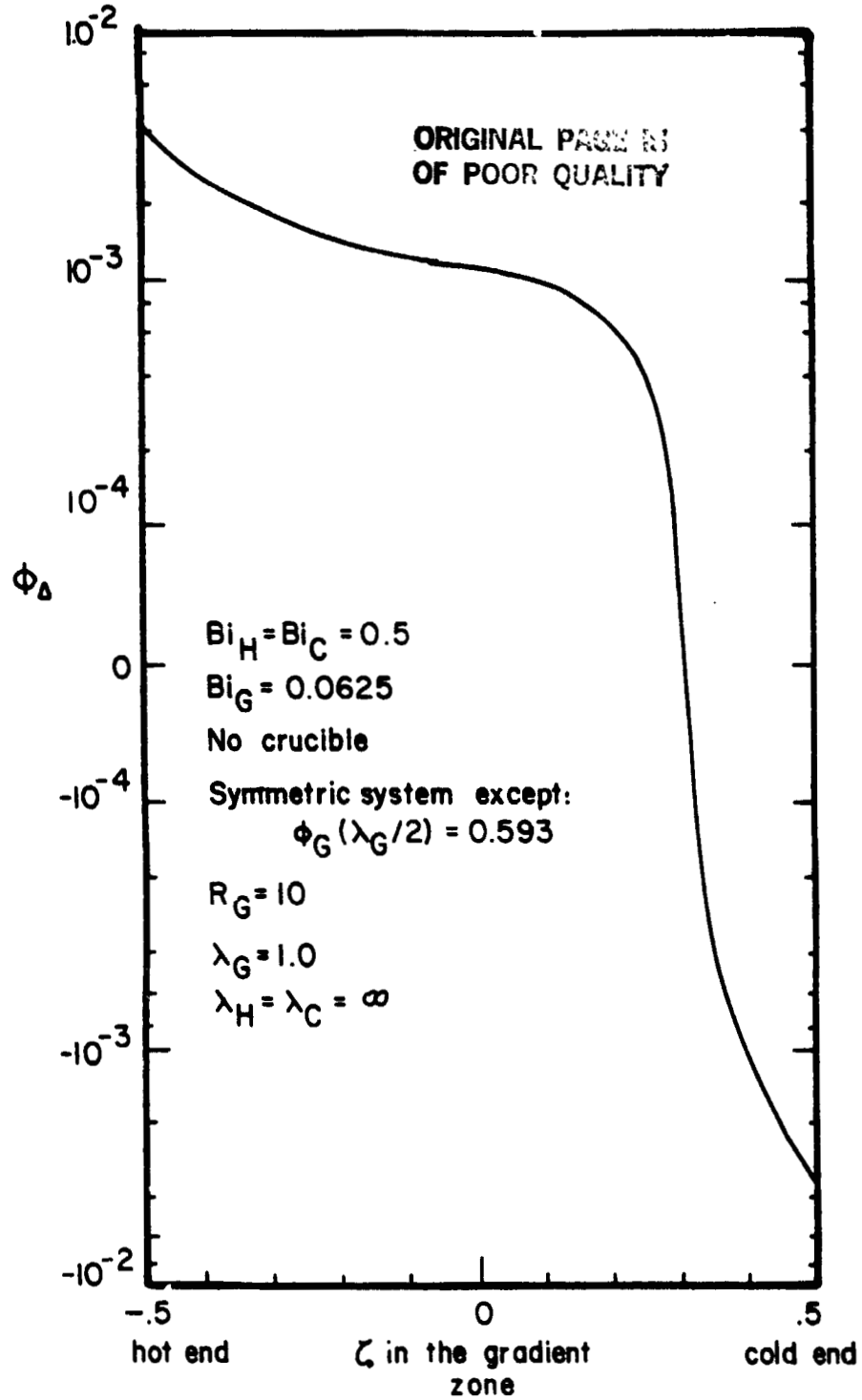

Fig. 4.18a. Demonstration of the procedure used to obtain an appoximately constant isotherm shape in the gradient zone. No crucible, symmetric system and $\lambda_G = 1.0$.

ORIGINAL PAGE IS
OF POOR QUALITY

$Bi_H = Bi_C = 0.5$

$Bi_G = 0.0625$

No crucible

Symmetric system except:

$\Phi_G(\lambda_G/2) = 0.593$

$R_G = 10$

$\lambda_G = 1.0$

$\lambda_H = \lambda_C = \infty$

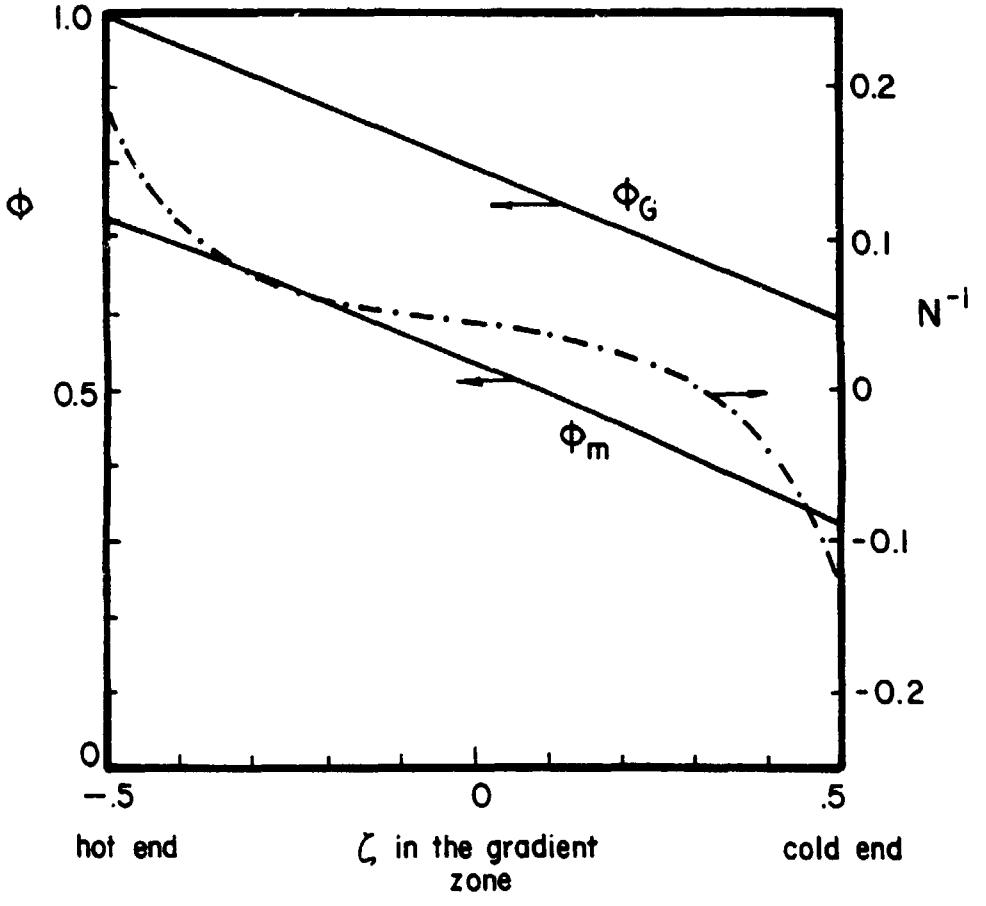

Fig. 4.18b. Demonstration of the procedure used to obtain an approximately constant isotherm shape in the gradient zone. No crucible, symmetric system and $\lambda_G = 1.0$.

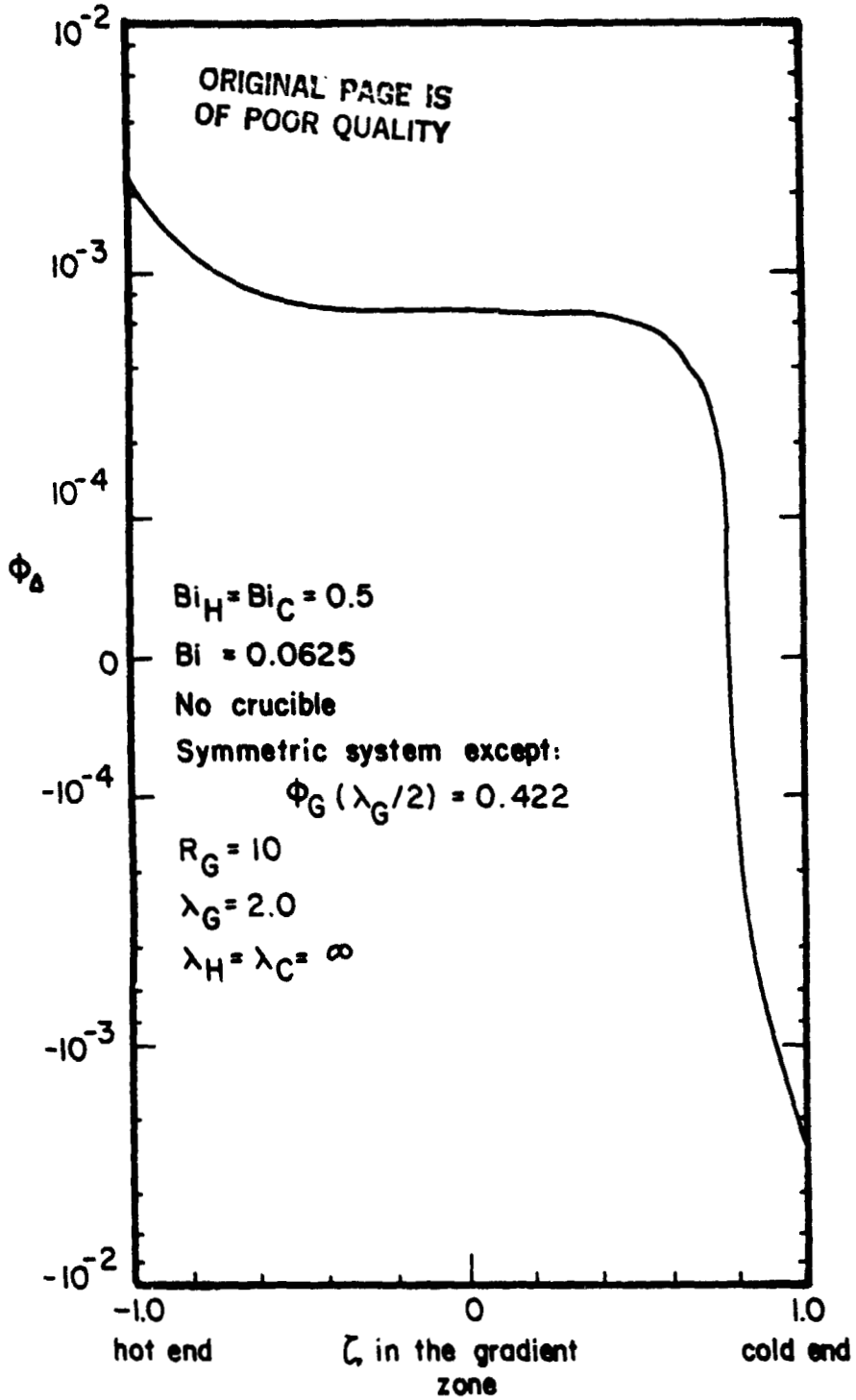

Fig. 4.19a. Analogous to Fig. 4.18a except the gradient zone is longer; i.e., $\lambda_G = 2.0$.

$Bi_H = Bi_C = 0.5$

$Bi_G = 0.0625$

ORIGINAL PAGE IS
OF POOR QUALITY

No crucible

Symmetric system except:

$\Phi_G(\lambda_G/2) = 0.422$

$R_G = 10$

$\lambda_G = 2.0$

$\lambda_H = \lambda_C = \infty$

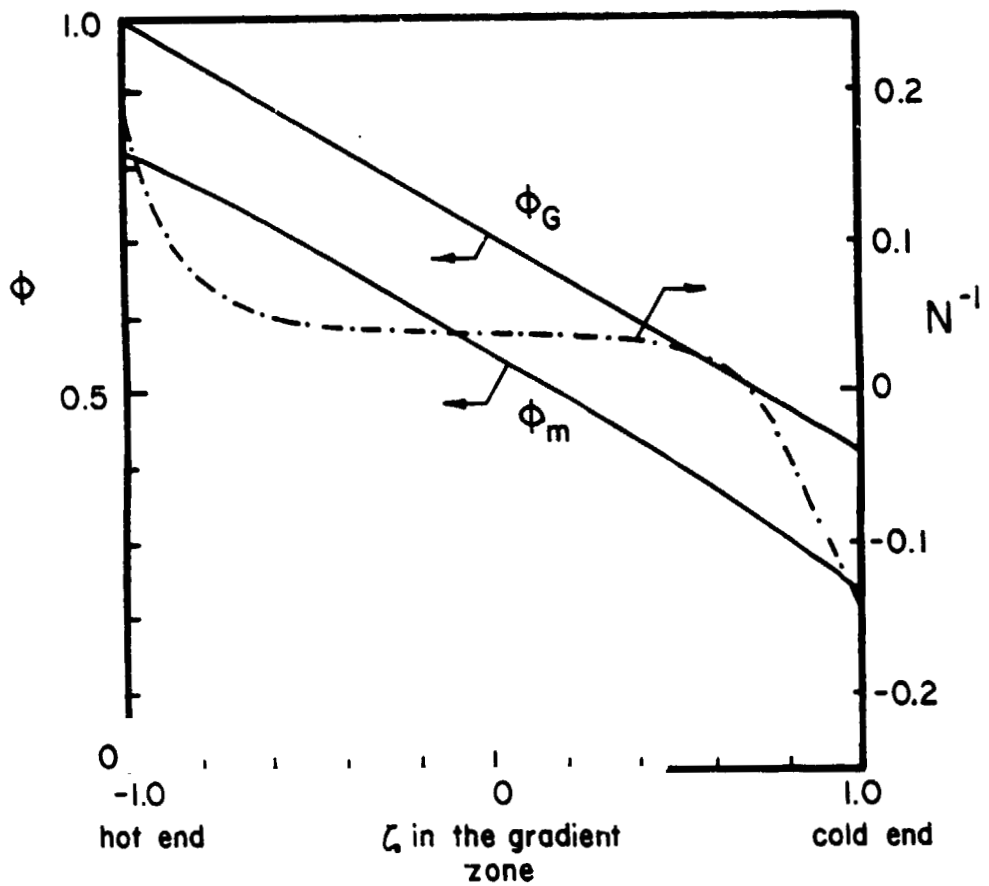

Fig. 4.19b. Analogous to Fig. 4.18b except the gradient zone is longer; i.e., $\lambda_G = 2.0$.

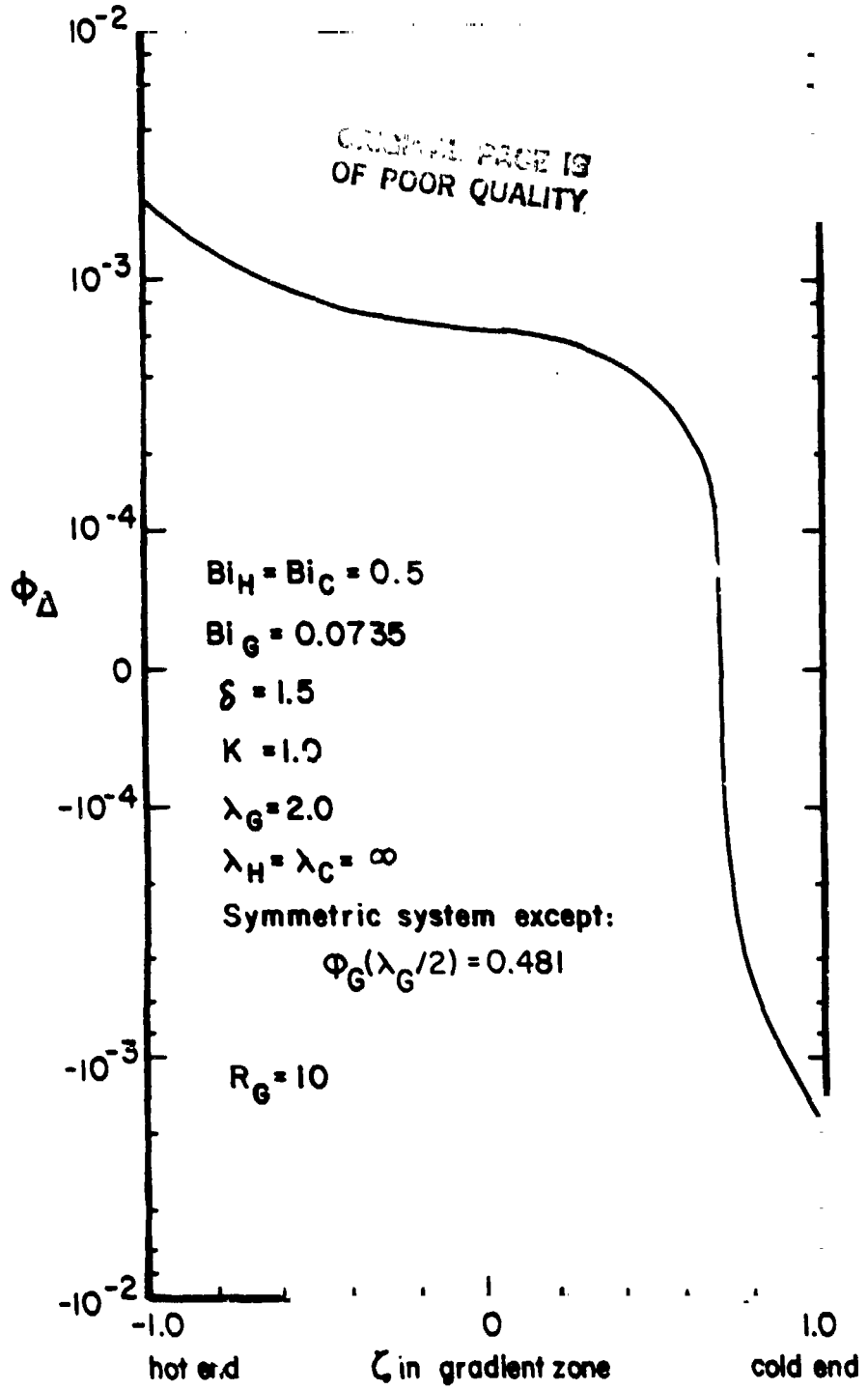

Fig. 4.20a. Analogous to Fig. 4.19a except a crucible is present; i.e., $\delta = 1.5$.

$Bi_H = Bi_C = 0.5$

$Bi = 0.0735$

$\delta = 1.5 \quad K = 1.0$

Symmetric system except:

$\Phi_G(\lambda_G/2) = 0.481$

$R_G = 10$

$\lambda_G = 2.0$

$\lambda_H = \lambda_C = \infty$

ORIGINAL PAGE IS
OF POOR QUALITY

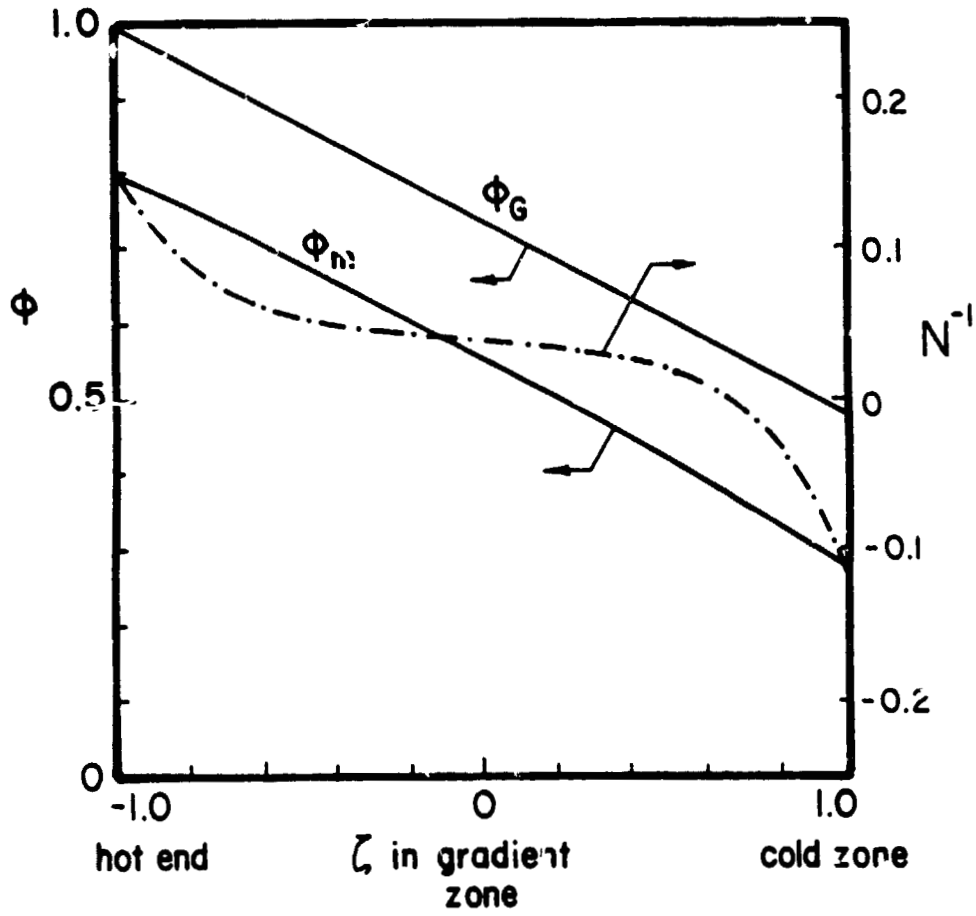

Fig. 4.20b. Analogous to Fig. 4.19b except a crucible is present; i.e., $\delta = 1.5$.

ORIGINAL PAGE IS
OF POOR QUALITY

TABLE 4.5

Description of the systems used in Figures 4.18, 4.19, and 4.20.

	Case		
	1	2	3
Figure	4.18	4.19	4.20
δ	1.0	1.0	1.5
λ_G	1.0	1.0	2.0
$Bi_H = Bi_C$	0.5	0.5	0.5
$Bi_H^{**} = Bi_C^{**}$	0.471	0.471	0.291
$d\theta_m/d\zeta$ moving fin model	-0.407	-0.289	-0.259
$\phi_G(\lambda_G/2)$ (eq. [4.39])	0.593	0.422	0.481
$\phi_G - \phi_m$ (eq. [4.40])	0.297	0.211	0.241
Bi_G^{**} (eq. [4.43])	0.0625	0.0625	0.0491
Bi_G	0.0625	0.0625	0.0735
ϕ_Δ	0.00127	0.000903	0.000811

Symmetric system except $\phi_G(\lambda_G/2) \neq 0$

$\lambda_H = \lambda_C = \infty$

Desired value of N is 20

ORIGINAL PAGE IS
OF POOR QUALITY

Figure 4.20, which considers a system similar to that of Fig. 4.19 except $\delta = 1.5$, demonstrates that the presence of a crucible is adequately accounted for in this procedure.

The procedure outlined in this section is not intended as a generalized design method leading to optimized heat transfer for a typical Bridgman growth system. Systems of practical interest do not behave as those in Figs. 4.18 to 4.20 due to the generation of radial temperature variations at the growth interface (c.f., section 4.3). Its intent, rather, is to accentuate three features concerning the radial temperature distribution in the charge:

(1) Heat transfer in the gradient zone is a useful tool for altering the interface shape in the gradient zone.

(2) Where appropriate, results from one-dimensional models can be used to help predict radial temperature variations in the charge. In the model developed in this section, ϵ . [4.38] is seen to provide at least order of magnitude accuracy.

(3) Generation of radial temperature variations at the interface ($R_K \neq 1$ and/or $Pe_S R_H \neq 0$) is detrimental for achieving a region about the interface which has a small and relatively constant isotherm curvature.

DISCUSSION OF THE TWO-DIMENSIONAL RESULTS

Radial temperature variations within the charge have been shown in section 4 to attenuate rapidly with axial distance from the location at which they are generated. This behavior permits the formulation of a thermal design criteria, leading to satisfactory interface shape, for systems in which radial temperature variations created at the interface are not present. In summary:

ORIGINAL PAGE IS
OF POOR QUALITY

The interface should be located in a gradient zone which is made approximately adiabatic through the use of a thermal insulating material (i.e., low k_G) placed between the hot and cold zones and radiation shields in the furnace cavity gap to decrease k_G. The gradient zone should be sufficiently long so that radial temperature gradients generated in the hot and cold zones have largely attenuated at the interface location; this length is approximately one to two charge diameters and depends on the effect of the crucible in reducing the rate of attenuation of these radial gradients (see section 4.2.2). The exact location of the interface within the gradient zone is chosen so that the shape of the interface is slightly curved toward the solid in order to inhibit the propogation of defects generated at the boundary crucible surface. Additionally, small amounts of heat transfer to the charge in the gradient zone can be used to alter the interface shape as desired, or to maintain a large axial region of nearly constant isotherm curvature (c.f., section 4.4.3).

The thermal design is complete at this stage if the axial temperature gradient in the melt at the interface is sufficiently large to satisfy the constitutionaly supercooling requirement. If the axial gradient is not sufficiently large, however, techniques to increase its value can be investigated while attempting to maintain satisfactory interface shape.

Radial temperature variations generated at the interface are, however, the dominant factor with regard to the interface shape. The procedure outlined above, therefore, does not lead to desirable interface shapes unless the interface effect can be eliminated. This issue is of particular importance for the growth of semiconductor materials which have values of R_K greater than unity; for such materials, the interface effect tends to produce an interface shape which is curved in the adverse direction, i.e., toward the melt.

ORIGINAL PAGE IS
OF POOR QUALITY

Counteracting the Effects of Radial Temperature Variations Generated at the Growth Interface

The analysis of section 4.1 suggests that heat transfer from the furnace to the charge tends to produce isotherm shapes which are concave toward the solid. Such heat transfer in the gradient zone thus serves to make the interface shape more favorable if it is originally concave toward the melt. The gradient zone, in such a case, resembles an extension of the hot zone furnace. The potential for completely eliminating an adverse interface curvature may be estimated by comparing the value of ϕ_Δ produced at the interface due to the interface effect (eq. [4.30]) to a representative value of ϕ_Δ caused by heat exchange with the furnace at the prevailing Biot numbers. The value of ϕ_Δ at the end of an adiabatic gradient zone (see section 4.2) may be used to estimate this latter value of ϕ_Δ. If radial temperature gradients caused by heat transfer to the charge are of comparable magnitude, or larger, than those generated due to the interface effect, such heat transfer in the gradient zone may prove useful in reversing an adverse interface curvature. If, on the other hand, radial temperature gradients caused by heat transfer to the charge are less than those generated at the interface, this technique can not be expected to change the direction of the shape of the interface.

A decrease in the value of δ likewise decreases the magnitude of the radial temperature gradients generated at the interface, as shown in Fig. 4.12. The value of δ can be decreased by either an increase in the charge diameter or by a decrease in the thickness of the crucible. A decrease in δ, while not eliminating the interface effect, may be useful in combination with heat transfer to the charge as described in the previous paragraph.

The ideal method of dealing with the interface effect is to eliminate it entirely. If this is possible, the design procedure for obtaining the desired interface shape, described in section 5, once again becomes useful. The cause of the interface effect is the change in the axial temperature gradient within the charge at the growth interface which is not present in the crucible. Efforts to eliminate the interface

ORIGINAL PAGE IS
OF POOR QUALITY

effect therefore must either (1) remove the change in axial gradient within the charge at the interface or (2) produce an equivalent change in axial gradient within the crucible.

Equation [4.26] suggests that the slope change at the interface disappears for an appropriate value of the lowering rate, V, when $R_K < 1$. The efficacy of this technique depends, however, on the interplay between the value of V required to eliminate the slope change at the interface and the effect of V on the constitutional supercooling requirement. Further, this technique is not applicable when $R_K > 1$.

The electron potentials are not equal in the solid and liquid portions of the charge. The passage of an electric current across the growth interface produces or absorbs heat (depending on the direction of the current) by virtue of the Peltier effect. Such heat can be used to eliminate the change in axial temperature gradient at the interface caused by the change in thermal conductivity and the liberation of latent heat. Further, this technique also counteracts the decrease in the axial temperature gradient in the liquid at the interface which occurs when $R_K > 1$. Rewriting the heat balance at the interface in order to include Peltier heating/cooling yields:

$$(R_K - 1)G_L = Pe_s R_H + \frac{S_e T_i i'' D}{k_s (T_{f,} - T_{f,c})} \qquad [5.1]$$

where: $G_L = G_S$ in order to eliminate the slope change at the interface

S_e = Seebeck coefficient

I'' = current per unit cross sectional area

$S_e T_I I''$ = rate of generation of Peltier heat per unit cross sectional area

T_I = absolute solidification temperature

Using germanium as an example (S_e = 70 μV/K, T_I = 1211 K), eq. [5.1] shows that the required current density is in excess of 200 amps/cm^2 for typical operating conditions. Such large current densities may be difficult to attain experimentally and may produce significant Joule heating

ORIGINAL PAGE IS
OF POOR QUALITY

effects. Although each case should be examined individually, it appears that Peltier heating is not a viable method for eliminating the slope change at the interface.

Peltier heating/cooling has, however, greater potential for modifying the interface shape in small amounts. For example, a flat interface shape may be made slighity concave toward the solid by the application of a small amount of Peltier cooling. This technique yields a similar result as that of transferring small amounts of heat to the charge in the gradient zone as described in section 4.4.3.

The interface effect may also be eliminated by producing a slope change in the crucible at the interface which is equal to that in the charge. This may be done by adding the appropriate amount of heat to the crucible in a very narrow region near the axial location of the interface. The remainder of the gradient zone may be adiabatic if desired. A thin crucible, being to a greater extent thermally one-dimensional than a thicker crucible, is more desirable in this respect.

Recommendation For Further Research

This work considers furnace boundary conditions as an independent variable which, in combination with the other system parameters, determines the interface shape. It would be useful, however, to be able to solve the inverse problem. I.e., what must the furnace boundary conditions be in order to produce a desired interface shape? There may be multiple solutions or no solution at all. In the first case, such results would provide a direct indication of the thermal design required for satisfactory interface shape; in the second case, the knowledge that no set of furnace boundary conditions exists which can produce the desired interface shape indicates that other parameters of the growth system require alteration. The ability to make such conclusions requires a computer solution of the appropriately modeled inverse heat transfer problem.

The harmful consequences of the interface effect for semiconductor crystal growth warrant an independent experimental investigation. Growth experiments utilizing variable thickness and thermal conductivity of the crucible and thermal conductivity ratios of the charge (metals for $R_K < 1$ and semiconductors for $R_K > 1$) will provide results for comparison with the analysis of section 4.3.

The technique presently considered most suitable for counteracting the interface effect is that of locally heating the crucible near the interface in combination with a thin crucible. Analysis is first required in order to verify the potential of this method. The relationship between the thickness of the crucible and the amount and distribution of heat transfer to the surface of the crucible to the radial gradients generated in the charge will require the solution of an appropriate two-dimensional thermal model. Thin crucibles are expected to require less heat transfer compared to thicker crucibles in order to eliminate the interface effect. Thin crucibles of sufficient structural strength may be obtained through the use of a metallic crucible; a uniform and chemically inert interior coating, able to withstand stresses created by differential thermal expansion, remains problematic.

ORIGINAL PAGE IS
OF POOR QUALITY

ORIGINAL PAGE IS
OF POOR QUALITY

REFERENCES

1. Carslaw, H. S., and Jaeger, J. C., "Conduction of Heat in Solids", 2nd ed., Oxford University Press, Amen House, London (1959).

2. Boyce, W. E., and DiPrima, R. C., "Elementary Differential Equations and Boundary Value Problems", 2nd ed., Wiley, N.Y. (1969).

3. Ogata, K., "Modern Control Engineering", Prentice-Hall, Englewood Cliffs, N.J., (1970).

4. Rohsenow, W. M., and Choi, H. Y., "Heat, Mass and Momentum Transfer", Prentice-Hall, 1st ed., Englewood Cliffs, New Jersey (1961).

5. Chang, C. E., and Wilcox, W. R., J. Crystal Growth 21, 135 (1974).

6. Fu, T.-W., and Wilcox, W. R., J. Crystal Growth 48, 416 (1980).

ORIGINAL PAGE IS
OF POOR QUALITY

APPENDIX A: DEVELOPMENT OF THE FIN EQUATIONS FOR THE TWO-DIMENSIONAL THERMAL MODEL

With the assumptions of Section 3.2, each of the concentrically located fins (i.e., inner charge, outer charge, crucible, gradient zone annulus) can be considered as a moving fin. According to Carslaw and Jaegar [1], the axial temperature distribution for the fins in the hot and cold zones is given by the following equations:

$$k_{loc} A_{in} \frac{d^2T_{in}}{dZ^2} - A_{in} V \rho c_p \frac{dT_{in}}{dZ} + \frac{T_{out} - T_{in}}{R_{in,out}} = 0 \qquad [A.1a]$$

$$k_{loc} A_{out} \frac{d^2T_{out}}{dZ^2} - A_{out} V \rho c_p \frac{dT_{out}}{dZ} + \frac{T_{in} - T_{out}}{R_{in,out}} + \frac{T_{cr} - T_{out}}{R_{out,cr}} = 0 \qquad [A.1b]$$

$$k_{cr} A_{cr} \frac{d^2T_{cr}}{dZ^2} - V(A \rho c_p)_{cr} \frac{dT_{cr}}{dZ} + \frac{T_{out} - T_{cr}}{R_{out,cr}} + \frac{T_f - T_{cr}}{R_{cr,f}} = 0 \qquad [A.1c]$$

where: A = cross sectional area of a fin
R = thermal resistance per unit length between fins

subscripts:

loc = local charge phase, liquid or solid
in = inner charge fin
out = outer charge fin
cr = crucible
f = hot or cold zone furnace

ORIGINAL PAGE IS
OF POOR QUALITY

When considering the fins within the gradient zone, T_f and $R_{cr,f}$ in eq. [A.1c] change to T_G and $R_{cr,G}$, the subscript "G" denoting the gradient zone annulus. Further, there is an additional equation representing the gradient zone annulus:

$$k_G A_G \frac{d^2 T_G}{dz^2} + \frac{T_{cr} - T_G}{R_{cr,G}} = 0 \qquad [A.1d]$$

The radial geometry of the concentric fins shown in Fig. 3.2 specifies the cross sectional areas and thermal resistances in eqs. [A.1]. The cross section areas A_{in} and A_{out} are chosen equal; therefore, $D_{in} = D/\sqrt{2}$. The radial locations for the representative temperatures of the fins are $D_1/2$, $D_2/2$ and $D_3/2$ for the inner and outer charge fins and crucible fin respectively; they are chosen so that there is an equal area within the fin to either side:

$$D_1 = \sqrt{}/2 \qquad [A.2a]$$

$$D_2 = \sqrt{3/4}\ D \qquad [A.2b]$$

$$D_3 = \left[(\delta^2+1)/2\right]^{1/2} D \qquad [A.2c]$$

The thermal resistances can then be expressed as (Rohsenow and Choi [4]):

$$R_{in,out} = \frac{\ln\sqrt{3}}{2\pi k_{loc}} \qquad [A.3a]$$

$$R_{out,cr} = \frac{\ln\sqrt{\frac{4}{3}}}{2\pi k_{loc}} + \frac{\ln\left(\frac{\delta^2+1}{2}\right)^{1/2}}{2\pi k_{cr}} \qquad [A.3b]$$

ORIGINAL PAGE IS
OF POOR QUALITY

$$R_{cr,F} = R_{cr,G} = \frac{\ln\left(\frac{}{1\ \delta^{-2}}\right)^{1/2}}{2\pi k_{cr}} + \frac{1}{h_{1oc}\pi D_{cr}} \qquad [A.3c]$$

where: $\delta = D_{cr}/D$

h_{1oc} = heat transfer coefficient from furnace or gradient zone annulus to the surface of the crucible, based on the outer diameter of the crucible

Substituting eqs. [A.2] into eqs. into eqs. [A.1] and non-dimensionalizing the resultant expression yields eqs. [3.2] and [3.3].

ORIGINAL PAGE IS
OF POOR QUALITY

APPENDIX B: APPROXIMATE INTERFACE CURVATURE

This appendix employs simple approximations in order to develop a useful relation between isotherm curvature and the axial and radial temperature gradients obtained from one- and two-dimensional thermal models.

An isotherm within the charge is assumed to be spherical; its shape can then be represented by a single number -- its radius of curvature. The axial distance between the locations of an isotherm at the center and the surface of the charge is denoted by Z_ϕ. The assumed geometry, shown in Fig. B.1, yields the following relation between Z_ϕ and the isotherm curvature:

$$\frac{Z_\phi}{D} \equiv \zeta_\phi = -\frac{N-(N^2-1)^{1/2}}{2} \simeq -\frac{1}{4N} \quad (\text{for } |N| \gtrsim 3) \qquad [B.1]$$

where N is the radius of curvature of the isotherm in number of charge radii. Equation [B.1] yields a positive value of N when the isotherm is concave toward the solid as shown in Fig. B.1. If the axial gradient does not vary greatly over the cross section:

$$\zeta_\phi \simeq \frac{\phi_{sc}}{d\phi_m/d\zeta} \qquad [B.2]$$

where: $\phi_{sc} \equiv \phi(\zeta = 1/2) - \phi(\zeta = 0)$

Substituting eq. [B.2] into [B.1]:

$$N \simeq -\frac{1}{4}\,\frac{d\phi_m/d\zeta}{\phi_{sc}} \qquad [B.3]$$

For the purpose of relating ϕ_{sc} to ϕ_Δ, the heat conduction equation within the charge is used:

ORIGINAL PAGE IS
OF POOR QUALITY

$$\frac{1}{\rho}\frac{\partial}{\partial \rho}\left(\rho \frac{\partial \phi}{\partial \rho}\right) + \frac{\partial^2 \phi}{\partial \zeta^2} - Pe \frac{\partial \phi}{\partial \zeta} = 0 \qquad [B.4]$$

If the Pe term is neglected and if it is assumed that $\partial^2\phi/\partial\zeta^2$ is not a function of ρ, the resulting temperature distribution in the radial direction is parabolic. In this case, it is easily shown that:

$$\phi_\Delta = \tfrac{1}{4}\,\phi_{sc} \qquad [B.5]$$

Using eq. [B.5] in eq. [B.3]:

$$N \simeq -\frac{1}{16}\,\frac{d\phi_m/d\zeta}{\phi_\Delta} \qquad [B.6]$$

Equation [B.6] indicates that isotherm curvature is small (i.e., large N) when the axial temperature gradient is large as well as when the radial temperature gradients are small.

ORIGINAL PAGE IS
OF POOR QUALITY

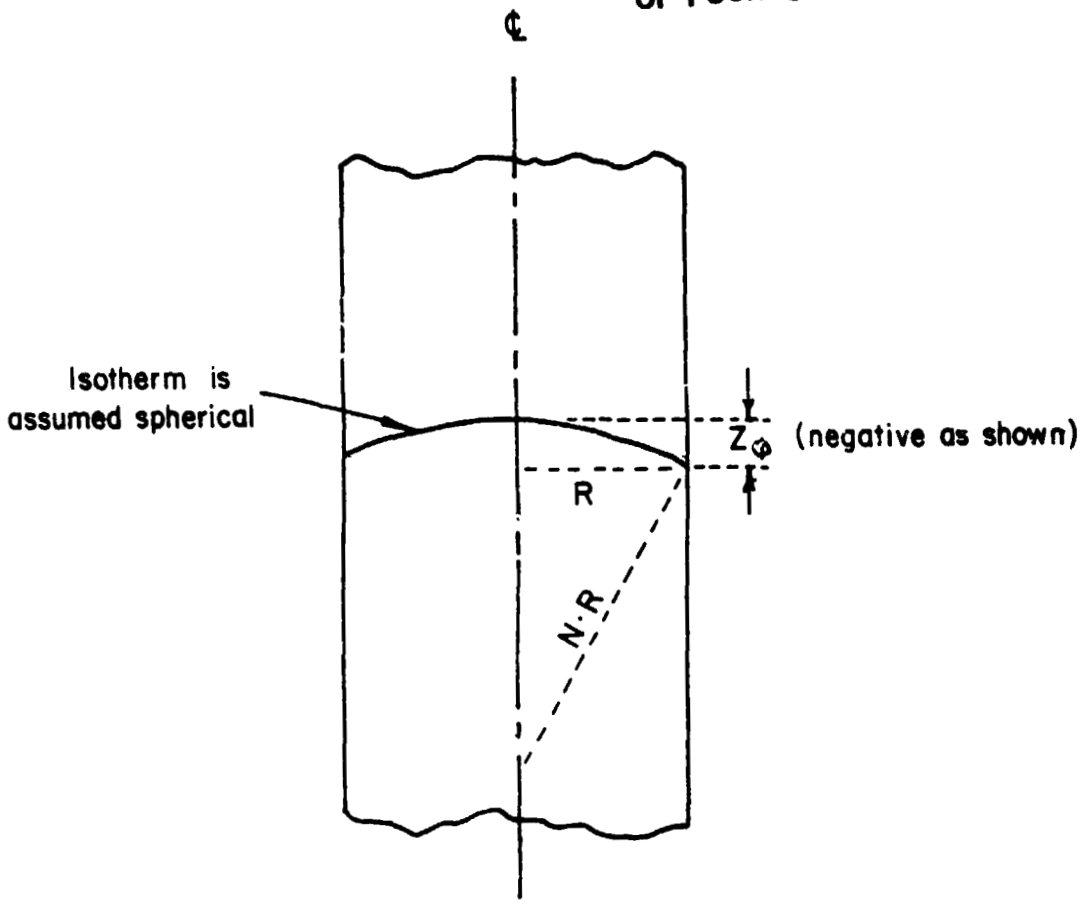

Fig. B.1. Assumed geometry used to calculate an approximate isotherm curvature. N is positive for the isotherm curvature shown above.

ORIGINAL PAGE IS
OF POOR QUALITY

II. EXPERIMENTAL DETERMINATION OF THE PELTIER COEFFICIENT OF InSb IN CONTACT WITH ITS MELT

The developed theoretical framework presented in the last report has been used in conjunction with experimental results (current-induced growth layer thickness data) to calculate the Peltier coefficient of doped InSb in contact with its melt. Estimates were made of the error resulting from time dependent geometry ($A \neq \pi(D/4)^2$, $D = f(t)$), and composition. The Peltier coefficient thus obtained was compared with those calculated from published Seebeck coefficients (thermoelectric power); agreement is found to be excellent.

PROCEDURE AND RESULTS

The Peltier coefficient is calculated using equation [1]:

$$\pi = \frac{\rho H (R_1 - R_2)}{J} \qquad [1]$$

and values of R_1 and R_2 obtained from the layer thickness and the temporal characteristics of the current pulses:

$$R_i = \frac{X_i}{t_i} \qquad [2]$$

where: X_i = layer thickness (current-on or current-off)
t_i = duration (current-on or current-off)

The Peltier coefficient, if determined by eq. [1] is directly dependent on the heat of fusion, H. The search for precise H data in the literature revealed values ranging from from [illegible] J/g to 213.4 J/g. Consequently, the heat of fusion of InSb was experimentally determined using a Perkin-Elmer DTA 1700 differential thermal analyzer with a Perkin-Elmer System 7/4 thermal analysis controller. Aluminum

ORIGINAL PAGE IS
OF POOR QUALITY

(H = 398.2 j/g) and antimony (H = 164.8 j/g) were used as calibration standards for the system. For a heating rate of 5°C/min, the data from the standards were reproducible and selfconsistent to ±2%. The heat of fusion for undoped semiconductor grade InSb was measured to be 238.1 ±6 j/g (13.48 kcal/mol). The crystal diameter data needed to determine the current density were obtained using a precision micrometer stage mounted on a Nomarski interference contrast microscope (with integral cross-hairs). The measurements were made on polished and etched samples normal to the growth direction.

It was found that crucible design and the location of the control thermocouple have profound influences on the characteristics of growth layers produced by passing pulses of direct current across the crystal/melt interface during growth. The effect of Joule heating in the hot zone on growth layer characteristics varied from extensive to almost non-existent (manuscript in preparation).

The Peltier coefficient of InSb was calculated from the dimensions of contiguous current-induced growth layers. Representative growth layer thickness data, illustrating the effect of various crucible designs and temperature control schemes, are shown in Figs. 1, 2 and 3. Also shown are the calculated Peltier coefficients. Defining the error associated with each set of data as the standard deviation divided by the arithmetic average expressed as a percentage, it is seen (Fig. 1) that even though the measured layer thickness varies by more than 60%, the calculated Peltier coefficient (-0.082 V) has a precision of better than ±12% For conditions of current pulsing with temperature control from the base of the crucible (Fig. 2), where the layer thickness varied by more than 77%, the average calculated Peltier coefficient is found to be -0.084 V (±7.8%). The Peltier coefficient calculated from growth layer thicknesses obtained using a special BN/composite crucible and current pulses of 19.8 A/cm^2 is -0.097 V (±3%) (see Fig. 3). This last result is from a series of current pulsing experiments with different current densities but otherwise identical configurations. Using 9.8 A/cm^2 current pulses, the average calculated Peltier coefficient is -0.097 V (±10%). The larger error associated with these data can be traced to an inability to

ORIGINAL PAGE IS
OF POOR QUALITY

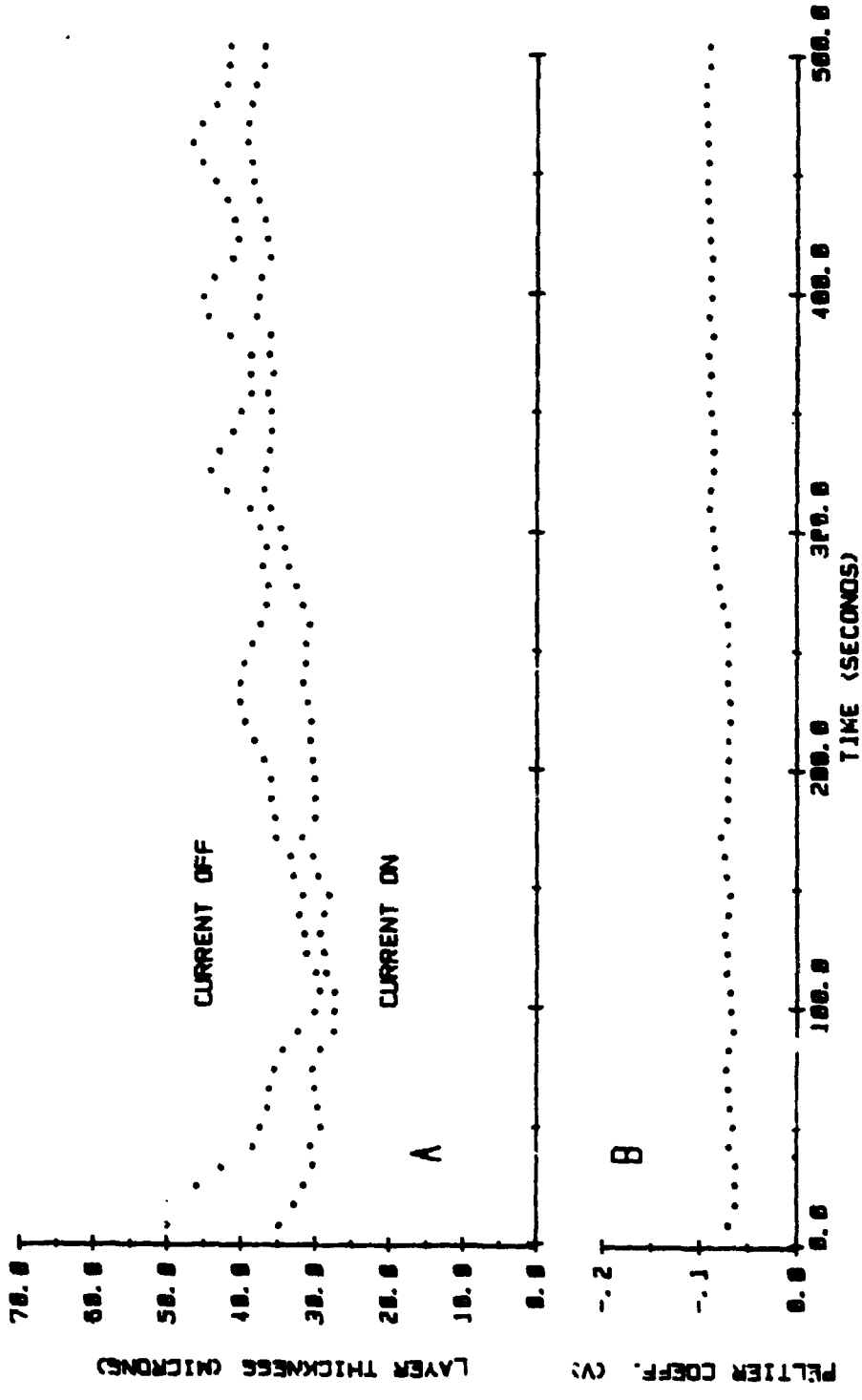

Figure 1. Growth with current pulses of short duration: graphite crucible, control thermocouple at heat pipe.
a) growth layer thickness
b) Peltier coefficient calculated from growth layer thickness

ORIGINAL PAGE IS
OF POOR QUALITY

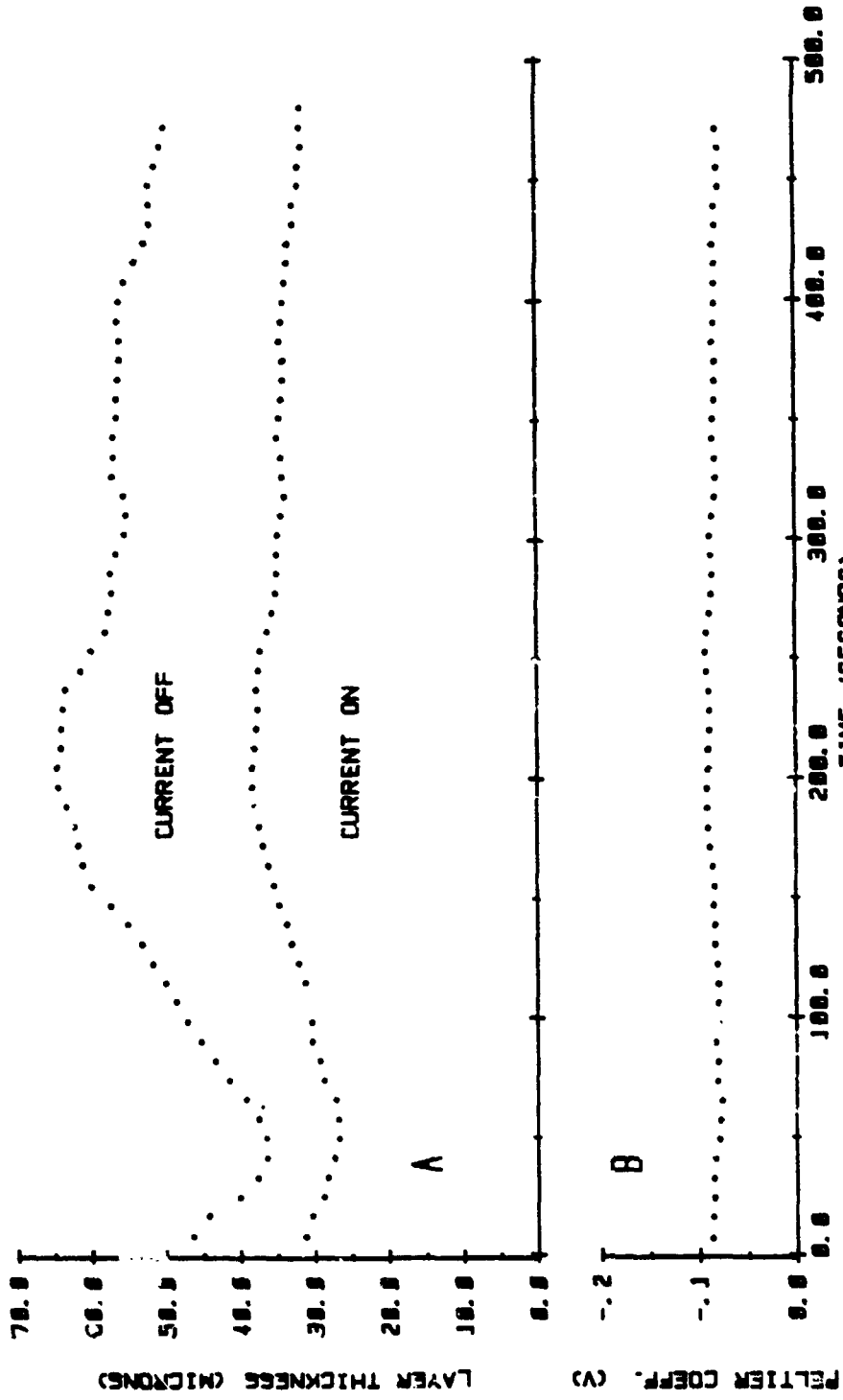

Figure 2. Growth with current pulses of short duration: graphite crucible, control thermocouple at base of the crucible.
a) growth layer thickness
b) Peltier coefficient calculated from growth layer thicknesses

ORIGINAL PAGE IS
OF POOR QUALITY

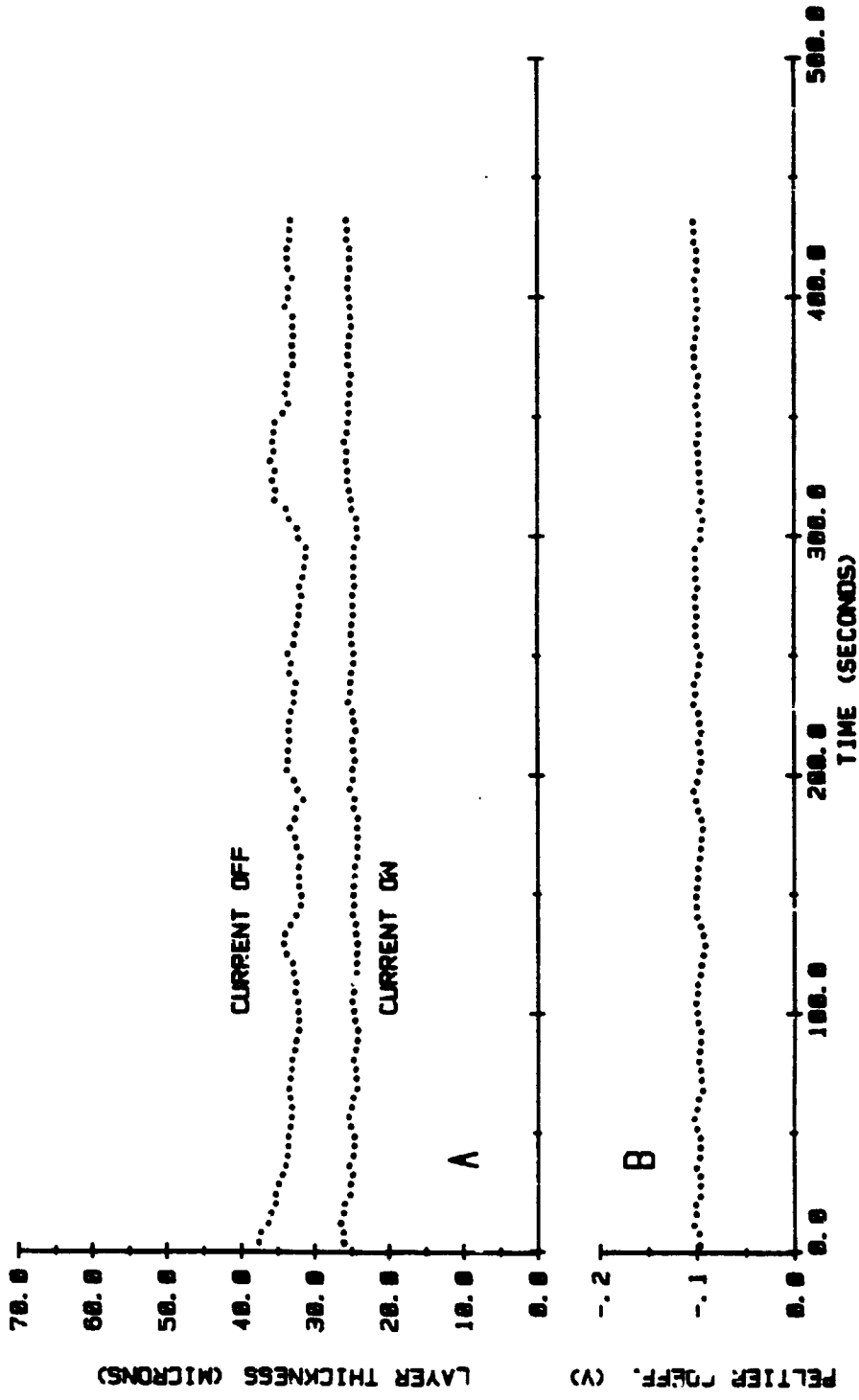

Figure 3. Growth with current pulses of short duration:
Bi-composite crucible, control thermocouple at heat pipe.
a) growth layer thickness
b) Peltier coefficient calculated from growth layer thicknesses

ORIGINAL PAGE IS
OF POOR QUALITY

duration (20s) this assumption is inaccurate and the overall layer thickness cannot be used as data to calculate π. However, interface demarcation superimposed on pulses of long duration permits the measurement of the interface velocity in the critical transition region (current-off to current-on) with a temporal resolution that is consistent with the constraints placed on the use of eq. [1] and such experiments are therefore expected to yield viable data for the determination of Peltier coefficients. The growth velocity changes that occur on the application of direct current for extended time periods were, therefore, also used to calculate the Peltier coefficient. The average Peltier coefficient calculated from three 9.5 A/cm^2 long duration current pulses was -0.1064 V ($\pm$6%). Two long growth layers produced by 17.3 A/cm^2 current pulses resulted in an average Peltier coefficient of -0.096 V ($\pm$2%). Long duration growth layers produced by Peltier heating also produced viable data for calculation of the Peltier coefficient. The average Peltier coefficient calculated from three -12.2 A/cm^2 (20s) layers was -0.113 V ($\pm$3%). The results are tabulated in Table 1.

ERROR ANALYSIS FOR THE EXPERIMENTALLY DETERMINED PELTIER COEFFICIENT

It should be pointed out that the area of the crystal/melt interface (even for 100% central facet) is not exactly related, through the physical constant $\pi/4$, to the width of the sample segment. Crystals grown in the [111] crystallographic direction exhibit threefold symmetry and related to it a varying degree of external faceting which prevents the system from assuming a cylindrical shape. The extent of external faceting can vary from near zero to 100% depending on the radial temperature gradient, growth rate acceleration and growth kinetics of the given system. For the case of minimal external faceting the relationship $A = (\pi/4)D^2$ (for the area of the crystal/melt interface) is a good approximation if the crystals are cut so as to contain the axis of rotation in the surface analyzed (as in this study). This relationship increasingly underestimates the area of the crystal cross section as the extent of external faceting approaches 100%. (For this exteme case, the external shape of the crystal would be triangular.) In effect, at 100% external faceting conditions, π assumes the value of $9/4(3)^{1/2} = 3.8971$ which is

ORIGINAL PAGE IS
OF POOR QUALITY

accurately measure the thickness of the growth layers produced by current pulses of such relatively low density. As a result of the small current-induced segregation change between growth layers, the differential chemical etching, used to reveal the growth layers, was insufficient to clearly delineate the current-on to current-off transition. For the reason cited above: greater precision in layer thickness measurements, growth layers produced from current pulses of 29.6 A/cm^2 led to a calculated Peltier coefficient of -0.099 V with a precision of $\pm 3\%$. In an experiment where current pulses of 39.7 A/cm^2 were used, the Peltier coefficient was found to be -0.087 V with a precision of $\pm 6\%$. An explanation for this relatively low value of the Peltier coefficient and the low precision (when compared with the other experiments in the series) is given below.

The Peltier coefficient is a materials property and as such expected to remain constant over the entire growth process and for various growth configurations. Conspicuous for these results is that the same Peltier coefficient is obtained although pulse duration, current density, dopant level and dopant type were varied. Moreover, the various experiments used as a basis for the calculations were conducted in different thermal configurations (i.e. with different crucible and temperature control configurations). This finding is taken as a confirmation of the validity and applicability of the theoretical framework. Furthermore, it indicates that, for the growth of (short time duration) current induced layers, the effect of bulk heat flow perturbations (Joule heating) can be separated from transient interface heat balance considerations (Peltier effect). Thus, the long term variation in layer thickness is controlled by the changing temperature gradients in the liquid and solid caused principally by transient bulk heat flows. On the other hand, the fundamental relationship between the dimensions of contiguous layers (layers generated by a pulse sequence) and the Peltier effect (i.e. eq. [1]) remains unchanged.

The basic premise for using eq. [1] to calculate the Peltier coefficient is that the interfacial temperature gradients remain virtually unchanged over a given pulse sequence. For direct current pulses of long

ORIGINAL PAGE IS
OF POOR QUALITY

TABLE 1

EXPERIMENTALLY DETERMINED VALUES OF THE PELTIER COEFFICIENT OF InSb

t_{on}/t_{off} (sec)	Dopant	Current Density (A/cm^2)	Peltier Coeff. (V)	Error (±%)
2/6	Te	16.8	-0.082	12
2/6	Te	13.0	-0.084	5
1/3	Ge	9.8	-0.097	10
1/3	Ge	19.8	-0.097	3
1/3	Ge	29.6	-0.099	3
1/3	Ge	39.7	-0.087	6
20/100	Ge	9.5	-0.106	5
20/100	Ge	17.3	-0.096	2
20/100	Ge	-12.2	-0.113	3

ORIGINAL PAGE IS
OF POOR QUALITY

an error in excess of 24%. InSb crystals have been grown exhibiting the full range of external faceting though those that reached 100% were highly susceptible to twinning. Those crystals from which current-induced growth data were taken were intermediate in external faceting. It is estimated that the areas obtained using the relationship for circular cross section are in error by less than 10%. An underestimation in area translates directly to an error in calculated current density and thus leads to a calcualted Peltier coefficient which is lower than the actual value.

Due to changes in meniscus height and/or perturbations in the bulk heat flow, the diameter of a growing crystal is time dependent in nature. In addition, the external morphology will change as the diameter assumes a new dimension. The concomittant changes in current density also appear as variations in the calculated Peltier coefficient. This is evident in the increased error associated with the data obtained from layers produced by 39.7 A/cm^2 pulses (Table I). In the related experiment the diameter is 1.12 cm at the beginning of the pulsing sequence. It is 1.19 cm at the end, an area increase of 11%. The calculated Peltier coefficient, when corrected for this change in diameter, is -0.097 V which is closer to the values (-0.097 V, -0.097 V, -0.099 V) calculated for the other current densities (9.8 A/cm^2, 19.8 A/cm^2, 29.6 A/cm^2 respectively) in that sequence of experiments.

The effect of meniscus height change on crystal diameter was investigated analytically using the expression of Bardsley et al[1]:

$$h = \left[\beta^2(1-\sin\theta_L) + \left(\frac{\beta\cos\theta_L}{4r}\right)^2\right]^{1/2} - \frac{\beta\cos\theta_L}{4r} \qquad [3]$$

where: h = meniscus height
r = crystal radius
$\beta = 2\sigma_{l,g}/\rho_l g$
$\sigma_{l,g}$ = surface tension
g = gravitational acceleration
θ_L = angle made to the vertical by the meniscus at the liquid/solid interface

ORIGINAL PAGE IS
OF POOR QUALITY

The derivative of eq. [3] with respect to r was evaluated to determine the change of meniscus height with respect to crystal radius:

$$\frac{dh}{dr} = -\left[\frac{\beta^2 \cos^4\theta_L}{256r^6\beta^{-1}(1-\sin\theta_L)+16r^4(1-\sin^2\theta_L)}\right] + \frac{\beta\cos\theta_L}{4r^2} \qquad [4]$$

For the representative values:

$$\beta = 0.21 \quad (\sigma = 600 \text{ erg/cm}^2)$$
$$\theta_L = 20^\circ$$
$$r = 0.50 \text{ cm}$$

the derivative gives dh/dr = -0.17 cm/cm. During the growth of 20 A/cm^2 layers (Fig. 3), the crystal radius was found to increase by 117 μm. Thus, according to the above expression (eq. [4]), the meniscus should decrease by 20 μm. The net interface displacement calculated from the initial layer thickness transient is 24 μm. Considering the inherent error in calculating the steady state pull rate (including melt height drop) and the uncertainty in the values of β and θ_L the agreement between the calculated and experimentally determined values of the interface displacement is remarkable but may be fortuitous.

COMPARISON OF THE EXPERIMENTALLY DETERMINED PELTIER COEFFICIENT WITH THOSE CALCULATED FROM THE PUBLISHED SEEBECK COEFFICIENTS: DEPENDENCE ON DOPANT TYPE AND DOPANT LEVEL

The Peltier coefficient can be directly calculated from the measured thermoelectric power (Seebeck effect) using the Kelvin relations[2]. The Peltier coefficient is related to the Seebeck coefficient by the absolute temperature:

$$\pi(T) = \alpha(T)T \qquad [5]$$

where α is the Seebeck coefficient. The Seebeck coefficient, as measured by various investigators, is tabulated in Table 2. Though not all

ORIGINAL PAGE IS
OF POOR QUALITY

measurements were made at the melting point it has been shown both theoretically and experimentally that the thermoelectric power of InSb is a very weak function of temperature and is independent of doping level and type at high temperatures[3,4]. The value of π calculated is the difference in the Peltier coefficients of the liquid and solid at the melting point:

$$\pi_{l/s} = (\alpha_s - \alpha_l) T_m \qquad [6]$$

For all calculations the Seebeck coefficient for liquid InSb was taken to be -40 $\mu V/^{o}K$[5] (except Blum and Ryabtsova[6] who give the difference, $\alpha_s - \alpha_l$). The experimentally determined values of $\pi_{l/s}$ (Table 1) are in excellent agreement with those listed in Table 2.

CONCLUSIONS

It has been shown that the Peltier coefficient of semiconductor/melt systems can be calculated directly from the dimensions of contiguous pairs of current-induced growth layers. This technique is applicable to systems which (1) exhibit high resolution differential chemical etching behavior or (2) permit measurement of the thickness of current-induced layers (eg. high spatial resolution measurement of changes in dopant distribution caused by the current pulses). It should be noted that the InSb/melt system is optimized with respect to the boundary conditions and assumptions of this analysis, namely, the heat absorbed at the crystal/melt interface due to the Peltier effect is of the same order as the heat released as a result of solidification (i.e. heat of fusion). In this way, the effect of the current pulses was to produce a substantial change in the microscopic rate of growth for that portion of the duty cycle when the current was on. This permitted the accurate determination of the Peltier coefficient since it was directly proportional to the difference in the rate of growth current-on/current-off. For other systems, it will be necessary to choose an impressed pulling rate and current density that are commensurate with this condition. The assumption of constant rates of growth during both portions of the pulsing sequence should be verified through superimposed interface demarcation.

ORIGINAL PAGE IS
OF POOR QUALITY

TABLE 2

PELTIER COEFFICIENT OF InSb CALCULATED FROM PUBLISHED VALUES OF THE SEEBECK COEFFICIENT

Investigator	Seebeck Coeff. ($\mu V/^{o}K$)	Peltier Coeff. (V)
Rose et al[2]	-130 ($773^{o}K$)	-0.071a
Glazov (s)[5]	-150 ($798^{o}K$)	-0.0878
Glazov (l)[5]	-40 ($803^{o}K$)	
Tauc[3]	-150 ($750^{o}K$)	-0.0878
Ehrenreich (calc.)[4]	-160 ($750^{o}K$)	-0.0958
Blum and Ryabtsova (s/i)[6]	-235 ($798^{o}K$)	-0.1875

ORIGINAL PAGE IS
OF POOR QUALITY

REFERENCES

1. W. Bardsley, F.C. Frank, G.W. Green and D.T.J. Hurle, J. Cryst. Growth 232, 341 (1974).

2. R.M. Rose, L.A. Shepard and J. Wulff, The Structure and Properties of Materials Vol. IV, John Wiley and Sons, Inc., New York, 168 (1966).

3. J. Tauc, In: Photo and Thermoelectric Effects in Semiconductors, International Series of Monographs on Semiconductors Vol. 2, Pergamon Press, New York, 49 (1962).

4. H. Ehrenreich, J. Phys. Chem. Solids 9, 129 (1959).

5. V.M. Glazov et al., op. cit., 323.

6. A.I. Blum and G.P. Ryabtsova, Sov. Phys. Solid State 5, 692 (1959).

III. COMPUTER OPERATED BRIDGMAN GROWTH SYSTEM WITH GRADIENT CONTROL ZONE

ORIGINAL PAGE IS OF POOR QUALITY

A Bridgman-Stockbarger crystal growth system which allows for controlled heat transfer during crystal growth has been designed and constructed. It consists of two vertically aligned Na-filled heat pipes separated by a gradient control region which is variable in length as well as composition. The furnace operating temperature range is 500°C to 600°C in vacuum and inert gas atmospheres, excluding hydrogen. The furnace can accommodate crucible sizes of up to 1.9 cm diameter and 46 cm in length.

Two dc servo motors controlled by a standard closed-loop servo system provide for crucible lowering/raising and rotation functions. An optical encoder on the motor shaft allows the crucible position to be monitored at all times. Crucible lowering rates can be varied from 0.036 cm/hr to 180 cm/hr using a gear reduction from 171 to 171,000; crucible rotation can be varied from 0.05 rpm to 30 rpm. All motor functions controlling lowering/raising are digitally interfaced.

DIGITAL TEMPERATURE CONTROLLER

The temperature control function of the two independently operated heat pipes is performed digitally. Although there is some degradation in the monitoring signal (temperature in millivolts) because of inherent sampling effects, there are significant advantages to digital control which include the greater range of compensators and time varying control functions.

The first step in the design of the compensator involved the formulation of a model of the open-loop system performance, i.e., relating the measurable outputs to the variable inputs. The temperature of the heat pipe is related to the power input by a first-order differential equation:

ORIGINAL PAGE IS
OF POOR QUALITY

$$\frac{dT}{dt} = \frac{Q}{C} + \frac{T_a - T}{RC}$$

where: T = temperature
T_a = ambient temperature
Q = power (in Watts)
R = overall furnace resistance (°C/Watt)
c = overall furnace capacitance (Watt·sec/°C)
t = time

The controller could then be designed according to the following control specifications:

(1) No steady state error to step inputs of power;
(2) No overshoot (undershoot);
(3) Temperature settles in <500 secs.

A P-I (proportional and integral) compensator was designed in the continuous time domain:

$$K(s) = \frac{K_p(s + K_i)}{K_p}$$

$$K_p > \frac{8RC - t_s}{t_s R}$$

and

$$K_i < \frac{(K_p R + 1)^2}{4R^2 K_p C}$$

where t_s is the desired settling time.

In this manner the control variables, K_p and K_i, could be calculated based on the furnace parameters and control requirements.

Characterization of the furnace parameters R and C was done by measuring the static and dynamic open-loop system response of temperature for step inputs of power.

ORIGINAL PAGE IS
OF POOR QUALITY

Experiments revealed that (a) the heating efficiency is greatest for vacuum and deteriorates as the inert atmosphere changes from argon to helium because heat losses increase by conduction and (b) the system time constant decreases as the atmosphere changes from vacuum to argon to helium.

Since the compensator is implemented digitally, it must be discrete as well as the temperature input to the controller. A 16 bit A/D converter with a theoretical temperature resolution of $\pm 0.04^{o}C$ for a chromel/alumel thermocouple is used to sample the furnace temperature. Discrete representation of the controller is achieved by using the bilinear transformation:

$$M(nT) = M[(n-1)T] + E(nT)\left[K_p + \frac{K_p K_i T}{2}\right] + E[(n-1)T]\left[-K_p + \frac{K_p K_i T}{2}\right]$$

where:
- M = control response, i.e., power input
- E = error = temperature set point temperature
- T = sampling time
- n = present time step
- (n-1) = one time step previous

The output from the computer is discrete and is reconstructed to give a continuous output to the furnace using a D/A converter. The functional block diagram of the closed-loop system is:

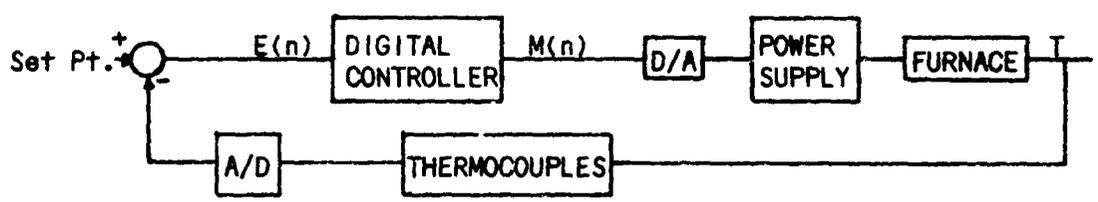

During the control loop, five thermocouples can be monitored, the point reference is timed digitally and power is measured at each time step.

CHARACTERIZATION OF THERMAL BEHAVIOR

Furnace characterization for determination of the temperature distribution in the heat pipe regions and gradient reigon has been initiated. The temperature was measured along the central axis of a graphite rod completely filling the heat pipe cavity. Measurements were made for vacuum (400-600 μm), argon and helium with $T_H = T_C = 600^oC$ and a gradient region length of 2D (D = diameter of graphite = 0.75"). The material used for the gradient region was an insulating, low density Al_2O_3 cylinder. The measurements show that within the top heat pipe, as anticipated, the graphite rod is about 65% isothermal. Near the top, the temperature decreases because of heat losses to the surroundings; the temperature decrease is greatest for helium and smallest for vacuum. In the lower heat pipe there is a significant drop in temperature toward its lower end. For helium only about 45% of the cavity length is isothermal; for argon and vacuum, the temperature decrease extends from top to bottom. The non-isothermal behavior orginates in (a) the heat losses at the end of the graphite and in (b) the reduced thermal coupling of the heat pipe to the graphite in lower conducting atmospheres. In the gradient region the temperature drops off about 6^o, indicating radial heat losses to a non-ideal insulator.

Characterization of the thermal behavior of the furnace cavity is being continued iteratively making use of the two-dimensional heat transfer model so as to arrive at an optimized configuration for the gradient control region.

IV. MAGNETIC FIELD ASSISTED MELT STABILIZATION IN VERTICAL BRIDGMAN GROWTH

SUMMARY

Making use of the prototype ASTP multipurpose furnace, the effects of transverse magnetic fields of up to 3.8 kGauss on macro- and microsegregation was investigated during growth of Ga-doped germanium. This particular system was selected for the study since it permitted a comparative analysis with results obtained during growth in a reduced gravity environment.

It was found that the macrosegregation behavior for the same cooling rate as used in the space experiment was significantly different and was, in fact, similar to that observed for regular ground based growth experiments. The results indicate clearly that while transverse magnetic fields will suppress turbulent convection, they will not result in diffusion controlled segregation during vertical Bridgman growth.

The microsegregation behavior in the presence of a magnetic field is of interest insofar as current induced interface demarcation generates distinct magnetic field induced segregation anomalies which are normally not encountered. While no comprehensive analysis of this effect has thus far been conducted, there are strong indications that the electric field induced perturbations of segregation can provide details concerning the solute boundary layer characteristics for magnetic field assisted growth.

Evidence was found for a reduction in the degree of radial segregation asymmetry. This finding is of interest since the change in radial segregation was not associated with a measurable change in growth interface morphology. It suggests that the convective melt flow pattern, rather than the growth interface morphology, controls radial segregation, and that the melt flow pattern changed with the application of the external magnetic field.

ORIGINAL PAGE IS
OF POOR QUALITY

PUBLICATIONS

THESES:

1. T. Jasinski, "Thermal Analysis of the Vertical Bridgman Semiconductor Crystal Growth Technique", Ph.D. Thesis, Department of Mechanical Engineering, MIT, December 1982.

2. H. Herring, "Magnetic Field Assisted Melt Stabilization in Vertical Bridgman Growth", Masters Thesis, Department of Materials Science and Engineering, MIT, February 1983.

OPEN LITERATURE:

1. C. A. Wang, J. R. Carruthers and A. F. Witt, "Growth Rate Dependence of the Interface Distribution Coefficient in the System Ge-Ga", J. Crystal Growth 60 (1982), 144.

2. T. Jasinski, W. M. Rohsenow and A. F. Witt, "Heat Transfer Analysis of the Bridgman-Stockbarger Configuration for Crystal Growth, Part I: Analytical Treatment of the Axial Temperature Profile", J. Crystal Growth (in print).

3. E. D. Bourret, J. J. Favier and A. F. Witt, "Segregation During Directional Melting and its Implications on Seeded Crystal Growth: A Theoretical Analysis", J. Crystal Growth (in print).

4. T. Jasinski, W. M. Ronsenow and A. F. Witt, "Heat Transfer Analysis of the Bridgman-Stockbarger Configuration for Crystal Growth, Part II: Analytical Treatment of the Radial Temperature Distribution", in preparation for J. Crystal Growth.

5. M. J. Wargo and A. F. Witt, "Determination of the Peltier Coefficient From Current Induced Growth Layers: InSb/Melt", in preparation for J. Crystal Growth.

6. E. D. Bourret and A. F. Witt, "Basic Factors Controlling Seeded Melt Growth of Concentrated Alloys", in preparation for J. Crystal Growth.

7. C. A. Wang, J. R. Carruthers and A. F. Witt, "Crystal Growth Behavior in Vertical Bridgman Configuration", in preparation for J. Crystal Growth.

STAFF ENGAGED IN THIS RESEARCH PROGRAM

Principal Investigator:	August F. Witt
Co-Principal Investigator:	Warren M. Rohsenow
Post-Doctoral Associate:	Michael J. Wargo
Engineering Assistant:	Clifford J. Herman
Technician:	Joseph P. DiMaria
Graduate Students:	Hamlet H. Herring, III
	Thomas J. Jasinski
	Christine A. Wang
Secretary:	Gloria Landahl

ORIGINAL PAGE IS
OF POOR QUALITY

Fluid Flow in Crystal Growth: Analysis of the Floating Zone Process

Principal Investigator: Robert A. Brown

SUMMARY

This research program is aimed at a fundamental understanding of the interactions of heat, mass and momentum transport in crystal growth from the melt. Emphasis has been on studies of the small-scale floating zone process and on a prototype of the vertical Bridgman growth system. In both systems detailed numerical calculations have been used to disect the interplay between fluid convection and dopant segregation. Calculations are based on newly developed finite-element techniques that make feasible the complete solution of solidification problems that include convection in the melt, and on computer-implemented perturbation analysis of solution multiplicity and stability. These numerical methods have also been successfully extended to include the interactions between a melt/gas meniscus with heat transfer in meniscus-defined crystal growth systems and to model the transition to a cellular morphology in a solidification interface.

1. Scope of Research Program

Our research is composed of a set of theoretical and computational studies directed at a fundamental understanding of the interactions of fluid mechanics and heat and mass transport in crystal growth from the melt, especially by the vertical Bridgman and floating zone process.

ORIGINAL PAGE IS
OF POOR QUALITY

The techniques for analysis and the quantitative insights developed in this research have broad application in a variety of melt growth systems (see list of Publications at the end of this report) and have made it possible to model Bridgman-Stockbarger and floating zone systems that are being used in ground-based experimental studies. Combining our detailed models with careful experiments hopefully will lead to quantitative pictures of the transport phenomena in each growth system and to well controlled space experiments.

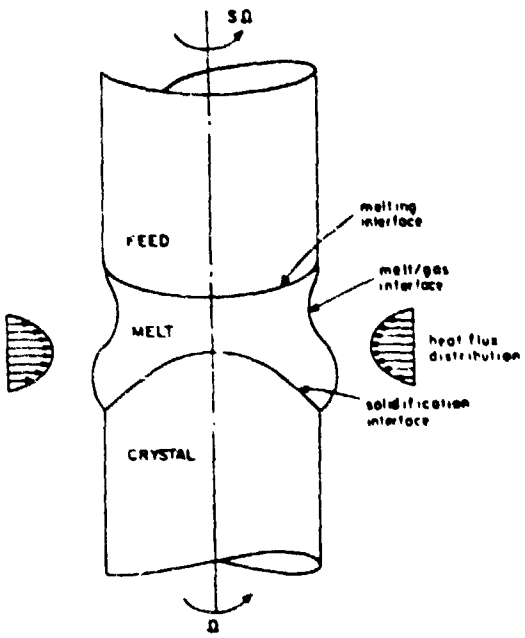

Figure 1:
Schematic of Floating Zone Process.

Modelling of a melt crystal growth system is a formidable task. Most of the complications are seen by considering the floating zone process presented schematically in Fig. 1. Here a cylindrical rod of a multi-component and polycyrstalline material is melted and re-solidified into a single crystal by using a short circumferential heater (either resistance or RF) that translates slowly along the axis of the rod. The molten zone forms between the crystal and feed rods and is held in place by surface tension. Its size is governed by heat transfer and limited by instabilities that originate at the melt/gas meniscus. In practice on earth, the radius of the rods and the height of the zone are nearly equal and range roughly be-

tween 0.5 and 3 centimeters. A quantitative understanding of the physics of a small-scale floating zone process requires analysis of the couplings between the convection in the melt, the heat transfer in melt, crystal and surroundings, the shapes of the melt/solid and melt/gas interfaces and the transport of solutes in the melt.

Our first approach toward understanding these interactions has been to decouple them along lines dictated by the physics of typical semiconductor growth systems; the separations used here are shown on Figure 2 where the numbers in parenthesis refer to publications listed on page 3. In the first three years of NASA support, research projects have focused on analysis of heat transfer in growth systems with melt/solid and melt/gas interfaces, on the convection in melt growth driven by crystal rotation, buoyancy and surface tension differences and on solute segregation caused by these flows.

In each research project, a combination of analytical modelling and computer-aided calculations is being used to develop both a qualitative understanding of the relevant physics and quantitative models of the vertical Bridgman and floating zone processes. To do this, state-of-the-art numerical methods have been developed for handling solidification problems and for studying the multiplicity of flow fields in nonlinear convection problems. These methods give us the capability of accurate calculations of the flow field and mass transfer near the solidification interface. This ability has been demonstrated through analyses of the effects of melt/solid interface shape and natural convection on radial segregation in a prototype of the vertical Bridgman system [7-8] and by a study of the evolution of a microscopic cellular morphology at a solidification interface [12-13]. Both studies are highlighted below.

The Bridgman calculations will be compared directly to experimental results gathered in the new vertical Bridgman system under construction in A.F. Witt's research group at M.I.T. This collaboration promises the first detailed comparison between the modelling of convection in melt growth and experimental segregation results. Similar calculations are underway for small-scale floating zone system and we hope to compare these to experiments that are being carried out at Westec Corporation in Pheonix.

ORIGINAL PAGE IS
OF POOR QUALITY

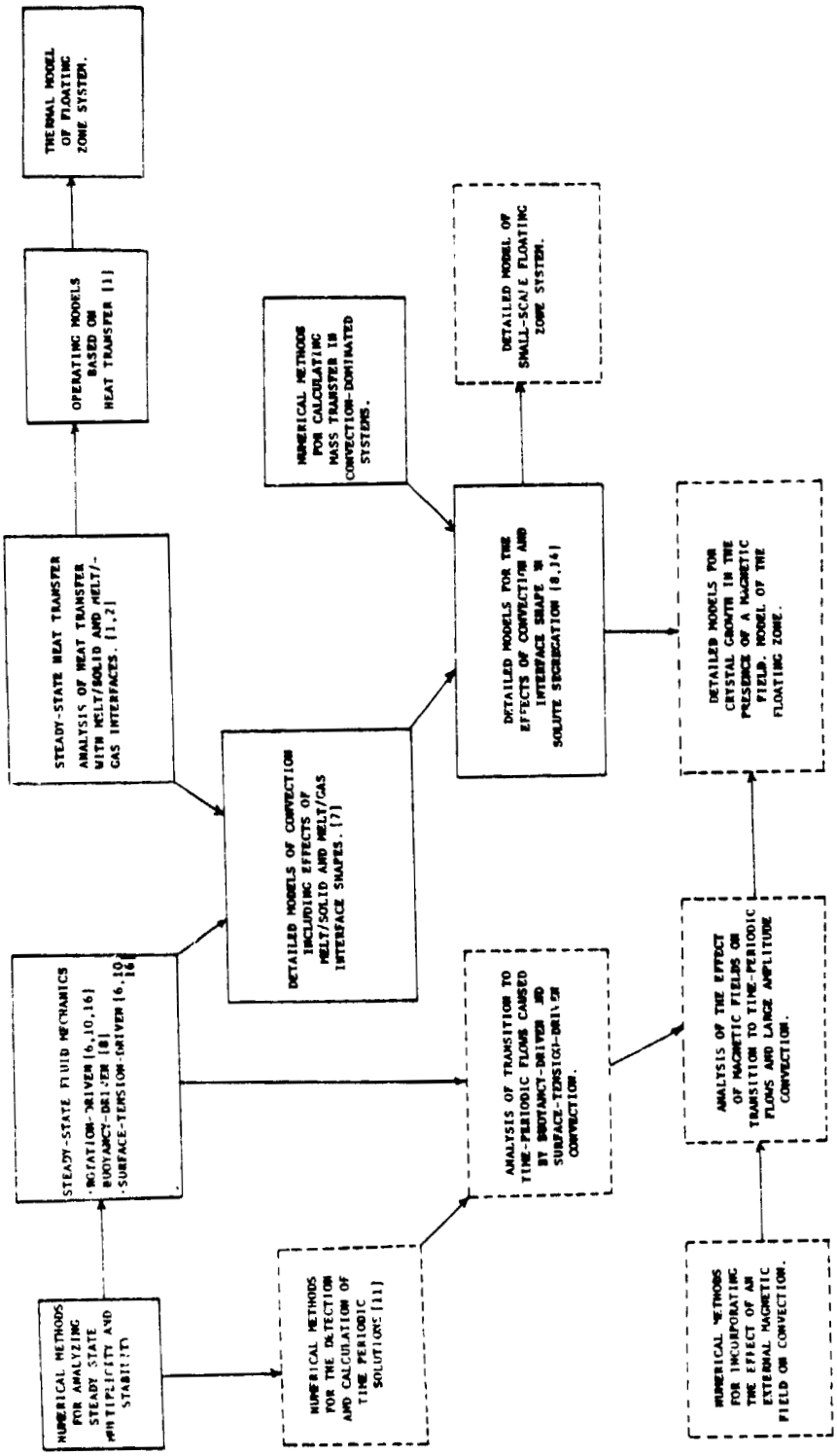

Figure 2. Schematic of Research in Melt Crystal Growth.

ORIGINAL PAGE IS
OF POOR QUALITY

To understand the complicated interaction between solute segregation and natural convection in melt growth geometries we have analyzed the details of the flow structure and transitions in natural convection in melts confined within cylindrical and rectangular containers. These studies have lead to systematic methods for tracking changes in steady state flows and for detecting the onset of time-periodic convection that leads to axial dopant striations in melt growth (Hurle et al. 1974 and Carruthers 1976). These calculations and the insight they supply for simulation of melt crystal growth are described in [5, 7, 9].

The four research projects described here and the personnel involved are:

1. Coupling between rotationally-driven, surface-tension-driven, and electromagnetically-driven convection and solute transfer in a small-scale, gravity-free zone (G.M. Harriott and J. Duranceau).

2. Fundamental studies of flow transitions in natural convection (Y. Yamaguchi*, C.J. Chang*, P. Sackinger).

3. Effect of buoyancy-driven convection on melt/solid interface shape and radial segregation in vertical Bridgman growth (C.J. Chang*).

4. Microscopic modelling of melt/solid interface dynamics (L.H. Ungar).

RESEARCH SUMMARY

Fluid Mechanics of a Small-Scale Floating Zone

Analytical and numerical methods have been applied to study the flows driven by rotation and surface-tension-differences is a prototype for the small-scale floating zone system proposed for space experiments. Both mech-

*Graduated during period 10/1/81 - 9/31/82.

ORIGINAL PAGE IS
OF POOR QUALITY

anisms for convection are important for these experiments. Marangoni flows driven by temperature (and possibly composition) differences may be unavoidable in space, while convection induced by deliberate crystal rotation causes well characterized radial segregation patterns that can be used to calibrate experimental results to theory.

G.M. Harriott has developed analytical methods for calculating the cellular flows driven by these mechanisms and the deflections of the melt/gas meniscus caused by these flows when the zone is almost a circular cylinder. The studies of rotating flows are based on expansions for small Reynolds number $Re \equiv \Omega RH/\nu$, where R is the radius of the rods, H is the height of the zone, and ν is the kinematic viscosity. The details of this analysis are contained in the manuscript [6]. One major result is the cellular structure of the flows produced by rotating the top rod at the rate $s\Omega$ and the bottom surface at rate Ω . Depending on the rotation ratio s and the aspect ratio of the zone $\Lambda \equiv R/H$, there may by either one or two toroidal secondary cells in the zone. For a range of these parameters the second cell does not fill the cross-section of the zone and a stagnation line may intersect the surface of the growing crystal. This stagnation surface can have a drastic effect on solute segregation as discussed [6]. The flow structures calculated for small Reynolds number are shown on Figure 3.

Harriott's analytical results have been compared to detailed finite element calculations that are possible for a wide range of Reynolds number [10]. The asymptotic results are within ten percent of the numerical solutions up to Re = 50 and hence are very useful estimates of the fluid flow in the microzone. These flows have also been used in radial segregation studies [16].

Finite element calculations for flows with exact counter-rotation (s = -1) at higher Reynolds numbers have uncovered multiple steady flows beyond a critical value that depends on aspect ratio, as depicted in Figure 4. The new flow fields do not have the reflective symmetry between the two toroidal cells normally expected for s = -1 and evolve toward increasing

ORIGINAL PAGE IS
OF POOR QUALITY

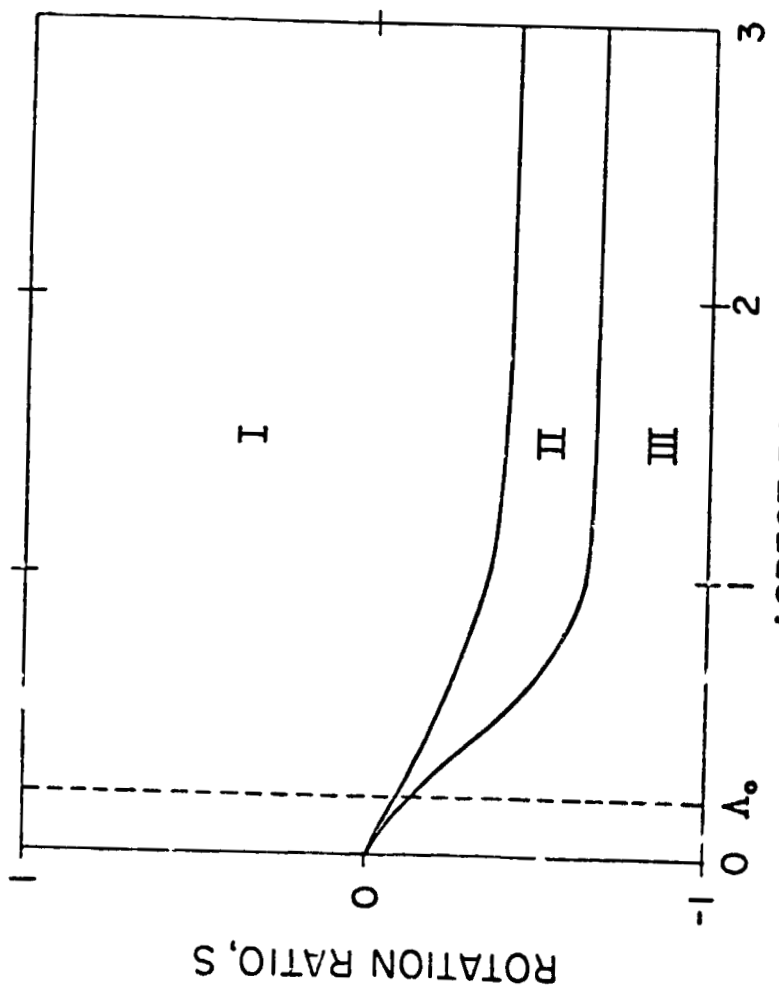

Figure 3. Phase diagram of flow structure as a function of aspect ratio Λ and rotation ratio s. The number regions refer to: (I) a single cell filling zone; (II) two cells, one spread over only a part of the zone's radius; (III) two cells over the entire radius.

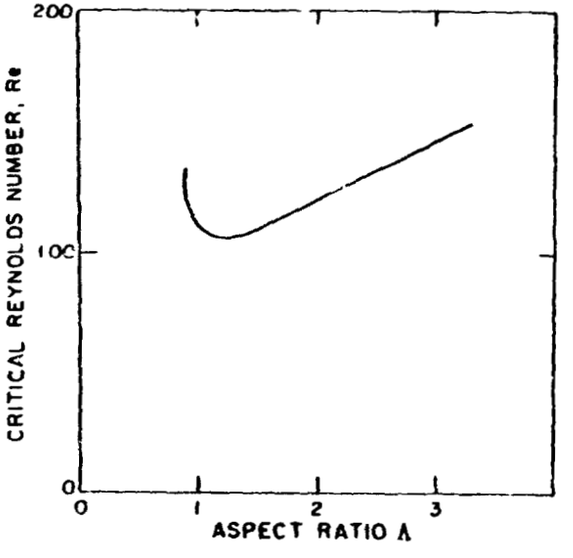

Figure 4. Critical Reynolds number for onset of asymmetric flow in a counter-rotating liquid zone.

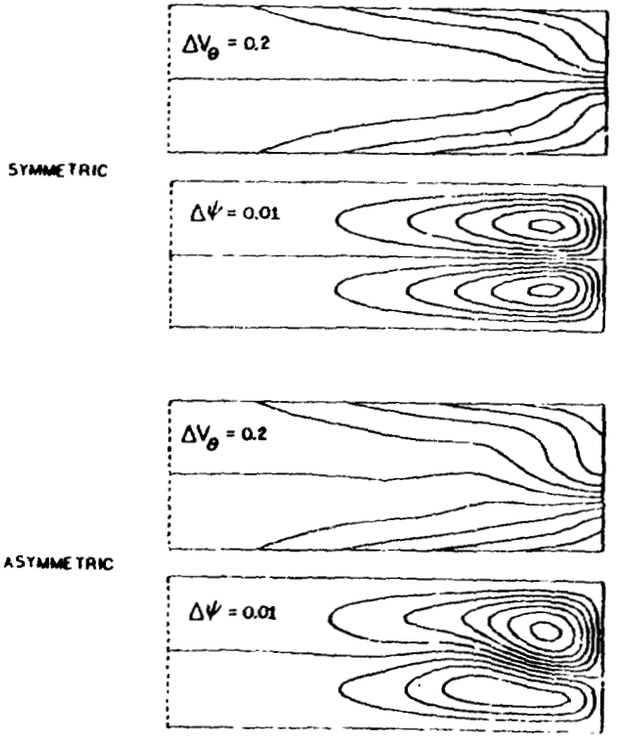

Figure 5. Sample symmetric and asymmetric flows for x = -1, Re = 175, and A = 3.

ORIGINAL PAGE IS
OF POOR QUALITY

ORIGINAL PAGE IS
OF POOR QUALITY

Reynolds number. Some flows in the symmetric and asymmetric flow families at the same value of Re are shown as Figure 5. Mathematical arguments indicate that the stability of the fluid flow changes at the bifurcation point so that only the asymmetric flows would be observed experimentally. Also, as explained in [10], changing from exact counter-rotation or adding gravity to deform the cylindrical meniscus ruptures the bifurcation point into two separate families of flows with stable flows existing on each family. These are new and exciting fluid mechanical predictions and experimental verification is underway using the micro-zone apparatus constructed by A.D. Little for NASA.

The mathematical concepts and numerical techniques for detecting, tracking and calculating the stability of multiple steady states was first laid out by L.H. Ungar in our research group in a related study [3] of the effects of melt volume, gravitational acceleration, and rotation rates on the stability of a rigidly rotating liquid zone held together by surface tension. Harriott has also applied these ideas to analyze the effect of the rotationally-driven flows on the maximum length of a cylindrical zone.

Our approach to the study of Marangoni convection in the floating zone geometry has paralled the research on rotating flows described above. First, analytical forms, similar to those derived in [6], have been calculated for flow fields that are valid in zones only slightly distorted from a cylinder at low Marangoni and Prandtl numbers. The results are cast in terms of a temperature distribution (see Figure 1 for a qualitative picture) that is incident on the meniscus and the structure of the cellular flows that result from the differences in surface tension. The constraints of the melting temperature at the crystal faces limit realistic temperature profiles to cubic polynomials with the maximum temperature between the two ends. This distribution always results in two toroidal cells that flow inward at the crystal faces and so are opposite from the flow induced by counter-rotating the seed and crystal. The combined effects of Maragoni and rotationally-induced flows are presently being studied to determine the strategy for crystal rotation that leads to the smallest amount of radial segregation of dopant.

Real floating zones have neither flat melt/solid interfaces nor cylindrical menisci. J.L. Duranceau has adapted finite-element solution schemes to solve for the rotating flows in deformed floating zones. Meniscus shapes are calculated by solution of the Young-Laplace equation (see [3]) which neglects the coupling of viscous normal stress to the deformation of the zone. The analysis in [6] and computational checks in [14] show this to be an extremely good assumption for the low capillary numbers ($C_A = \mu\Omega R/\sigma$) characteristic of silicon floating zones. Figure 6 demonstrates a typical change in the cellular flow structure caused by the meniscus deformation for a one centimeter diameter silicon zone. Changing the shape of the melt/gas interface has caused an order-of-magnitude decrease in the intensity of the top cell; this change will have a significant effect of radial dopant segregation.

To relate these results to actual floating zones requires heat transfer analysis for determining the proper length and volume of the melt as well as the shapes of the freezing and melting phase boundaries. The framework for this analysis has been laid in related studies by Ettouney ([1-2], also see Ettouney et al. (1982)) of Edge-Defined Film-Fed Growth of thin silicon sheets and the analysis of the floating zone is underway.

Fundamental Studies of Flow Transitions in Natural Convection:

The complicated patterns for buoyancy-driven convection in melt crystal growth systems and the importance of the location in terms of temperature gradients of the transition between laminar and time-periodic convection have emphasized the need for the development of numerical techniques for probing structure and transitions in natural convection. We have undertaken such an investigation while focusing on the simply defined heat transfer systems of a vertical cylinder heated from below

ORIGINAL PAGE IS
OF POOR QUALITY

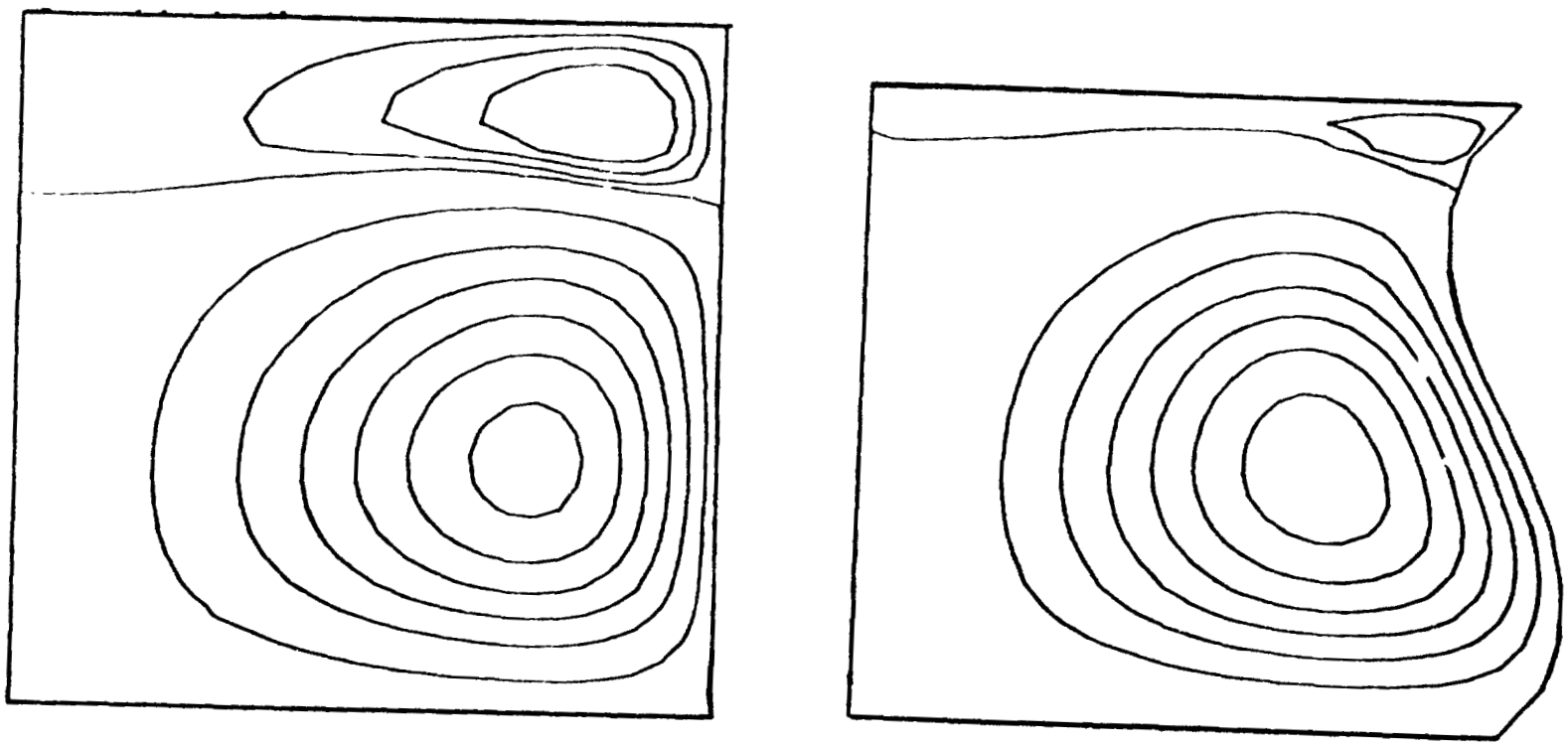

(a) cylindrical zone

(b) deformed zone

Figure 6. Comparison of streamlines for cylindrical zone and one deformed by gravity; Re = 50, G = 10 and s = -3/4 .

and a rectangular cavity heated from the side; these two systems are described next. Finally, the analysis has been extended to include the interaction between natural convection and a deformable melt/solid phase boundary in a study of flow structure in a two-phase analog of the vertical cylinder problem.

The Vertical Cylinder Heated From Below

The vertical cylinder configuration was chosen because of geometrical similarities to the vertical Bridgman system and because of the availability of previous theoretical (Charlson and Sani 1970, 1971, 1975) and experimental (Liang et al. 1969, Olson and Rosenberger 1980) results for checks of our results. We have combined finite-element techniques with the computer-aided methods developed in [3] for detecting and tracking multiple solutions to map out the steady axisymmetric flows that satisfy the Boussinesq equations for natural convection. The results of this study as discussed in [5] and in more detail in [9]. A typical solution structure is shown as Figure 7 for a cylinder with height L twice its radius R and a conducting sidewall; here the Nusselt number for the top surface Nu^t of the cylinder is plotted against Rayleigh number $Ra = \beta g(T_H - T_c)L^3/\alpha)$ for each family of flows identified in our calculations. The static state corresponds to $Nu^t=1$ and is the stable state up to the first critical value $Ra = 1.2 \times 10^4$ where two families of single-celled flows are stable and equally probable in experiments. The flows in these families differ only in the direction of the circulation, either up or down along the center of the ampoule, and are otherwise identical. Our predicted location for the critical point is within three percent of the value calculated by Charlson and Sani (1970) using linear stability analysis.

For a Prandtl number of one, the single-celled flows increase in intensity with increasing Ra until both families turn toward decreasing values of Rayleigh number at a limit point near $Ra = Ra_\ell = 6 \times 10^4$. This limit point marks the loss-of-existence of single-celled flows for increasing Ra

ORIGINAL PAGE IS
OF POOR QUALITY

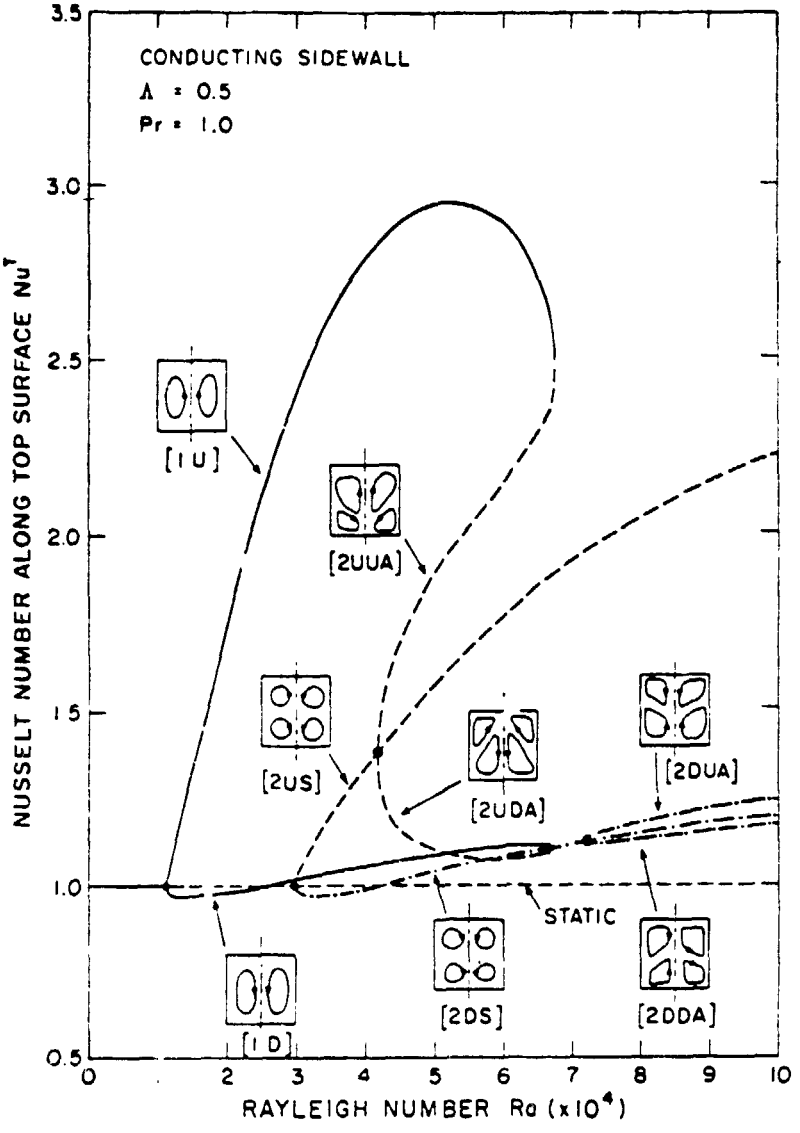

Figure 7. Bifurcation diagram for a vertical cylinder with conducting sidewall; Pr = 1 and Λ = 0.5.

ORIGINAL PAGE IS
OF POOR QUALITY

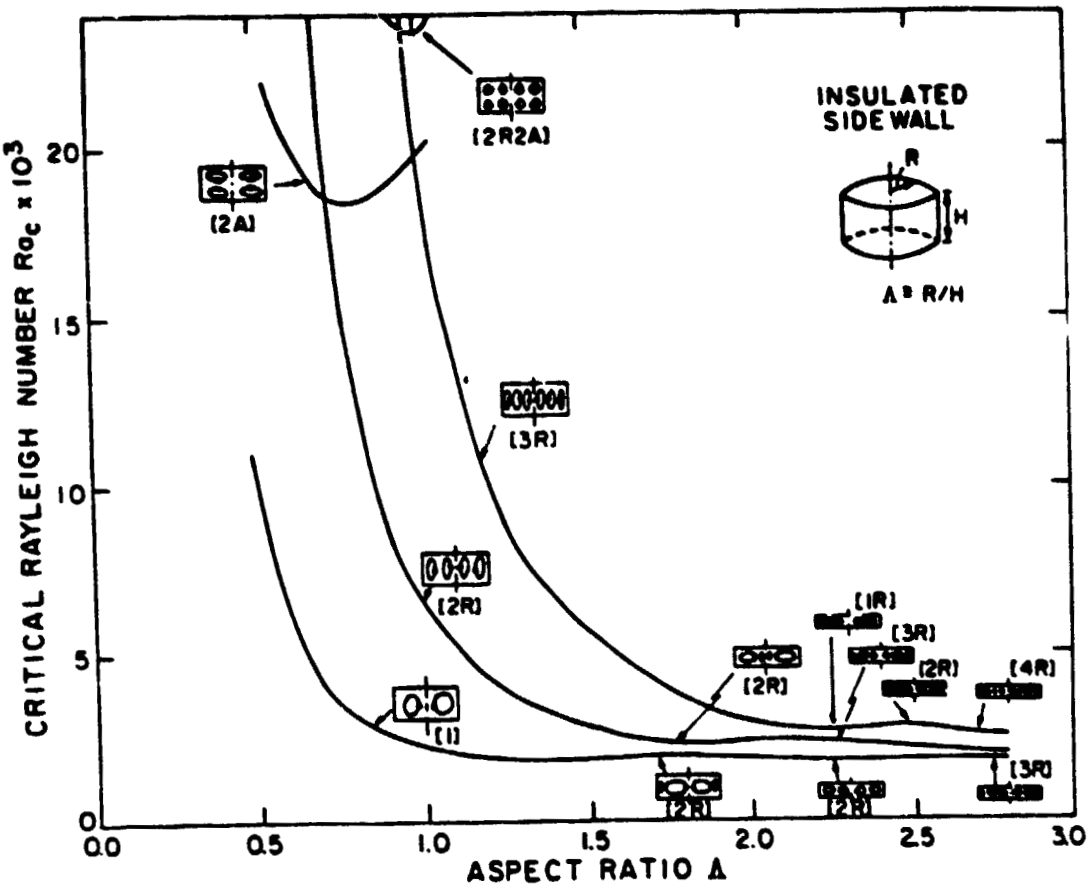

Figure 8. Loci of three lowest critical Rayleigh numbers as a function of aspect ratio for a cylinder heated from below with rigid sidewalls.

and may well mark the upper bound for steady state axisymmetric flows. As depicted in Figure 7, the two families of single-celled flows join families of flows with two cells stacked axially in the cylinder. These two cell flows branch from the static state at a second critical Rayleigh number $Ra = 3.1 \times 10^4$.

Extensive calculations reported in [9] have shown that the limit point in the primary family of cellular flows (see Figure 5) is generic for Prandtl numbers between 100 and 1, for either insulated or conducting rigid sidewalls, and a wide range of aspect ratio. This finding differs from results obtained in our research group and by Jones et al. (1976) for a cylinder with shear-free walls, where the first family of cellular flows that bifurcate from the static state seem to evolve continuously toward higher values of Ra. We believe that the differences in the flow structures for cylinders with slippery and rigid walls is linked to the breaking of second-order critical points that exist for the problem with shear-free sidewalls. The loci of the lowest three critical Rayleigh number for a cylinder with rigid, insulated sidewall is shown in Figure 8; each curve denotes the location of simple bifurcation points and intersections correspond to second-order bifurcation or double-points. Note that the curve for the mode occurring at the lowest value of Rayleigh number does not intersect the curves for higher modes and that the form of the cellular flow that evolves from each critical value changes continuously along the lowest mode. This behavior is distinctly different from the result for the cylinder with shear-free sidewalls (Liang et al. 1969 and Rosenblat 1982) where the form of the convection changes abruptly at double points. We feel that the behavior of the critical curves and the existence of the limit points for rigid walls can be explained through the transition between slippery and no-slip boundaries acting as a higher-order imperfection that destroys double points. Asymptotic analysis is underway that will hopefully confirm this hypothesis.

The Onset of Time-Periodic Flows in a Rectangular Cavity Heat From the Side.

Although the importance of the transition between laminar and time-periodic convection has been well established (see the review paper by Carruthers (1976)) few theoretical or experimental studies have been directed at quantitatively understanding this transition in systems of interest in crystal growth of semiconductors. The most notable experiments are those of Hurle et al. (1974) on the onset of oscillatory convection in a rectangular boat of gallium heated from the side. Crochet et al. (1982) have used time-dependent finite difference methods to track the evolution of a GaAs melt in a rectangular boat with slightly different thermal boundary conditions from those considered by Hurle and have found values of Rayleigh number where the flow is oscillatory.

Our approach to detecting the onset of these oscillations has focused on the approach of bifurcation theory (Iooss and Joseph 1980) that identifies the onset of stable time-periodic solutions as a Hopf bifurcation point between the family of time-periodic states and one of laminar flows. As outline in the Ph.D. thesis of C.J. Chang and in the manuscript [11], these bifurcation points occur where a pair of complex conjugate eigenvalues of the linearized and discrete version of the Boussinesq equations cross the imaginary axis. Chang has calculated these eigenvalues for the horizontal boat geometries considered by Hurle and Crochet. Sample isotherms and streamlines are shown in Figure 9 for Pr = 0.015 and an aspect ratio (length to height) of two; the stability of each flow is denoted along with the eigenvalues (scaled with ν/H^2) for the unstable modes. Complex eigen-values correspond to the onset of oscillatory convection.

One of the most important results obtained thus far is the sensitivity of the structure of the laminar flow and the critical Rayleigh number for the onset of the convection to the each value of the Prandtl number. This point is made by the results for Pr = 0.03 shown on Fig. 10. Here the first transition detected from the base laminar flow is to a second family of steady flows, not to an oscillatory state. The structure of the new laminar

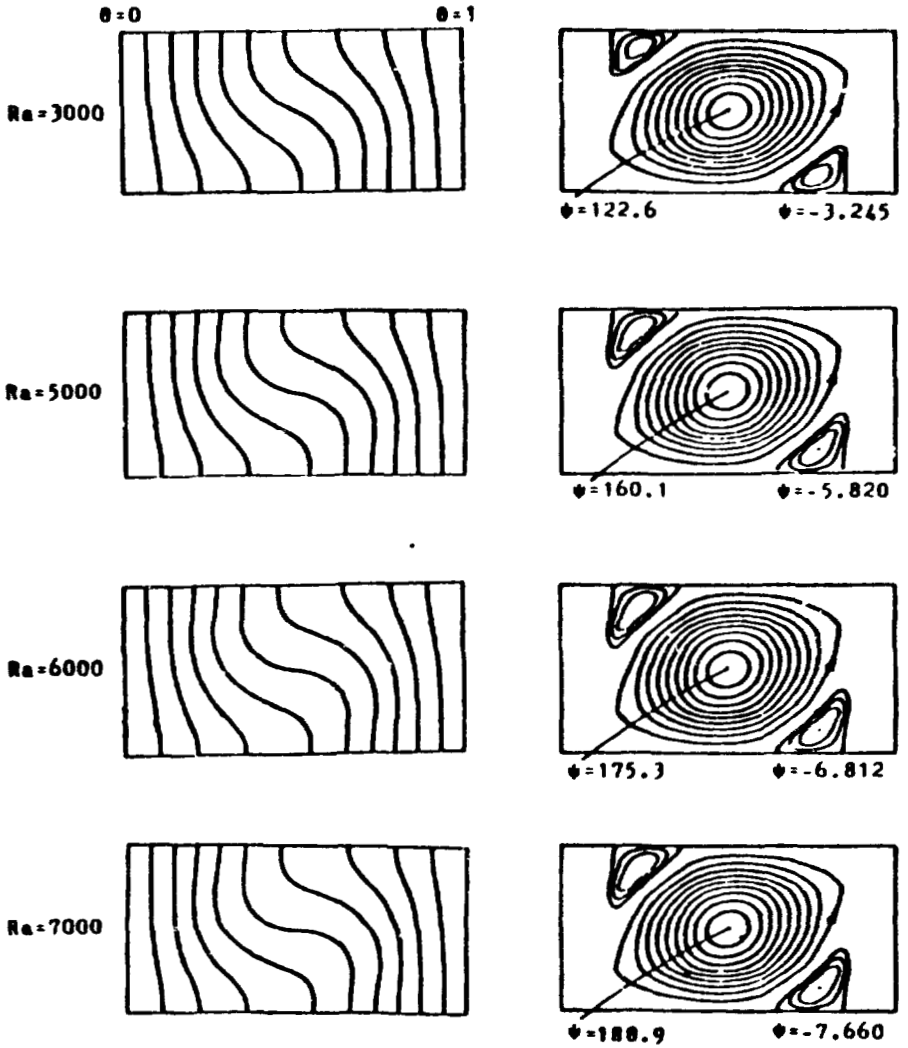

	STABILITY	EIGENVALUES WITH REAL POSITIVE PARTS
Ra=3000	Stable	None
Ra=5000	Unstable	121.9±370.0j
Ra=6000	Unstable	174.0±399.4j
Ra=7000	Unstable	225.4±423.7j

ORIGINAL PAGE IS OF POOR QUALITY

Figure 9. Linear stability analysis of Hurle's experiment for Pr = 0.15, L/H = 2 , insulated top and bottom and rigid walls.

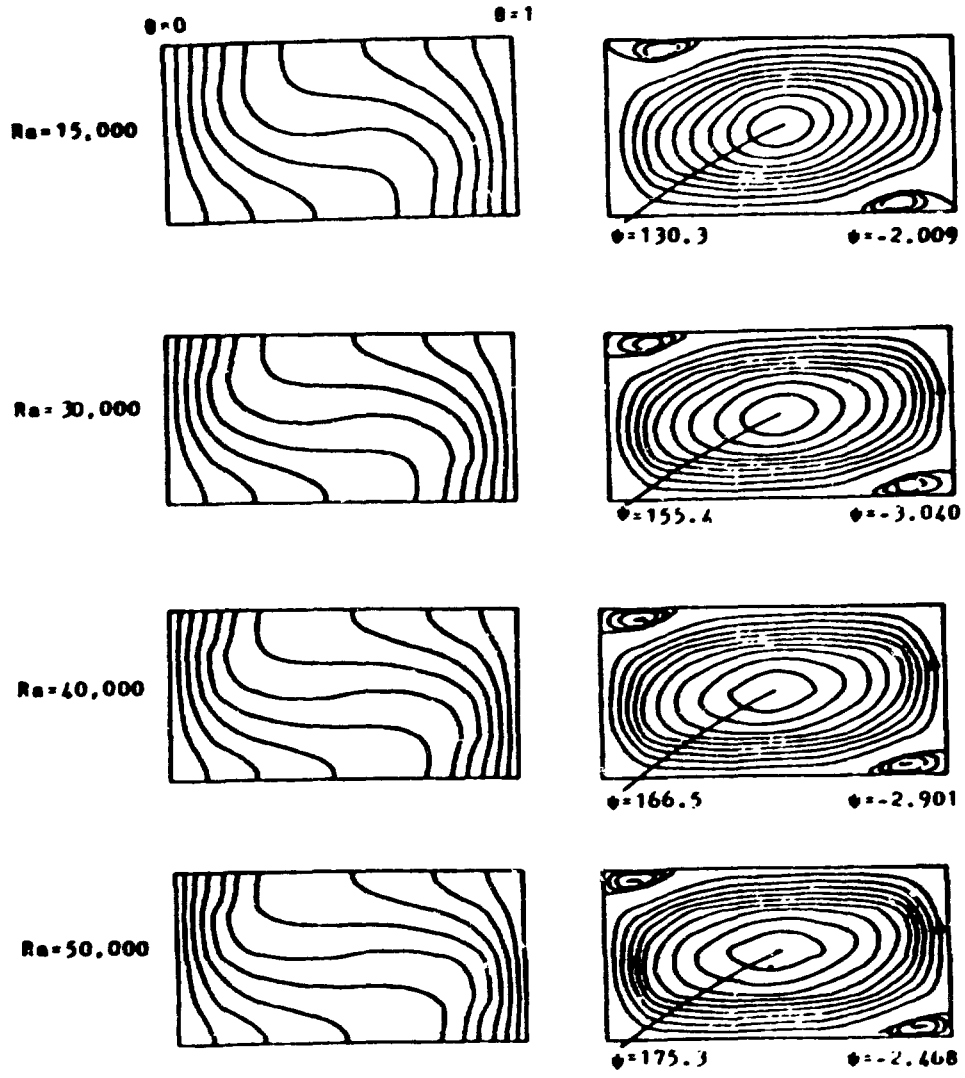

	STABILITY	EIGENVALUES WITH REAL POSITIVE PARTS
Ra=15,000	Stable	None
Ra=30,000	Stable	None
Ra=40,000	Stable	None
Ra=50,000	Unstable	69.54

Figure 10. Linear stability analysis of Hurle's experiment for Pr = 0.3, L/H = 2 , insulated top and bottom and all rigid walls.

ORIGINAL PAGE IS
OF POOR QUALITY

flow for Pr = 0.03 and further transitions to oscillatory states will be discussed in [11].

Effect of Melt/Solid Interface on Flow Structure and Transitions

An important consideration in the analysis of convection and mass transport in melt crystal growth is the role of the melt/solid in influencing the structure of laminar flows and the location of transitions to time-periodic convection. One goal of our research has been to extend the methods for computer-aided analysis of nonlinear structure to solidification systems that combine both buoyancy-driven convection in the melt and the complications of the unknown location of the melt/solid phase boundary. We have successfully reached this goal through a sequence of calculations using progressively more advanced numerical methods.

Finite element methods [2] were developed first for steady solidification models that neglect the fluid flow in the melt. The reasoning behind the use of these simple models is two-fold. First, they are good descriptions of heat transport for many crystal growth geometries, especially in a low-gravity environment; our notion of such an "operating model" for a meniscus-defined growth technique is displayed in the work of Ettouney et al. (1982). Secondly, novel numerical methods are more effectively developed for these less complicated systems and then extended to account for bulk convection in the melt. This strategy has been successful in the development of finite-element techniques by Chang [4] for analyzing the interaction of melt/solid interface shape and buoyancy-driven convection in a model system where melt and solid are held in a cylindrical ampoule placed in a vertically destabilized temperature gradient.

When the cylinder is heated from below (Figure 11a) the melt/solid system is a two-phase analog of the natural convection problem considered above and in [5,9]. The same techniques developed for analyzing multiple steady flows in the single-phase problem have been extended to the

ORIGINAL PAGE IS
OF POOR QUALITY

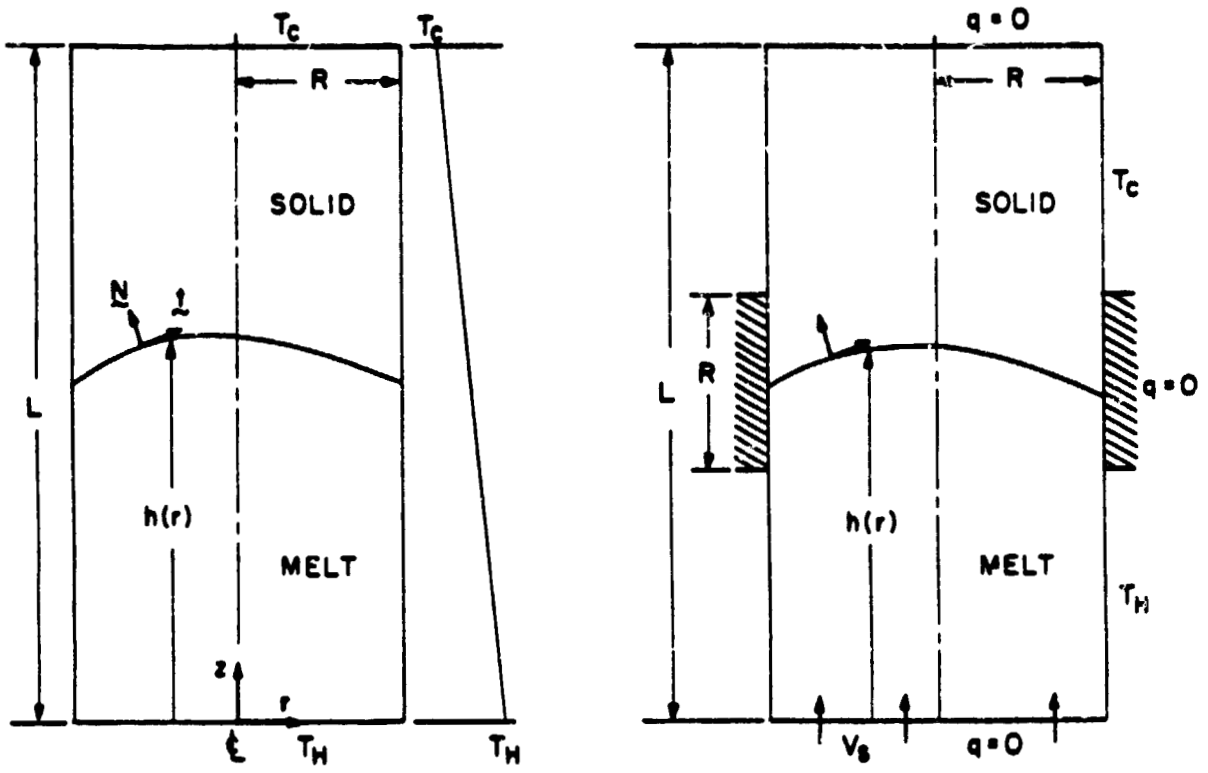

(a) RALEIGH-BENARD PROBLEM

(b) PROTOTYPE OF VERTICAL BRIDGMAN-STOCK BARGER SYSTEM

Figure 11. Model two-phase systems: (a) Rayleigh-Bénard and vertical Bridgman geometries.

two-phase geometry to understand the role of the melt/solid interface on the structure of laminar flows. As is seen by comparing the bifurcation diagrams Figures 7 and 12, the presence of the melt/solid interface has very little effect on the structure of the weakly nonlinear cellular flows that originate along the static state, but changes qualitatively the structure of the flow families far from the bifurcation points. Most noteably, the 1U and 1D flows result in different shapes of the melt/solid interfaces as shown by Figure 13.

The loss of symmetry between the 1U and 1D flow fields signals an imperfection that ruptures the secondary bifurcation point that exists along the 2U family in the single-phase problem and results in the continuous transition in the two-phase system between flows in the 1D and 2U families.

Although the boundary conditions for the two-phase Rayleigh-Bénard problem are extremely idealized, the flow structure for this problem gives much detail about the more complicated vertically destabilized Bridgman system (see Fig. 11b) of interest in crystal growth. As is discussed in [7], the Rayleigh-Bénard and Bridgman systems can be connected mathematically through the thermal boudnary conditions and the flow structure can then be thought of in terms of a continuous transition between the two systems. The fruitfulness of this approach is demonstrated on Figure 14 where a sample bifurcation diagram and flow fields for the Bridgman system are displayed. Notice that the patterns of the streamlines and the existence of the limit point Ra_ℓ are qualitatively unchanged between the Rayleigh-Bénard and Bridgman systems.

Effect of Buoyancy-Driven Convection on Melt/Solid Interface Shape and Radial Segregation in Vertical Bridgman Growth.

Melt/solid interface shape and segregation in the crystal are the most easily measured indicators of the role of convection in melt growth systems (Kim et al. 1978, Wang and Witt 1980). Previous calculations of

ORIGINAL PAGE IS
OF POOR QUALITY

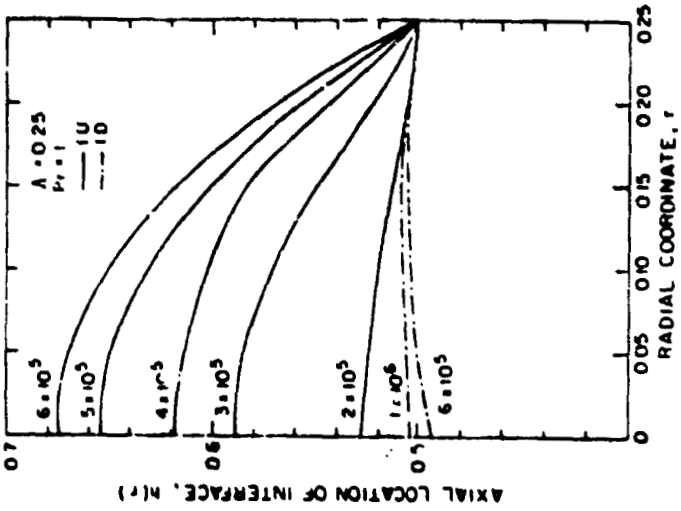

Figure 13. Melt/solid interface shapes for 1U and 1D flows in two-phase Rayleigh-Bénard problem.

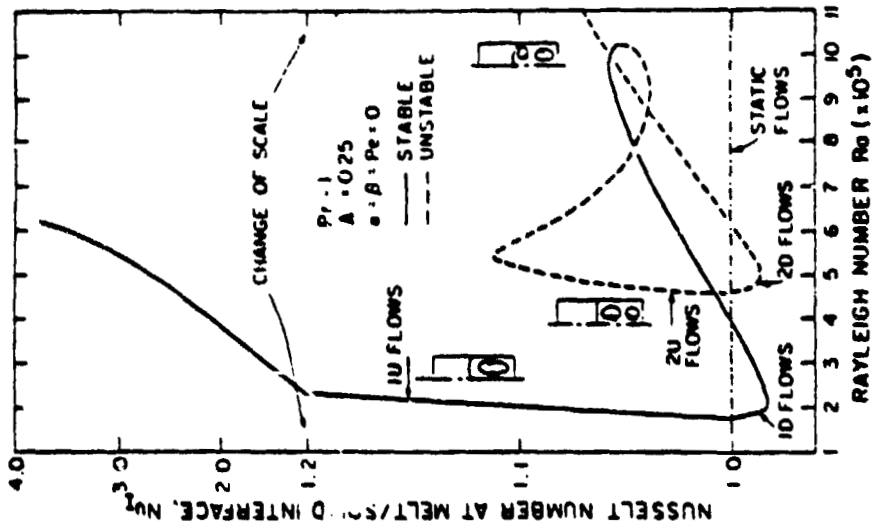

Figure 12. Bifurcation diagram for two-phase Rayleigh-Bénard problem; A = 0.25 and Pr = 1 .

ORIGINAL PAGE IS
OF POOR QUALITY

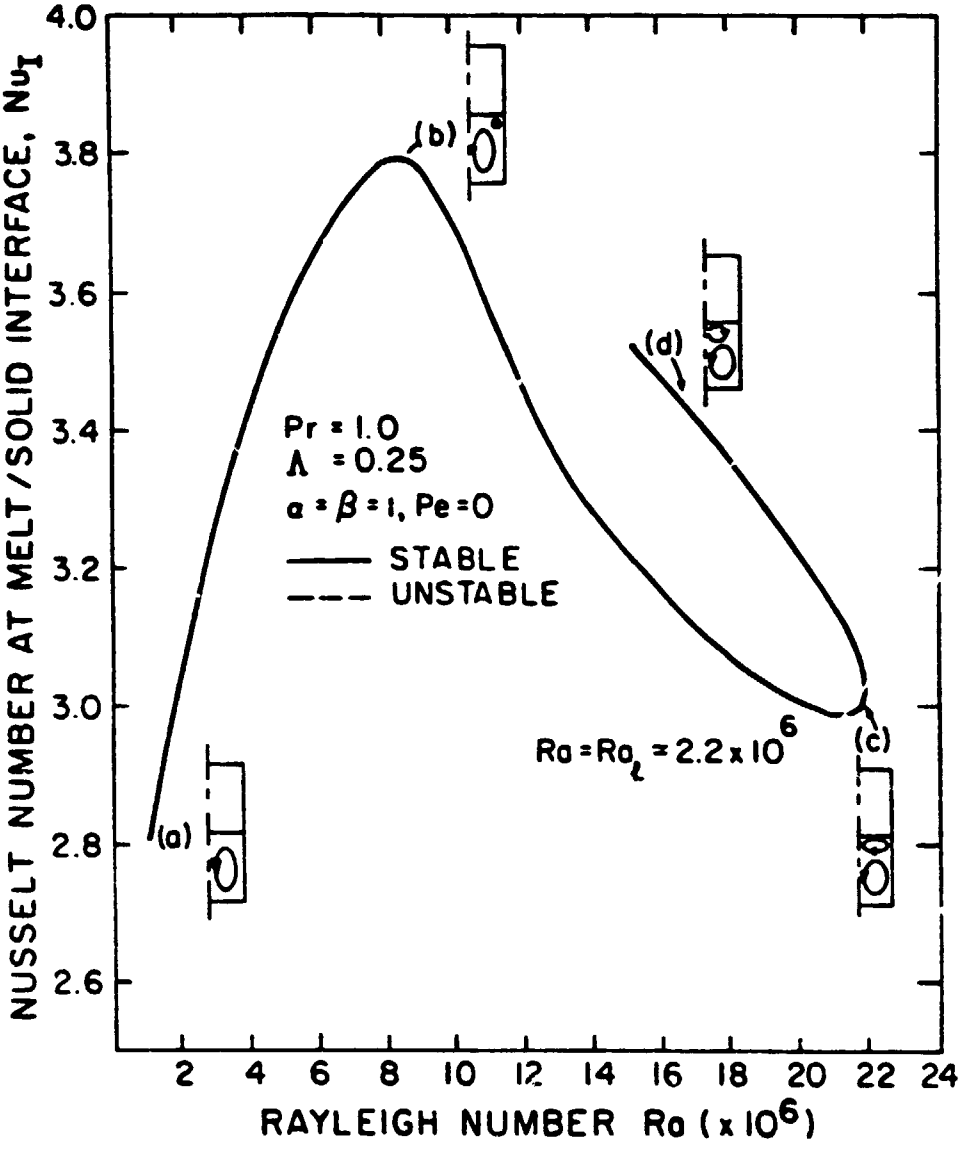

Figure 14. Bifurcation diagram for vertically destabilized Bridgman system.

convection in melt growth do not account for the shape of the melt/solid interface or for realistic heat transfer conditions and thus cannot simulate experimental results. The numerical methods developed by Chang [4] make possible these calculations in a wide variety of small-scale growth systems.

Chang's algorithm has been used at M.I.T. to study convection and mass transfer of a dilute component in thermally stabilized and destabilized vertical Bridgman systems; the stabilized system is the same as shown in Figure 11b with the ampoule and furnace flipped over. These caluclations are aimed at modelling the Gallium-doped Germanium experiments of Chris Wang in the Materials Science Department at M.I.T. and will supply a basis for evaluating convection in other earth-bound experiments related to NASA's program on directional solidification. The results discussed below are taken from the more complete report [8]. Sample isotherms and streamlines calculated in the stabilized geometry are shown as Figure 15 for Pr = 0.01 and a dimensionless growth rate Pe = 0.01 which corresponds to moving the ampoule at roughly 10 μm/sec. The melt/solid interfaces in these calculations are not flat, but slightly curved because of radial temperature gradients at the edges of the gradient region and because of convective heat transfer. Interfaces are shown in Figure 16 that correspond to the flow fields given in Figure 15. These curved interfaces together with the convection in the melt cause radial segregation of the dopant in the crystal.

Chang has calculated the solute distribution in a steady state analog of Bridgman growth using the velocity fields and interface shapes predicted from his convection calculations. Figure 17 shows the distribution of solute along the solidification interface for Rayleigh numbers up to 10^4 for the gallium-doped germanium system of Wang; the Schmidt number is 10 and the segregation coefficient is 0.1 . Almost no radial segregation was present in the absence of natural convection (Ra = 0) because the melt/solid interface was sensibly flat ; see Figure 16. As the convection level was increased, the delivery of solute to the interface became uneven radially until at Ra = 1×10^3 the radial segregation of gallium was maximized. At Ra = 1×10^4 radial segregation is still appreciable and the much used boundary-layer

ORIGINAL PAGE IS
OF POOR QUALITY

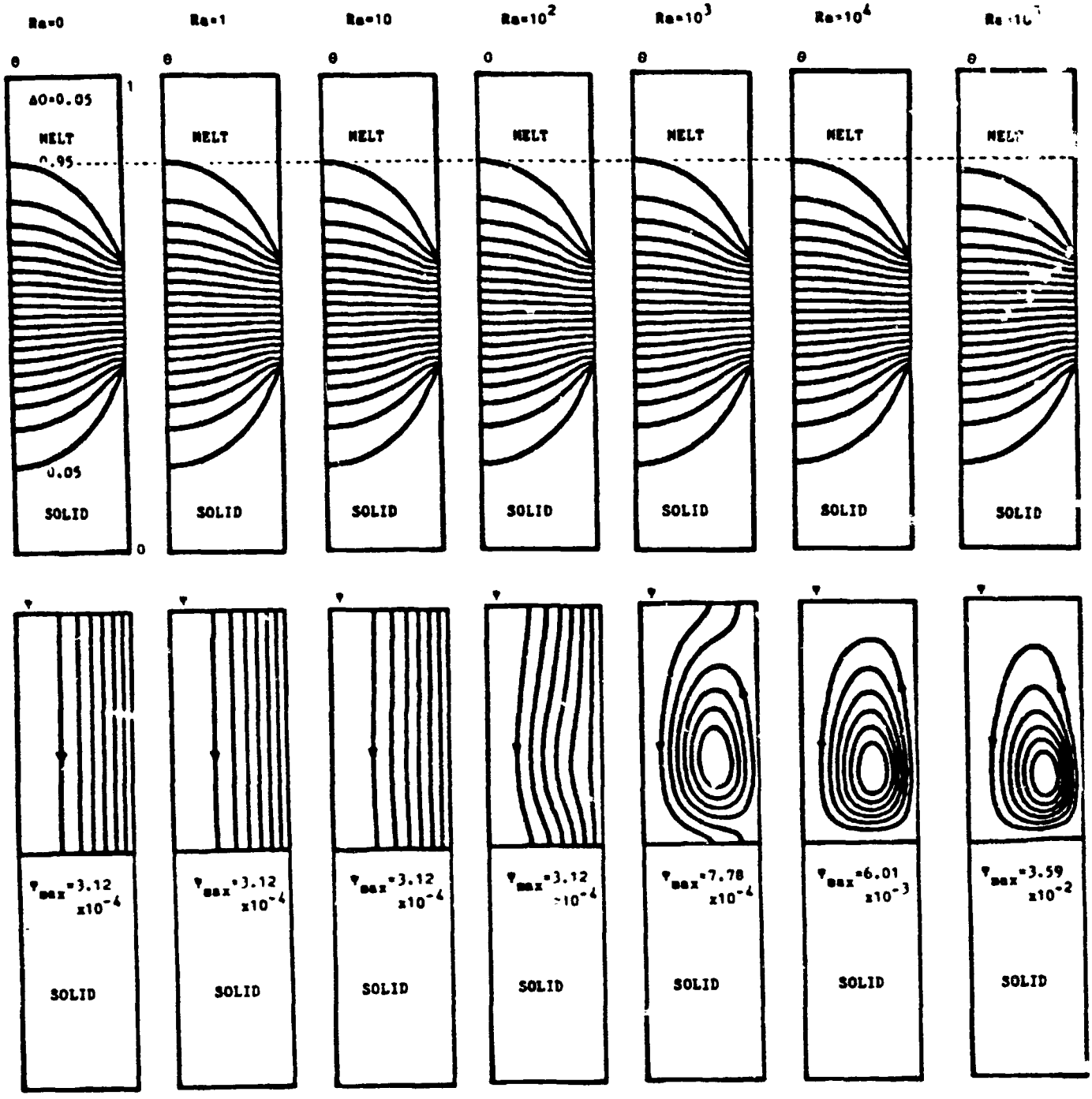

Figure 15. Isotherms and streamlines for vertically stabilized Bridgman system: Pr = 0.01 , Pe = 0.01 , and Λ = 0.25 .

ORIGINAL PAGE IS
OF POOR QUALITY

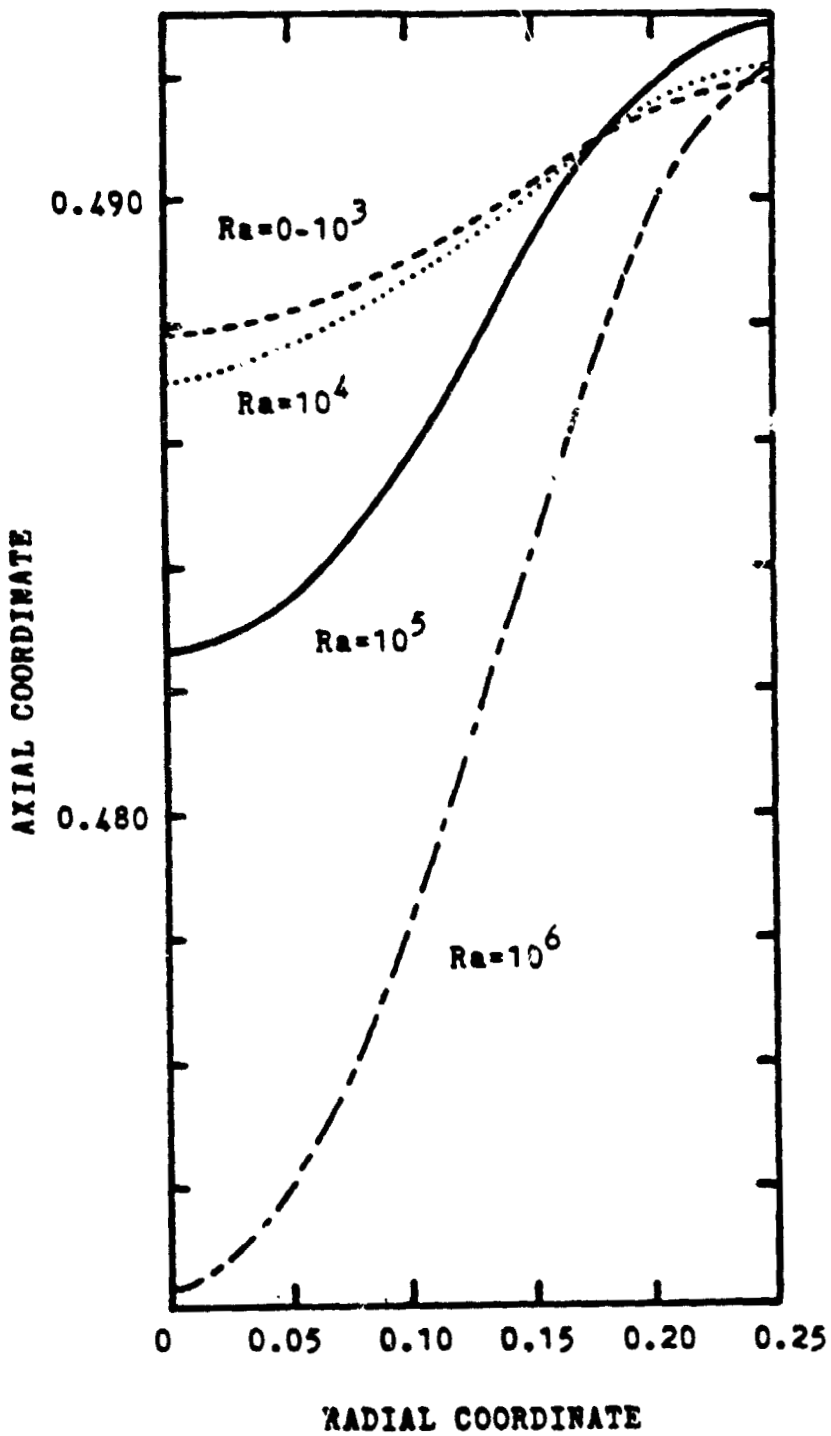

Figure 16. Melt/solid interface shapes for the flow and temperature fields shown in Figure 15.

ORIGINAL PAGE IS
OF POOR QUALITY

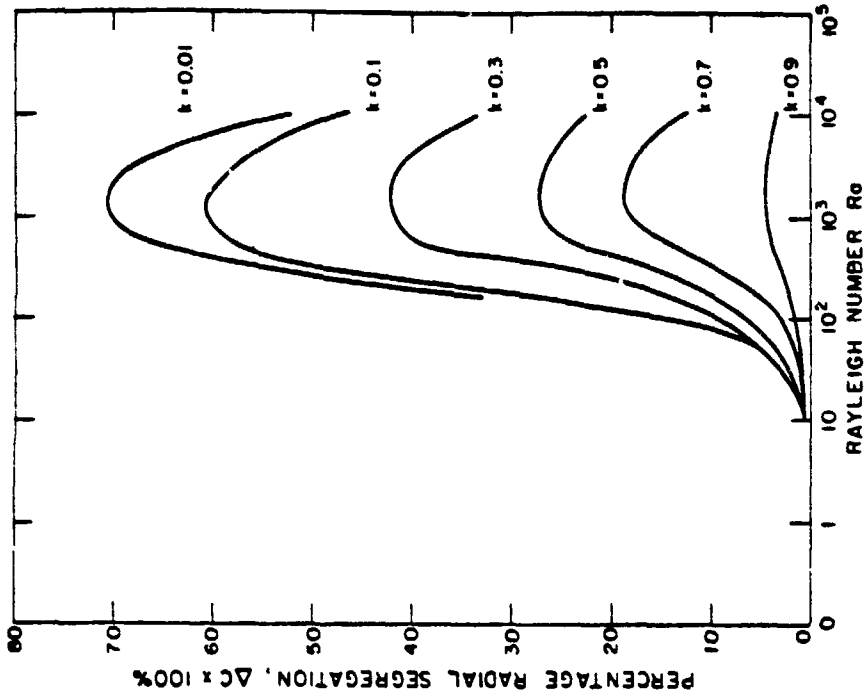

Figure 18. Percentage of radial segregation along the melt/solid interface as a function of Ra.

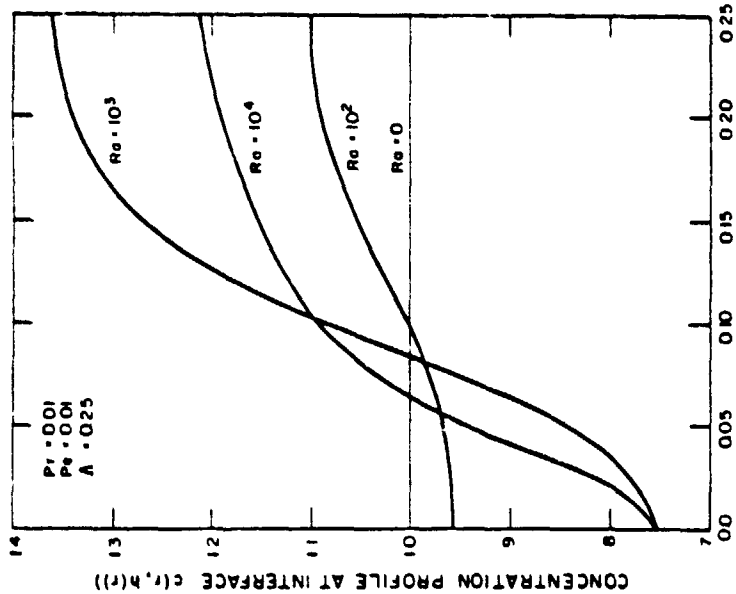

Figure 17. Concentration profiles along the melt/solid interface as a function of Rayleigh number.

approximations for calculating dopant distributions are not applicable. The cencentration fields at higher convection levels tend toward a uniform core, with regions of rapid change in dopant level near each boundary, this structure marks the start of the formation of boundary layers on these surfaces. The amount of radial segregation is plotted on Figure 18 as a function of Rayleigh number and segregation coefficient for Sc = 10.

The sensitivity of melt/solid interface shape and dopant segregation to such important parameters as the length of the gradient zone and the ratio of conductivities between melt and solid are established in [8].

Microscopic Modelling of Melt/Solid Interface Dynamics

Morphological stability theory describes the tendency of a microscopically smooth solidification front separating a binary melt from its solid to develop undulations that lead to cellular and dendritic interfaces. Although the onset of these instabilities has been studied using linear stability analysis (Mullins & Sekerka 1964) and by weakly nonlinear analysis (Wollkind and Segal 1970), metallurgists still lack a theoretical understanding of the microscale behavior of highly deformed interfaces. Our research has concentrated on efficient calculation of large amplitude deformations of a melt/solid interface and on the effect of various system properties (temperature gradient, growth rate, material properties, and grain boundaries) on the structure of the interface.

By adding the variation of the melting point temperature with the mean curvature of the solidification interface, Ungar and Ettouney [12] have developed a numerical method for calculating the shapes of solidification interfaces on the microscale. These numerical methods have been used to study a simplified model for directional solidification where the temperature gradient is assumed to be linear throughout both melt and crystal and uneffected by the morphology of the melt/solid interface. The assumptions

ORIGINAL PAGE IS
OF POOR QUALITY

leading to this model are often valid and have been made by other researchers (Hunt 1979, Langer 1980). The calculations shown here are for parameter values close to those appropriate for the Pb-Sb system studied theoretically in Coriell and Sekerka (1980) and experimentally by Morris and Winegard (1965). When the interface shape was taken to be periodic with a given wavelength the linearized results of Mullins and Sekerka (1964) were recovered and steady state interfaces with finite-amplitude cellular morphologies were calculated.

The evolution of these interfaces with decreasing temperature gradient G (increased constitutional instability) is depicted on Figure 19a for a dimensionless growth rate Pe = 0.8 by the maximum deflection of the solidification from; a sample shape is shown as Figure 19b. The shape family first evolves subcritically (to large temperature gradients) and is unstable. At a critical value of G the shape family turns toward smaller values of |G| and the cellular forms regain stability and should be observable. The characteristic "molar" shape of the melt/solid interface was reported by Holmes and Gatos (1981). Increasing the growth rate changes the structure of the shape family from sub- to super-critical and results in an "s-shaped" shape family with two regions of stable interfaces; see [12] for details.

Introducing a grain boundary in the melt/solid interface changes the structure of the constitutional instability. Analytical and numerical results for the one-sided model discussed above [13] show that the grain boundary ruptures the bifurcation between the planar and cellular interfaces. When the bifurcation point is subcritical, adding the grain boundary leads to loss of stability at a limit point, as shown on Figure 19. When the original transition is super-critical (the case for high growth rates), adding the grain boundary leads to a smooth transition to a highly curved interface with no change in stability. These results are contrary to previous linear analyses (Coriell and Sekerka 1973a, 1975b) for grain angles near 90° which predict that the pressure of the grain does not affect the point of exchange of stability. Ungar has shown that, for temperature gradients near the critical value for the cellular instability, the steady

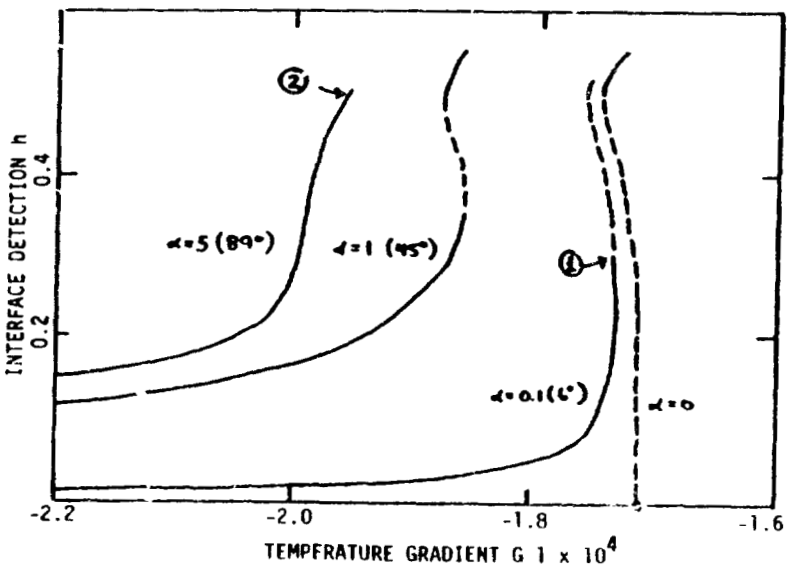

Figure 19a. Cellular interface shapes represented by a plot of the maximum deflection of the interface as a function of temperature gradient. Crystals with grain angles of α are also shown.

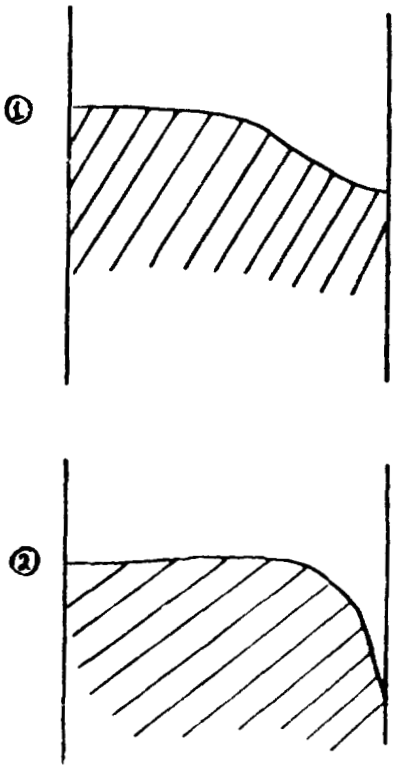

Figure 19b. Shape interface shapes corresponding to the points (1) and (2) on Figure 19a.

ORIGINAL PAGE IS
OF POOR QUALITY

interface shapes are singular functions of the grain angle α and a regular perturbation analysis in this parameter, as performed by Coriell and Sekerka, fails. The correct singluar analysis predicts the critical temperature gradient for the existence of the limit point mentioned above varies as $(\alpha)^{2/3}$. The details of this analysis will be presented in [13].

ORIGINAL PAGE IS
OF POOR QUALITY

REFERENCES

Carruthers, J.R., Origins of convective temperature oscillations in crystal growth melts. J. Crystal Growth 32, 13-26 (1976).

Charlson, G.S. and Sani, R.L., Thermoconvective instability in a bounded cylindrical fluid layer. Int. J. Heat Transfer 13, 1479-1496 (1970).

Charlson, G.S. and Sani, R.L., On thermoconvective instability in a bounded cylindrical fluid layer. Int. J. Heat Mass Transfer 14, 2157-2160 (1971).

Charlson, G.S. and Sani, R.L., Finite amplitude axisymmetric thermoconvective flows in a bounded cylindrical layer of fluid. J. Fluid Mech. 21, 209-229 (1975).

Coriell, S.R., Cordes, M.R., Boettinger, W.J. and Sekerka, R.F., Convective and interfacial instabilities during unidirectional solidification of a binary alloy. J. Crystal Growth 49, 13-28 (1980).

Coriell, S.R. and Sekerka, R.F., Morphological stability near a grain boundary grove in a solid-liquid interface during solidification of a pure substance. J. Crystal Growth 19, 100-105 (1973a).

Coriell, S.R. and Sekerka, R.F., Morphological stability near a grain boundary grove in a solid-liquid interface during solidification of a binary alloy. J. Crystal Growth 19, 285-293.

Crochet, M.J., Geyling, F.T., van Schaftingen, J.J., Finite element simulation of oscillatory motions in semiconductor crystal growth melts. Bell Laboratories Tech. Report. Jan. 1982.

Ettouney, H.M., Brown, R.A., Kalejs, J.P., Analysis of operating limits of edge-defined film-fed crystal growth. J. Crystal Growth submitted (1982).

Hunt, S.D., Keynote Address: Cellular and primary dendrite spacings in Solidification and Casting of Metals, 3-9, 1979.

Hurle, D.T.J., Jakeman, E. and Johnson, C.P., Convective temperature oscillations in molten gallium. J. Fluid Mech. 64, 565-576 (1974).

Iooss, G. And Joseph, D.D., Elementary Stability and Bifurcation Theory. Springer-Verlag, New York, 1980.

Jones, C.A., Moore, D.R. and Weiss, N.D., Axisymmetric convection in a cylinder. J. Fluid Mech. 73 353-388 (1976).

Kim, K.M., Witt, A.F., Lichtensteinger, M. and Gatos, H.C., Quantitative analysis of the effects of destabilizing vertical thermal gradients on crystal growth and segregation: Ga-doped Ge. J. Electrochem. Soc. 125, 475-480 (1978).

Langer, J.S., Instabilities and pattern formation in crystal growth. Rev. Mod. Phys. 52, 1-28 (1980).

Liang, S.F., Vidal, A. and Acrivos, A., Buoyancy-driven convection in cylindrical geometries. J. Fluid Mech. 36, 239-256 (1969).

Mullins, W.W. and Sekerka, R.F., Stability of planar interface during solidification of a dilute binary alloy. J. Applied Physics 35, 444-451 (1964).

Olson, J.M. and Rosenberger, F., Convective instabilities in a closed vertical cylinder heated from below. Part 1 Monocomponent Gases. J. Fluid Mech. 92, 609-629 (1979).

Rosenblat, S. Thermal convection is a vertical circular cylinder. J. Fluid Mech. 122, 395-410 (1982).

Wang, C. and Witt, A.F., Annual Report of the Materials Processing Center, M.I.T., 1980.

Wollkind, D. and Segal, L., A nonlinear stability analysis of the freezing of a dilute binary alloy. Philos. Trans. R. Soc. Lond. 268A, 351 (1970).

ORIGINAL PAGE IS
OF POOR QUALITY

PRESENTATIONS (Since - 1/1/82)

ORIGINAL PAGE IS
OF POOR QUALITY

1. R.A. Brown, "Fluid Mechanics of a Floating Zone," Float Zone Workshop Pheonix, (February 1982).

2. C.J. Chang and R.A. Brown, "Natural Convection and Mass Transfer in Directional Solidification," Spring National Meeting of AIChE, Orlando (March 1982).

3. R.A. Brown, "Multiple Steady States in Free Surface Problems," Department of Chemical Engineering, Clarkson College (April, 1982).

4. R.A. Brown, "Natural Convection and Mass Transfer in Vertical Bridgeman Growth," Invited paper Annual Meeting of American Ceramic Society, Cincinnati (May 1982). Abstract in Bull. Amer. Cer. Soc. 61, 432 (1982).

5. R.A. Brown, "Buoyancy-Driven Convection in Melt Crystal Growth," Invited paper, National Congress on Theoretical and Applied Mechanics, Cornell University (June, 1982).

6. G.M. Harriott, "Fluid Mechanics of a Small-scale Floating Zone," Department of Chemical Engineering, University of Virginia (April 1982).

7. G.M. Harriott, "Fluid Mechanics of a Small-Scale Floating Zone," Department of Chemical Engineering, North Carolina State University (April 1982).

8. R.A. Brown, "Natural Convection in Melt Crystal Growth," Department of Chemical Engineering, Lehigh University (October 1982).

9. R.A. Brown, "Natural Convection in Melt Crystal Growth" Centre de Etude Nucleaire, Grenoble (October 1982)

10. Y. Yamaguchi, C.J. Chang, and R.A. Brown, "Finite Element Calculation of Steady Axisymmetric Flows in a vertical Cylinder heated from below." 75th Annual Meeting of the AIChE, Los Angeles (November 1982).

11. L.H. Ungar, H.M. Ettouney, and R.A. Brown, "The Effect of Grain Boundaries on the Morphological Stability of Crystals Grown from the Melt," 75th Annual Meeting of the AIChE, Los Angeles (November 1982).

12. G.M. Harriott and Brown, R.A., "Multiple Steady Flows in a Differentially Rotated Drop," 35th Meeting, Fluid Dynamic Division of APS, Rutgers (November 1982). Abstract in Bull. Amer. Phys. Soc. 27, 1167 (1982).

13. R.A. Brown, Y. Yamaguchi, and C.J. Chang, "Effect of Aspect Ratio on Natural Convection in a Vertical Cylinder Heated From Below," 35th Annual Meeting, Fluid Dynamics Division of APS, Rutgers (November 1982). Abstract in Bull. Amer. Phys. Soc. 27, 1169 (1982).

14. R.A. Brown, "Modelling Crystal Growth at Two Levels of Detail," Bell Laboratories, June 1982.

15. R.A. Brown, "Heat Transfer and Fluid Mechanics in Melt Crystal Growth," Material Processing Center Symposium on Mathematical Modelling, M.I.T., October, 1982.

16. R.A. Brown, "Modelling of the Floating Zone Process", Meeting of the NASA Floating Zone Working Group, Pheonix, February, 1982.

PUBLICATIONS

1. Ettouney, H.M. and Brown, R.A., Effect of heat transfer on melt/solid interface shape and solute segregation in edge-defined film-fed growth: finite element analysis. J. Crystal Growth 57, 313-329 (1982).

2. Ettouney, H.M. and Brown, R.A., Finite element methods for steady solidification problems. J. Comput. Physics 48, xxx-xxx (1982).

3. Ungar, L.H. and Brown, R.A., The dependence of the shape and stability of a captive drop on multiple parameters. Philos. Trans. R. Soc. Lond. 306A, 457-480 (1982).

4. Chang, C.J. and Brown, R.A., Finite element methods for buoyancy-driven convection near a melt/solid phase boundary. In Proc. Second National Symposium on Numerical Methods in Heat Transfer, McGraw-Hill, 1982.

5. Brown, R.A., Yamaguchi, Y. and Charg, C.J., Natural convection in melt crystal growth: the influence of flow pattern on solute segregation. In Proc. National Congress on Theoretical and Applied Mechanics, ASME, 1982.

6. Harriott, G.M. and Brown, R.A., Flow in a differentially rotated cylindrical drop at low Reynolds number. J. Fluid Mech. 126, 269-285 (1983).

7. Chang, C.J. and Brown, R.A., Natural convection in steady solidification: finite element analysis of a two-phase Rayleigh-Bénard problem. J. Comput: Physics submitted (1982).

8. Chang, C.J. and Brown, R.A., Radial segregation induced by natural convection and melt/solid interface shape in vertical Bridgman growth. J. Crystal Growth submitted (1982).

9. Yamaguchi, Y., Chang, C.J. and Brown, R.A., Multiple buoyancy-driven flows in a vertical cylinder heated from below. Proc. R. Soc. Lond. submitted (1982).

10. Harriott, G.M. and Brown, R.A., Flow in a differentially rotated cylindrical drop at moderate Reynolds number. J. Fluid Mech. submitted (1982).

11. Chang, C.J. and Brown, R.A., The onset of time-periodic flows of a low Prandtl number fluid in a rectangular cavity heated from the side. Int. J. Num. Meth. in Fluids in preparation (1982).

12. Ungar, L.H. and Brown, R.A., Nonlinear analysis of cellular melt/solid interfaces. Acta Metallurg. in preparation (1982).

13. Ungar, L.H. and Brown, R.A., Effect of grain boundaries on the evolution of cellular melt/solid interfaces. Acta Metallurg. in preparation (1982).

14. Duranceau, J. and Brown, R.A., Rotationally-driven flows in deformed floating zones. J. Crystal Growth, in preparation (1982).

15. Harriott, G.M. and Brown, R.A., Flow structure and dopant segregation in a floating zone driven by rotation and surface-tension gradients. Int. J. Heat Mass Transfer, in preparation (1982.)

16. Harriott, G.M. and Brown, R.A., Mass transfer driven by rotation in small scale floating zones. J. Crystal Growth, in preparation (1982).

PERSONNEL

Dr. C.H. Chang: Supported by NASA. Ph.D. September 1982. Currently with Texas Instruments, Dallas.

Mr. Y. Yamaguchi: Supported by Mitsubishi Chemical Industries, Ltd. M.S. August 1982. Currently with Mitsubishi.

Mr. G.M. Harriott: Supported by NASA. In fifth year of study toward Ph.D.

Mr. L.H. Ungar: Supported by NSF Fellowship and Department of Chemical Engineering, M.I.T.. In fourth year of study toward Ph.D.

Mr. J.L. Duranceau: Supported by NASA and Department of Chemical Engineering, M.I.T.. In second year of study toward Ph.D.

Mr. P. Sackinger: Supported by NASA and NSF Fellowship. In first year of study toward Ph.D.

ORIGINAL PAGE IS
OF POOR QUALITY

Solutal Convection and Its Effects on Crystal Growth in Binary and Pseudo-Binary Systems with Large Liquidus-Solidus Separation

Principal Investigators: Robert A. Brown
and
August F. Witt

SUMMARY

This report details the first year of a theoretical and experimental study into solutal convection and its effects on crystal growth and segregation in binary and pseudo-binary systems with large liquidus-solidus separation. Significant progress has been made toward the goals of this research. Theoretical analyses of melting and equilibration on melt and solid have yielded new insights into the first stages of crystal growth of binary compounds; a simple, one-dimensional model of directional solidification has been used to examine transient behavior in non-dilute systems; and finite-element methods have been developed for simultaneously calculating thermal- and solutal-driven convection, temperature, and concentration fields and the melt/solid interface shape in vertical Bridgman growth. Experiments at MIT have focused on the melt growth of PbSnTe which has been carried out successfully in both a liquid-encapsulated Czochralski and vertical Bridgman configurations. Research in a parallel collaborative study in the Metallurgy Division of the Centre d'Etudes Nucleaires de Grenoble has centered on the growth of GeSi in a Bridgman furnace.

SCOPE OF PROGRAM

During solidification, conventional doped semiconductor systems exhibit growth and segregation behavior which is in quantitative agreement

with established theoretical concepts for mass transfer and fluid flow. There exists mounting evidence, however, that systems with large liquidus-solidus separation exhibit segregation and morphological characteristics that cannot be reconciled with the conventional pictures for convection in the melt which rely on thermal gradients to create density gradients for driving motions of the melt. In non-dilute systems density differences caused by the rejection of solute during solidification give rise to buoyancy-driven flows that are not accounted for in segregation theory. The goal of our research and of the parallel research programs led by Dr. J. J. Favier of the Metallurgy Division of the Centre d'Etudes Nucleaires at Grenoble is to understand the role of solutal-driven convection in crystal growth of materials with large separation of the liquidus and solidus curves. Experimental and theoretical programs are underway at both institutions and the collaboration has been fueled by trips by E. D. Pourret and R. A. Brown to Grenoble and by J. J. Favier to M.I.T.

The experiments focus on separating out the effects of solutal-driven convection in vertical Bridgman growth of binary and pseudo-binary cyrstals. To do this, two systems are being considered that should exhibit qualitatively different flow behavior. The French group is studying (Rouzaud 1982) Bridgman growth of GeSi (Ge - 5% Si alloy) with the crystal on the bottom. In this configuration, the mean (cross-sectional average) axial temperature increases with distance into the melt and is stabilizing with respect to buoyancy-driven flows. During growth, the heavier component (silicon) is rejected at the solidification front and thus the mean axial composition profile is also stabilizing. Hence, the only convective motions expected in this system are those caused by radial gradients of temperature and composition induced by curvature of the melt/solid interface. The furnace recently designed in Grenoble for these experiments (Rouzaud 1982) will have small radial gradients (theoretically zero) over a nine centimeter length of the furnace while maintaining a 50°C/cm axial gradient.

Experiments at MIT have centered on the growth of PbSnTe, a pseudo-binary compound, which when grown in the thermally stable Bridgman configuration rejects the less dense component (SnTe) at the inter-

face and so leads to a density profile in the melt that is unstable. Much more rampant convection is expected here than in the GeSi system. Progress toward these experiments is described below.

The two experimental programs are coupled together by theoretical calculations being developed at MIT for the steady convection in prototypes of these experiments. The calculations are based on the finite element algorithm developed by Chang (Chang and Brown 1982) for computing simultaneously the temperature, velocity, and pressure fields in the melt, the temperature field in the crystal, and the shape of the melt/solid phase boundary for a single-component melt. A great deal of thermo-physical data is necessary to successfully model either of these experimental systems. Only in the GeSi system is the data available (Dismuke and Kim 1974). A thorough literature survey of the PbSnTe system (Adornato 1981) has exposed large gaps in the knowledge of this system, especially in the melt. For example, such routine data as the thermal conductivity of the melt has not been measured. Without this data, the matching of calculations to experiments will be extremely tenuous.

RESEARCH SUMMARY

Basis Factors Controling Seeded Melt Growth of Concentrated Alloys.

Experiment design and execution:

Basic studies of semiconductor crystal growth from the melt have in the past been mainly concerned with the behavior of dilute (doped) alloy systems. Recently, however, focus is being placed on more complex pseudobinary systems (HgCdTe, PbSnTe, GeSi, GaInSb, etc.) in which the liquidus-solidus separation becomes larger. A large liquidus-solidus gap may lead to major complications for experiment design and execution since the growth interface temperature is a pronounced function of composition and thus subject to change by several tens of degrees during the course of a growth experiment. Complications in solidification of such crystals arise primarily from uncertainties concerning the growth interface temperature and the location and shape of the crystal-melt interface within a given thermal gradient region. A seeded melt-growth experiment in a Bridgman-type con-

figuration can be conducted either by establishing melt-seed contact or by partial melting of a single crystal ingot and subsequent regrowth. This last procedure was adopted, for example, in growth experiments under reduced gravity conditions (Witt et al. 1978). In both approaches the actual location of the seed-melt interface within the thermal gradient region is controlled by the prevailing compositions of the contacting phases. The concentrated alloys, the growth interface temperature at the end of the back-melting (seeding operation) as well as during equilibration assumes a value which is a priori unknown but is somewhere between the solidus and liquidus temperatures, which in such systems may differ by as much as 100°C. The consequences of this uncertainty in the value of the interface temperature are apparent in Fig. 1 which provides a schematic axial temperature distribution in a Bridgman growth configuration. Accordingly, if the growth interface temperature is close to the liquidus temperature, the indicated location of the ampoule is adequate; if, however, the interface temperature approaches the solidus temperature, the depicted growth configuration will lead to failure of the experiment.

A further experimental complication arises from the requirement of growth interface "planarity" which is considered essential if radial compositional homogeneity in the absence of convection is to be achieved. While it is feasible in Bridgman configurations to control heat flow for the establishment of growth interface planarity at a given temperature (Fig. 2), it is beyond the state-of-the-art to achieve interface planarity at a given temperature (parallel heat flow) over a temperature range of about 100 °C. A solution, in principle, can be found if, for transient melting and growth, the time (composition) dependence of the growth interface temperature is theoretically or experimentally determined and heat flow conditions are continuously adjusted so as to maintain interface planarity under transient growth conditions.

The complications associated with seeded crystal growth of systems with large liquidus-solidus separation are related to diffusive mass transfer within and between the liquid and solid phases involved. Since mass transfer in the liquid phase is strongly affected by convection, any meaningful growth experiment must be carried out either in the absence of convection or under conditions of controlled convection.

ORIGINAL PAGE IS
OF POOR QUALITY

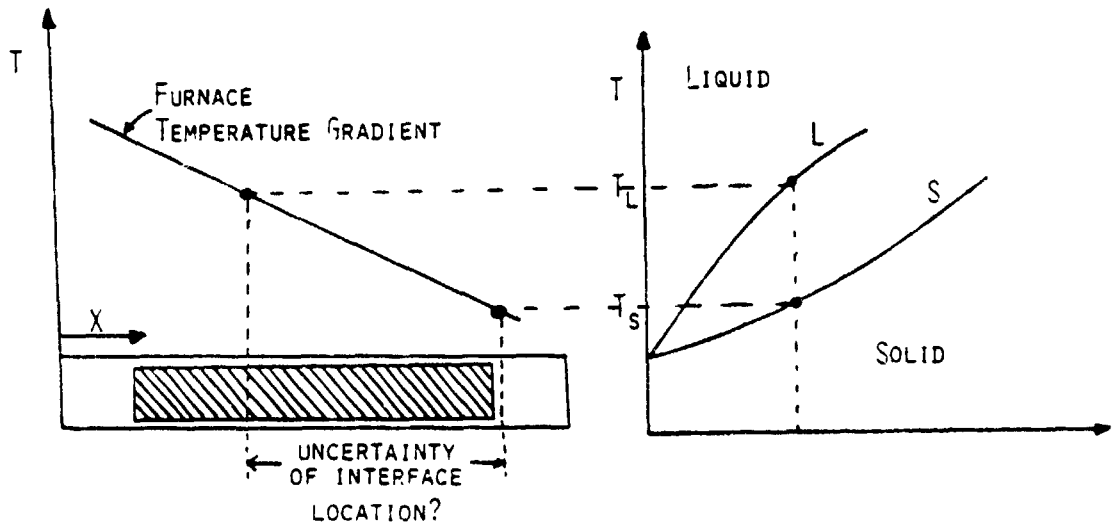

Figure 1. Uncertainty of interface location in systems with large liquidus-solidus separation.

ORIGINAL PAGE IS
OF POOR QUALITY

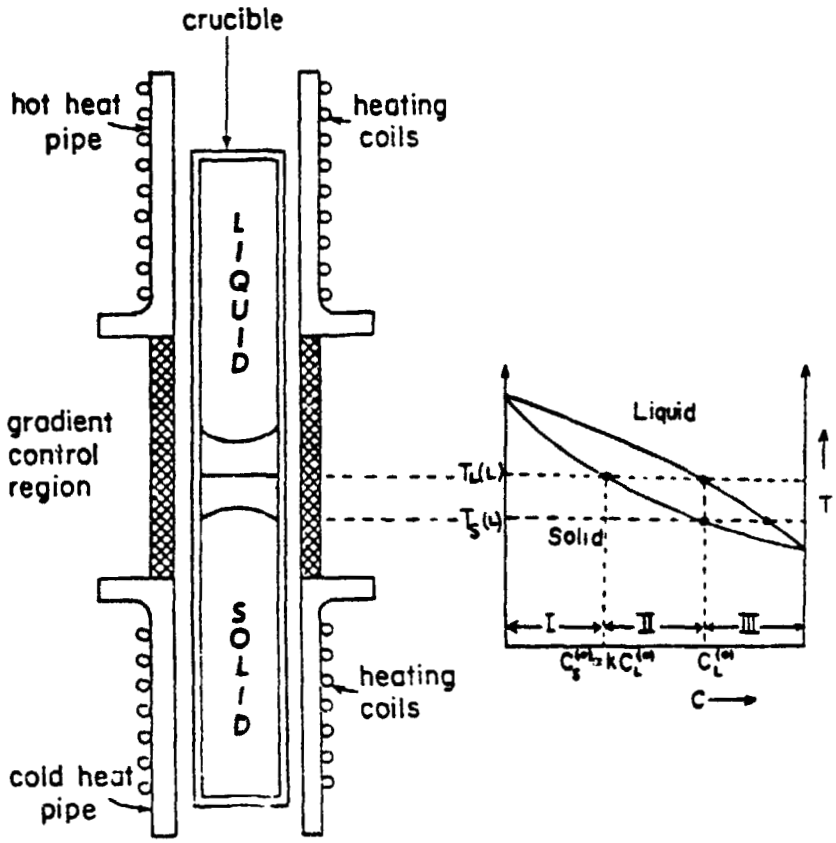

Figure 2. Schematic of Bridgman growth of non-dilute binary crystal.

Melt-Seed Contact and Equilibration.

In a binary system, such as the one schematically indicated in Fig. 2, there is only one set of compositions, C_S and C_L, at a given temperature for which the liquid phase and the contacting solid phase are in thermodynamic equilibrium; for example, $C_L = C_L^{(o)}$ and $C_S = C_S^{(o)}$ at $T_{L(L)}$. This particular configuration must be considered as hypothetical since it is not normally realized in seeded crystal growth experiments. A whole range of concentrations can be encountered for both the solid and the liquid phase at the beginning of the equilibration period, i.e., when the melt contacts the seed. For example, the seed composition is often identical to that of the melt. Any configuration departing from equilibrium yields instabilities, and diffusional transfer takes place through the liquid-solid interface. In the subsequent analysis, the interface temperature at the time of arrest is taken to be the liquidus temperature at the concentration of the melt so that there are no additional phenomena due to a supercooled melt. The range of composition chosen for the seed should be limited to regions I (Fig. 2) and II since in region III the seed would melt to an extent determined by the thermal gradient in the furnace and the resulting increase in the melt concentration would decrease its liquidus temperature.

The free energy curves drawn at $T_{L(L)}$ for the liquid and the solid phases are shown in Figs 3 and 4. A solid at $C_S^{(o)}$ in region I (Fig. 3) cannot form a liquid at temperature $T_{L(L)}$. The transition from $C_S(o)$ to a value of lower free energy can occur by diffusion of the solute through the interface and yield an equilibrium configuration at the interface. If diffusion in the liquid is much faster than in the solid ($D_L >> D_S$) or in the presence of intense convective mixing, no boundary layer build-up in the liquid phase occurs (assuming infinite length to eliminate end effects) and the transformation is essentially isothermal (path <1> in Fig. 3). As the ratio $\alpha = D_S/D_L$ increases, a solute boundary layer will form ahead of the solid-liquid interface. The interface composition in the liquid phase decreases, which induces a simultaneous increase

ORIGINAL PAGE IS
OF POOR QUALITY

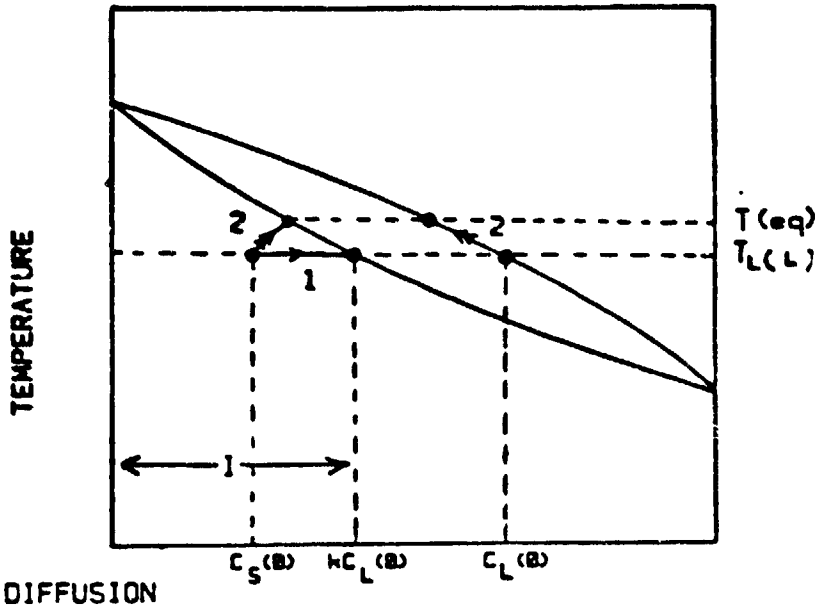

1- ISOTHERMAL DIFFUSION
($D_L >> D_S$)

2- SOLIDIFICATION

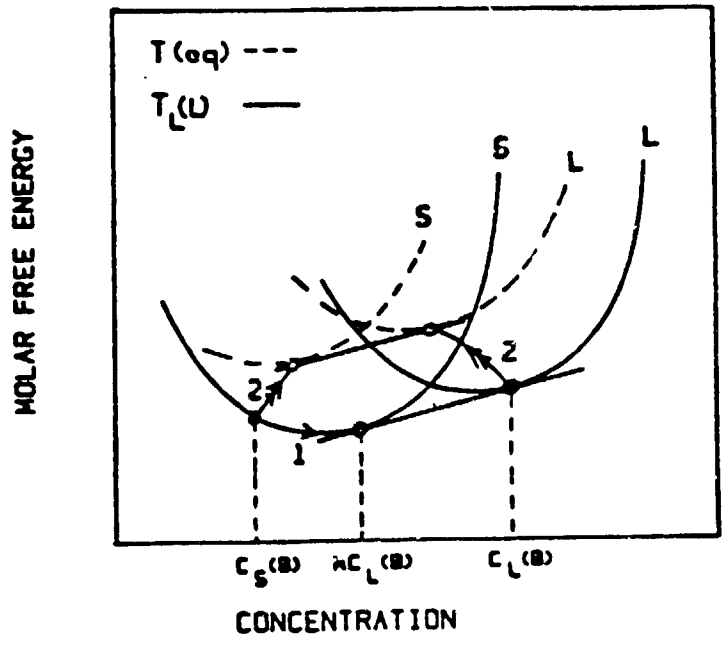

Figure 3. Thermodynamic behavior of a system for which the seed composition is at $C_S(0)$ in region I and the melt composition is at $C_L(0)$. The initial temperature of the interface is $T_L(L)$.

ORIGINAL PAGE IS
OF POOR QUALITY

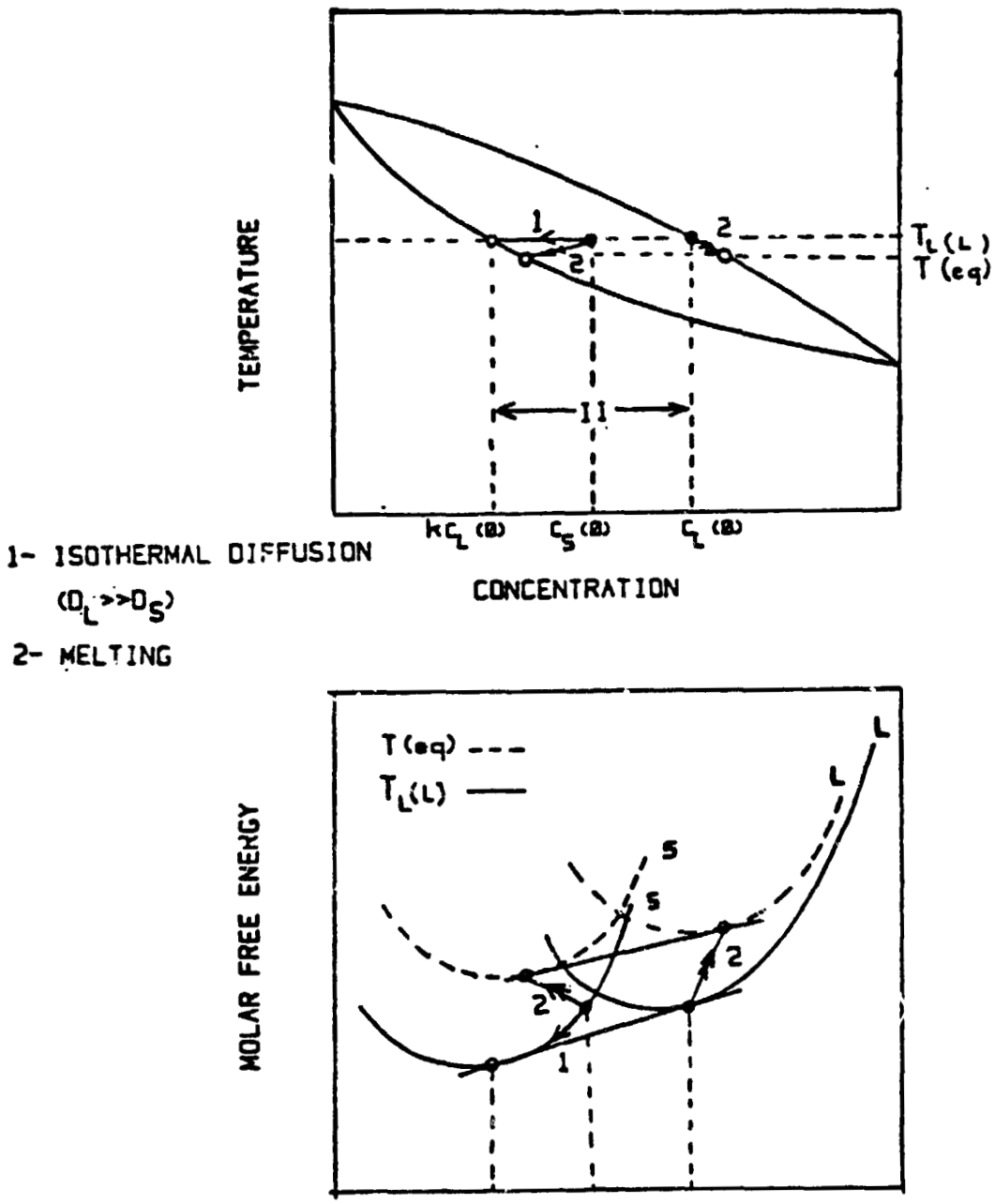

Figure 4. Thermodynamic behavior of a system for which the seed composition is at $C_S^{(0)}$ in region II and the melt composition is at $C_L^{(0)}$. The initial temperature of the interface is $T_{L(L)}$.

in the interface temperature according to the shape of the liquidus curve (path 2 in Fig. 3). Subsequently, the interface moves toward the liquid and solidification occurs during equilibration.

In region II of the phase diagram (Fig. 4) the solid can form a liquid, which lowers its free energy toward an equilibrium configuration. The extent to which the seed melts is limited by the mass transfer through the interface, the thermal gradient in the furnace and the dilution effect resulting from melting of the seed. If $D_L >> D_S$, as for the case of the seed composition in region I, the process is isothermal. As $\alpha = D_S/D_L$ increases, the interface temperature drops due to the solute diffusion layer in the liquid phase and equilibration occurs through melting of the seed. Melting of the seed is expected to be a rapid, diffusionless process; the resulting dilution of the melt can then result in partial resolidification. In region III, an increase in the melt composition due to melting of the seed will induce further backmelting until equilibrium is reached.

The above thermodynamic considerations are useful to predict if the equilibration step is accompanied by solidification ($C_S^{(o)}$ in region I) or by melting ($C_S^{(o)}$ in region II); it, however, fails to give quantitative data for the evolution of the concentration and temperature at the liquid-solid interface and in both bulk phases. Ghez and Small (1981; also see Small and Ghez 1979) have solved the problem of mass transfer involved in the equilibration process for the formulation of heterostructures by liquid phase epitaxy. An analysis of equilibration during seeding in melt-growth differs from their treatment for the thermal field governing the process and for the simultaneous change of the bulk melt concentration as mentioned earlier. It then involves a solution for the coupled heat and mass transfers in both phases, the interface conditions being tied to thephase diagram. Such a Stephan problem has not yet been solved analytically. However, the expected results can be qualitatively assessed. In Fig. 5, regions I and II are referred to as "stable" and "unstable" respectively with regard to the morphological stability of the interface in each configuration. For convenience, one introduces

ORIGINAL PAGE IS
OF POOR QUALITY

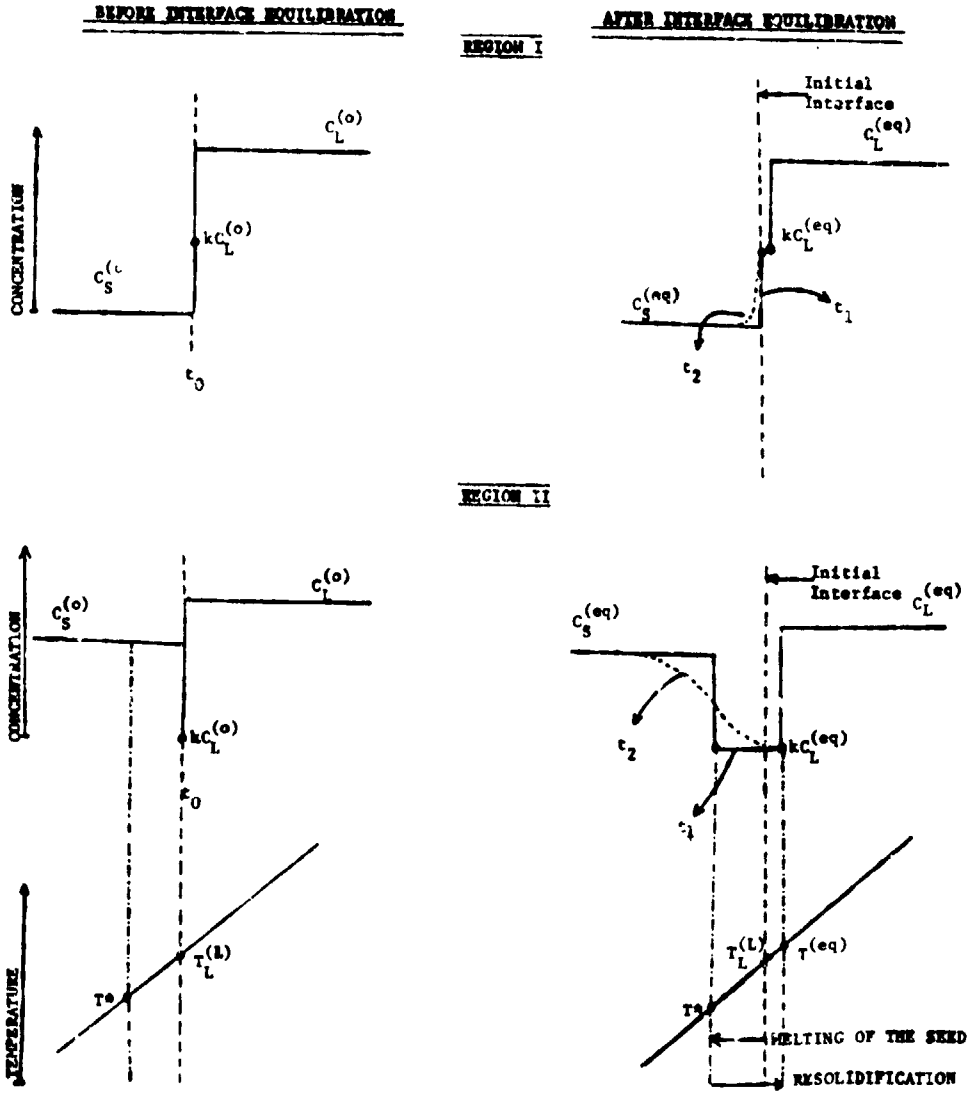

Figure 5. Compositional inhomogeneities due to equilibration in the crystal once re-growth is initiated.

ORIGINAL PAGE IS
OF POOR QUALITY

the ratio of the initial bulk seed composition to the initial bulk melt composition, $p = (C_C^{(o)}/C_L^{(o)})$. From the previously stated assumption, the interface temperature is the liquidus temperature $T_{L(L)}$ and the system is maintained in a positive stabilizing thermal gradient. The solid then is in a stable configuration in region I, if $p < k$, $k < 1$ or $p > k$, $p > 1$, since the temperature of the interface is below the solidus temperature for the range of concentration between $C_S^{(o)}$ and $C_S^{(eq)}$ ($C_S^{(eq)}$ is the interface composition in the solid once equilibrium is reached.). In the liquid phase, the temperature is at the liquidus temperature at the interface and above it further from the interface. According to the consitutional supercooling criteria (Rutters et al. 1953), the system is in a stable configuration.

In region II, the system is subject to morphological instabilites and steep temperature gradients are required to maintain stability if $p > k$, $k < 1$ or $p < k$, $k > 1$. Initial conditions such that $p < k$, $k < 1$ or $p > k$, $k > 1$, corresponding to the bulk seed composition in region I are then favorable since it prevents regions of supercooled liquid or superheated solid. The concentration profiles expected in the crystal after equilibration and are presented in Figure 5 for each initial condition, discussed above. If the seed is initially in region I, a transition region of uncontrolled growth is expected in which the concentration increases rapidly, due to uncontrolled solidification. If the seed is initially in region II, a decrease in the concentration is expected in the region of uncontrolled growth, due to melting and eventual partial resolidification, as discussed earlier. It is important to note that the exact concentration profiles in the region of uncontrolled growth are strongly dependent on the level of convective mixing in the melt.

Crystal Growth and Characterizations of PbSnTe.

Experimental research has focused on techniques for the melt growth of single crystal PbSnTe and for the characterization of its segregation behavior. Both the vertical Bridgman and Czochralski techniques have been used successfully to grow PbSnTe. In the Bridgman

technique, a precast charge of PbSnTe is loaded into a quartz ampoule that is tapered on the bottom to seed the crystal. The ampoule is positioned in the vertical furnace described by Witt (1981) and melted. Directional solidification is driven by lowering the ampoule from the bottom of the furnace and the onset of solidification is by heterogeneous nucleation caused by the temperature at the bottom of the ampoule dropping below the solidus temperature of PbSnTe melt. When the included angle of the tapered ampoule exceeded 60°, the grains in the poly-crystal grew toward the side of the ampoule and left a single crystal in the cylindrical portion of the ampoule. Heterogeneous nucleation was suppressed completely by seeding the melt with a single crystal of PbSnTe with <100> orientation. Results of experiments with seeded growth are described in [3] and highlighted below.

The PbSnTe crystals grown by either the Czochralski or vertical Bridgman methods were soft and cleaved easily along the [100] direction. Special care was needed to minimize mechanical stresses in the crystal induced during preparation of the crystal; for example, both ultrasonic cleaning and high-speed mechanical polishing had to be avoided. Good quality polishing of slices cut with a low-speed wire saw was obtained by sequentially:

1. Polishing with 5 μm Al_2O_3 powder on a glass plate.
2. Polishing with 0.3 μm Al_2O_2 on a felt pad.
3. Polishing with 0.05 μm Al_2O_3 on a felt pad.
4. Polishing with a Clorox-Syton mixture (one-to-one by volume) on a felt pad.

The quality of the crystal surface was controlled by Normarski interference microscopy. This procedure yielded perfectly polished surfaces that were the source material for studies of differential etching.

Striations in the crystals grown by the Czochralski method were revealed using the Norr electrolytic etch (6 volts for 4 minutes). Compositional traces made by the electron microprobe confirmed that this etching differentiates between PbTe and SnTe rich regions. This etchant has failed to reveal the concentration variations caused by

ORIGINAL
OF POOR

Peltier pulsing in the vertical Bridgman configuration. The cause of this failure is not completely understood, although one possible explanation is the lack of sensitivity of the etchant to small concentration fluctuations. This point is being investigated further.

Since the large liquidus-solidus separation in the PbSnTe system caused a pronounced composition dependence of the growth on the interface temperature, it was of interest to analyze both the growth and segregation behavior in the region of the seed-melt interface. We have done this using composition analyses (wt. % Sn) based on electron microprobe scans for crystals grown in the vertical Bridgman system; complete results are reported in [3]. The axial composition profiles are shown in Figure 6 for the two crystals (A and B) whose growth parameters are summarized in Table I and indicate the existance of a "transition region" between the seed and the crystal grown at constant lowering rate; in this region the Sn concentration changes from that of the seed to the melt composition resulting from dilution of the charge by the partial melting of the seed. Using microprobe scans with 11 μm spacings this transition region is found to have a thickness of 400 and 150 μm for the crystals A and B, respectively.

The origin of the region of uncontrolled growth was deduced from the length of seed meltback (7 mm in both crystals) and the composition of the initial region of growth. Upon meltback of the seed, with the crystal-melt interface at the liquidus temperature, a melt region is generated in which the Sn concentration is significantly less than in the bulk melt. Since, during the ensuing equilibration period the Sn concentration in this region increases because of the diffusion and convection of Sn from the bulk melt, the liquidus temperature will increase and cause crystal growth at the melt/solid interface without pulling of the crystal. The magnitude of this uncontrolled growth is a function of the compositions of the seed and bulk melt, the extent of meltback, the length of melt, and the degree of compositional equilibration of the melt. In terms of these parameters, the difference in the widths of the uncontrolled growth regions in crystals A and B is attributed to the lower Sn concentration in the seed of A which results

ORIGINAL PAGE IS
OF POOR QUALITY

in a lower interface temperature during meltback and more extensive uncontrolled growth during equilibration of the melt, than for crystal B.

It is significant that, within the error limits of the analysis, the composition of the initial portion of controlled growth is the same for both crystals. The short equilibration period of only 40 minutes for crystal A points to the fact that convective mixing was the prevalent mechanism for obtaining compositional uniformity of the melt. As is seen in Figure 6, the axial composition profiles for the first 3 mm of growth in crystals A and B are identical within error bounds for the microprobe. Tin also was found to be distributed uniformly across the radius of each crystal as shown in Figure 7. Strictly, this result is inconclusive since a uniform Sn concentration can result from either a flat melt/crystal interface in the absence of convection or from a curved interface coupled with so rampant convection that a thin and uniform boundary layer forms along the interface and isolates the crystal from radial segregation. When taken together, the radial and axial segregation behavior point to convection in the melt, especially adjacent to the interface.

Modelling of Growth and Convection in Non-Dilute Binary Systems.

We have pursued two approaches in our efforts to model the directional solidification of binary crystals. In the first, the transients in growth rate and composition caused by changes in the ampoule pull rate or the temperature of the surroundings are being studied using a simple, time-dependent one-dimensional model for solidification. In the second set of calculations, the more detailed finite-element calculations are being used to determine the fluid flow and melt/solid interface shapes in a steady-state prototype of the Bridgman system. The motivation and approach to each of these analyses is laid out below.

OF P

ORIGINAL
OF POOR

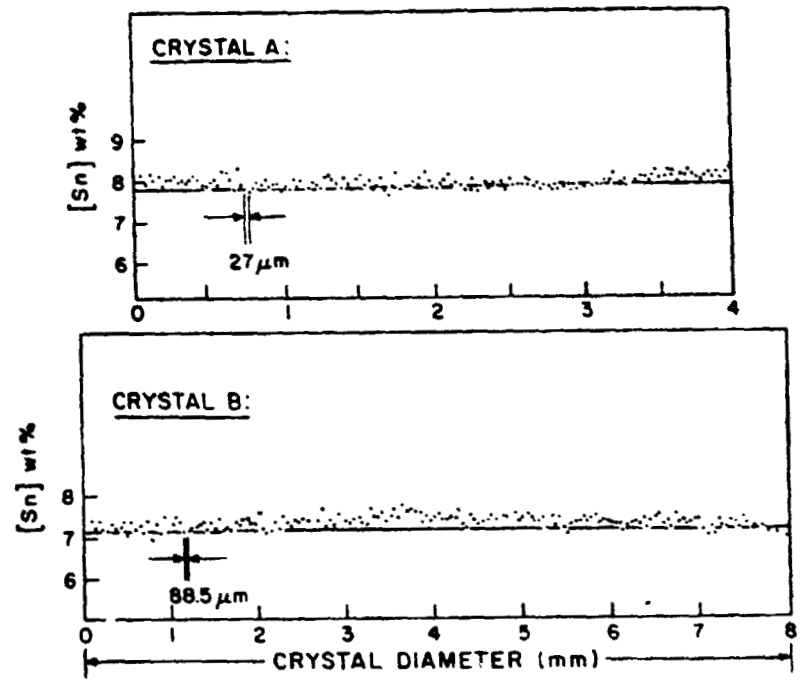

Figure 7. Radial solute segregation in $Pb_{0.7}Sn_{0.3}Te$ crystals A and B grown at V = 0.5 μm/sec.

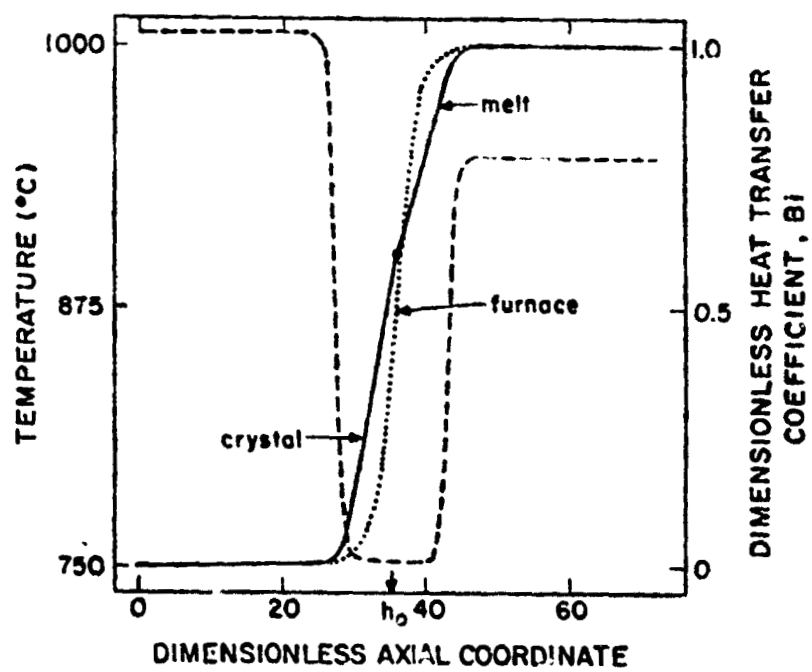

Figure 8. Distribution of furnace temperature and heat transfer coefficient for the static ampoule.

ORIGINAL PAGE IS
OF POOR QUALITY

One-Dimensional Modelling of Transients in Directional Solidification.

When the melting point of the crystal is strongly dependent on the composition of the melt at the melt/solid interface the rate of equilibrium of the growth velocity to changes in the pull rate depends on the rate of equilibration of the composition field in the melt as well as on the time for equilibration of the thermal field. In fact, for typical binary and pseudo-binary melt growth systems, e.g., HgCdTe, PbSnTe, and GeSi, the time scale for mass diffusion is much larger than the one for heat and it controls the rates of any transients in the growth system.

We have developed a one-dimensional (in the axial direction) model of heat and mass transport in a Bridgman system that contains all the gross features of the growth when mass transfer is controlled by diffusion. Even in this case the resulting equations describe a moving boundary problem for the location with time of the melt/solid interface, the concentration profile in the melt and the temperature profile in both phases. The boundary immobilization method first developed by Landau (see Ettouney and Brown 1982) is used to discretize this equation set on a finite difference mesh fixed in space and the system of nonlinear ordinary differential equations that results are solved using a variable step-size Runge-Kutta integration scheme. Applications of this scheme to the growth of PbSnTe are discussed below.

When the thermal and mass diffusivities are much different, i.e., when the Lewis number $Le \equiv D/\alpha_T$ is not close to unity, the equation set is numerically stiff and the Runge-Kutta scheme is forced to march in very small time increments in order to maintain a prescribed level of accuracy. The levels of accuracy and efficiency in the integration scheme necessary for repeated detailed simulations of real growth systems have been reached by solving the original set of 60-100 coupled differential equations by an implicit (Gear 1976) integration scheme that is numerically stable for larger time steps. This technique requires the solution of a set of nonlinear algebraic equations at each time step, but allows

ORIGINAL PAGE IS
OF POOR QUALITY

Table I. Conditions for Growth of PbSnTe.

Parameter	Crystal A	Crystal B
Seed Composition (% SnTe)	7.2	11.1
Charge Lowering Rate (μm/sec)	0.5	0.5
Initial Melt Aspect Ratio (h(o)/a)	15.0	6.8
Initial Melt Composition (% SnTe)	30	30
Weight of Charge (grams)	3	14.7
Equilibration Time Prior to Growth	40 min	12 hours
Gas Atmosphere Above B_2O_3	Ar (1atm)	Ar (1 atm)

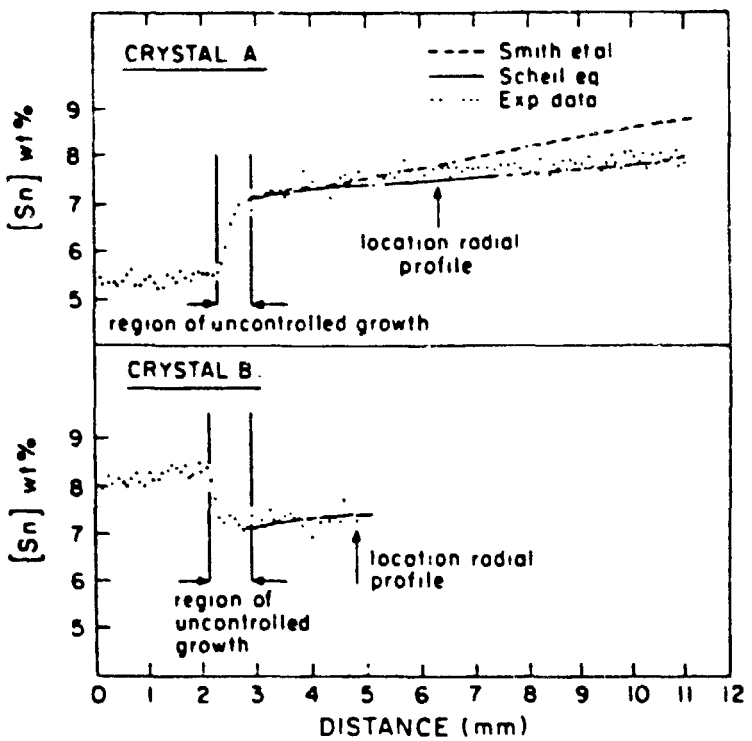

Figure 6. Axial solute segregation in crystals A and B of $Pb_{.7}Sn_{.3}Te$.

much larger time steps for numerical stability. Comparisons between the Runge-Kutta and implicit integration schemes show the implicit methods to be most efficient.

Calculations are reported in [3] for the growth of $Pb_{0.8}Sn_{0.2}Te$ in a vertical Bridgman system under convectionless conditions. The numerical simulations are carried out for an ampoule with 0.5 cm radius being pulled initially at a growth rate of 0.5 μm/sec. The temperature profile along the wall of the furnace is shown in Figure 8 along with the dimensionless heat transfer coefficient between the furnace and the ampoule. The transient that appears at the beginning of pulling was simulated by starting the numerical simulation with the temperature profile for a stationary and equilibrated ampoule. As the ampoule moves the temperature changes toward the solidus temperature as illustrated by the five temperatures shown on Figure 9. These curves correspond to the following steps in growth:

<0> the equilibrated system (t = 0 sec).

<1> displacement of the ampoule by 1 cm: V = 0.5 μm/sec and t = 2×10^4 sec.

<2> displacement of the ampoule by 2 cm: V = 0.5 μm/sec and t = 4×10^4 sec.

<EQ> equilibration of ampoule after growth rate arrest at t = 4×10^4 sec: V = 0 and t = 6×10^4 sec.

<3> displacement of the ampoule by 3 cm after resumption of pulling at t = 6×10^4 sec; V = 0.5μm/sec and t = 8×10^4 sec.

The 3.5°C rise in interface temperature during the period of equilibration in the middle of the run corresponds to a decrease in the SnTe concentration at the interface as it's gradient was flattened by diffusion toward the bulk of the melt. This point is illustrated on Figure 10 where the solute distributions corresponding to each of these points in the experiment are shown. During the initial period of pulling, the solute diffusion layer grew at the interface. Upon stopping the ampoule, solute diffusion away from the interface dominated over the small amount of SnTe rejection caused by the uncontrolled growth and the solute composition decreased the interface. After the resumption of pulling

ORIGINAL PAGE IS
OF POOR QUALITY

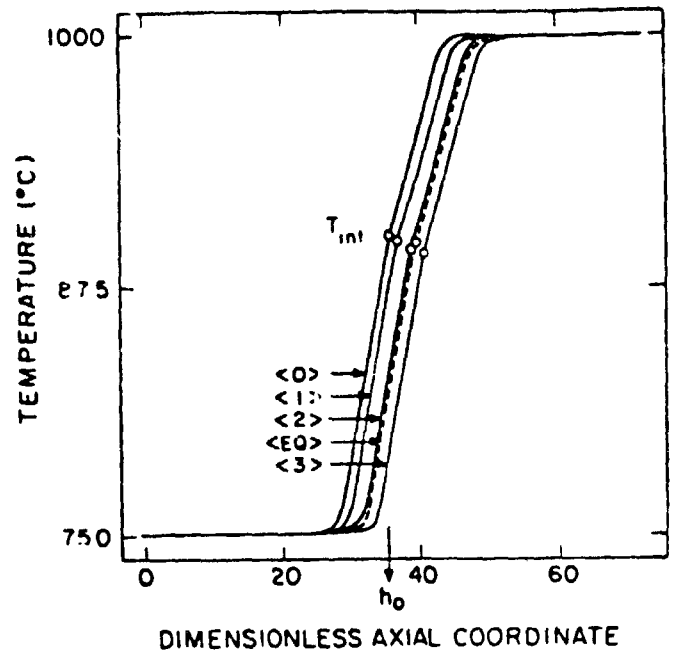

Figure 9. Variation of axial temperature profile during growth of $Pb_{0.8}Sn_{0.2}Te$ crystal at V = 0.5 μm/sec . Curves correspond to specific times during the transition to steady growth and equilibrium in the melt.

Table II. Interface Temperatures During Transient Growth of PbSnTe .

Point	Time (10^4 sec)	Temperature T(h(t))(°C)
<0>	0	900.8
<1>	2	895.3
<2>	4	891.5
<EQ>	6	895.0
<3>	8	890.0

ORIGINAL PAGE IS
OF POOR QUALITY

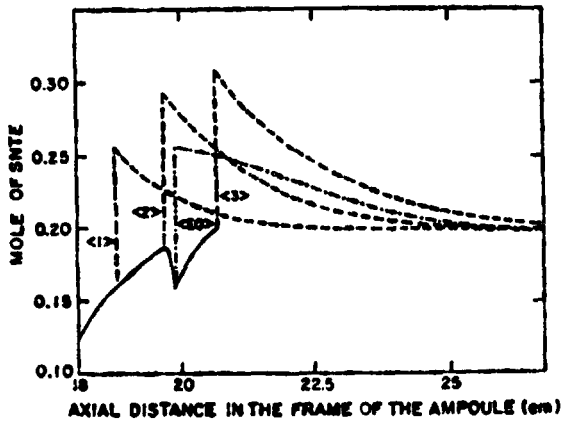

Figure 10. Concentration of SnTe in the crystal during initial transient for V = 0.5 μm/sec, a short equilibration period, and a resumption in pulling. Concentration profiles in the melt are also shown for several interface positions.

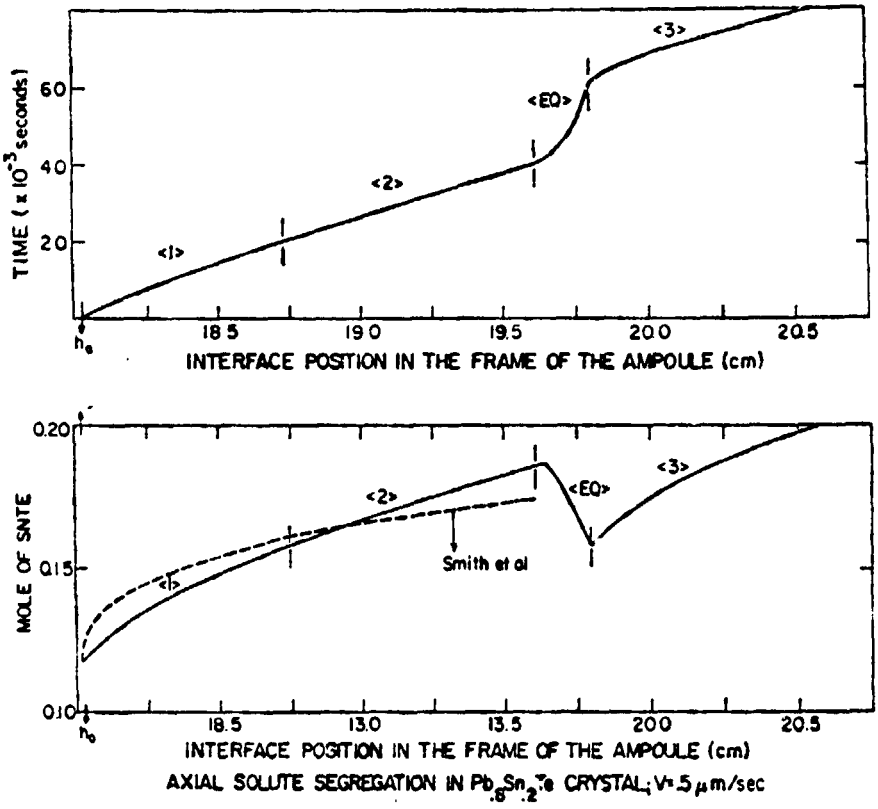

Figure 11. Interface position as a function of time for the sequence of pulling rate changes described for Fig. 10.

the solute profile started to develop a new gradient, but followed a different transient than at the onset of the run, because a non-planar solute profile existed at $t = 6 \times 10^4$ sec.

The time history of the ratio of growth rate to pull rate R(t)/V is shown on Figure 11, with markers to show the different steps of the simulated run. Steady state is not reached during the first two centimeters of ampoule translation, as shown by the failure of R(t)/V to reach unity. End effects in the concentration profile make it impossible for the growth rate to ever reach the pull rate. The coupling between the growth rate and the transient transfer of solute is the major difference between growth of dilute and non-dilute alloys. To make clear the importance of this coupling, we calculated the initial transient for the growth of a dilute alloy with thermal properties identical to those used for PbSnTe, but with the melting point fixed at 901°C. This case is plotted on Figure 12 as the dashed curve and shows the much more rapid thermal equilibrium that is possible in the dilute system.

The one-dimensional model for directional solidification described in [3] is also being used to model transient behavior in other binary (GeSi) and pseudo-binary (HgCdTe) systems with large liquidus-solidus separation; these results will be reported in [4].

Finite Element Calculations of Solutal Convection

Melt/solid interface shape and segregation in the crystal are the most easily measured indicators of the role of convection in melt growth systems. New numerical methods developed by Chang and Brown (1982) make possible the solution of the full free-boundary problem governing small-scale crystal growth systems. Chang's algorithm has been used at M.I.T. to study convection and mass transfer of a dilute component in thermally stabilized and destabilized vertical Bridgman systems; results of these calculations are described in Chang and Brown (1982).

Peter Adornato has modified this algorithm to include the coupling between the solute, temperature and velocity fields caused by solutal-driven convection and by the phase diagram. These modifications are straight forward for calculations at low solutal Rayleigh numbers and for completely stabilized systems like GeSi. In these calculations, the convection driven density differences is weak, solutal boundary-layers are broad, and the moderate separation of liquidus and solidus leads to small displacement of the interface. Our calculations to date have focused on the GeSi system being studied in Grenoble.

For systems with a large gap between liquidus and solidus (HgCdTe for example) the deformation of the interface caused by radial segregation may be severe. In systems that are unstable with respect to either the axial solute or temperature profile convection will be severe and thin solute boundary layers will form along the ampoule and the interface. In the next year, the multi-grid method developed by Chang (1982) will be adapted to attempt to calculate these cases.

BIBLIOGRAPHY

Adornato, P.M., Thermophysical properties of PbSnTe: Literature Review. Internal Report, Department of Chemical Engineering, M.I.T., 1981

Chang, C.J. and Brown, R.A., Radial segregation induced by natural convection and melt/solid interface shape in Bridgman growth. J. Crystal Growth submitted (1982).

Dismuke, J.P. and Kim, W.M., A survey of interface stability criteria in the elemental alloy systems: Ge-Si, Bi-Sb, and Se-Te. J. Crystal Growth 22 287-294 (1974).

Ettouney, H.M. and Brown, R.A., Finite element methods for steady solidification problems. J. Comp. Physics, in press (1982).

Gear, C.W., Numerical Initial Value Problems in Ordinary Differential Equations, Prenctice-Hall, Englewood Cliffs, 1972.

Ghez, R. and Small, M.B., Growth and dissolution of ternary III-V compounds by liquid phase epitaxy and the formation of heterostructures. J. of Crystal Growth 52, 699-702 (1981).

Rouzaud, A., Rapport advancement sur l'etude de la convection thermosolutale dans un alliage germanium-silicum. Center D'Etudes Nucleaires de Grenoble, 1982.

Rutter, J.W., Chalmers, B., A prismatic substrate formed during the solidification of metals. Can J. Phys. 31, 15 (1953).

Small, M.B. and Ghez, R. Growth and dissolution kinetics of III-V heterostructures formed by LPE. J. Appl. Phys. 50 (8), 5322.

Witt, A.F., Heat flow control segregation in direction solidification, Annual Report of Materials Processing Center, M I.T., 1981.

Witt, A.F., Gatos, H.C., Lichtensteiger, M. and Herman, C.J., Crystal growth and segregation under zero gravity: Ge, J. Electrochem. Soc. 11 (1978) 1832.

PRESENTATIONS (Since - 1/1/82)

1. Bourret, E.D. and Witt, A.F., "Second Crystal Growth of Pseudo-Binary Systems with Large Liquidus-Solidus Separation," Annual Meeting of American Ceramics Society, Cincinati, May 1982.

2. Bourret, E.D., Derby, J.J., Brown, R.A. and Witt, A.F., "Segregation Effects During Growth of Pseudo-Binary Systems with Large Liquidus-Solidus Separation," International Aeronautics Federation, Paris, October 1982.

3. Brown, R.A., "Natural Convection in Melt Crystal Growth," Centre de Etude Nucleaire, Grenoble (October 1982).

4. Bourret, E.D., "Crystal Growth of PbSnTe, "Centre de Etude Nucleaire, Grenoble (October 1982).

PUBLICATIONS

1. Bourret, E.D., Favier, J.J. and Witt, A.F., Segregation during directional melting and its implications on seeded crystal growth. J. Crystal Growth in press (1982).

2. Bourret, E.D. and Witt, A.F., Basic factors controling seeded melt-growth of concentrated alloys. J. Crystal Growth, submitted (1982).

3. Bourret, E.D., and Derby, J.J., Brown, R.A., and Witt, A.F., Segregation effects during growth of pseudo-binary systems with large liquidus-solidus separation. Proc. International Aeronautics Federation, Paris 1982.

4. Derby, J.J., Bourret, E.D., Witt, A.F. and Brown, R.A., Dynamics of Bridgman growth of pseudo-binary crystals with large liquidus-solidus separation. J. Crystal Growth in preparation (1982).

5. Adornato, P.M. and Brown, R.A., Solute-driven convection in vertical Bridgman growth of a non-dilute binary crystal. J. Crystal Growth in preparation (1982).

PERSONNEL

1. Dr. E.D. Bourret: Supported by NASA. Research Associate.

2. Mr. P.M. Adornato: Supported by NASA. In third year of study toward Ph.D.

3. Mr. J.J. Derby: Supported by NASA and NSF Fellowship. In second year of study toward Ph.D.

Analysis of Polymer Melt Processing Operations

Principal Investigator: David K. Roylance

RESEARCH ABSTRACT

This report outlines the equations which govern the nonisothermal flow of reactive fluids, and describes the means by which finite element analysis can be used to solve these equations for the sort of arbitrary boundary conditions encountered in industrial practice. The performance of the computer code is illustrated by several trial problems, selected more for their value in providing insight to polymer processing flows than as practical production problems. Although a good deal remains to be learned as to the performance and proper use of this numerical technique, it is undeniably useful in providing better understanding of today's complicated polymer processing problems.

RESEARCH REPORT

Introduction.

Finite element analysis offers great promise for reducing the empiricism often found in polymer processing design, since it is well suited for modeling the complicated boundary conditions and material properties encountered in industrial practice. Although the method is now well accepted in structural stress analysis, its use in fluid transport situations is less widespread. We have sought to exploit some of the many advantages of the finite element method in polymer fluid processing analysis, and this paper describes some of our work in chemorheology.

Reactive flows have several advantages in polymer processing in comparison with more traditional melt-flow techniques. Perhaps the most significant of these is the energy savings which result from the elimination of the several melting stages necessary in such technologies as extrusion or injection molding. However, these advantages are offset to some degree by the complexity of the process, which renders the empirical approach to process development difficult in the extreme.

The flow velocities in such processes are governed by the fluid viscosity, which is a strong function of temperature and molecular weight. The temperature in turn is affected by the viscous dissipation and the heat released or consumed

by the reaction, and the reaction rate is also a strong function of temperature. All of these variables interact and change in such a way as to make an intuitive grasp of the process almost impossible, and there is obviously an advantage to being able to provide some sort of mathematical or numerical simulation of the process.

The finite element scheme to be described below is very useful for obtaining numerical solutions for reactive flows with arbitrary boundaries, and such a technique is well suited for detailed analysis of real industrial processes. However, we argue that the greatest value of the method may not be in these detailed calculations, but in the degree to which the method can enhance the process designer's intuition. For this latter purpose, it is often sufficient to run only very small and inexpensive trial problems; these can elucidate the manner in which the various problem parameters interact, so that the designer develops a much improved "feel" for the problem. It is likely that most real advances in processing technology will continue to be made more by Edisonian innovation than by detailed mathematical calculations. But since today's processes have become so complicated, such a technique as the finite ele-

ment method can be a powerful adjunct to intelligent intuition.

Theoretical background.

The equations which govern the nonisothermal flow of a reactive fluid are derived in several texts on transport phenomena and polymer processing (e.g. refs. 1,2). Regarding velocity, temperature, and concentration of unreacted species as the fundamental variables, the governing equations can be written as:

$$\rho[\partial u/\partial t + u\bullet\nabla u] = -\nabla p + \mu\nabla^2 u$$

$$\rho c[\partial T/\partial t + u\bullet\nabla T] = Q + k\nabla^2 T$$

$$[\partial C/\partial t + u\bullet\nabla C] = R + D\nabla^2 C$$

(A list of nomenclature is attached.) The similarity of these equations is clear. In all cases, the time rate of change of the transported variable (velocity, temperature, or concentration) is balanced by the convective or flow transport terms (e.g. $u\bullet\nabla C$), the diffusive transport (e.g. $D\nabla^2 C$), and a generation term (e.g. R).

ORIGINAL PAGE IS
OF POOR QUALITY

The analyst seeks expressions for the space- and time-dependent velocities, temperatures and concentrations which satisfy these equations and also the problem's boundary conditions. It is generally the boundary conditions which make real problems intractable: even if one were able to describe the boundaries mathematically, the resulting expressions would not likely be amenable to closed-form solution. In addition, many of the "constants" in the above equations are often nonlinear functions of the problem variables. In reactive polymer processing, one might encounter such expressions as the following:

$$\eta = \eta_0 \dot{\gamma}^{n-1} \exp[E_1/R_g T] \exp(\beta p) (mw^{3.4})$$

$$Q = (\eta/2)(\dot{\gamma}:\dot{\gamma}) + R(\Delta H)$$

$$R = -k_m \exp(E_2/R_g T) C^m$$

It is clear that all of these expressions, taken together, constitute a mathematical situation which must be approached with caution. Even though it is not overly difficult to incorporate them into a numerical scheme, which we have done, it is important to proceed slowly enough to develop the proper experience in the computer code's behavior before tackling full-blown problems.

Computer Model.

We have sought to develop a finite element code which is able to predict polymer fluid velocities, stresses, temperatures, and degrees of chemical conversion in a variety of flow geometries and for a variety of fluid material properties. Space limitations prohibit our listing here the full derivation of the finite element equations from the above differential equations, but there exist several well developed means by which this may be done. The reader is directed to standard texts (3,4) for a more complete description, and we will just state here that we employ the Galerkin method of weighted residuals, together with isoparametric mapping and interpolation, to replace the differentials by integrals which can be evaluated numerically over small subregions ("elements"). The results of these numerical integrations are then assembled into a set of simultaneous algebraic equations which can be solved numerically.

The salient features of our code can be listed briefly as follows: (1) Velocity, temperature, and chemical conversion are taken as nodal unknowns, so that coupled incompressible

viscous flow and diffusive-convective heat and mass transport may be modeled. (2) Incompressibility is enforced by a "penalty" formulation employing selective reduced integration. This approach requires the use of double precision arithmetic with a concommitant reduction in the amount of available core, but it has several programming advantages which usually outweigh this drawback. (3) The code is developed primarily for plane and axisymmetric flows. We have coded a three-dimensional capability, but generally feel that the expense of running three-dimensional problems is not justified for most of our modeling research. (4) The code includes several models for the effect of shear rate, temperature, pressure, and chemical conversion on the fluid viscosity. These nonlinear models have not yet been researched extensively, however, and the exploration of the interative schemes needed for their proper use constitutes a major goal for future research. We have also coded a capability for viscoelastic fluid effects (ref. 5), but currently feel that this difficult aspect of polymer flow is being researched satisfactorily by other workers. (5) Convective transport of heat or chemical species can be handled either by a conventional Galerkin treatment or by the convenient but still controversial "optimal upwinding" approach. (6) The code can treat transient problems by

means a two-point "theta-method" time-stepping algorithm. The dynamic algorithm is also useful in nonlinear problems, in which the final fluid state may be approached dynamically from an estimated initial state. (7) The code is capable of a variety of iterative treatments of nonlinear problems, including Newton-Raphson iteration and incremental load methods.

Some additional discussion is warranted concerning the treatment of convective effects beyond what has been mentioned in item (5) above. Momentum convection ($\rho u \cdot \nabla u$) is generall negligible in comparison with the viscous terms due to the high viscosities of polymer fluids, but the convective terms tend to dominate the energy and mass transport equations due to the generally low thermal and mass diffusivities. The programming of the convective terms presents no special problems in the Galerkin approach beyond the need to store and solve unsymmetric matrices, but it is well known that the presence of strong convective terms tends to create oscillations in the final solutions which can be large enough to destroy their value. This instability is related to the tendency of convection to produce large downstream gradients which the finite element grid cannot resolve. A largely ad hoc procedure known as "upwinding"

has been used in both finite element and finite difference work which seems to alleviate this problem by providing a greater numerical weight to the upstream portion of the element. Hughes (6) has published a very convenient means of upwinding, in which the sampling points in the numerical integration scheme are simply moved upstream an appropriate distance. We have made extensive use of the Hughes upwinding technique, but the reader is cautioned that this method is regarded as controversial by many workers. A provocative paper by Gresho (7) details many of the possible pitfalls in upwinding, and states a strong preference for grid refinement as the appropriate cure for convection-induced instabilities.

Selected Numerical Results.

Nonreactive entry flow. Figure 1 shows the streamlines for a 4:1 entry flow. Here a grid of 100 four-node linear elements was used to model the upper symmetric half of a plane capillary, and a fully-developed Poiseuille velocity was imposed on the reservoir entry as a boundary condition. The streamlines are identical with published experimental and numerical results, although the grid used here was not

intended to be fine enough to capture the weak recirculation which develops in the stagnant corner of the reservoir.

The temperature contours for convectionless flow are shown in figure 2, which shows a hot region at the entrance of the capillary due to the combination of high viscous energy dissipation there and its distance from cool boundaries to which heat may be conducted. These isotherms are normalized on the maximum centerline temperature expected for Poiseuille flow in the capillary.

The importance of thermal convection relative to conduction is given approximately by the Peclet number $Pe = UL\rho c/k$, where U and L are a characteristic velocity and length. Figure 3 plots the variation of temperature along the centerline for various values of the Peclet number, and it can be seen that the effect of increased thermal convection is to sweep the cooler upstream flow particles into the capillary, with a resulting lowering of the temperatures overall and a shift downstream of the hot spot near the throat. The relatively coarse grid used in this problem produced unstable Galerkin results for Peclet numbers higher than approximately ten, and the higher degrees of thermal convection were computed using the upwinding formulation.

Further tests with refined grids should be completed to assess the accuracy of the upwinded solutions, although the plots in figure 3 appear reasonable.

One-dimensional reactive flow. As a preliminary trial problem in our computations of reactive flow, we have studied a simple situation in which a fluid obeying first-order chemical kinetics moves at constant velocity and temperature in the positive x direction. Here only the mass-transport equation is operative, and it takes the simple form:

$$u(dC/dx) = -KC + D(d^2C/dx^2)$$

This equation is solved easily, and for nonzero values of the diffusion coefficient D two boundary values for C must be specified. One of these is the initial concentration at the inlet, and the other requires a consideration of the outlet conditions. Here several possibilities exist, and we have studied the case in which the concentration of the outlet reservoir is allowed to rise to meet that supplied by the flow; this is equivalent to specifying a zero concentration gradient at the outlet. For the case of negligible diffusion (D=0), the second-order term vanishes from the

above equation and the downstream boundary condition cannot be specified. The solution is then a simple exponential, in which the reactive species vanish according to first-order kinetics as they are carried downstream at constant velocity.

Figure 4 shows the computed and exact predictions for reactive group concentration as a function of distance along the channel. The Galerkin values are nearly exact, but it is clear that upwinding leads to erroneous results in the small-diffusion case. The upwinding has introduced an artificially high diffusivity and a zero concentration gradient at the outlet, and such artifacts must be considered as possibilities when upwinding is used.

Two-dimensional nonisothermal reactive flow. Figure 5 shows the contours of constant conversion for a two-dimensional analog of the flow discussed in the previous section. Here again, a simple uncoupled problem is treated in which the material parameters are taken to be independent of the solution variables, and in which the velocity conditions are prescribed. The concentration is taken to have a fixed value at the inlet and a zero gradient at the outlet, as before. The two-dimensionality of the problem is con-

tained in two features: the velocity is taken to be parabolic, ranging from a maximum at the centerline to zero at the walls (a Poiseuille flow); and now diffusive heat and mass transport can occur in both the x and y direction. For the low diffusivities shown, mass diffusion in the x direction is negligible, as was demonstrated in the previous section. However, the concentration gradients in the y direction are substantial, so that diffusive transport in that direction is appreciable even at D = 0.01. At D = 0.001, even the y diffusion is negligible, so the concentration contours simply represent a fluid which moves in the x-direction while reacting by first-order kinetics. The concentrations along the centerline are then identical with the D = 0.01 curve of figure 4.

Figure 6 shows the contours of constant temperature which result from this flow (with D = .001), where the temperature boundary conditions were set to zero at the entry and along the top and bottom surfaces. The temperature gradient at the outlet was allowed to become zero, similar to the concentration gradient. The results obtained for the temperature field are of course dependent on the values chosen for fluid properties. To avoid using space here for a detailed discussion of the dimensional analysis used for

selecting these parameters, we will state simply that in figure 6 the viscous dissipation and reaction heat make approximately equal contributions to the internal heating (Brinkman and Damkoehler numbers both equal to three).

Conclusions.

The numerical model described above has a significant present ability to simulate a wide range of problems in polymer processing. At the same time, it is small enough to permit easy implementation in even rather small processing facilities, and for quick familiarization by process designers. We feel such a capability will lead to a significant advance in industry capability for process development and optimization.

Nomenclature.

c	specific heat
C	concentration of reactive species
D	diffusion coefficient
E_1	activation energy for viscosity
E_2	activation energy for reaction
k	coefficient of thermal conduction
k_m	reaction rate preexponential factor
K	overall reaction rate
m	reaction order
mw	molecular weight

ORIGINAL PAGE IS
OF POOR QUALITY

n power-law exponent for viscosity
p pressure
Q internal heat generation
R internal species generation
R_g gas constant
T temperature
u velocity or velocity vector
β factor for pressure dependency
$\dot{\gamma}$ shear rate
η viscosity
η_0 viscosity coefficient
ρ density
ΔH heat of reaction
∇ gradient operator

Literature Cited.

1. Bird, R.B., W.E. Stewart, and E.N. Lightfoot: "Transport Phenomena," John Wiley & Sons, Inc., New York, 1960.

2. Middleman, S.: "Fundamentals of Polymer Processing," Mc Graw-Hill Co., New York, 1977.

3. Zienkiewicz, O.C.: "The Finite Element Method," McGraw-Hill Co., London, 1977.

4. Huebner, K.H.: "The Finite Element Method for Engineers," John Wiley & Sons, Inc., New York, 1975.

5. Collins, B.R., S.M. Thesis, MIT, Cambridge, 1981.

6. Hughes, T.R.J., W.K. Liu, and A. Brooks, J. Comp. Physics, vol. 30, pp. 1-59, 1979.

7. Gresho, P.M., and R.L. Lee, Computers and Fluids, vol. 9, pp. 223-253, 1981.

Figure Captions

Figure 1 - Streamlines for nonreactive 4:1 entry flow, Newtonian fluid with imposed Poiseuille flow at inlet.

Figure 2 - Contours of constant temperature for convectionless entry flow, with heat generation by viscous dissipation only.

Figure 3 - Entry flow centerline temperatures at various Peclet numbers.

Figure 4 - Degree of conversion along channel in one-dimensional reactive flow.

Figure 5 - Isoconversion contours in two-dimensional reactive flow at two different mass diffusivities, Galerkin calculations.

Figure 6 - Isothermal contours in two-dimensional reactive flow, Galerkin calculation. Heat generation by viscous dissipation and reaction heating.

LIST OF PUBLICATIONS

Roylance, D.K., "Use of 'Penalty' Finite Elements in Analysis of Polymer Melt Processing," Polymer Engineering and Science, vol. 20, pp. 1029-1034, 1980.

Roylance, D.K., "Finite Element Modeling of Nonisothermal Polymer Flows," Computer Applications in Applied Polymer Science, American Chemical Society Symposium Series, No. 197, pp. 265 - 276, 1982.

C. Douglas and D. Roylance, "Finite Element Analysis of Nonisothermal Polymer Processing Operations," Proceedings of the Fourth International Symposium on Finite Element Methods in Flow Problems, Tokyo, July 1982.

C. Douglas and D. Roylance, "Chemorheology of Reactive Systems: Finite Element Analysis," Organic Coatings and Plastics Chemistry, American Chemical Society, September 1982.

ORIGINAL PAGE IS
OF POOR QUALITY

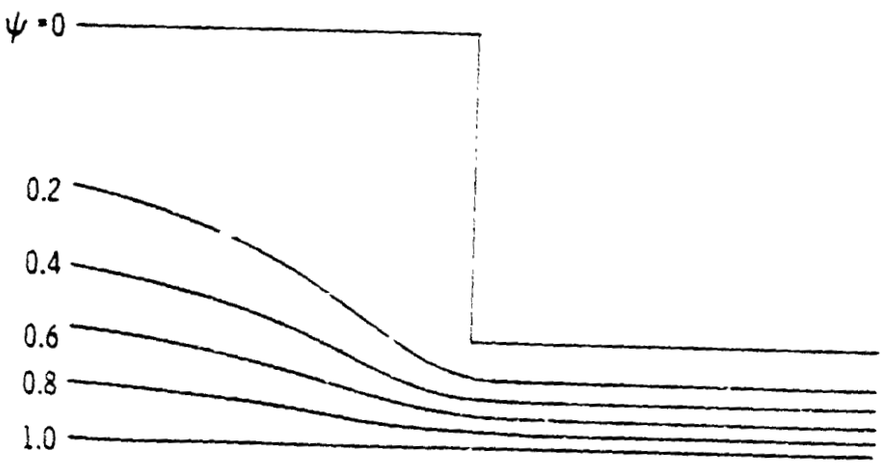

Figure 1 - Streamlines for nonreactive 4:1 entry flow, Newtonian fluid with imposed Poiseuille flow at inlet.

ORIGINAL PAGE IS
OF POOR QUALITY

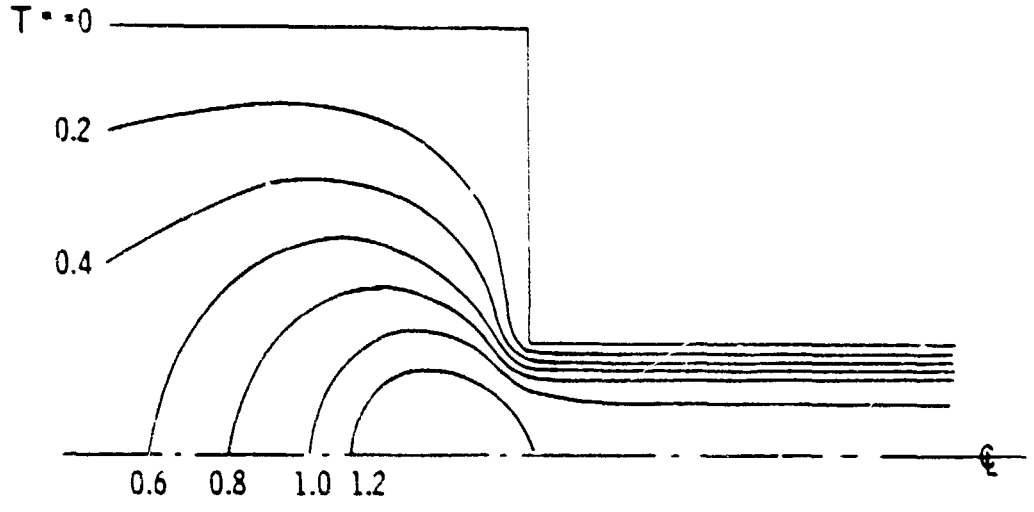

Figure 2 - Contours of constant temperature for convectionless entry flow, with heat generation by viscous dissipation only.

OF POOR QUALITY

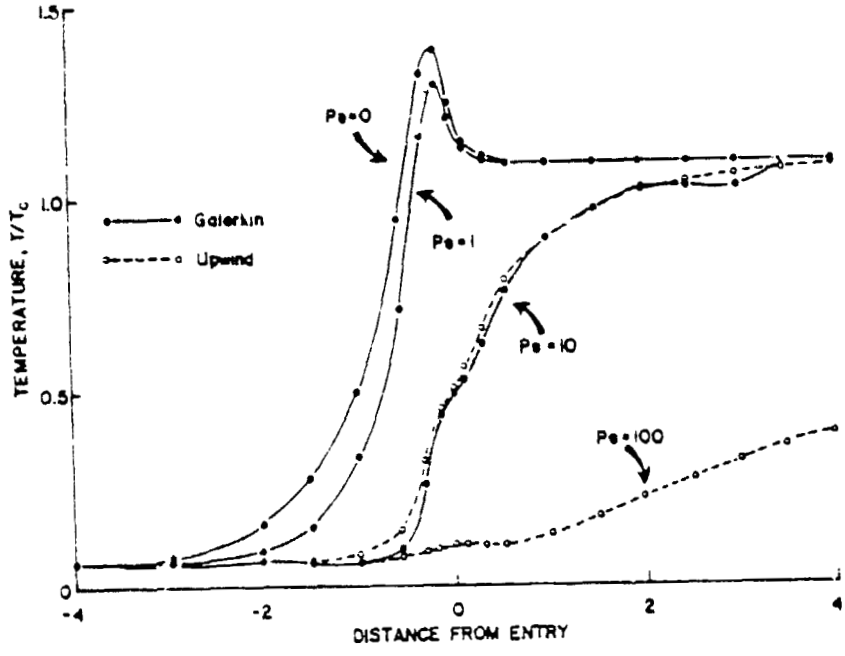

Figure 3 - Entry flow centerline temperatures at various Peclet numbers.

ORIGINAL PAGE IS
OF POOR QUALITY

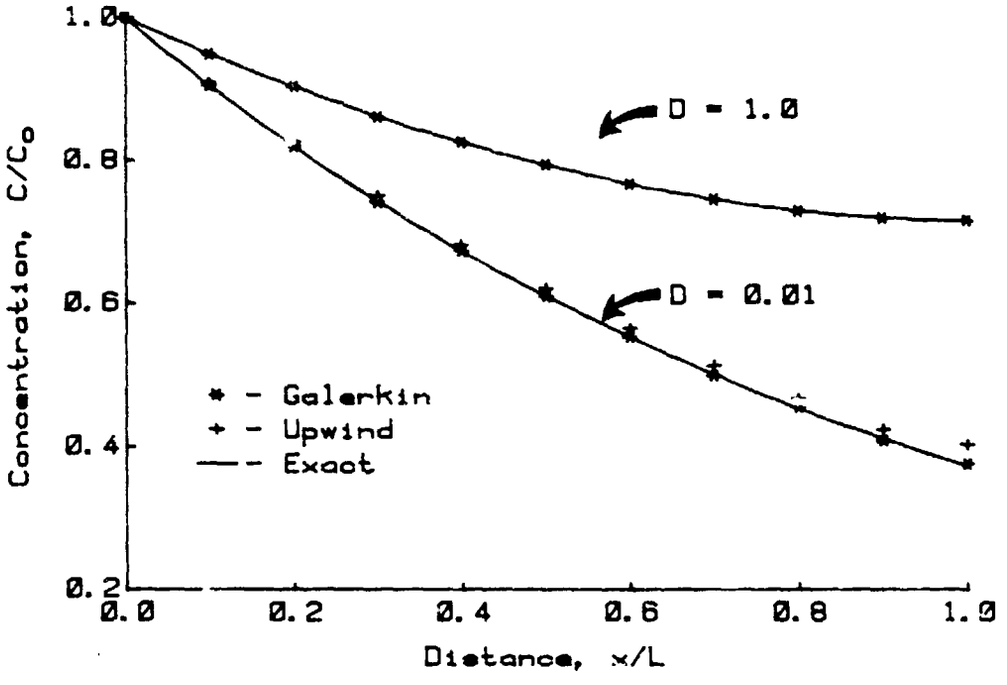

Figure 4 - Degree of conversion along channel in one-dimensional reactive flow.

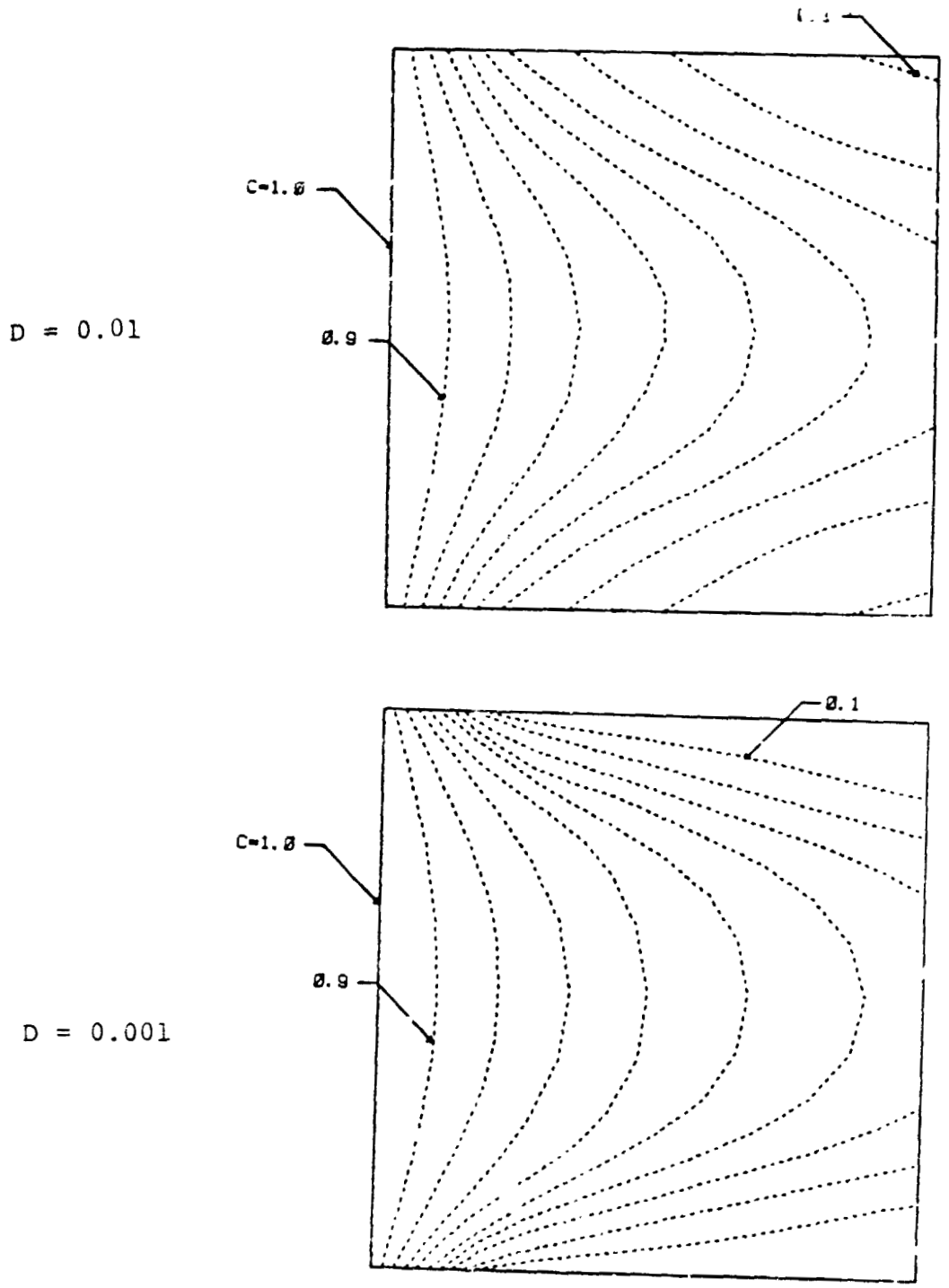

Figure 5 - Isoconversion contours in two-dimensional reactive flow at two different mass diffusivities, Galerkin calculations.

ORIGINAL PAGE IS
OF POOR QUALITY

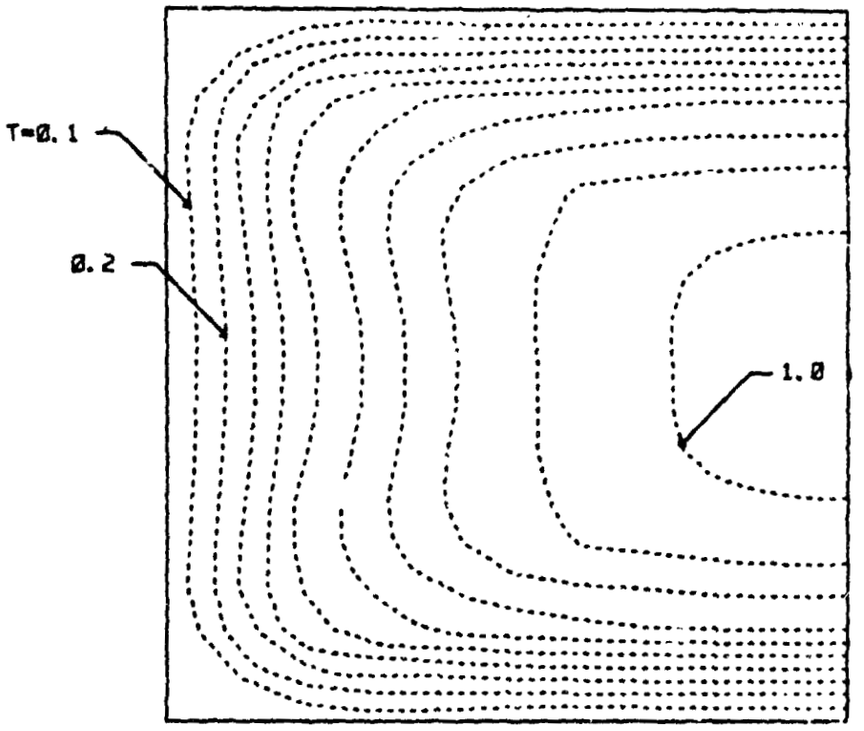

Figure 6 - Isothermal contours in two-dimensional reactive flow, Galerkin calculation. Heat generation by viscous dissipation and reaction heating.

ORIGINAL PAGE IS
OF POOR QUALITY

Studies of Metals Electroprocessing in Molten Salts

Principal Investigator: Donald R. Sadoway

RESEARCH ABSTRACT

Molten salts are very important solvent systems in which the electrodeposition of a wide variety of metals may be conducted. However, solid electrodeposits from molten salts are typically incoherent, powdery and/or dendritic. Fluid flow patterns in the electrolyte are being observed by a laser Schlieren imaging technique in order to determine how mass transport affects the morphology of the metal deposit and thus improve our understanding of the electrodeposition process. Studies are being conducted on the same metal, zinc, both in aqueous electrolytes in which coherent solid electrodeposits are produced, and in transparent molten salt electrolytes. Process variables such as current density and composition of the electrolyte are adjusted to change the morphology of the electrodeposit and thus to permit the study of the nature of electrolyte flow in relation to the quality of the electrodeposit. The results of this work will be helpful in electrochemical cell design and will serve as a data base for subsequent mathematical modeling of fluid flow in such systems.

RESEARCH REPORT

The present study is unique in that it seeks to explain the poor quality of solid electrodeposits in molten salts through a consideration of the effects of fluid flow of the electrolyte. The same metal is being electrodeposited in separate experiments from aqueous solutions and molten salt electrolytes. Transparent cells allow observation of electrolyte circulation patterns by a laser Schlieren optical technique.

ORIGINAL PAGE IS
OF POOR QUALITY

Zinc has been chosen as the metal to study. It can be deposited both from aqueous chloride and molten chloride electrolytes; furthermore, both types of electrolyte systems are transparent to visible light, an important property which permits the use of noninvasive optical techniques of flow measurement.

As this project is the first of its kind at the Materials Processing Center, much effort was previously spent in building up an electroprocessing laboratory. Facilities such as those for flow visualization by laser Schlieren imaging were acquired. These include a pneumatically supported research grade optical bench measuring 4' x 6'. The present optical arrangement is capable of recording the laser images in any of these formats: 35 mm photographic film, 8 mm movie film, or 1/2-inch videocassette. Of course, the necessary electrochemical instrumentation such as a potentiostat, waveform programmer, coulometer, and X-Y and strip chart recorders have also been acquired.

Phase I of the zinc plating study was devoted to the electrorefining of zinc in aqueous acid chloride solutions. Working at room temperature without the need for furnaces and controlled atmosphere cells allowed concentration on perfecting the optics of the system. Following a survey of the literature on acid zinc chloride solutions, a study of the chemistry of these solutions was conducted with the purpose of identifying the dominant ionic species present as a function of $ZnCl_2$ concentration, alkali chloride concentration, and pH. The purpose of this study was to identify the conditions under which zinc is present as a single ionic species. The literature survey showed that other studies of zinc electrodeposition have been confounded by ill-defined chemistries. In this project, two specific studies were performed. First, a single thermodynamic model of the aqueous acid zinc chloride system was constructed to calculate the distributions of Zn^{2+}, $ZnCl^{+}$, $ZnCl_2$, and $ZnCl_4^{2-}$ as functions of concentration and pH. Thermodynamic data were those reported in the literature.

Figure 1 shows that as long as one is restricted to the binary electrolyte system, $ZnCl_2$-H_2O, there is no concentration for which a single zinc species dominates. As a result, a third component was added to the electro-

ORIGINAL PAGE IS
OF POOR QUALITY

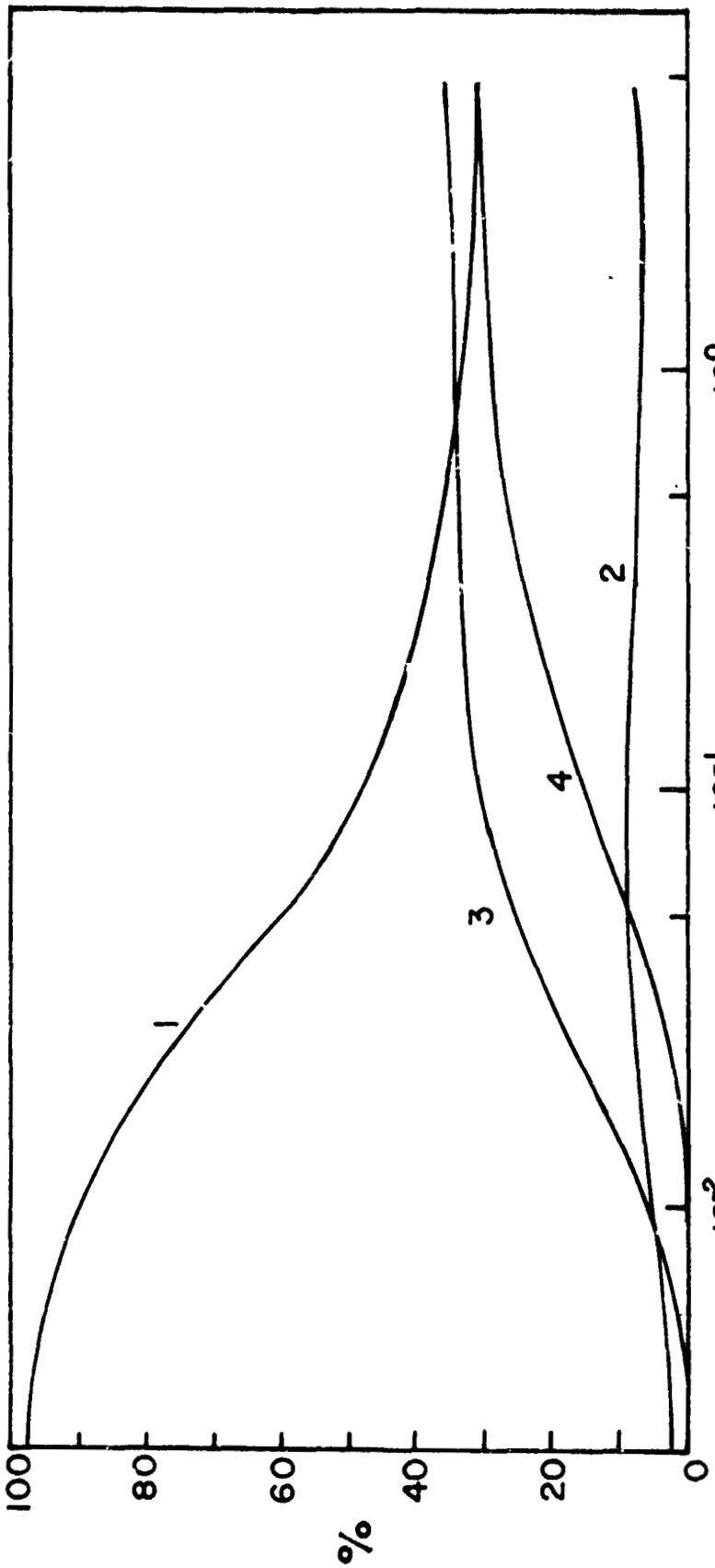

Figure 1. Relative concentration of free and complexed zinc species as a function of molar concentration of $ZnCl_2$. Curves 1, 2, 3, 4 refer to Zn^{2+}, $ZnCl^{+}$, $Zn\,Cl_2$, and $ZnCl_4^{2-}$, respectively.

ORIGINAL PAGE IS
OF POOR QUALITY

lyte in order to displace the complexation equilibria through the presence of excess chloride ion in the amount of 3 M NaCl. Under these conditions the concentration of $ZnCl_2$ varied from 0.01 M to 1 M, with zinc present only as fully complexed $ZnCl_4^{2-}$. Secondly, titrations were performed to determine the operating range of pH such that the solutions were free of oxychlorides and hydroxide complexes. It was concluded that the optimum pH was in the vicinity of 2-3.

Phase II of the work was the study of the electrochemistry of zinc reduction. Many contradictions in electrochemical behavior were discovered in the literature. These, in many cases, were attributable to incomplete control of bath chemistry. Measurements of critical overpotential were made potentiostatically. Figure 2 shows a typical current vs. time curve from such an experiment. Figure 3 shows a derived quantity, the induction time, plotted as a function of applied potential for two different concentrations of $ZnCl_2$. The critical overpotential, η_c, of 65 mV is defined by the intersection of the two curves on the plot. Confirmation of this quantity was given by similar plots of other time constants of the system.

The third phase of the work was the study of convective flow during electrodeposition. Electrorefining experiments were conducted in cells of three different electrode configurations, shown in Figure 4. In the TF (top free) arrangement, the anode is located below the cathode and is facing downward so that its dissolution does not disturb the electrolyte flow pattern near the cathode. The AT (anode on top) configuration combines the two convective flows, one due to cathodic deposition and the other due to anodic dissolution. Finally, in the G (for grid) configuration, the cathode is no longer a physical barrier to the falling electrolyte. Deposition was performed potentiostatically. Current was recorded for a wide range of overpotentials and compositions. Flow patterns in the electrolyte were observed by laser Schlieren imaging. During the experiments, photographs were made in synchronization with an event marker on the chart paper to permit correlations between the electrochemistry and fluid dynamics.

ORIGINAL PAGE IS
OF POOR QUALITY

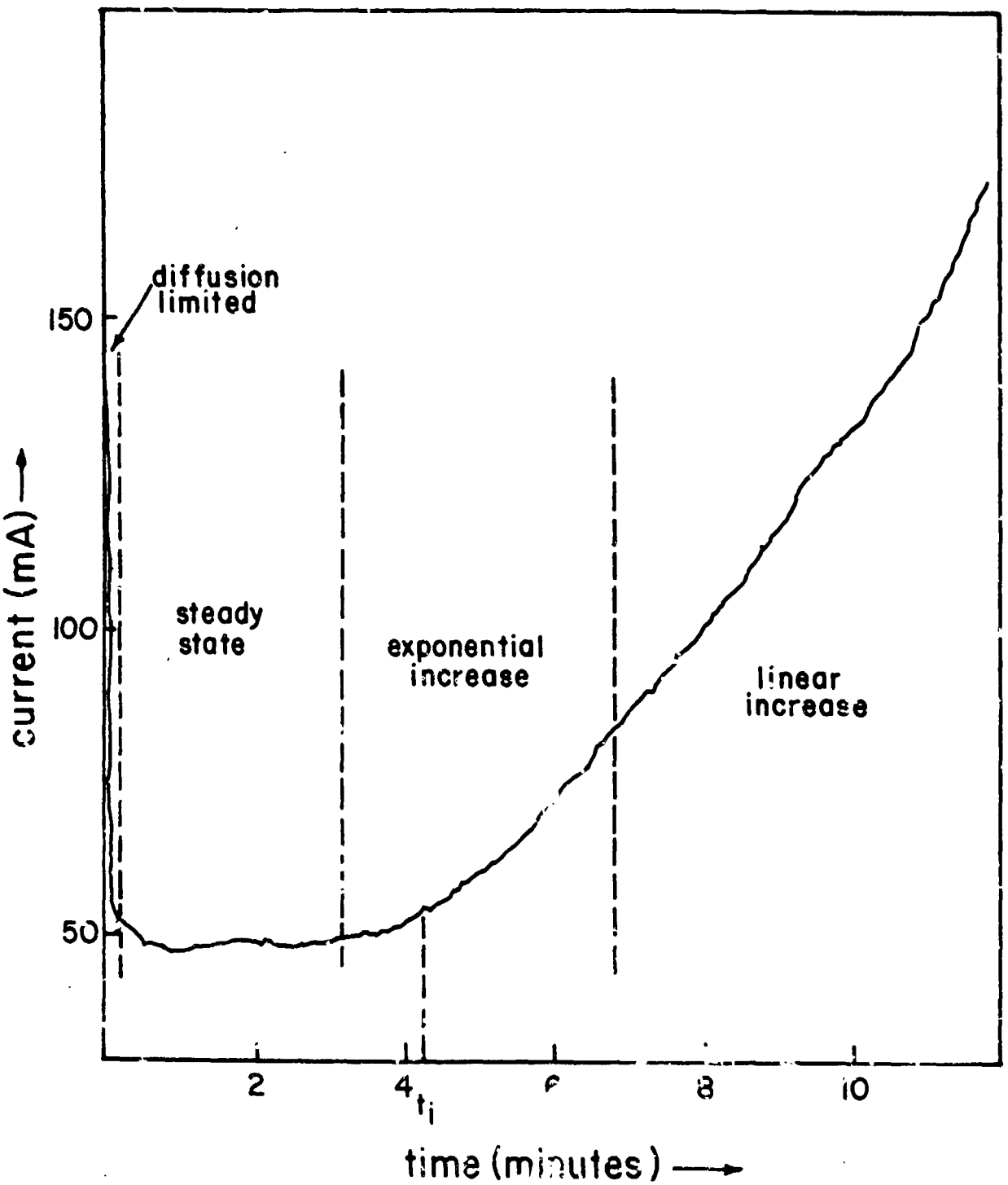

Figure 2. Current-time plot for the determination of the critical overpotential, η_c, in Solution I. Applied overvoltage was 150 mV.

ORIGINAL PAGE IS
OF POOR QUALITY

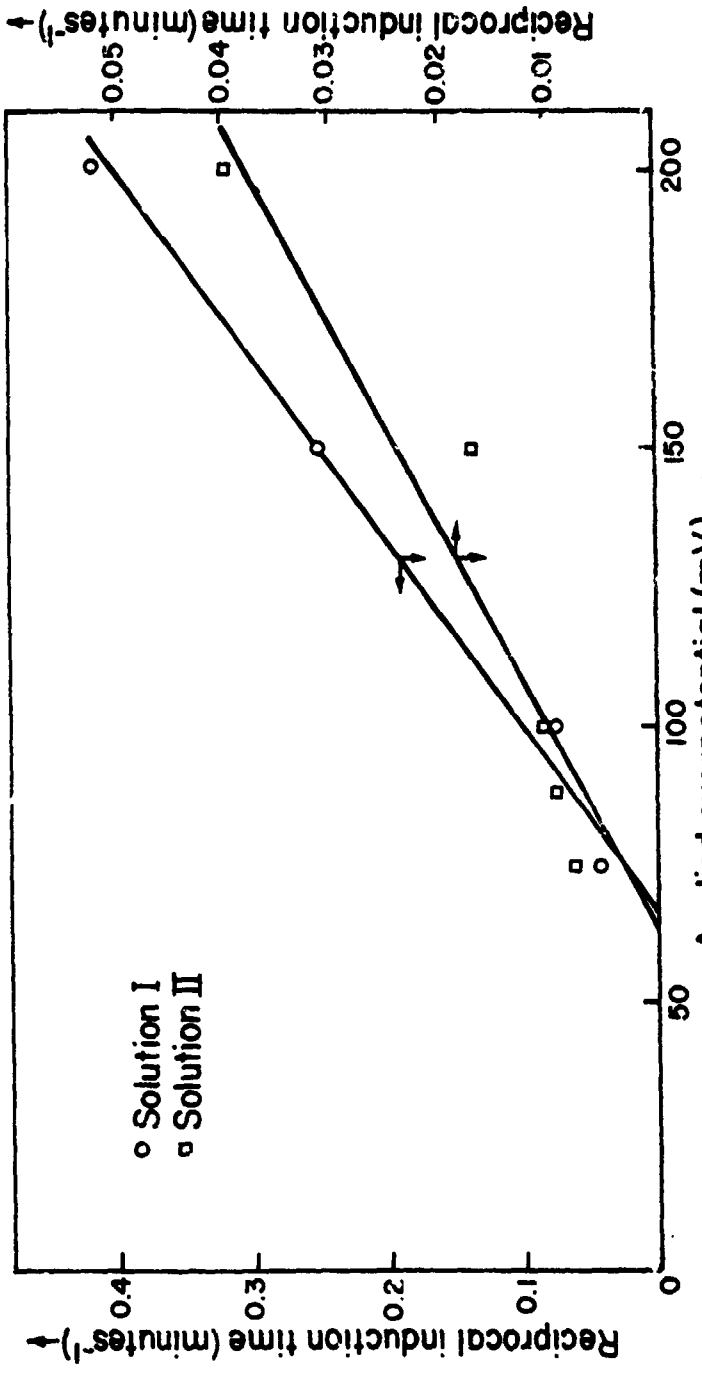

Figure 3. The dependence of induction time for dendrite growth on applied overpotential.

C-4

ORIGINAL PAGE
OF POOR QUALITY

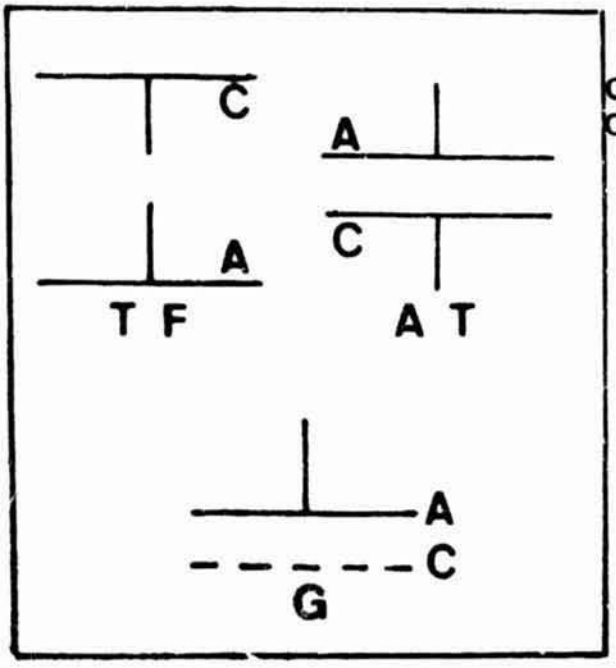

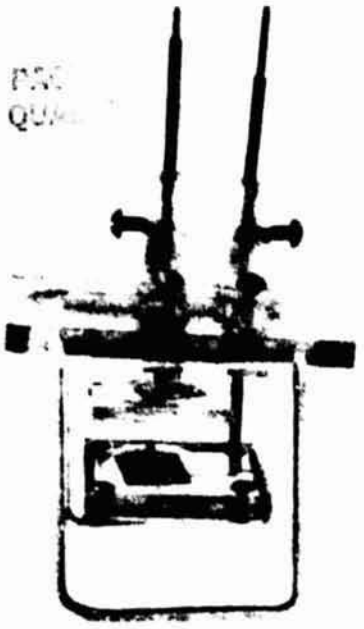

A T

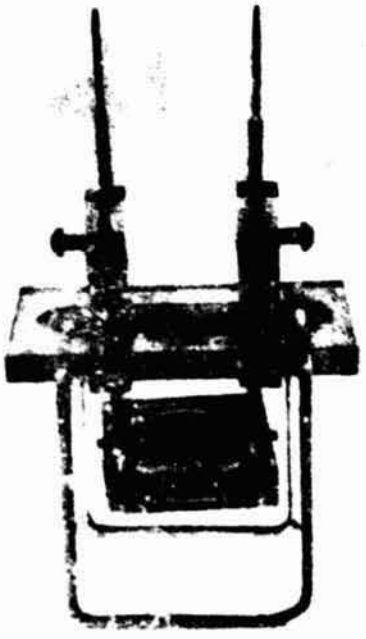

T F

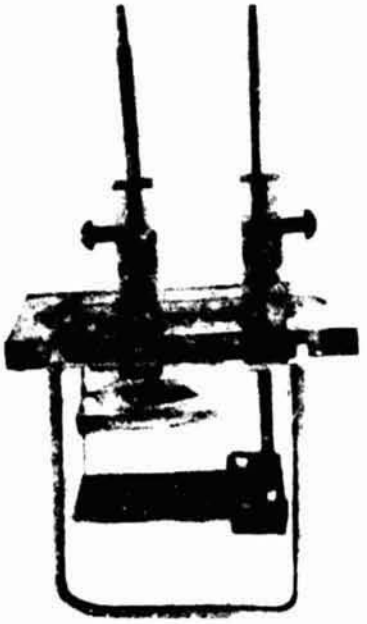

G

Figure 4. Electrode configurations used in the present study.

ORIGINAL PAGE IS
OF POOR QUALITY

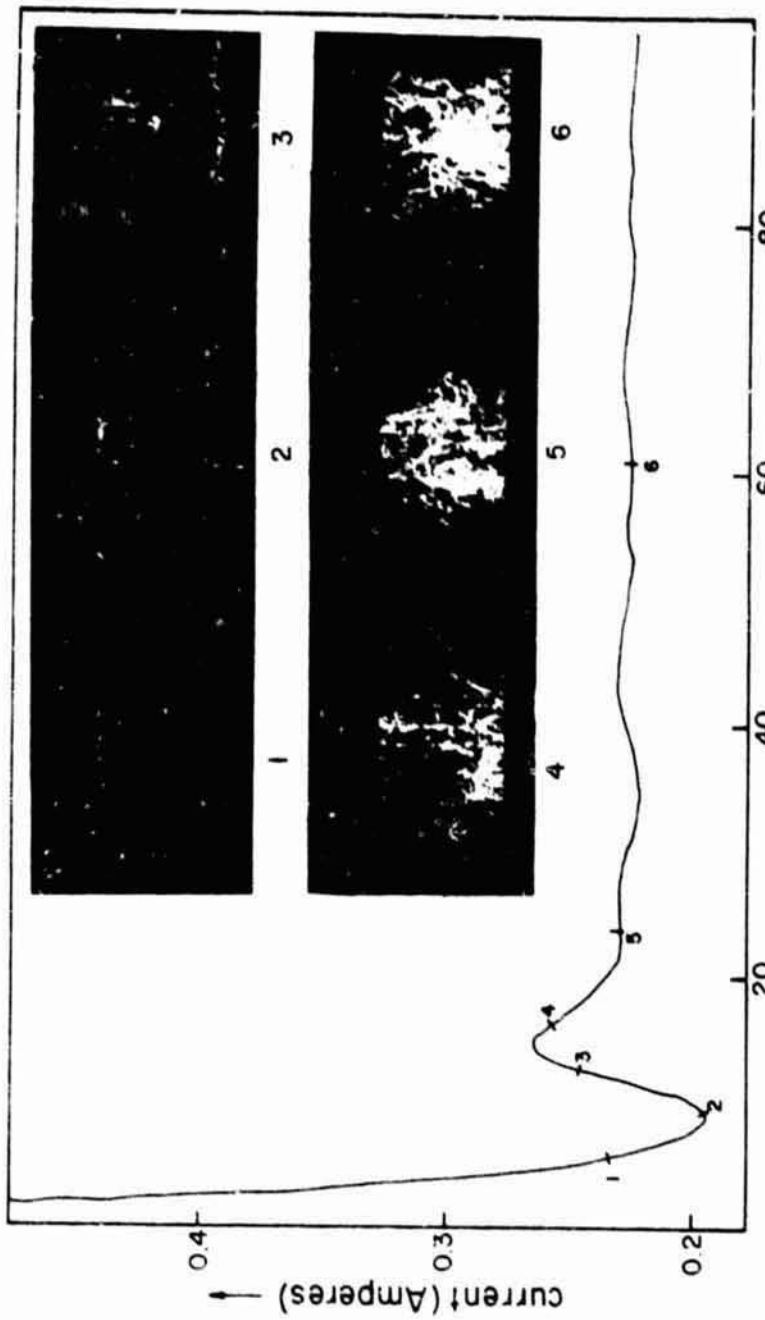

Figure 5. Electrolyte flow patterns during potentiostatic deposition of zinc from solution II, η = 250 mV, AT electrode configuration. Anode surface is at the top of the picture frame; cathode surface is at the bottom.

Figure 5 shows the compilation of the current-time plot and the laser Schlieren photographs for an experiment in which the AT electrode configuration was used. The salient features are as follows. First, dissolution at the anode occurs before deposition at the cathode. The plane of intersection of ascending and descending plumes is closer to the cathode than to the anode. The anodic plumes, which by this time have already started necking, push their rising counterpart outward and soon a toroidal convection cell is established. The electrolyte flows downward in the center and upward at the edge. Quantitative results of such quantities as steady-state current and various critical time constants were also obtained below and at the limiting current. Correlations of these quantities with concentration agree well with results in the literature. They indicated that the Rayleigh numbers involved were high enough (in excess of 5000) that convection is turbulent and independent of electrode dimensions.

These encouraging results are now being extended to molten salt cells. This will allow the comparison between electrolyte systems. Furthermore, through liaison with NASA staff at the Marshall Space Flight Center, thought is being given to studying low gravity electrodeposition. This would further reveal the role of turbulence and convective forces in electrodeposition operations.

LIST OF PUBLICATIONS

1. A. A. Abdelmassih, "Effect of Fluid Flow on Zinc Electrodeposits from Acid Chloride Electrolytes", S. M. Thesis, M. I. T., February 1982.

2. P. T. Rogers, "Fluid Flow Studies of Molten Salt Electrolytic Cells by Laser Schlieren Imaging", S. B. Thesis, M. I. T., June 1982.

3. A. A. Abdelmassih and D. R. Sadoway, "Laser Schlieren Studies of Aqueous Zinc Chloride Electrolysis", in Chloride Electrometallurgy, P. D. Parker and P. Duby, editors, TMS-AIME, Warrendale PA, 1983.

Adaptive Materials Processing

Adaptive Control of Welding Processes

Principal Investigator: Thomas W. Eagar

RESEARCH ABSTRACT

The objective of this research is to use modern digital signal analysis techniques to determine natural oscillations occurring in the welding arc voltage and to attempt correlation of these signals with defects in the welds. Work was initiated in the spring of 1981 by purchase of a dedicated minicomputer. During the previous reporting period, the computer was brought on-line and a number of test welds were made which proved that disturbances to the welding process could be detected in either the time domain or in the frequency domain. Unfortunately the noise levels from the commercial welding power supply were of the same order of magnitude as the measured disturbances. In the past year, a more sophisticated welding power supply has been designed and built, computer software and hardware have been upgraded, and signals from additional welds have been analyzed. The results continue to be encouraging, but the optimum signal analysis technique has not yet been determined.

RESEARCH REPORT

The two greatest problems identified in the previous report period were the extraneous noise generated by the commercial welding power supply and the distortion caused by recording the welding voltage on magnetic tape. Both of these problems have been overcome in the current report period.

The first problem was overcome by acquiring a 600 amp DC (rms) transistorized current regulator manufactured by Alexander Kusko, Inc.

This was delivered in January 1982; and after a period of initial testing, the regulator has proven extremely useful. The regulator can maintain a welding current constant to within 1%, thus permitting a high signal-to-noise ratio. The regulator is linear to more than 20 kHz which permits the use of precisely pulsed current when necessary. Figure 1 compares the current stability of a commercial constant current welding power supply with the regulator obtained with the Kusko supply. These tests were made on a large carbon block resistor. The coarse steps of ± 5 amperes are due to the sensitivity of the A/D converter used to record the signal. The actual regulation of the Kusko supply is better than ± 0.5 ampere at this current level.

The second problem of distortion of the signal by the AM magnetic tape has been corrected by software modifications to the computer which allow a direct 10 kHz sampling rate. Figure 2 shows a square wave as measured by the new direct input technique compared to the same square wave as recorded on the magnetic tape. The direct input technique is clearly superior.

In addition to these software improvements for direct input of the welding process data, a complete signal analysis package was acquired from Signal Technology, Inc. during the summer. This package has saved considerable time during the past few months by permitting emphasis on study of welds rather than on software development.

The initial welds were produced with constant welding current. Although this technique did produce measurable signals during the previous report period, recent tests have shown that this technique is not as sensitive as an impulse or square wave current signal. Figure 3 shows the frequency response of the welding voltage on a stainless steel plate and an aluminum plate at constant current. Although there are minor differences in the signal, the spectrum is generally only white nosie. Figure 4 shows the spectrum on the same materials using a square wave current generated by the Kusko transistorized power supply. The harmonics of the square wave input are clearly observed, but it will be noted that

ORIGINAL PAGE IS
OF POOR QUALITY

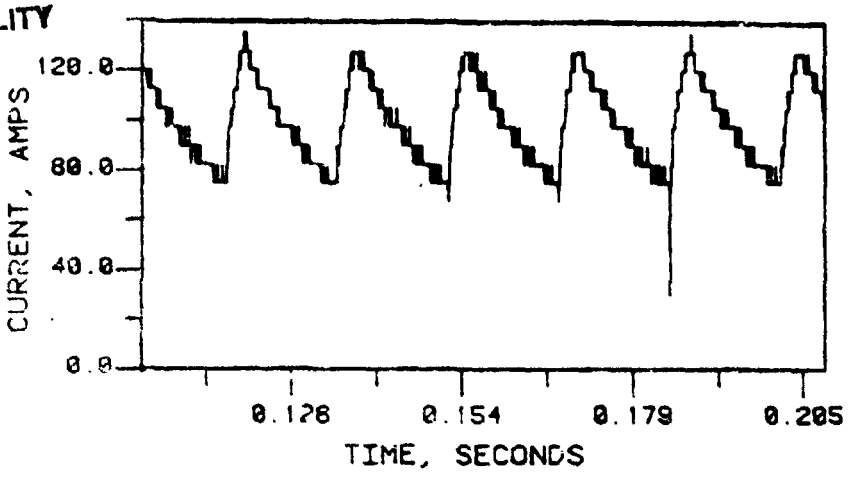

STANDARD DC POWER SUPPLY

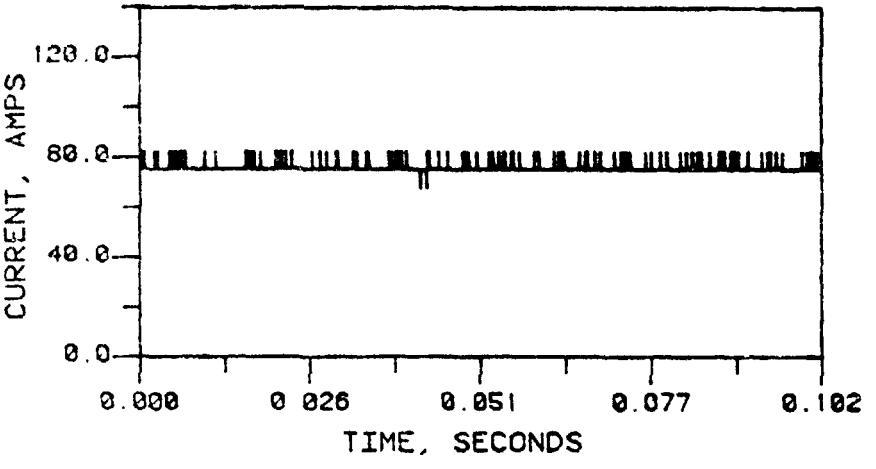

TRANSISTORIZED REGULATOR
WITH BATTERY

Figure 1.

ORIGINAL PAGE
OF POOR QUALITY

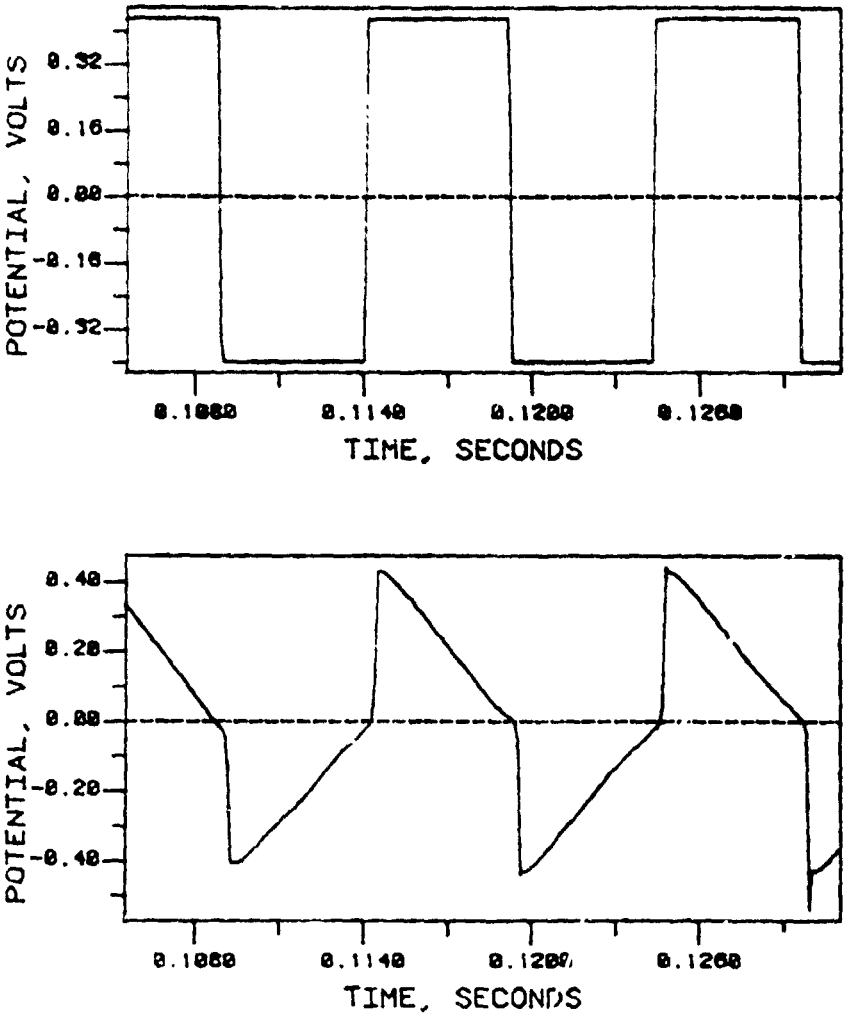

DIRECT INPUT (TOP) VS RECORDED INPUT (BOTTOM)

Figure 2.

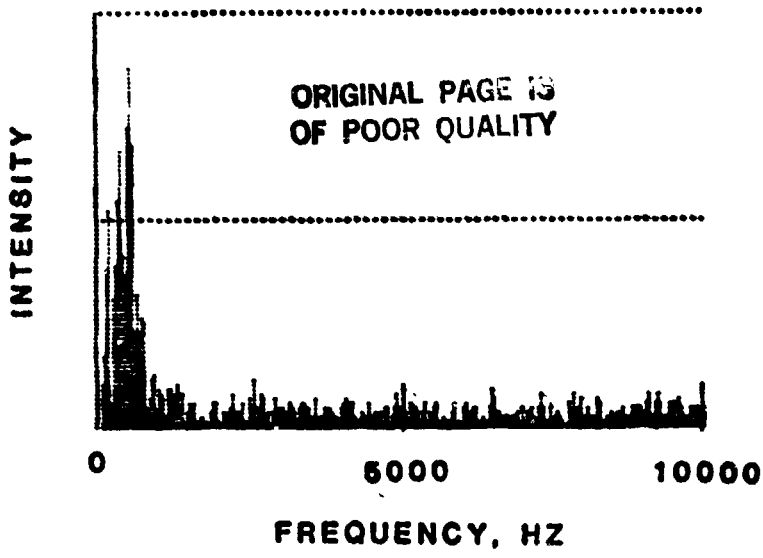

Steel

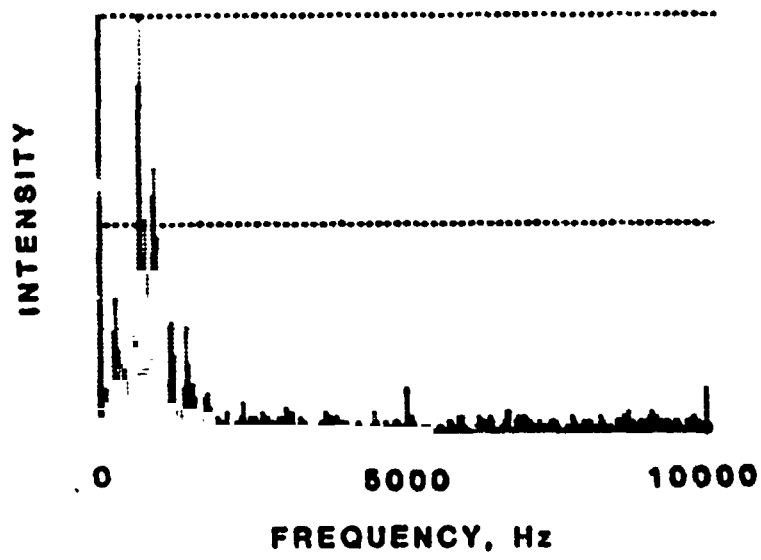

Aluminum

Magnitude transform of DC welds

Figure 3

ORIGINAL PAGE IS
OF POOR QUALITY

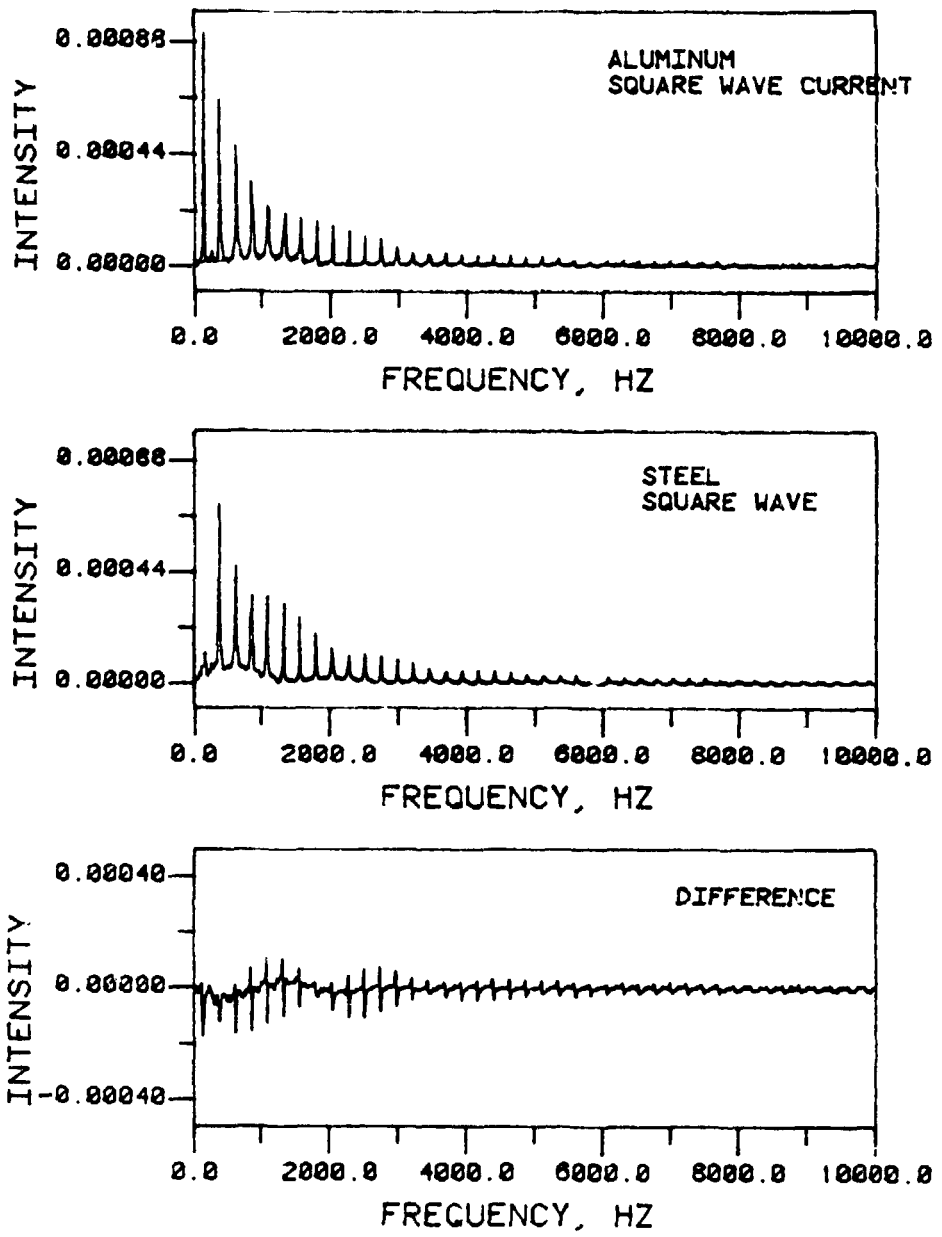

Magnitude Transform of Square Wave Welds

Figure 4.

the envelope surrounding the peaks of these harmonics is different for steel and for aluminum. A simple square wave response generates harmonic peaks which decay exponentially. This exponential decay is distorted for both aluminum and steel but in a different pattern for each. These patterns are very reproducible.

It was also noted that the DC arc voltage level varies between steel and aluminum. This is shown in Figure 5 which represents the shift in arc voltage when welding over a steel-aluminum laminate. These tests show, at least in principle, that welding over regions with chemical variations results in changes in the arc voltage. Studies have begun to test changes in voltage caused by welding over slag inclusions, but the results are inconclusive at present.

Figure 6 shows the change in arc voltage caused by minor disturbances in the shielding gas. These disturbances are more readily observed in the time domain (Figure 6) than in the frequency domain (Figure 7).

CONCLUSIONS

Progress has been made in both the welding equipment and in the signal analysis techniques during the past year. The problems have been solved sufficiently that the project can concentrate on analysis of actual weldments during the current year. This will permit analysis of the frequency response of specific defects, as well as determination of the ultimate sensitivity of this control technique. In addition, welding signals will be analyzed by Nyquist plots in order to determine the transfer function for the process. These results will permit an accurate evaluation of the ultimate usefulness of this technique of weld quality monitoring.

ORIGINAL PAGE IS
OF POOR QUALITY

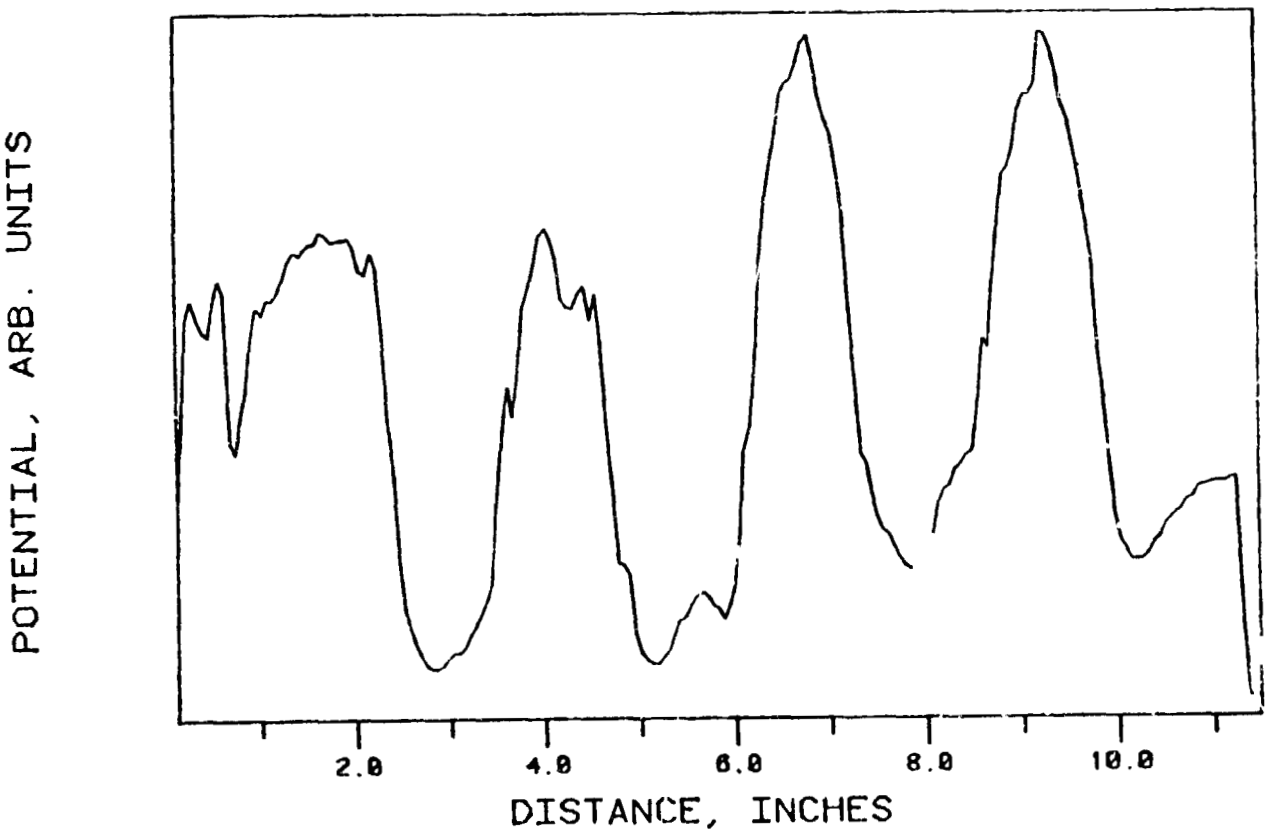

VOLTAGE CHANGES ACROSS A STEEL-ALUMINUM LAMINATE

Figure 5.

ORIGINAL PAGE IS
OF POOR QUALITY

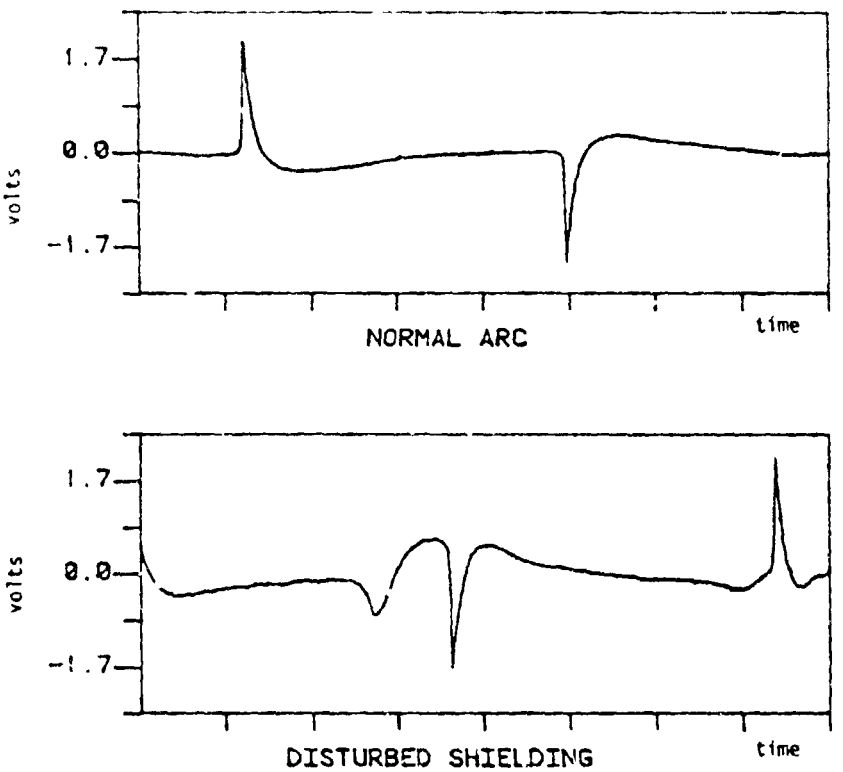

Figure 6. Effect of shielding gas on real time signal.

ORIGINAL PAGE IS
OF POOR QUALITY

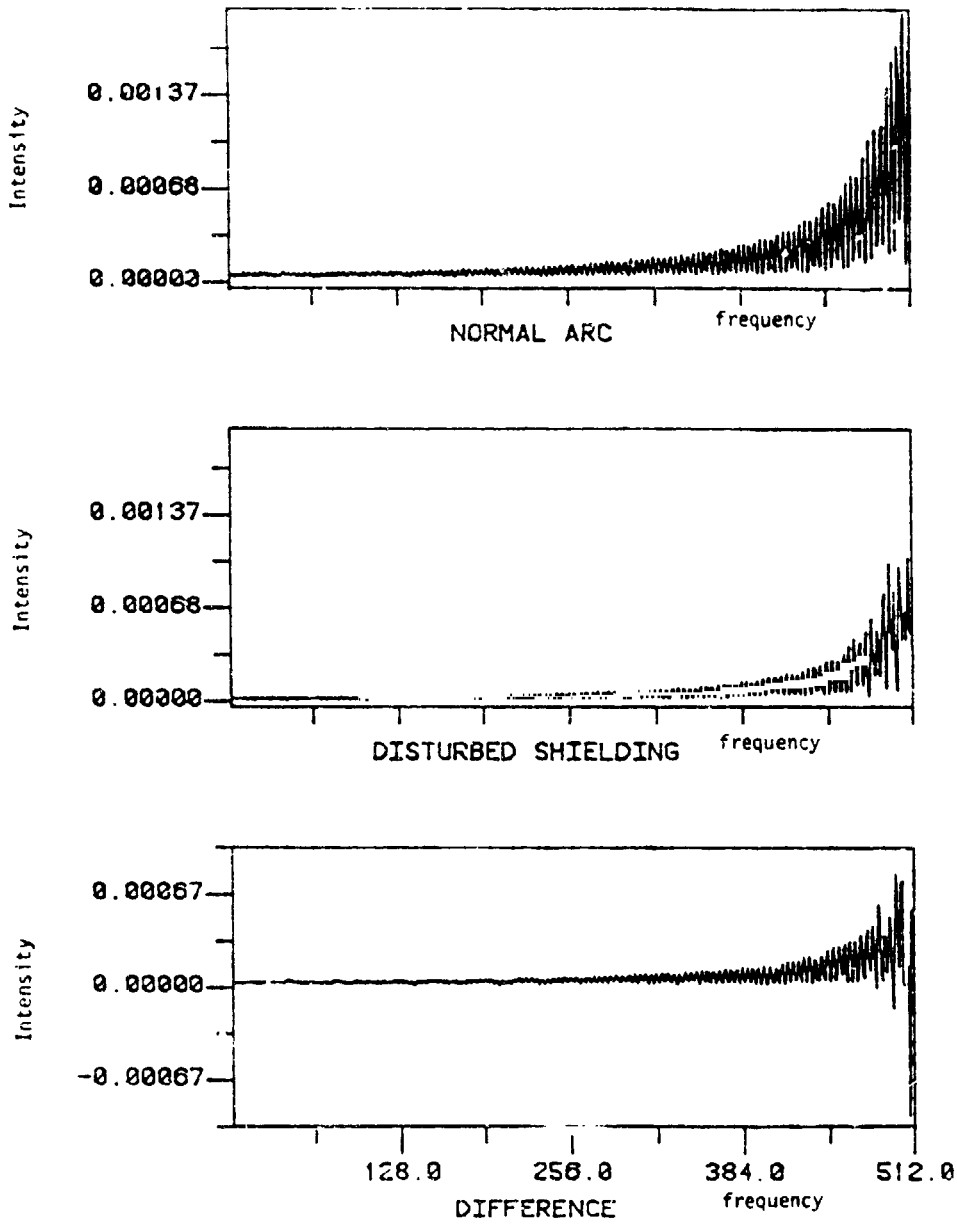

Figure 7. Effect of shielding gas on magnitude transform.